

Design, Analysis and Experimental Investigation of a New Scroll Expander Based Trigeneration System

by

Md. Ali Tarique

A Thesis Submitted in Partial Fulfillment
of the requirements for the Degree of

Doctor of Philosophy

in

Mechanical Engineering Program
Faculty of Engineering and Applied Science
University of Ontario Institute of Technology

Oshawa, Canada

© Md. Ali Tarique. 2014

Abstract

Current technologies of using conventional energy produce a large amount of waste heat which can potentially be recovered in the form of useful work to use in our day to day life. This initiative not only optimizes the energy usage but also contributes to mitigating environmental impact of fossil fuel. There are also two main sources of renewable energy, solar and geothermal that can be used as an alternative to fossil fuel based options. Harnessing of this energy with appropriate low cost technology could be a promising method of alternate energy utilization. However, there are some developed technologies which are already in use to generate medium to large scale of power or power and heat (co-generation). But small scale trigeneration with a single source of energy has not yet been developed. In this research work a small scale trigeneration system is designed, built and experimentally investigated for simultaneous generation of power, heating and cooling.

This integrated system combines a power and cooling cycles where the source heat is used to generate power through a scroll expander and a portion of the heat is used in an ejector cooling system. The residual heat which is normally released to the environment in this type of power cycle is captured as much for hot water heating or space heating. Ammonia-water is used for both the power cycle and the cooling cycle. The experimental investigation of this thesis work analyzed the performance of a scroll based heat engine working with low temperature heat source within the trigeneration facility. Coupling trigeneration and renewable makes a very strong scheme to supply not only low-carbon electricity and low-carbon heat, but also cooling, in an integrated system with high utilization factor. The first part of the work is to study the performance of the heat engine that consists of custom built expander, boiler and condenser in an ammonia water Rankine cycle system. The second part is to determine the utilization of the heat engine driven by low grade heat source in a small scale trigeneration unit. Ammonia water is suitable for low temperature Rankine power cycle, because of its non-azeotropic

properties. The source of heat can be at relatively low and intermediate temperatures in the range of 80°C – 200°C. This heat can be derived from a multitude of sources including solar panel collectors, biomass combustion, biofuel, recovered waste heat etc. Due to the trigeneration feature, the utilization factor of the heat source or fuel energy with this system exceeds 90%. The experimental result shows a maximum isentropic efficiency of 67% and an overall energy efficiency of maximum 7% at 120°C source temperature, while the exergy efficiency is about 30%. The experimental result also shows that the concentration of ammonia is a dominant factor in determining the optimum efficiency with a range of ammonia-water mixture. 40% ammonia concentration found optimum, however higher concentration drastically reduces the work output. In the trigeneration facility, the cooling and heating can be adjusted without affecting power generation. Finally, it can be concluded that from the optimization results, if mass production is put in place, the system shows a high economic competitiveness with respect to conventional power generation methods which require multiple individual systems to provide the same results.

This system is very new and novel with unique features, which would resolve various energetic and environmental issues and provide potential solutions to residential applications. It is also aimed to make such systems suitable for restaurants, hospitals, commercial buildings, social centres, farming facilities and to use in remote locations. The ultimate goal is to produce a viable commercial product.

Keywords: Trigeneration, exergy analysis, optimization, solar power tower, gasification, Fischer-Tropsch synthesis

Acknowledgements

I am extremely pleased to express my sincere, profound and deepest gratitude to my supervisor Dr. Ibrahim Dincer, the renowned professor of **Mechanical Engineering** at the University of Ontario Institute of Technology for giving me this opportunity to conduct research on the “**Scroll expander Based Trigeneration System**” and to pursue my PhD in mechanical engineering. I do sincerely acknowledge his very active and close supervision, continuous encouragement and directions throughout the course of this research. I also express my deepest thanks to him for his insightful suggestions and wholehearted support.

I am especially grateful to Dr. Calin Zamfirescu for his valuable input, research ideas and expert opinion that has given quality dimensions and notable impetus to this work. His presence in the laboratory has always inspired and influenced my work in and outside of the laboratory.

I would like to express my special thanks to Camilo Casallas, who assisted me in setting up the experimental systems and install the data acquisition system.

I would also like to extend my thanks to Snehanshu Sikdar, Manjurul Islam, A.B.M Salahuddin, and Kamrun koli for their willful and constructive contributions. Their kind support and encouragement have been of great value in my research work.

Last but not least, my heartfelt gratitude goes to my wife Shahin Jesrine, beloved son Taseen Jawad and daughter Zariat Ali. Their patience and prudence constantly encouraged me throughout this work. Also, my special thanks to my mother, brother, and sisters for their loving support and blessings from a distance.

Table of Contents

Abstract.....	i
Acknowledgements.....	iii
Table of Contents.....	iv
List of Figures.....	vii
List of Tables.....	xii
Nomenclature.....	xiv
Chapter 1: Introduction.....	1
1.1 Energy Outlook.....	2
1.2 Single Generation, Cogeneration and Trigeneration.....	8
1.3 Motivation.....	11
1.4 Objectives.....	14
1.5 Thesis Outline.....	16
Chapter 2: Literature Review.....	17
2.1 Power Cycles.....	17
2.2 Cooling Cycles.....	23
2.3 Working Fluids For Vapor Power And Cooling Cycles.....	25
2.4 Trigeneration Systems.....	27
2.5 Scroll Expanders.....	29
2.6 Ejectors.....	31
2.7 Heat Exchangers.....	32
2.8 Closing Remarks.....	32
Chapter 3: Trigeneration System Description and Prototype Development.....	34
3.1 System Description and Thermodynamic Cycle.....	34
3.2 Trigeneration System Prototype.....	38
3.3 Scroll Expander Development.....	45
3.4 Ejector Development.....	50
3.5 Heat Exchangers.....	52
3.6 Oil Heater.....	54

3.7 Closing Remarks.....	55
Chapter 4: Experimental Investigation	56
4.1 Experiment 1: Investigations with the Prototype System.....	56
4.2 Experiment 2: Expander Performance Determination with Compressed Air.....	64
4.3 Experiment 3: Ejector Performance Determination.....	65
4.4 Experiment 4: Vapor Generator Investigation.....	67
4.5 Experiment 5: Working Fluid Pump Calibration.....	68
4.6 Experiment 6: Oil Heater Testing and Calibration	69
4.7 Measurement Devices and Accuracy.....	69
Chapter 5: Analyses	74
5.1 Energy and Exergy Analyses of Trigeration System	74
5.2 Ammonia-Water Mixture.....	77
5.3 Geometrical Analysis of Scroll Machine.....	80
5.4 Energy and Exergy Analyses of Scroll Machine	91
5.5 Heat Exchangers Analysis	94
5.6 Ejector Analysis.....	100
5.7 Optimization	105
5.8 Closing Remarks.....	109
Chapter 6: Results and Discussion.....	110
6.1 Experimental Results	110
6.1.1 Uncertainty Propagation	110
6.1.2 Experiment 1	111
6.1.3 Experiment 2.....	123
6.1.4 Experiment 3	127
6.1.5 Experiment 4.....	131
6.1.6 Experiment 5.....	132
6.1.7 Experiment 6.....	133
6.1.8 Discussion.....	135
6.2 Modeling and Numerical Simulations	136
6.2.1 Expander Geometrical Simulations	136

6.2.2 Expander Thermodynamic Simulation	140
6.2.3 Trigeration Cycle Simulations	141
6.3 Comparative Assessment of Trigeration System	151
6.4 Improved Trigeration System and Optimization.....	162
Chapter 7: Conclusions and Recommendations.....	173
7.1 Conclusions.....	173
7.2 Recommendations.....	174
References.....	175

List of Figures

Figure 1.1 Availability of conventional energy resources [data from Ruehl, 2012].....	3
Figure 1.2 Current share and 2050 prediction for energy supply [data from European Commission (2006)]	4
Figure 1.3 Energy demand in Canada [data from Statistics Canada (2008)].....	6
Figure 1.4 Energy demand in Canada [data from Statistics Canada (2008)].....	6
Figure 1.5 Canadian energy demand by fuel type and Canadian residential power, heating and cooling demand [data from Statistics Canada (2008)]	7
Figure 1.6 Black-box representation of a) single generation, b) cogeneration, and c) trigeneration systems	9
Figure 1.7 GHG mitigation potential by year 2100 [data from IPCC (2007)].....	10
Figure 3.1 Ammonia-water based trigeneration system with Rankine and ejector cycle integration.....	35
Figure 3.2 Thermodynamic cycle for the trigeneration system	37
Figure 3.3 Ammonia-water based trigeneration system prototype, as built	39
Figure 3.4 CAD drawing showing the relative placement of the main components of the trigeneration system.....	41
Figure 3.5 Photograph of the trigeneration system	41
Figure 3.6 Photograph detail of the working fluid pump and liquid receiver.....	43
Figure 3.7 Detail photograph of the air-cooled oil cooler.....	44
Figure 3.8 The installation of the metering valve for liquid injection	44
Figure 3.9 Removal of the bypass valve and journal bearing of the original Bristol H20R483DBE scroll module; the journal bearing was replaced with a radial roller bearing.....	45
Figure 3.10 Novel scroll expander / generator assembly.....	47
Figure 3.11 Scroll wraps of the scroll unit (fixed scroll – left side, orbiting scroll – right side)	48
Figure 3.12 Modifications and additions to scroll unit and shaft.....	48
Figure 3.13 Detail photograph of the expander housing: a) upper cap, b) top body, c) bottom body, d) assembled expander, e) thermal insulation	49
Figure 3.14 Expander-generator clutch arrangement.....	49
Figure 3.15 Ejector drawing as-built.....	51
Figure 3.16 Photograph of the ejector as installed in the system.....	51
Figure 3.17 Immersed cooling coil setup connected to the ejector system.....	52
Figure 3.18 Heat exchanger design specification	53

Figure 3.19 Photograph details of the realised heat exchangers: a) front view of inner circuit, b) side view of inner circuit, c) baffles detail for the shell side circuit, d) shell, e) thermally insulated vapor generator, f) condenser.....	54
Figure 3.20 Heater construction.....	55
Figure 4.1 Setup for expander investigation with compressed air.....	64
Figure 4.2 Photograph for air flow rate measurement system at expander discharge	65
Figure 4.3 Setup for Experiment 3 – ejector performance determination.....	66
Figure 4.4 Photograph of the experiment 3 setup	67
Figure 4.5 Photograph of the setup for Experiment 5.....	68
Figure 4.6 Data acquisition systems for temperature monitoring.....	70
Figure 4.7 Hot wire anemometer used for air velocity measurement.....	71
Figure 4.8 Clamp-on ammeter and multi-meter used for current and voltage measurement	71
Figure 4.9 Power sources used to run the DC motors within trigeneration system....	72
Figure 4.10 Level gauge used as part of flow rate determination method for cooling coil.....	72
Figure 4.11 Laptop used for experimental data recording	73
Figure 5.1 Temperature variation during liquid vapor phase change of ammonia water solutions at 3000 kPa	77
Figure 5.2 Vapor and liquid equilibrium lines for ammonia water.....	78
Figure 5.3 Comparison of heat transfer profile in a vapor generator working with steam vs with ammonia-water mixture at 50% concentration	78
Figure 5.4 Representation of scroll wraps and conjugacy points.....	80
Figure 5.5 Representation of the scroll geometry in the complex plane (or polar coordinates).....	82
Figure 5.6 Definition of the interpolation circle between inner and outer scrolls	83
Figure 5.7 Expansion phases and gas chambers formed between the scrolls	85
Figure 5.8 Leakage flow of a scroll compressor	88
Figure 5.9 Expanding chamber generating boundary work due to pressure forces and orbiting movement	91
Figure 5.10 Thermodynamic model for scroll expander.....	93
Figure 5.11 Extended surfaces for heat transfer.....	96
Figure 5.12 Genetic algorithm for optimization	105
Figure 5.13 Multiobjective optimization of multigeneration systems [modified from Dincer and Zamfirescu (2014)].....	107

Figure 6.1	Selection of the period of relative steady-state for data processing	112
Figure 6.2	Thermodynamic cycle determined for Experiment 1, Run 1	113
Figure 6.3	Thermodynamic cycle determined for Experiment 1, Run 2	115
Figure 6.4	Thermodynamic cycle determined for Experiment 1, Run 4	116
Figure 6.5	One subset of recorded temperature data for Run 4	117
Figure 6.6	Identification of a period of quasi-stable operation for Run 4	117
Figure 6.7	Heat input supplementation manoeuvre to maintain steam generation ...	118
Figure 6.8	Thermodynamic cycle obtained in open loop operation (Run 4)	119
Figure 6.9	Thermodynamic cycle with lower working fluid flow rate and expansion of vapors close to saturation	119
Figure 6.10	Thermodynamic cycle for Run 5	121
Figure 6.11	Thermodynamic cycle for Run 6	122
Figure 6.12	Trigeneration cycle data for Run 7	123
Figure 6.13	Isentropic efficiencies before and after rectification	125
Figure 6.14	Volumetric efficiencies before and after rectification	126
Figure 6.15	Level reading and liner data fitting for Experiment 3, Run 1	128
Figure 6.16	Temperature drop and liquid level data recorded for Run 2	129
Figure 6.17	Cooling rate and refrigerant mass flow rate determined for Run 2	130
Figure 6.18	Results for vapor generator testing—Experiment 4	132
Figure 6.19	Recorded and calculated data for oil heater calibration experiment, the temperature in the ceramic core of the heater is also shown	134
Figure 6.20	Super position of the actual scroll vane with the modeled scroll	138
Figure 6.21	Zoom showing the super position of the actual and modeled scroll for determination of starting angles	138
Figure 6.22	The chamber cavity volume and the derivative $V'(\theta)$ of the actual expander, determined based on numerical simulation of the expander geometry	139
Figure 6.23	Results of the expander simulation with air and validation with experimental data	140
Figure 6.24	Efficiency comparisons between cogeneration and trigeneration	142
Figure 6.25	Energy distribution dependant on mass flow diverted to the ejector	142
Figure 6.26	Efficiency over the ammonia concentration spectrum	143
Figure 6.27	Power output behaviour versus ammonia concentration	144
Figure 6.28	Water heating and ambient cooling behaviours versus ammonia concentration	144

Figure 6.29 Optimum ammonia concentration versus arbitrary base	145
Figure 6.30 Cogeneration power output and water heating trends based on concentration of ammonia.....	146
Figure 6.31 Trigeneration and cogeneration power output trends based on concentration of ammonia.....	147
Figure 6.32 Trigeneration and cogeneration water heating trends based on concentration of ammonia.....	147
Figure 6.33 Effect of pump ratio on the efficiency	148
Figure 6.34 Effect of pump ratio on energy outputs	148
Figure 6.35 Boiler temperature effect on the efficiency	149
Figure 6.36 Boiler temperature effect on energy outputs	150
Figure 6.37 COP trend curve as function of CPR for two main entrainment ratios .	150
Figure 6.38 Trigeneration system with ammonia-water compression-expansion ...	152
Figure 6.39 Qualitative representation of the thermodynamic cycle of the power generating section of the trigeneration system.....	153
Figure 6.40 Qualitative representation of the thermodynamic cycle of the refrigeration section of the trigeneration system.....	154
Figure 6.41 Predicted T-s diagram of Ammonia-water heat Rankine cycle trigeneration system (power generation subsystem cycle)	155
Figure 6.42 Predicted T-s diagram of Ammonia-water heat Rankine cycle trigeneration system (refrigeration subsystem cycle)	155
Figure 6.43 Exergy destructions for compression-expansion trigeneration system .	157
Figure 6.44 Exergy destructions for ejector-expander based trigeneration system ..	158
Figure 6.45 Cooling performance of a refrigeration system with COP of 1 using electricity from the grid which is assumed to be from a simple heat power plant.....	158
Figure 6.46 Cooling performance comparison between trigeneration and conventional refrigeration systems in terms of cooling unit per energy input in form of heat.....	159
Figure 6.47 Temperature of the oil in two scenarios with different power inputs....	159
Figure 6.48 Representation of thermal inertia of heater determined by oil cooling .	160
Figure 6.49 Comparative assessment of proposed (top) and conventional (bottom) systems.....	161
Figure 6.50 Improved ejector-expander based trigeneration system	162
Figure 6.51 Predicted <i>T-s</i> diagram of the improved and optimized the trigeneration system	165
Figure 6.52 Exergy destruction in the components of the improved and optimized trigeneration system (in percent)	166

Figure 6.53 Influence of ammonia concentration and temperature of the saturated vapor (T_{4v}) on power generation efficiency (η_1).....	166
Figure 6.54 Genetic algorithm optimization process: the convergence for trigeneration energy efficiency (left axis) and the increase of the number of generations (right axis)	167
Figure 6.55 Genetic algorithm optimization process: change of the ammonia concentration (x) and of the temperature of the saturated vapor at heat source (T_{4v}) with the flow fraction diverted to the ejector (f)	167
Figure 6.56 Temperature profiles at vapor generator for three values of LMTD	169
Figure 6.57 Pareto frontiers of two-objective optimization for the trigeneration system when vapor generator cost minimization and the revenue from power generation are the objective functions to be maximized.....	169
Figure 6.58 Pareto frontier for two-objective optimization considering the cost of vapor generator and the power generation efficiency as objective functions.....	171
Figure 6.59 Pareto frontiers for two-objective optimization considering the cost of vapor generator and the trigeneration efficiency as objective functions	172

List of Tables

Table 3.1 Description of thermodynamic states for the trigeneration system (Figure 3.1).	35
Table 3.2 Thermodynamic processes within trigeneration system (Figure 3.1)	36
Table 3.3 Signification of graphical symbols used in system diagram from Figure 3.3.....	40
Table 3.4 Valves functions for the prototype trigeneration system	40
Table 3.5 Working fluid pump characteristics	42
Table 3.6 Characteristics of the circulation pump for thermal oil.....	43
Table 3.7 Constructive parameters of the custom-made ejector	51
Table 4.1 Description of tests runs for the “Experiment 1”	58
Table 4.2 Temperature and pressure sensors.....	70
Table 5.1 Balance equations for the trigeneration system.....	75
Table 6.1 Pressure increase while charging and the concentration in liquid phase... ..	111
Table 6.2 Uncertainty of ammonia-water concentration determination.....	112
Table 6.3 Temperature readings and calculated input heat flux.....	112
Table 6.4 Main results and uncertainty propagation for Experiment 1, Run 1	114
Table 6.5 Pressure increase while charging and the concentration in liquid phase ..	114
Table 6.6 Main results and uncertainty propagation for Experiment 1, Run 2	115
Table 6.7 Main results and uncertainty propagation for Experiment 1, Run 3	116
Table 6.8 Main results and uncertainty propagation for Experiment 1, Run 3	118
Table 6.9 Main results and uncertainty propagation for Experiment 1, Run 4	120
Table 6.10 Angular speed correlated with pressure drop and pressure ratio for Run 3	120
Table 6.11 Main results and uncertainty propagation for Experiment 1, Run 5	120
Table 6.12 Main results and uncertainty propagation for Experiment 1, Run 6	121
Table 6.13 Main results and uncertainty propagation for Experiment 1, Run 7	122
Table 6.14 Expander run with compressed air	124
Table 6.15 Calculated data and uncertainty propagation for Experiment 3 Run 1 ...	129
Table 6.16 Calculated data and uncertainty propagation for Experiment 3 Run 2 ...	130
Table 6.17 Calculated data and uncertainty propagation for Experiment 4	132
Table 6.18 Data collected from pump calibration.....	133
Table 6.19 Results from heaters calibration.....	133

Table 6.20 Determined geometrical parameters for the scroll wrap	137
Table 6.21 Expander functional parameters resulting from geometry simulation	139
Table 6.22 State point parameters for the compression-expansion trigeneration system	156
Table 6.23 Energy destruction in compression-expansion trigeneration system	156
Table 6.24 Performance of the compression-expansion trigeneration system	157
Table 6.25 Mass balance equations for the improved trigeneration system	163
Table 6.26 Energy balance equations for the improved trigeneration system	163
Table 6.27 Exergy balance equations for the improved trigeneration system	163
Table 6.28 State point parameters of the improved and optimized trigeneration system	164
Table 6.29 Assumptions considered for the improvement system optimization	164
Table 6.30 Performance parameters of the optimized system	165
Table 6.31 Exergy destructions for each component of the improved trigeneration system	166
Table 6.32 Equations and assumptions used for determination of the heat transfer area	171

Nomenclature

A	area [m ²]
<i>AS</i>	angular speed [RPM]
BV	ball valve
C	coefficient
\dot{C}_d	cost of exergy destruction [\$/year]
\dot{C}_{ei}	cost of environmental impact [\$/year]
\dot{C}_{tot}	exergetic cost rate [\$/year]
CPR	cooling to power ratio
E	energy [kJ]
ER	entrainment ratio
\dot{E}	energy rate [kW]
ex	specific exergy [kJ/kg]
\dot{E}_x	exergy rate [kW]
h	specific enthalpy [kJ/kg]
H	enthalpy [kJ]
I	interpolating
<i>l</i>	arc length [m]
<i>LPC</i>	levelized product cost [\$/kW]
MV	metering valve
m	mass [kg]
\dot{m}	mass flow rate [kg/s]
P	pressure [kPa]
q	quality
Q	heat [kJ]
\dot{Q}	heat rate [kW]

r	radius [m]
s	specific entropy [kJ/kg K]
S	entropy [kJ/K]
\dot{S}	entropy rate [kW/K]
SE_{ex}	exergetic specific emission [kg/kW]
SI	sustainability index
t	time [s]
T	temperature [K]
U	overall heat transfer coefficient [W/m ² K]
v	volume [m ³]
V	velocity [m/s]
w	weight [N]
W	work [kJ]
X	concentration
\dot{Z}_{tot}	capital cost rate[\$/year]

Greek Letters

η	efficiency
ω	angular velocity [rad/s]
\mathcal{T}	torque [Nm]
σ	scroll wrap height [m]
ϵ_u	utilization factor
θ	orbiting angle
φ	involute angle
$\rho(\varphi)$	radius of curvature of the involute
θ	orbiting angle

φ_{e0}	initial angle of the external involute
φ_{i0}	initial angle of the internal involute
φ_{es}	starting angle of the external involute
φ_{is}	starting angle of the inner involute
$\rho(\varphi)$	radius of curvature of the involute
Δz	change of level in level gauge [mm]

Subscripts

0	surroundings
2gen	cogeneration
3gen	trigeneration
b	boundary
c	center
cl	clearance
com	compression
cv	control volume
dis	discharge
e	external
i	internal
en	energy
ex	exergy
in	input
max	maximum
o	outer
out	output

P	pump
Q	heat
R	receiver
rev	reversible
suc	suction

Chapter 1: Introduction

Energy is one of the major building blocks in the development of mankind. Energy has been required by life it began. In the primitive ages, the human being was only powered by biological materials from living organisms or by the burning of wood. As we moved forward, technological development came into effect and energy sources started diversifying. Oil, gas and coal became the main sources of energy. However, with the increasing population growth and the rising consumption of these depleting energy sources, sustainability became a concern. Another major concern also evolved: the environmental impact related to the energy consumption for the purpose of power, heating and cooling. Societal needs and environmental awareness must be taken into account together when the strategic development of energy is to be determined.

The search for useful energy for the development of mankind is one of the main historical quests. As the population increases the growth in energy consumption dictates the need of further exploration for abundant energy. In 2009, petroleum, natural gas, coal, and nuclear power accounted for 92% of the energy use with various renewable energy sources accounting for the remaining 8% (Ruehl, 2012). Energy moves people and goods; produces electricity; heats residences and other buildings; and is used in manufacturing and other important industrial processes.

Low grade heat is abundantly available in renewable energy sources and also in the industrial activity that typically rejects heat into environment. Interest for using low grade heat from solar energy, geothermal, ocean thermal, biomass combustion, heat rejected by fossil fuel-based power plants, air conditioning and refrigeration systems, and other industrial platforms grew dramatically with the global awareness of greenhouse effect and global warming due to carbon based fuel combustion. By using recovered waste heat of any nature that would otherwise be lost in the power generation process and becomes highly sustainable.

With the context of the growing energy consumption, depleting fossil fuels, environmental impact and above all utilization of environmentally benign sustainable energy, the concept of multigeneration has evolved. Multiple product generation with power plant technology started with the idea of cogeneration. Cogeneration is a means of generating heat and electric power simultaneously from the same energy source.

A further development of power generation technology which goes beyond cogeneration is the trigeneration, a case in which power, heating and cooling is produced by an integrated system. Besides being energy efficient, trigeneration using waste heat recovery or other clean sources of heat eliminates or reduces the emissions of greenhouse gases (specific to conventional power generation or heating systems). Furthermore, due to generation of three marketable commodities – power, heating and cooling – trigeneration can potentially reduce the return of investment when compared with power only (single generation) and cogeneration.

In the present work, the development of a trigeneration system based on an ammonia-water Rankine cycle is presented. The experimental research concluded with the practical realization of a Rankine heat engine prototype of approx. 1 kW power and heat recovery for service hot water generation. The system integrates an ejector cooling cycle with an application for cooling in the range of temperatures suitable for air conditioning.

In this introductory chapter, the energy outlook is reviewed in order to emphasise the importance of renewable thermal energy sources, especially at low grade and to justify the opportunity of development of advanced power cycles for trigeneration. Subsequently, the motivation of this work is exposed and the research objectives are stated. The chapter concludes with an outline of the thesis.

1.1 Energy outlook

The purpose of harnessing and converting energy to its useful form is to meet societal needs such as: electric power, mechanical power, heating supply and heat removal for cooling. Electrical power as well as mechanical power is highly effective forms of energy which are essentially required in the industrial, transportation and tertiary sectors. It has also residential use to run various household equipment and appliances. For human comfort, energy has a great role in all level of population strata. From cooking to heating, cooling, lighting and even for amusement, people are using energy.

Two aspects must come into balance in a harmonious energy system: energy supply and energy demand. This creates an energy market which is generally regulated by the authority for power generation. The available prospects show that energy demand will increase yearly whereas the conventional energy resources required for power generation will decrease. When the energy demand is divided to the population number, the energy demand per capita is

obtained. According to Ruehl (2012), the energy consumption in 2010 has been approx. 17 TW, whereas according to the United Nations (2013) the global population was close to 7 billion. Thence, the energy consumption per capita has been 2.46 kW; this figure reflects the fact that current worldwide energy demand is about 2.5 kW. If this demand is maintained in the future, the energy demand will reach 5 kW per capita in probably next 20 years when due to the natural tendency, the worldwide population will be doubled (United Nations, 2013). Regional energy uses also grew from 1990 to 2008: the Middle East increased by 170%, China by 146%, India by 91%, Africa by 70%, Latin America by 66%, the USA by 20%, the EU-27 block by 7%, and world overall grew by 39% (Ruehl, 2012).

The proven reserves of conventional energy resources in the form of coal, petroleum, natural gas and uranium are reported in Ruehl (2012). Also, if one takes into account the predicted demand of these resources, their availability can be determined. The resource availability in terms of years is shown in Figure 1.1. Coal is the most abundant resource with repositories proven for approx. 120 years. Of course, the continuous depletion of conventional (non-renewable) energy puts pressure on the current generation to take sustainable energy approaches, which will ensure a fair access to resources for the future generations.

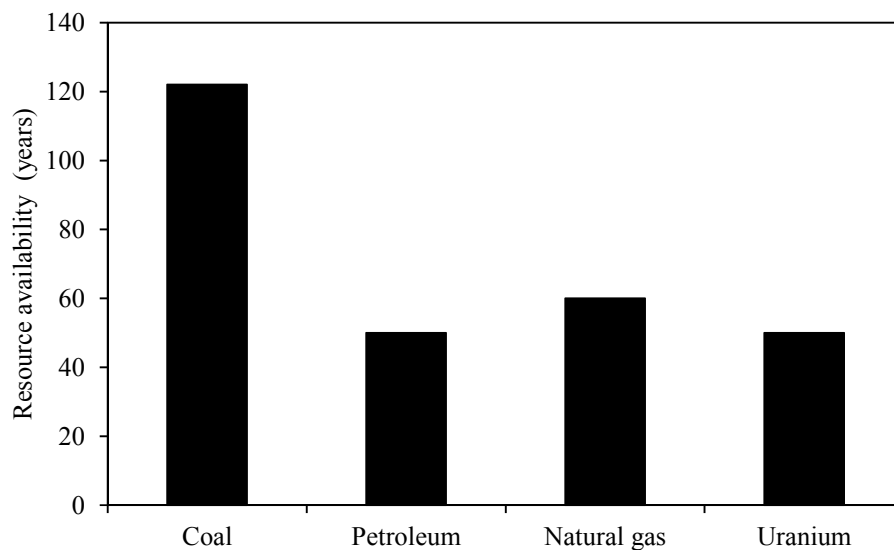


Figure 1.1: Availability of conventional energy resources [data from Ruehl, 2012].

Sustainability imposes an increased supply of renewable energy worldwide, whereas the dependence on fossil fuels must be limited. Nuclear energy itself can be viewed as sustainable pathway since prospects exist to develop thorium-based reactor in the future, which opens the door toward a more abundant energy. Furthermore, with the envisaged development of nuclear hydrogen production and nuclear process heat, nuclear energy appears to be one of the key sources for worldwide supply.

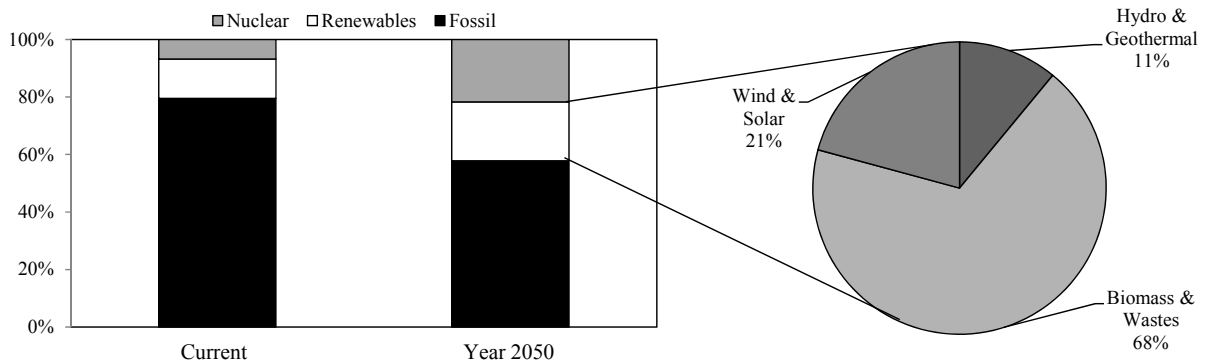


Figure 1.2: Current share and 2050 prediction for energy supply [data from European Commission (2006)].

Figure 1.2 shows the share of energy supply by kinds for today and the predictions for 2050. The share of renewable energy will increase from the current, approx. 8.5% to 25% in 2050. Currently, the overwhelming majority of renewable energy is due to hydropower, biomass combustion and geothermal. It appears that biomass and waste materials combustion will remain the lead of biomass supply by 2050 with 68% renewables share (or approx. 17% of total).

Further from the chart shown in Figure 1.2, one can conclude that energy sources that manifest in the form of high temperature heat will represent an important share among renewable energies in the future. A fastest growing renewable source is the solar energy. Solar power involves using solar cells to convert sunlight into electricity or using a parabolic concentrator to heat water for hot water system or to produce steam to run a heat engine. Sunlight entering through window can be used as a passive heating of a building. Solar energy, radiant light and heat from the sun, have been harnessed by humans since ancient times using a

range of ever-evolving technologies. Solar energy with modern technological advancement can contribute as an alternative renewable energy source for versatile use.

Solar technologies are broadly used currently in photovoltaic power generation, water heating, and steam generation and as a heat source of the absorption cooling. Also, with properly designed building orientation and its construction materials, a large amount of solar heat can be captured for naturally circulated space heating. Beside solar, the geothermal is another form of renewable energy transferred in the form of heat.

Geothermal energy is gaining its popularity due to its lack of dependence on the weather. It harnesses the heat energy present underneath the Earth. Two wells are drilled. One well injects water into the ground to provide water. The hot rocks heat the water to produce steam. The steam that shoots back up comes out through the other hole(s) and is used to drive turbines, which power the electric generators. When the water temperature is below the boiling point of water, a binary system is used. A low boiling point liquid is used to drive a turbine and generator in a closed system similar to a refrigeration unit running in reverse.

Biomass was being used as the primary source of energy for heating and cooking at homes and process heat since long. Wood is the largest biomass energy source to date. However, garbage or other renewable resources such as corn or other vegetation are largely used nowadays to generate electricity. When garbage decomposes, the methane produced is captured in pipes and later burned to produce electricity. Bioethanol is a readily available, clean fuel made of biomass feed stocks. It produces considerably lower emissions on combustion and it only releases the same amount of carbon dioxide as plants bound to consume while growing.

Energy is demanded generally in the form of power, heating and cooling as the basic need for the modern society. Figure 1.4 shows the energy demand in Canada for different sectors. Only 74.1% of energy input is available as useful energy to the economy sectors, fact that illustrates the energy losses associated with energy conversion and production of about 25.9%. The energy demand is shared almost equally by industrial and transportation sectors which are the most important consumers. Also, the residential, commercial, institutional and agricultural demand altogether represent 35% of total Canadian energy demand.

In 2008, total worldwide energy demand was 474 exajoules (132,000 TWh). This is equivalent to an average power use of 15 terawatts (2.0×10^{10} hp). The annual potential for renewable energy is solar energy 1,575 EJ (438,000 TWh), wind power 640 EJ (180,000 TWh),

geothermal energy 5,000 EJ (1,400,000 TWh), biomass 276 EJ (77,000 TWh), hydropower 50 EJ (14,000 TWh) and ocean energy 1 EJ (280 TWh); US EIA (2009).

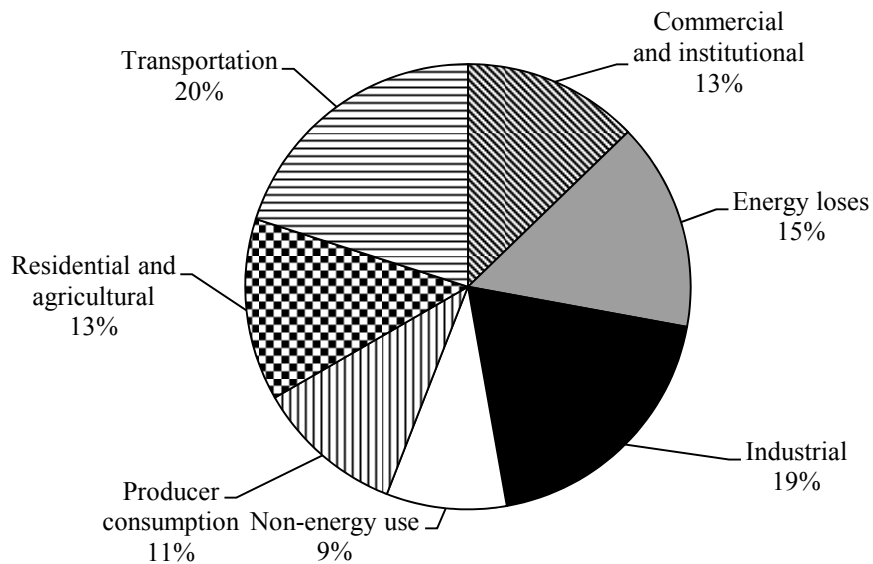


Figure 1.3: Energy demand in Canada [data from Statistics Canada (2008)].

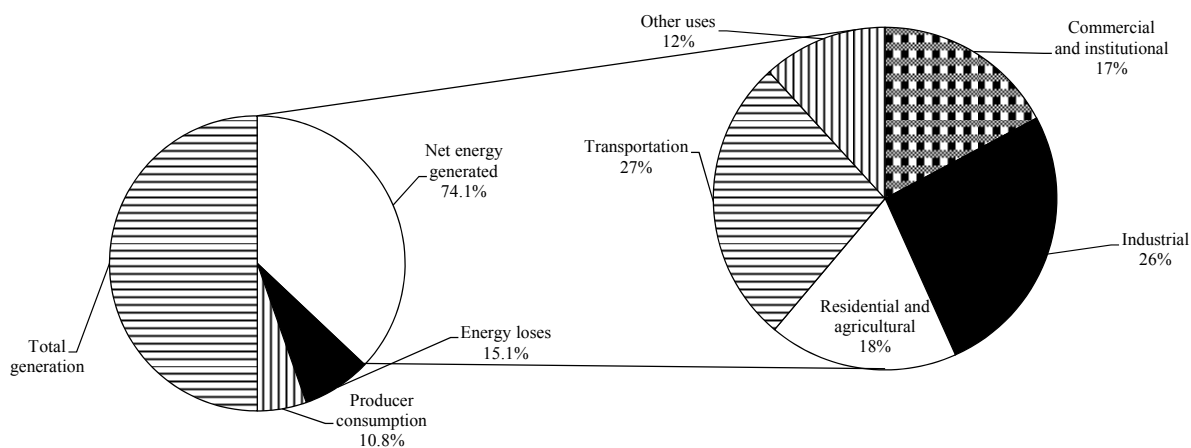


Figure 1.4: Energy demand in Canada [data from Statistics Canada (2008)].

The Canadian energy demand is shown in Figure 1.5 in terms of fuel type. Most of the demand is due to refined petroleum products (41%) which mostly go to the transportation sector. Natural gas and electricity have demand in all Canadian sectors. In residential sector,

natural gas is used for heating in overwhelming majority of households, whereas power is used for lighting, and appliances. Another important side of power consumption in households is for air conditioning.

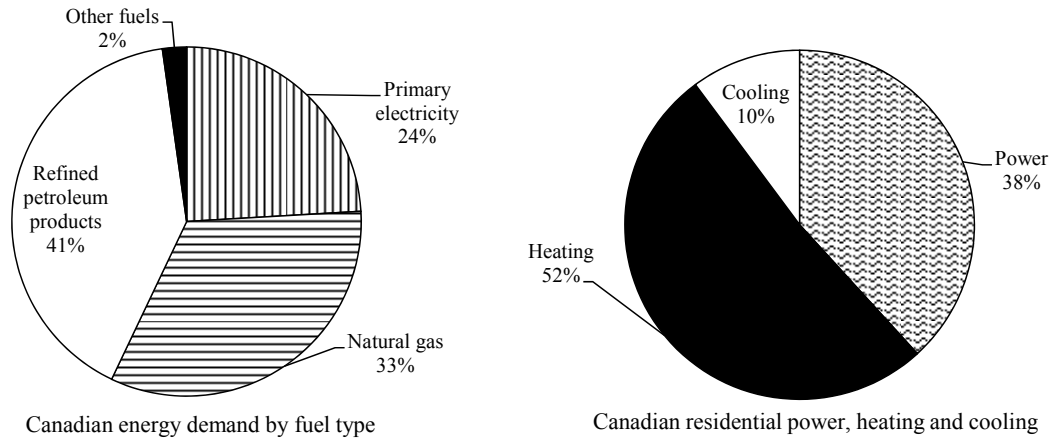


Figure 1.5: Canadian energy demand by fuel type and Canadian residential power, heating and cooling demand [data from Statistics Canada (2008)].

Over 40% of the average home's energy consumption is used for heating. The percent of household power used for cooling (for running freezers, refrigerators and air conditioning) can be estimated to about 21%. This figure has been found as an annual average for USA households in US EIA (2009) and it is assumed to be the representative for both USA and Canada. Under this assumption and based on residential power and natural gas consumption from Statistics Canada (2008), the following average demand is determined: 38% power (for lighting and appliances other than cooling and air conditioning), 52% heating (space and water heating) and 10% cooling demand. The chart from Figure 1.5 shows this demand distribution.

Efficient use of energy is thus an important factor in consuming energy. Scientific principles and technological developments are the ongoing processes to optimize energy efficiency. Energy is a broad term whereas another useful term known as exergy determines the amount of maximum potential of useful work. Technological development is now more concerned about exergy analysis to optimize the system efficiency. All forms of energy calculations are done currently based on energy and exergy analysis.

1.2 Single generation, cogeneration and trigeneration

The demand of power, heating and cooling is obvious not only in residential sector but in many other sectors. The conventional approach is to provide these commodities using separate units. Typically, the power demand is satisfied by the electricity grid. The need for heating is fulfilled by the use of natural gas furnaces and cooling is generated by refrigerators and air conditioning units that typically are driven by electricity.

With the context of growing energy consumption, depleting fossil fuel, environmental impact and above all utilization of environment friendly sustainable energy, the concept of multigeneration system has been evolved. In this approach, an integrated system is devised which is able to deliver multiple commodities in an efficient manner. Multi generation with power plant technology started with the idea of cogeneration. Cogeneration is normally a means of generating heat and electric power simultaneously from the same energy source. Trigeneration brings an additional output in terms of cooling. Basically, a trigeneration system represents an integration of a power cycle, a refrigeration cycle and a heat recovery subsystem. One typical system configuration for trigeneration is adopted with the integration of an absorption chiller to facilitate the cooling demand with the same energy input. In this system, the waste heat of the power cycle is utilized to an absorption chiller for cooling purpose. A simple representation of single, co- and trigeneration systems is shown in Figure 1.6.

The idea of a smaller capacity trigeneration evolves with the possibility of using low grade heat sources available in renewable energy or waste heat. Low grade heat is abundantly available in renewable energy sources and also in the industrial waste that normally rejects heat to the environment. Interest for using low grade heat from solar energy, geothermal, ocean thermal, biomass combustion, heat rejected by fossil fuel-based power plants, air conditioning and refrigeration systems, and industrial processes plants grew dramatically with the global awareness of greenhouse effect and global warming due to carbon based fuel combustion. By using recovered waste heat of any nature that otherwise will be lost, the power generation process becomes highly sustainable. If the system operates with cogeneration or trigeneration technique, then the overall efficiency is increased. Besides being energy efficient, cogeneration and multi-generation using waste heat recovery or other clean sources of heat such as solar thermal energy, carbon dioxide emissions (specific to conventional power generation or heating systems) are reduced or even eliminated.

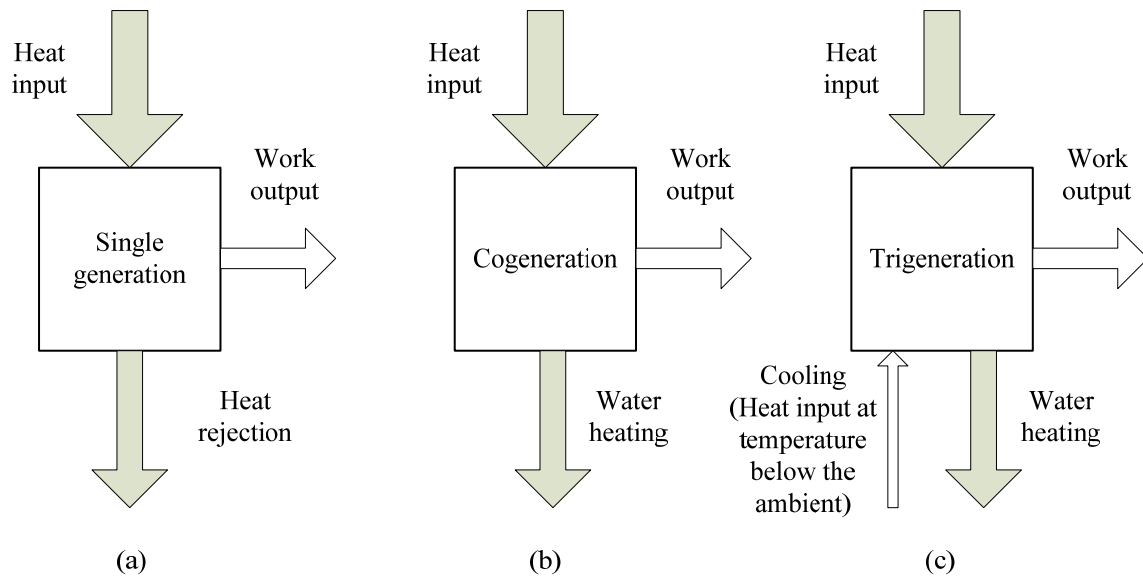


Figure 1.6: Black-box representation of a) single generation, b) cogeneration, and c) trigeneration systems.

Al-Sulaiman et al. (2011) has revised trigeneration opportunities and shown that integration of various technologies within a single overall system enhances the efficiency and revenues; and reduces the environmental impact and payback period. These benefits are higher when renewable thermal energy sources are used as input as shown in the paper by Dincer and Zamfirescu (2012). In this respect, heat engines that use an external heat supply have a great deal of potentials because in such systems, heat is transferred from the external source to the working fluid using a heat exchanger. This facilitates versatility in linking of the power cycle with a heat source such as solar, geothermal, ocean thermal, hot waste stream or flue gas streams from combustion processes.

Many research works have been performed on various configuration of heat engines, such as the organic Rankine cycle (ORC), Kalina cycle, steam Rankine cycle and ammonia-water variations of Rankine cycle. Zamfirescu and Dincer (2008) mentioned that Rankine cycle and its variations are excellent choices to use in a heat engine working with low grade heat sources. They also pointed out of achieving higher exergy efficiency of using ammonia-water as the working fluid with 150°C geothermal heat source. Thus, ammonia water low power capacity heat engines using low grade heat source is of particular interest for this thesis.

Depending on the process fluid and the heat quality, a careful selection of prime mover is essential. Quoilin et al. (2010) suggested that the use of positive displacement expanders is advantageous over turbo-machines for use in power generation at low and intermediate power range when low grade heat sources are the energy source. They had pointed out that due to the performance criteria, turbo-machines should have high tip speeds compared to smaller positive displacement machines.

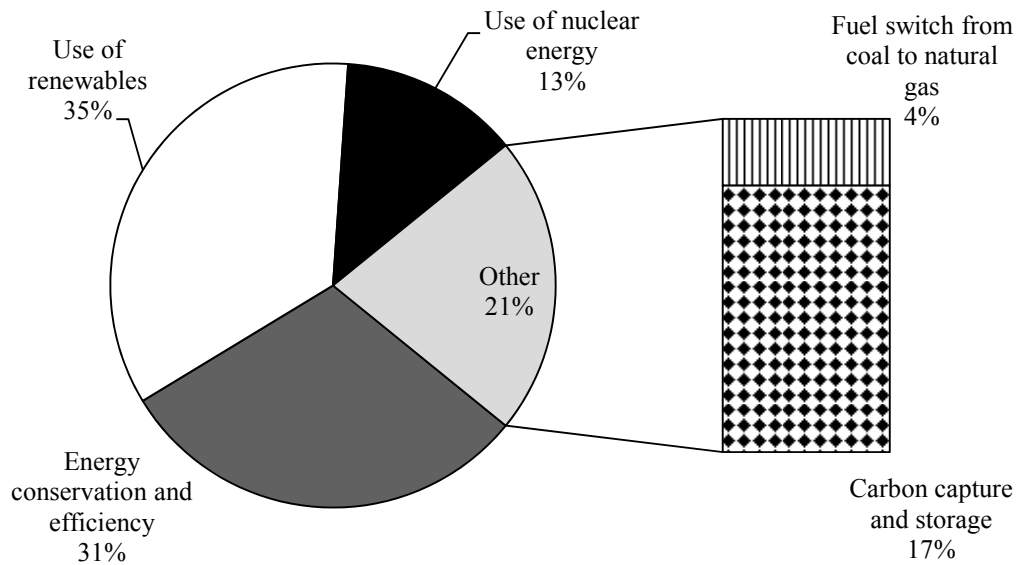


Figure 1.7: GHG mitigation potential by year 2100 [data from IPCC (2007)].

Yanagisawa et al. (1988), Nagatomo et al. (1999) and Kim et al. (2001) had investigated the performance characteristics of a scroll expander and found that at lower operating speed the isentropic efficiency is lower. This is because of the fact that at lower angular speeds, the leakage loss is more and also mechanical loss is more in scroll machine. By redesigning the bearing surfaces of the shaft, the mechanical losses can be minimized. Also ensuring to work at higher speed, the leakage loss can be reduced. This can be achieved by using ammonia water as working fluid which has high power production capacity due to desorption and resorption behaviour as a non-azeotropic mixture. Considering more advantage over drawbacks of using scroll unit, a scroll expander is determined to be a better choice for working as a prime mover in the heat engine developed in the present thesis.

While cogeneration itself helps to reduce CO₂ emissions significantly, a two-fold option of CO₂ emission reduction (or more) can be obtained by using renewable energy as an input source to trigeneration. Ahmadi et al. (2013) has shown that carbon emission reduction of more than two can be obtained when a cogeneration system is applied to combust biomass and generate power and heating. If more products are generated, the system efficiency gets increased even more and the carbon specific emission gets decreased seven times with respect to reference case of single generation. Also, the system efficiency is increased by 1.5 times. Due to a higher efficiency and multiproduct generation, the return of investment generally decreases as indicated in several examples presented in Dincer and Zamfirescu (2014).

The GHG mitigation potential from switching renewable energy is expected to become 35% among other measures as shown in Figure 1.7. This clearly shows that if a trigeneration system supplied by renewables is developed important carbon mitigation is obtained. Hence, trigeneration represents one of the solutions for greenhouse gas mitigation and as such financial encouragement from the government in this technology development is highly probable.

1.3 Motivation

Energy being an inseparable part of human life demands the most efficient use of its sources. Trigeneration systems draw interest in this regard, as exposed in the previous section. The purpose of this research work is to analyze the performance of a scroll based heat engine working with low temperature heat source in a trigeneration facility. Linking trigeneration to heat sources derived from renewable, makes a very strong scheme to the supply not only low-carbon electricity and low-carbon heat but also cooling in an integrated system with high utilization factor. The first part of the work focuses on heat engine prototype development. The second part analyses and assesses the system performance driven by low grade heat source provided as hot thermal oil. The system is further compared with potential competitors and conventional solution for power, heating and cooling at small scale (e.g., residential). The motivational aspects of this work are as follows:

- a) Energy system is ever changing and differs widely across regions. Every energy source has substantial environmental and economic impacts that ripple through the connected systems that form the environment and shape of society. New technologies and societal wants and needs will bring continuous change to where we get our energy from and how we use it.

Throughout human history, the ways in which one produces and uses energy have changed. Often, one part of the system changes gradually while another is quickly transformed. Almost all the nuclear power plants in the U.S.A. were built in the course of twenty years. Almost all of the wind generated electrical capacity in the world has come online in the last few years. While our transportation system has been driven by petroleum for decades, it has not always been so. Our transportation system moved from domination by animal power to coal (for trains and shipping) to petroleum in steps that each took only a few decades, after a new technology showed clear advantage. These sweeping and unpredictable changes in energy system will doubtlessly happen again and again, while other parts of the system will change remarkably slowly. Any change in the energy system impacts both the environment and the economy. Most or all increase in energy production and use will damage aspect of the environment, and need to be considered in the context of current energy practices. By better understanding the components of energy system, their interconnections and how these things have changed in the past, one can make more informed decisions about our energy future. Development of trigeneration systems in general and small scale scroll expander based, ones may help in this respect.

- b) Energy development is the ongoing effort to provide sufficient primary energy sources and secondary energy forms to fulfill civilization's needs. It involves both installation of established technologies and research and development to create new energy-related technologies. Major considerations in energy planning include resource depletion, supply production peaks, security of supply, cost, impact on air pollution and water pollution, and whether or not the source is renewable.
- c) Technologically, advanced societies have become increasingly dependent on external energy sources for transportation, production of many manufactured goods, and delivery of energy services. This energy allows people who can afford the cost to live under otherwise unfavourable climatic conditions through the use of heating, ventilation, and/or air conditioning. Level of use of external energy sources differs across societies, as do the climate, convenience, levels of traffic congestion, pollution production, and greenhouse gas emissions of each society.
- d) Expanding human populations generally require an increased consumption and dependence on external energy sources. Research, development and practice of energy efficiency and

conservation by the populace allow a degree of mitigation of this dependence. Wise energy use embodies the idea of balancing levels of human comfort and energy consumption by researching and implementing effective and sustainable energy harvesting and utilization measures.

- e) Trigenation systems gained importance recently due to their higher efficiency compared to conventional systems. Utilizing the same amount of an energy source, it is possible to obtain more useful outputs rather than only one. Power, heating and cooling are highly required commodities with market value which can improve the return on investment for trigenation systems as compared to single generation and cogeneration.
- f) Global energy consumption is increasing drastically with the increase of world population and rapid industrialization. Consuming energy has a direct and indirect impact on the environment from energy production to energy utilization. The unprecedented increase in the emissions of harmful greenhouse gasses due to high level of use of fossil fuels in different energy sectors inspired the researchers to explore efficient methods of using renewable energy sources. Extensive research has been carried out exploring the potential of sustainable energy sources such as bio-fuels, biomass, municipal waste, solar, geothermal, wind, and industrial waste heat. Furthermore, efficient alternative technology to replace the existing production of the commodities that is primarily driven by the highly pollutant combustion of fossil fuels should also be researched. However, sustainable energy in the form of low grade heat source requires more than the conventional heat engine to harness this type of green energy. To exploit this heat source and make it usefully, an externally heat driven engine is the most suitable. In an external heat driven heat engine, the thermal energy from these renewable sources can be harvested and converted into useful work that can be used for smaller scale electric power generation. A well-known and established thermodynamic cycle to apply to the externally heat driven heat engine is Rankine cycle. Normally, steam is being used for this cycle when using fossil fuel. But for low grade sustainable energy sources steam Rankine cycle is not suitable because of the low heat flux. A process fluid with high molecular density has the characteristic of having the liquid-vapor phase change at a lower temperature than the water-steam phase change to extract more heat from low grade heat source.

g) Although this type of heat engine works on low grade heat source, the thermal efficiency is much lower due to heat waste in the condenser, higher energy irreversibility in the expander and single commodity energy utilization. Therefore, from both thermodynamic and economic points of view, a highly efficient low grade heat driven heat engines development has solid motivation. Conceptually, it is found that a sustainable heat driven heat engine in a trigeneration platform should have much higher efficiency than a single commodity heat engine. However, harnessing low grade sustainable energy is not suitable using conventional expansion devices like turbine.

1.4 Objectives

Tarique (2011) conducted an experimental investigation on scroll based low grade heat engine and the energy; and the exergy efficiency was evaluated. The results show a maximum isentropic efficiency of 67% and an overall energy efficiency of maximum 7% at 120°C source temperature, while the exergy efficiency is about 30%.

Moreover, scroll machines are commercially available and used by refrigeration industries for long in its developed design form. An off-the-shelf refrigeration scroll compressor can easily be converted to scroll expander to work as a prime mover in the proposed engine. Design, construction and analysis of a scroll based trigeneration unit are therefore the plan for the proposed research.

The purpose of this work is to investigate the performance of a scroll expander in an ammonia based Rankine cycle and to optimize the operating parameters in developing a highly efficient heat engine using low grade heat source. The main goals are:

- i. Use of sustainable energy to mitigate environmental impact,
- ii. Develop and tune the heat engine for best efficiency, and
- iii. Increase the utilization factor of heat source energy.

The objectives of the research work are as follows:

- a) To design a trigeneration system for power, heating and cooling in the range of 1 kW power. The system parameters are determined on the basis of source and sink temperature and the system output requirements. The heat source is hot thermal oil with temperature

in the range of 80°C to 160°C. The trigeneration system prototype will include an ammonia-water based power cycle and an ejector cooling cycle.

- b) To perform the energy and exergy analysis of the ammonia-water trigeneration system as designed and compared with other configurations to investigate for multigeneration systems. One performs the thermodynamic and heat transfer analysis to develop a precise system model of the heat engine. Exergy destruction for each component will be determined for the tested operating conditions.
- c) To construct and commission the trigeneration prototype system for experimental analysis based on design considerations.
- d) To perform experimental analysis of the trigeneration system with a lab setup. With the varying operating parameters, analyze the scroll expander performance and expansion process. The data acquisition system will be programmed and a plan of experimentation elaborating the through experimental information is collected.
- e) To analyze the experimental data and assess the performance of the trigeneration system. Determine the energy and exergy efficiency and COP of the trigeneration system. The energy and exergy analyses will help to understand the performance of a trigeneration system and its system components by determining the exergy destructions.
- f) To optimize the operational parameters of the trigeneration systems in improving the efficiency and energy utilization factor.

1.5 Thesis outline

This thesis comprises seven chapters structured as follows: Introduction, Literature review, Trigeneration system description and development, Experimental work, Analyses, Results and discussion, and Conclusions and recommendations. After this introductory chapter, a comprehensive literature review is presented on the following topics: thermodynamic cycles for power and for cooling with focus on Rankine cycle, trigeneration systems, turbines and expanders with focus on scroll expanders as an emerging technology, ejectors for steam cooling cycles, working fluids with focus on ammonia-water mixture and solution thermodynamics, heat exchangers with focus on ammonia-water desorber and resorber.

Chapter 3 of the thesis describes the development of trigeneration system and gradual development of the prototype in many phases and construction iterations. The experimental

work is described in Chapter 4 including methodology and uncertainty analysis. The analyses section in Chapter 5 concerns energy and exergy analyses of the system and components, scroll machine geometrical and thermodynamic analysis and modeling of the processes in heat exchangers.

The core chapter of the thesis is the Results and Discussion which is divided in four sections: “Experimental Results”, “Modeling and Numerical Simulations”, “Comparative assessment of trigeneration systems” and “System Improvement and Optimization”. Chapter 7 gives the concluding remarks, recommendation and future perspectives. The thesis includes an abstract, a reference list, nomenclature and lists of tables and figures.

Chapter 2: Literature Review

The concept of sustainable energy has been promoted as a fair solution to the complex problems that the growing demand for energy creates: pollution, depletion of energy sources, ethical aspects etc. In this framework, the idea of multigeneration systems evolved. These systems are an extension of conventional power generation plants which include additional subsystems integrated in a manner that the overall product is power, heating and cooling. Likewise, trigeneration systems are more complex than single generation systems, involving additional design and optimization issues related to system integration. In this chapter, the main issues and recent developments in power cycles, cooling cycles, working fluids, turbines and expanders and heat exchangers are reviewed from the literature with emphasis on trigeneration systems.

2.1 Power cycles

A thermodynamic cycle that generates power in the form of mechanical work is often referred to as a power cycle and it is generally used to convert heat (thermal energy) into work. General thermodynamic textbooks categorize power cycles in two main kinds: gas power cycles and vapor power cycles (see Cengel and Boles, 2010). In a gas power cycle, the working substance stays in the gas phase all the time whereas in vapour cycles, the vapor (gas) condenses to liquid in some processes of the cycle whereas liquid transforms into vapor during other processes (e.g., boiling). Gas power cycles include three totally reversible cycles – Carnot, Stirling and Ericson – and three main internally reversible cycles, namely Brayton, Otto and Diesel cycle.

Although heat engines based on Stirling and Ericson cycles are practically realisable, these machines appear to be uncommon in cogeneration systems or trigeneration systems. Stirling engines, though, have been successfully demonstrated for concentrated solar dishes for a long time (Jaffe and Poon, 1981). However, more recently, applications with Stirling engines for cogeneration have appeared in the literature (Kong et al., 2004). One major advantage of the Stirling cycle is that this engine can be coupled to an external heat source and heat sink through heat transfer processes. This offers versatility because at the heat source either a combustion process conducted externally can be coupled or a renewable energy source, such as concentrated solar radiation, can be connected. On the contrary, Otto and Diesel cycles are

restricted to fuels and processes with internal combustion. Nevertheless, internal combustion engines can be integrated into cogeneration and trigeneration systems, as shown in the literature (Khatri et al., 2010).

The Brayton power cycle possesses one interesting feature: it can be configured as an internal combustion engine, or as an externally heated heat engine. Therefore, this cycle has excellent versatility with respect to coupling to the heat source. Jaffe (1983) mentioned the application of the open-air Brayton cycle for solar dish concentrators. The successful application of the open-air Brayton cycle in three large scale central receivers for power generation with concentrated solar radiation is also mentioned in the review by Romero et al. (2002).

Vapor power cycles use a working fluid with liquid-vapor phase change within the cycle. At the low temperature side (heat sink) vapors convert to liquid which can then be pressurized by pumping under little expense of mechanical work. At the heat sink side, liquid is converted to vapor under heat addition and eventually expanded for work generation. The vapor power cycle was established by the Scottish inventor William Rankine using steam as the working fluid. Many types of vapor power cycles exist today with various working fluids, but the general name for these types of cycles is Rankine. This thesis focuses on the development of a particular Rankine cycle, therefore more emphasis is placed on Rankine cycles in this review.

Currently, most large electricity generation plants use steam as a working fluid in steam Rankine cycles. Zamfirescu and Dincer (2008) mentioned that the steam power cycle is used in 80% of all electric power generation systems throughout the world, including virtually all solar thermal, biomass, coal and nuclear power plants.

For small power generating plants with a low-temperature heat source (<450 K), steam is not the best choice for the working fluid because of its low vapour pressure and huge specific volume at those temperatures. Instead of steam, various organic fluids can be used for better efficiency in the range of low power and low source temperature applications. Rankine cycles with organic working fluids are known as organic Rankine cycles (ORC).

Typical working fluids are hydrocarbons, or halocarbons. There are commercial ORC engines powered by waste heat or solar heat (usually hot water at >85 °C) generating some 50 kW in a 20 °C environment, with an energy efficiency of about 10%. There is an abundance of published literature on the development of Rankine cycles operating with working fluids other

than water. Due to lower boiling temperatures and pressures, these fluids are capable of operating with low capacity heat sources. Furthermore, the number of applications of such heat engines is remarkably large.

The ORCs are quite relevant to the paradigm of efficient power production from renewable sources. Schuster et al. (2009) noted the following applications of low-capacity heat sources in externally supplied heat engines as follows: biomass combustion, solar desalination, waste heat recovery from biogas digestion. Zamfirescu et al. (2012) demonstrated the application of heat engines for small-capacity concentrated solar power and heat cogeneration. For all these cases, the heat source temperature is found to be limited to below 200°C.

We limit the scope of our literature review to a range of source temperatures up to 250°C, and denote this range as “low-temperature”. The reason for choosing this range relates to two aspects: the vast majority of renewable and sustainable energy sources fall within this temperature range and the current technology allows the use of positive displacement expanders or expander-generator units operating at temperatures below 250°C. While energy sources are identified suitable with respect to abundance, environment friendliness and cost effectiveness, the next step is to examine the suitable power cycle and working fluid to harness it.

There are several established configurations of the organic Rankine cycle which we review here as follows:

- ORC with basic configuration (including pump, vapor generator, turbine and condenser),
- Regenerative ORC with vapor extraction and regular working fluids,
- Regenerative ORC with retrograde working fluids and counter-current gas-liquid heat exchanger used as regenerator,
- ORC with retrograde working fluid using expansion of saturated vapor,
- Reheat-regeneration cycle configurations,
- Transcritical cycle configuration in which heat addition process evolves at supercritical pressure and eventually reaches supercritical temperature (see Chen et al., 2006).

An ORC of basic configuration which uses R134a as working fluid was developed by Hogerwaard et al. (2013) for scale applications. The system was conceived with off-the-shelf components from HVAC and automotive industries. For example, the vapor generator is a selected coil and fins evaporator for air conditioning application. The condenser is a typical

brazed plate heat exchanger. The working fluid pump is a sealed positive displacement one originally used for fuel injection in automotive engines.

Hogerwaard et al. (2013) used a scroll expander-generator unit developed and tested by Prof. Dincer group at UOIT during successive research phases reported previously as follows:

- Tarique (2011), Tarique et al. (2011) and Tarique et al. (2014a) studied, assessed experimentally and reported a 1 kW scroll expander unit using an ORC test bench which included an electrically heated vapor generator for the working fluid R134a. Power generation in the order of hundred W was proven and the optimal operation of the expander determined based of the experimental tuning.
- Hoque (2011) developed an ORC system using the scroll-expander-generator unit from Tarique (2011) within a hot air heated ORC test bench. In this case, hot air at temperature up to 160°C has been obtained within a closed duct; the heat from hot air is transferred to the ORC vapor generator using a finned coil evaporator. Enhanced power generation of few hundreds of W has been obtained.

A configuration of ORC which uses a vapor drum as thermo-mechanical accumulator for solar energy with low concentration is analyzed and assessed in Tarique et al. (2014b). The ORC is made to operate continuously and steadily during the daylight to produce power with a solar multiplicity factor of 3 using cyclohexane as working fluid. A calandria loop is used to generate the vapors which are accumulated under pressure in the drum tank. The cycle uses a scroll expander and due to thermo-mechanical storage is able to dump fluctuations in solar radiation intensity. The parametric optimization and comparative study of organic Rankine cycle for low grade waste heat recovery is described in Dai et al. (2009). Analysis and optimization of the low-temperature solar ORC is presented by Delgado-Torres and Garcia-Rodriguez (2010). A review of organic Rankine cycles (ORCs) for the recovery of low-grade waste heat is given by Hung (1997, 2001).

The use of organic zeotropic mixtures as working fluids in ORC is studied by Aghahosseini and Dincer (2013). Due to the change of temperature during vapor generation, the pinch point temperature difference and thence the exergy destruction at the vapor generator can be reduced.

Other zeotropic mixtures that are not based on organic chemicals are also considered as working fluids in Rankine cycles. One remarkable working fluid of this kind is the ammonia

water. Of course, the purpose of using ammonia-water in a power cycle is to take the advantage of temperature matching in the heat exchange processes with an excellent match of temperature profiles at sink and source.

In fact, matching the temperature profiles at sink and source is stringently important when the heat engine operates with low temperature differential. OTEC (ocean thermal energy conversion) applications are one example where ammonia-water Rankine cycles are best suited. In these applications, as mentioned above, the source temperature is in the range of 25-30°C, while the sink is at 4°C.

One of the best known types of ammonia-water power cycle is the Kalina cycle (Kalina 1983, 1984) in which the high pressure vapor are generated through a non-isothermal phase change process and after the expansion the low pressure mixture is cooled in a so called distillation and condensation subsystem which includes an absorber, a vapor-liquid separator and a condenser which eventually produces a slightly subcooled liquid (Marston, 1992). Bombarda et al. (2010) studied comparatively the application of Kalina and ORC for heat recovery and work generation from exhaust gas of Diesel engines. The performance of Kalina cycle with low-temperature heat sources is analysed in Hettiarachchi et al. (2007).

The literature review on Kalina cycle is briefly summarized as follows:

- Corman et al. (1995) demonstrated that Kalina cycle has better potential to recover heat from a topping cycle in an integrated power generation system.
- For a case study provided by Park and Sontag (1990), Kalina cycle performed better than multipressure steam Rankine cycle with 5% higher energy efficiency and 15% higher exergy efficiency.
- For a case study by Gajewski et al. (1989), the Kalina cycle showed 1.5% better efficiency than triple pressure steam Rankine cycle in the conditions when the Kalina system has been found more expensive than the steam system due to a more complicated heat exchanger system.
- DiPippo (2004) showed for a case study that Kalina cycle has a 3% better efficiency than an ORC.
- Jonsson and Yan (2001) reported that at temperatures higher than 300°C ammonia decomposition at small rate occurs which can generate technical problems with the power plant during long runs.

- Uehara and Ikegami (1993) studied Kalina cycle application for OTEC and showed that the exergy efficiency of power generation can be superior to 60%.
- Mlcak (2002) assessed the geothermal application of Kalina cycle.
- Bloomquist (2003) studied Kalina cycle integration into agricultural projects.

Although Kalina is the most common configuration of ammonia-water power cycle, several other ammonia-water based Rankine cycles were proposed in the literature. Desideri and Bidini (1997) studied ammonia-water Rankine cycle for geothermal applications and their parameter optimization. Roy et al. (2009) report a thermodynamic analysis of a low temperature $\text{NH}_3\text{-H}_2\text{O}$ Rankine cycle. The thermodynamic optimization of the performance of an ammonia-water Rankine cycle is reported in Pouraghaie et al. (2010). In Wagar et al. (2010), an ammonia-water based Rankine cycle is thermodynamically analyzed for renewable-based power production, e.g. solar, geothermal, biomass, oceanic-thermal, and nuclear as well as industrial waste heat. One remarkable feature of the ammonia-water cycle is that the ammonia concentration can be adjusted during the heat engine operation as a mechanism to adapt the cycle to possible fluctuation at the heat source or heat sink temperatures. The concentration can be varied from nil (zero) when the cycle runs with pure steam or 100% when the cycle becomes a pure ammonia Rankine cycle. Thus, ammonia-water Rankine cycle appears suitable to heat sources that are variable in nature, such as solar radiation. According to Wagar et al. (2010), the energy efficiency of this cycle can reach 30% with a heat source as low as 250°C . Koji et al. (2004) analysed heat recovery power generation with a purely ammonia Rankine cycle.

In Zamfirescu and Dincer (2008), a novel trilateral flash Rankine cycle (TRC) is described that uses no boiler, but rather the saturated liquid is flashed by a positive displacement expander for power generation. Because the cycle has no pinch point, the exergy of the heat source is better harvested provided that the heat source stream exchanges sensible heat with the working fluid. In the same time a better temperature match can be obtained at sink side heat exchanger which brings 7% improvement of exergy efficiency when compared with a case when the working fluid is steam for similar operating conditions.

A double stage configuration of the ammonia-water trilateral flash cycle for cogeneration purpose has been recently studied by Cetinkaya (2013). The double stage TRC showed better efficiency than the simple stage TRC for applications with 150°C temperature with the potential of 1.5 time increase of exergy efficiency.

2.2 Cooling cycles

The objective of this research project was to integrate a power and a cooling cycle to develop a trigeneration system. There are three basic refrigeration cycles that are suitable for smaller scale application: vapor compression cycle, absorption cycle, and ejector refrigeration cycle.

The most common technology uses the vapor compression refrigeration cycle, which provides excellent cooling but at a substantial cost because it is powered directly by mechanical energy taken from a motor. If electricity is provided to cooling for air conditioning through fossil fuel generated electrical power plants, which often have efficiencies of less than 40 percent, and is transmitted long distances through the power grid with consequent energy dissipation, the costs in terms of energy consumption and the emission of global warming effluents is enormous (Garris and Charles, 2005). Furthermore, vapor compression refrigeration generally uses hydro-fluorocarbon based refrigerants, which deplete the earth's ozone layer and further contribute to global warming. Also the compressor consumes substantial amount of electrical energy that again contributes to the emission of global warming effluents. The integration of vapor compression refrigeration in trigeneration system should be done either by driving the compressor directly by the turbine or by using a part of the generated electric power to drive an electric motor for compressor.

Better system integration for trigeneration is obtained when absorption or ejector cycles are used. In these cases, there is not any essential requirement of shaft power to drive any mechanical equipment of the refrigeration system. In absorption refrigeration system, heat is recovered to drive the vapor generator. For ejector cooling, steam (or another working fluid) is extracted from the turbine to power an ejector system. Two particular absorption cycles are generally used: LiBr-water and ammonia-water. These cycles show a COP (coefficient of performance) of the order of 0.8 or above and were used in past studies with trigeneration.

There are several approaches used to improve the performance of a single-effect absorption refrigeration system. Many literature sources were reviewed by Srihirin et al. (2001). Applying an ejector to the conventional absorption system is one of the remarkable alternatives. The appropriate installation configuration introduces the magnificent improvement of COP to nearly to that of a typical double effect absorption cycle machine. Moreover, according to the simplicity of the hybrid ejector-absorption refrigeration machine, its capital

investment cost is comparatively low when compared to other conventional high performance absorption cycle systems.

The ejector cooling cycle on the other way is interesting because it requires less moving parts and no stringent need of heat recovery for driving the vapor generator. This will reduce the investment because less hardware is required as compared to the absorption cycle. Ejector refrigeration is a thermally energized refrigeration system, which has an additional potential benefit of being capable of using environmentally friendly refrigerants, such as water. Omitting the moving parts by replacing the compressor with ejector achieved the advantage of reduced consumption of electrical energy, very little wear and a highly reliable system (Chang and Chen, 2000).

The steam ejector cooling cycle has been demonstrated in 1910 by Maurice Leblanc (Gosney, 1982) and gained its popularity in the early 1930s for air conditioning of large buildings (Stoecker, 1958). Although having certain limitations, steam-jet systems are regaining importances, particularly for industrial applications such as the chilling of water to moderate temperatures in process industries, pharmaceutical and chemical industries, manufacturing processes (Decker, 1993).

Ejector cycle (also denoted as jet refrigeration) having a significant characteristic of utilization of low temperature thermal energy is suitable to use solar energy. Solar energy available abundantly in nature is a perfect match thermodynamically to generate the primary fluid for an ejector refrigeration system. However, according to the characteristic of an ejector and the initial investment cost, the solar jet refrigerator system is suitable for the application of air-conditioning system rather than other refrigeration purposes at lower temperatures.

The solar jet air-conditioning system can cope up with the availability of energy source required to remove the increased cooling load, incoming with higher solar intensity. Solar cooling systems powered primarily by direct solar thermal energy is therefore an attractive option and improved performance can be achieved with an increase in available solar radiation (Khattab and Barakat, 2002).

Sokolov and Hearshgal (1990), developed two new configurations of efficient uses of the mechanical power in order to enhance the secondary pressure without disturbing the refrigeration temperature, which are: (1) the booster assisted ejector cycle and (2) the hybrid vapour compression-jet cycle. The hybrid compression-jet refrigeration system consists of a

conventional compression and ejector sub-cycles with heat exchanger. Their simulated results show that the compression enhanced ejector can significantly improve the system performance.

Sun (1997) conducted mathematical simulation of a solar hybrid system with ejector cooling. Steam is used for the ejector system while R134a is used as the refrigerant in compression sub-cycle. The simulated results showed that the COP of the hybrid unit could be raised up to 50% compared to the conventional vapour compression system.

The combined ejector-compression machine of Huang et al. (2001), allows the wasted heat from the superheated vapour refrigerant in the compression sub-cycle to drive the ejector sub-cycle. The cooling effect achieved from the ejector-cooling device is used to cool the liquid condensate of compression sub-cycle that has an enhancement of the COP of the system. The COP of the system was 10% improved.

2.3 Working fluids for vapor power and cooling cycles

Steam is the most common working fluid for vapor power cycle. Steam is also used in industrial scale vapor compression cycles for refrigeration. Beside steam, many other working fluids exist for vapor cycles, both for power generation and refrigeration. In the open literature there are comprehensive approaches regarding the appropriate selection of the best working fluid for both cases: i) power generation when the fluid must be selected such that the work generated by expansion is maximized or ii) refrigeration when a high COP must be achieved.

Available options can include pure working fluids or a mixture of working fluids, where the mixtures can be zeotropic or azeotropic. In particular, for a trigeneration system, a working fluid which shows good characteristics for both cooling and power cycles must be selected. This aspect is discussed subsequently after reviewing the main characteristics and options of working fluids.

The working fluid selection should be the result of technical, economical, and ecological analyses. Many criteria can be inferred as identified by Papadopoulos et al. (2010) or Tchanche et al. (2008). According to them, the most important fluid properties are: density, boiling enthalpy, liquid heat capacity, viscosity, thermal conductivity, melting point temperature, critical temperature, critical pressure, ozone depletion potential (ODP), global warming potential (GWP), toxicity, flammability and the zeotropic or azeotropic characteristic.

The atmospheric life time of the working fluid is also important. An example of this would be a comparison of R11 and R152. Harada (2007) reported that the life time of R11 is 45 years while R152 is only 0.6 years. However, R11 has a GWP of 6370 and ODP of 11, while R152 has a GWP of 187 and ODP of 0.

Harada (2007) emphasized the importance of the retrograde or regular behavior of the working fluid for low-capacity applications using R134a (regular) and R245fa (retrograde). Borsukiewicz-Gozdur and Nowak (2007) studied regular working fluids such as propylene, propane, R227ea, R236fa, RC 318. Schuster et al. (2009) analysed ORCs with cyclohexane, R245fa, R141b, R365mfc. Larioala (1995) studied R11, R113, R114, toluene, fluorinol ($\text{CF}_3\text{CH}_2\text{OH}$) application in ORC. Saleh et al. (2007) – studied 21 organic refrigerants and 10 other organic fluids for ORC, among which n-hexane had the highest critical temperature (234.67°C) and R41 the lowest (44.25°C). Mago et al. (2008) examined the application of R113, R123, R245ca, isobutane. Colonna et al. (2006) proposed siloxanes as working fluids for ORC; they identified four siloxanes, namely MM, MD4M, D4 and D5.

Some zeotropic mixtures of organic fluids were identified by Borsukiewicz-Gozdur and Nowak (2007) as propane-ethane. Another zeotropic working fluid is the ammonia-water, mentioned above. This working fluid is very relevant for trigeneration systems because of the following features:

- Better match for the temperature profiles of the heat exchangers by adjusting the ammonia concentration,
- Excellent performance in power cycles,
- Excellent performance in absorption refrigeration and possible good performance for ejector cooling systems,
- Abundant and cheap,
- Does not pose essential safety and material issues,
- It does not produce negative environmental impact,
- There is a good knowledge of thermo-physical characteristics and equation of state for ammonia water mixture.

Note that in this work, ammonia-water is the selected working fluid owing to its characteristics and arguably the best suitability for trigeneration. In the thesis, ammonia-water is modeled with Engineering Equation Solver (EES) developed by Klein (2013). In this

software, the ammonia-water equation of state developed by Ibrahim and Klein (1993) is implemented.

2.4 Trigeneration systems

Multi-commodity generation increases the efficiency and utilization factor of a power generation system. Cogeneration at large scale is an established technology which has proven advantage over single power generation.

In the present context of the environmental impact and energy consumption further improvement of cogeneration system to utilize as much input energy as possible with the major components co-sharing concept of trigeneration was evolved. Keeping the end product as heating, cooling and power several researches and experimental analyses are being continuing. However current situation of environmental awareness energy supply, energy conservation and cost are primarily considered.

Cardona and Piacentino (2003a) formulated a measurement methodology for monitoring trigeneration systems for office buildings. Also Cardona and Piacentino (2003b) elaborated a sizing methodology of trigeneration plants for the Mediterranean area and a plant validation scheme as described in Cardona and Piacentino (2004).

Míguez et al. (2004) studied the feasibility of a cogeneration system. Ziher and Poredos (2006) analysed the economics of a trigeneration system for a hospital application. Lin et al. (2007) discussed a household trigeneration system. Meunier (2002) analysed the impact of co- and trigeneration on climate change control.

Khatri et al. (2010) performed an experimental analysis of trigeneration system using diesel engine exhaust as a source of heat and the thermal efficiency obtained was 86.2%. However, they used diesel engine exhaust which has high environmental impact and does not fulfill the requirement to work as a standalone compact unit.

Kohlenbach et al. (2006) performed a simulation modeling of the performance of a trigeneration system. The trigeneration unit consisted of a 60 kW gas turbine in combination with a desiccant sorption wheel to provide fresh air dehumidification, evaporative cooling and power generation.

The system was implemented in a library facility and the simulated result was validated with practical performance. Conversely, they used gas turbine which has adverse impact on environment due to the use of fossil fuel.

Marques et al. (2010) performed a performance analysis of a pilot plant trigeneration unit. The unit uses a compression refrigeration cycle in addition to power generation and heating from the condenser. Their results showed a high energy conversion ratio. However, compression refrigeration cycle needs substantial amount of electrical power that has to be supplied from its own power or from an external source. This reduces the overall efficiency of the integrated unit.

Minciuc et al. (2003) in a case study of a trigeneration with an absorption chilling machine established the limits for the best energetic performance of trigeneration. Huangfu et al. (2007) investigated a trigeneration system with a micro-scale integrated cooling, heating and power. The system was based on an absorption chiller and internal combustion gas engine for the use of residential and small commercial buildings. Integration of the absorption though has advantage over compression refrigeration system cycle, it has got disadvantages of high initial cost low COP and high heat rejections.

Hasan et al. (2002) proposed an ammonia-water cycle that simultaneously generates power and cooling. This system has been expanded by Khaliq et al. (2009a) into a trigeneration type. Ratlamwala et al. (2010) developed a power and cooling system that integrates an absorption refrigerator with a fuel cell. These systems have better energy conversion efficiency when compared with two independent systems (a power cycle and a refrigerator). Khaliq et al. (2009b) presented a trigeneration system that includes a Li-Br absorption refrigerator, a heat recovery steam generator, and a steam Rankine cycle and uses 425°C–525°C recovered flue gas from industry. Al-Sulaiman et al. (2010) show a system integration of solid oxide fuel cell with Rankine cycle and absorption refrigerator for trigeneration.

Ahmadi et al. (2011) showed an improved efficiency and less environmental pollution with a trigeneration system that integrates a gas turbine cycle, a steam turbine cycle and a single effect absorption chiller. Also Ahmadi et al. (2013) studied a micro gas turbine system integrated with dual pressure heat recovery steam generator, an absorption chiller, an ejector refrigeration cycle, a domestic water heater and a proton exchange membrane electrolyzer. The system generates power, heating, cooling besides hydrogen production.

2.5 Scroll expanders

The expanders are positive displacement machines that are used in vapor expansion cycles to generate power. There are prime movers that affect mostly the efficiency of the power cycle. The prime movers used in vapor power cycles are of two types: positive displacement types which use the pressure difference to generate useful mechanical work and kinetic type or turbomachines which use the kinetic energy of expanded vapor to generate power.

Turbo-expanders operate at high pressure ratio. When one expands organic fluids the turbines need to have special construction as developed by Lariola (1995). Remarkable progress in the area of computational simulation of ORC turbines is attributed to Harinck et al. (2010). They had shown that real gas effects are crucial due to typical operation in the dense gas region. However, high efficiency is difficult to obtain with turbines when high pressure working fluids are used such as is the case in many types of ORC.

Yamamoto (2001) designed a turbine for a small scale ORC and obtained low isentropic efficiency (15-46%) when the heat input varied from 13 kW to 9 kW. In general, the ORC turbine is characterized by very high rotational speeds which for ORC turbines can reach 60,000 RPM or more. Arguably, designing and manufacturing ORC turbines can be considered expensive due to the fact that they are sensitive to operating conditions and therefore the design must be customized for each specific application. Furthermore, due to the tip leakages that are relatively constant with turbine size, operation at low capacities can be very inefficient. The fact is that at low capacity, the magnitude of the bypass flow is at higher percentage of the main stream.

Another option for ORC prime mover is a positive displacement expander (Brasz et al., 2005). Several kinds of those can be found suitable for ORC: axial piston, rolling piston, rotary vane, screw, scroll and other kinds. Badr et al. (1984) analysed the application of multivane expanders in Rankine cycles. Maurer and Zinn (1999) performed an investigation on axial piston expanders and had shown that its volumetric and isentropic efficiencies are approximately 30%, and 41% respectively. Wang et al. (2010) used a rolling piston type expander in an organic cycle ORC with R245fa using low grade solar heat source. It had achieved a maximum isentropic efficiency of 45.2%. Mustafah and Yamada (2010) analyzed a rotary vane expander with R245fa for a heat source temperature range of 60°C to 120°C. Furthermore, they had projected isentropic efficiencies of over 80%. For a range of capacities

from ten to a few hundred kW, twin screw expanders were found suitable (Smith et al. 1996). Screw expanders had shown good adaptability to the operating conditions as they are able to handle two phase flows (Infante Ferreira et al., 2004).

As mentioned previously, when operating with an organic working fluid the pressure ratio across the prime mover needs high value. For low capacities, the best choice of positive displacement expanders is the scroll type expander. Use of scroll expander in small scale organic Rankine cycle is a promising technology in harnessing low grade heat source. However, being the efficiency is low, it has advantages over other expanders of this smaller range. Reciprocating, screw, vane type, and other conventional expanders have a number of moving parts and their design features are complex. On the other hand, scroll compressor has less moving parts and very reliable in operation and maintenance. The geometry of scroll machines is simpler than that of screw because the scroll has 2D geometry, while the screw has a 3D geometry. Scroll units are quieter than screw type they are easier to manufacture for low capacity applications.

Nagatomo et al. (1999) investigated the performance characteristics of a scroll expander modified from a refrigeration compressor in an ORC. They had found a maximum expander isentropic efficiency of 74%. Also Yanagisawa et al. (1988) had modified a refrigeration scroll compressor to operate as an expander and tested it in an experimental loop operating with compressed air. They had found a maximum isentropic efficiency of approximately 75%. Husband and Beyene (2008) presented a theoretical model of low grade heat driven Rankine cycle with scroll expander and showed thermal efficiency of 11% for a fixed 10 kW work output. Kim et al. (2001) used a scroll expander in a low temperature heat recovery system, and had found its volumetric efficiency to be 42.3%. Zanelli and Favrat (1994) converted a hermetic scroll compressor to operate as an expander and tested it in a Rankine cycle. They found the maximum isentropic efficiencies of about 63% at a rotating speed of 2400 RPM. Harada (2010) tested a scroll expander modified from a refrigeration scroll compressor with R134a and R245fa. They had found its isentropic efficiency to be over 70% for 1 kW power output. It was found that the rotational speed slightly influences the performance, but the optimal expansion pressure ratio was determined to be approximately 3.3.

The geometrical modeling of scroll machines have been investigated by Bush and Beagle (1992) and Chen et al. (2002) based on involute curve theory. Mathematical expressions for

fluid pocket volumes are very important in thermodynamic modeling, and were developed by Wang et al. (2005). Thermodynamic models for scroll machines were presented by Lemort et al. (2009), Oralli et al. (2010), Harada (2010). Leakage or by-pass flows in scroll machines were studied by Tojo et al. (1986), and Puff and Krueger (1992). From these studies, the leakage flow regime is found between two limits: Fanno (isenthalpic flow) and isentropic flow, respectively.

2.6 Ejectors

Several theoretical and experimental studies address the application of ejectors with different design criteria for refrigeration and cooling systems. A number of thermally driven ejector cooling of various configuration have been examined where an ejector replaces the function of the compressor to compress the fluid to the condenser pressure (Meyer et al., 2009, Abdulateef et al., 2008).

One of the configuration of the ejector cooling known as thermal-driven steam-jet refrigeration system has several merits over the conventional electric-driven vapor-compression system (ASHRAE, 1979). Keenan et al. (1950), theoretically and experimentally analyzed the ejector for the first time using the thermodynamic equations. Their investigation is the foundation of ejector analysis and used by the fellow researchers. A number of refrigeration systems are configured with a goal to enhance the performance of the system.

Hung et al. (1999) show a 1-D analysis of ejector performance. Not only the operating conditions, but the ejector geometry affects the ejector performance in terms of cooling capacity, COP and critical backpressure pressure. The position of the primary nozzle is very important as it affects the level of the backpressure. Retracing the nozzle into the mixing chamber causes the cooling capacity and COP to increase with the expenses of critical condenser pressure. A single optimum nozzle position cannot be defined to meet all operating conditions.

Munday and Bagster (1977) showed that after exhausting from the nozzle, the primary flow fans out without mixing with the secondary flow and induce a converging duct for the secondary flow. This duct acts as a converging nozzle such that the entrained flow is accelerated to a sonic velocity at some place, i.e. hypothetical throat. After that, the mixing of the two streams starts with a uniform pressure.

2.7 Heat exchangers

In a thermodynamic cycle the heat transfer units are the key components to establish an efficient heat extraction mechanism. The heat exchanger is used for this purpose and its design parameters determine the effectiveness of the component. Broadly heat exchangers can be categorized as direct contact heat exchangers where there is no intervening surface between fluids and indirect contact heat exchangers, where there exist a partition between the fluids.

In microchannel heat exchangers (MCHEX) a set of wavy fins are normally connected to the external surface of the tubes to increase the heat exchange surface. MCHEX have attracted attention because they have a high heat transfer area per operational volume unit, and thus, high heat transfer coefficients. For a very small dimension, they provide a very large heat flux transfer.

Experimental and numerical study on microchannel and round-tube condensers in a R410A residential air-conditioning system is presented in Park and Hrnjak (2008). Shao et al. (2009) developed a numerical model of the serpentine of a microchannel heat exchanger. Also, Litch and Hrnjak (1999) studied ammonia condensation in microchannel condensers. Kim and Bullard (2001) developed a microchannel evaporator model for an air conditioning system. Tuo et al. (2012) developed an experimentally validated model for a parallel flow microchannel evaporator.

2.8 Closing Remarks

The literature review reveals that a number of researches were performed on low grade heat engine on single generation, cogeneration and some trigeneration set-ups. Theoretical and experimental analysis were performed with different types of expanders like reciprocating, vane type and screw expander etc. But scroll expander being simple in design with less rotating parts, valve less and less frictional surfaces has advantage over other positive displacement machines and is found suitable to act as a prime mover for this type of low power generating system. Also for trigeneration system a group of researchers examined the unit with absorption chillers as the cooling system and in few cases integrated compression refrigeration system. But absorption chiller being robust in design, complex in operation is not suitable to use as a standalone system. On the other hand compression refrigeration system needs a high electrical

power to run the compressor and thus for smaller scale power generation system, it is not suitable.

Investigating all the design and operational facts of the previous works, it is found that a scroll based trigeneration system with ejector cooling system has not yet been done and bears a high feasibility.

Chapter 3: Trigenation System Description and Prototype Development

3.1 System description and its thermodynamic cycle

The trigeneration system as addressed earlier is a single unit which generates simultaneously power, heating and cooling. The integration of the three subsystems (power, heating and cooling) is conceptually designed based on practical knowledge, thermodynamic principles and availability of technologies for the components. Also emphasis is given to the type of energy input which is considered as low grade heat source. Renewable energies such as solar, geothermal, waste heat or biomass combustion are considered the most suitable sources of energy in respect to environmental impact.

The system components are selected according to the input source and the desired capacity of the unit. Also based on the temperature level of the heat source the working fluid has been selected. However, before determining the final configuration of the system various alternatives were briefly analyzed thermodynamically. The following considerations are taken into account in designing the unit:

- Small stand-alone unit,
- Optimize energy and exergy efficiencies,
- Reduced environmental impact,
- Use of off-the-shelf equipment and components where possible,
- Cost effectiveness.

Based on the above considerations, the trigeneration system has been developed using a custom made scroll expander and ejector. The scroll expander has advantages over other prime movers that are discussed in previous chapters. For small scale operation, ejector cooling system has benefit over compression or absorption system because of simple design features. Also considering the heat source temperature ammonia-water is found a suitable choice.

Each of the individual systems integrated has their own subcomponents. Conversely, as a whole they share the basic components of the core unit. The system integrates a regenerative Rankine cycle with an ejector cooling cycle as shown in in Figure 3.1. The system is designed for low scale power generation in the kW range; it also generates heating of service water of tens of kW and produces 1-2 kW of refrigeration at approx. 5°C.

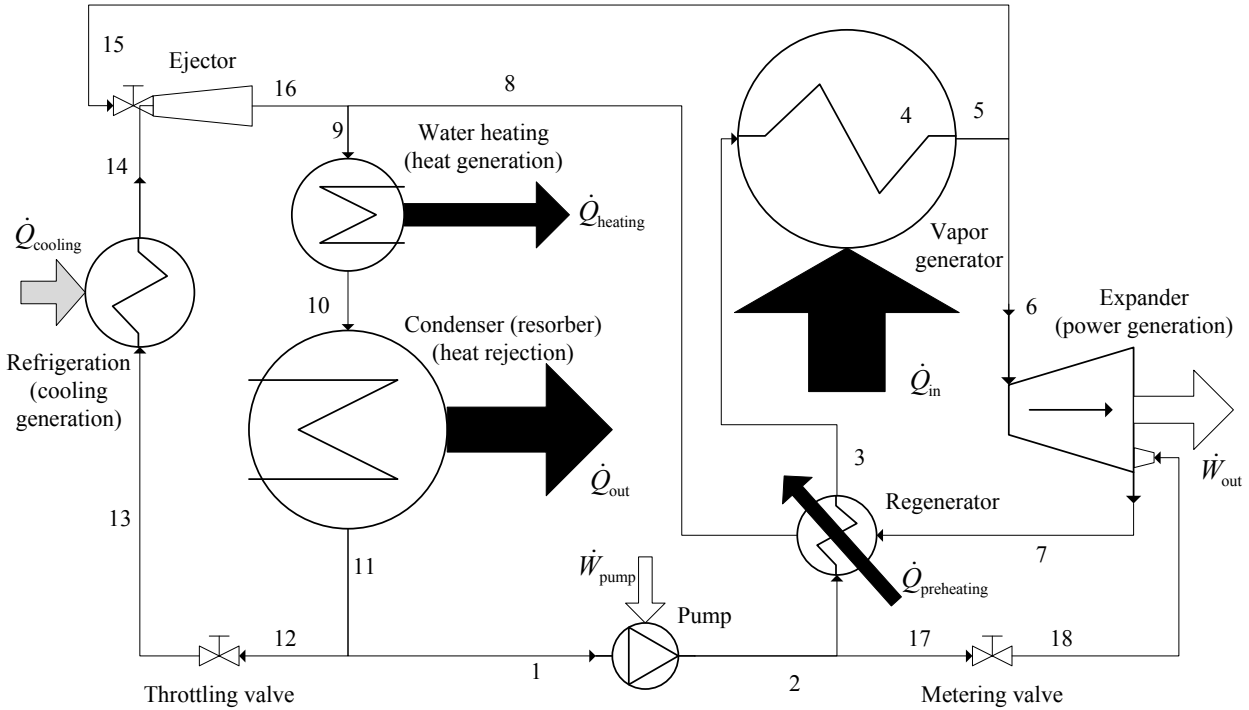


Figure 3.1: Ammonia-water based trigeneration system with Rankine and ejector cycle integration [black arrows = heat fluxes, grey arrow = cooling, white arrow = power].

Table 3.1: Description of thermodynamic states for the trigeneration system (Figure 3.1).

State	Description	State	Description
1	Saturated or slightly sub-cooled liquid	10	Low-quality two-phase fluid
2	Pressurized (subcooled) liquid	11	Saturated or slightly sub-cooled liquid
3	Preheated ammonia-water liquid	12	Liquid refrigerant toward evaporator
4	Saturated working fluid (inside vapor generator) 4' = saturated liquid; 4'' = saturated vapor	13	Throttled low-temperature refrigerant toward evaporator
5	Superheated vapor (few degrees superheating)	14	Saturated vapor of ammonia-water refrigerant
6	Superheated vapor toward the expander	15	Hot high-pressure vapor toward ejector
7	Expanded vapor (near vapor saturation)	16	Recompressed refrigerant at condenser pressure
8	Low-pressure working fluid at high quality	17	High-pressure liquid to metering valve
9	Slightly superheated low-pressure vapor	18	Cold liquid injection for lubrication

Table 3.1 gives the description of each of thermodynamic states shown in the diagram from Figure 3.1; also the thermodynamic processes are described in Table 3.2. The heat source

for the system is considered to be a hot fluid which exchanges sensible heat at the vapor generator.

The maximum temperature level of the heat source is assumed in the range of approx. 100°C to 160°C. Heat sources with temperature in this range are relatively abundant: combustion flue gases, solar energy at low concentrations, various industrial processes which waste heat, also heat rejected by topping cycles for power generation.

Table 3.2: Thermodynamic processes within the trigeneration system (Figure 3.1).

Process	Description
1-2	Pressurization of liquid (pumping)
2-3	Preheating (regenerator)
3-4-5	Vapor generation
5-6-15	Flow splitting of superheated vapor (#5 toward expander; #15 toward ejector)
6-7	Vapor expansion
7-8	Regeneration (heat release from two-phase flow)
8-9-16	Mixing of streams #8 and #16
9-10	Ammonia resorption and incomplete condensation
10-11	Complete condensation and heat rejection
11-1-12	Liquid flow splitting (#1 toward pump, #12 toward throttling valve)
13-14	Evaporation and heat absorption from cooling process
14-15-16	Ejector process (14-16 compression; 15-16 expansion)
17-18	Cold liquid injection for lubrication

Figure 3.2 shows the qualitative representation of the thermodynamic cycle of the trigeneration system, as a $T-s$ diagram. The power cycle is visible in the figure as 1-2-3-4-5-6-7-8-9-10-1. The ejector cooling cycle is represented by the line 1-13-14-15-7-8-9-10-1. The heat production process is represented by the line 9-10.

As shown in the figure, the whole unit is composed of a power cycle, a heat delivery process (9-10) and a cooling cycle. The power cycle which is the heart of the system is basically a Rankine cycle with ammonia-water. The cycle components are a vapor generator (ammonia desorber), an expander, a pump and a condenser (ammonia resorber). The vapor generator is supplied with heat using a heat transfer fluid. The vapour generated is supplied to the custom made scroll expander to convert the heat energy into mechanical energy. After expansion, the fluid goes to the condenser to release the heat to complete the cycle and flow back to the pump. During the condensation process some useful heat is generated for heating

service water. Note that the condensation process is accompanied by ammonia resorption into liquid.

The cooling system mainly consists of an ejector, an evaporator coil and some piping arrangements. A stream of high pressure ammonia-water vapour channeled from the vapor generator, flows through the ejector. An evaporator coil is attached to the ejector in the throat section, the other end being connected to the throttling valve supplied with liquid from the receiver placed at the bottom of the condenser.

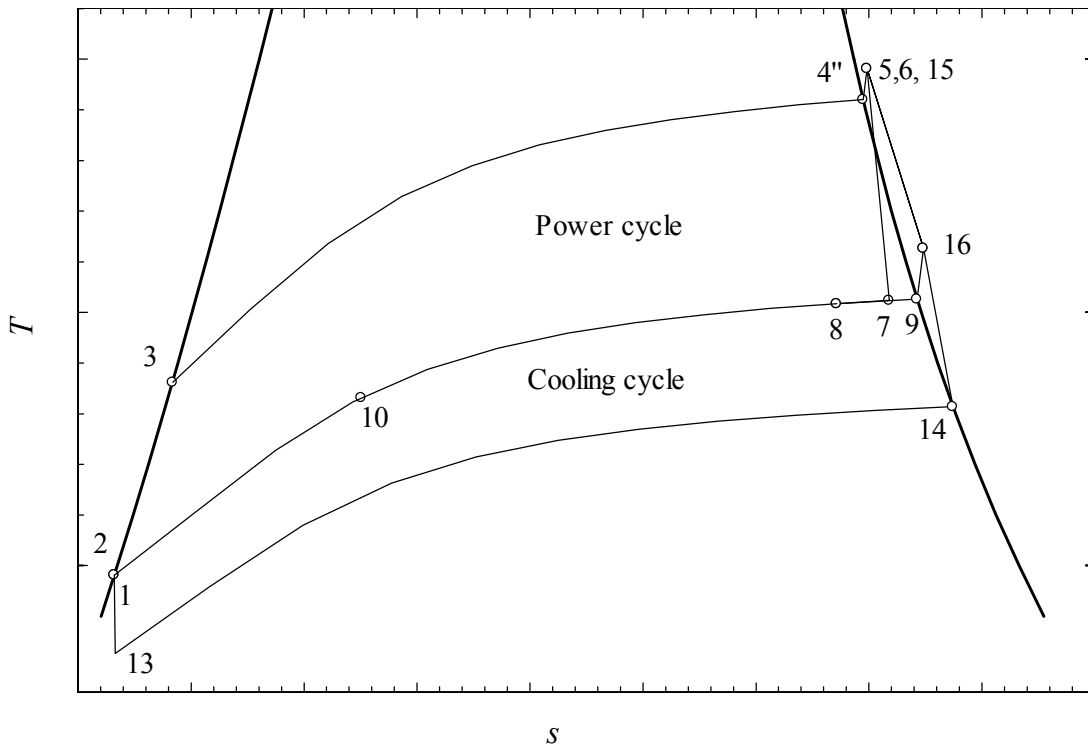


Figure 3.2: Thermodynamic cycle for the trigeneration system.

Steam passing through the ejector develops high velocity in the throat area and drops pressure substantially to induce the evaporation of the working fluid in the evaporator. The main vapor stream and the secondary vapour from the ejector thus mix together and flow to the diffuser section to build pressure. Finally, the mixed flows are routed to the condensing unit and complete the cycle.

There are some novelty aspects with the proposed trigeneration system as follows:

- The use of the ejector cooling in an integrated manner with an ammonia-water Rankine cycle is new.

- The resorption-condensation scheme (process 7-8-9-10-11) represents a new scheme which combines regeneration (process 7-8/2-3) with heat transfer for heat product generation (process 9-10) and heat rejection into the environment (process 10-11); in this scheme the temperature for cogeneration is upgraded due to the mixing process with the stream at the ejector output (process 8-16-9).
- A new oil-free scroll expander prototype is demonstrated having liquid working fluid injection for lubrication (this simplifies the hardware since for common applications the vanes in scroll machines are lubricated with oil).

3.2 Trigeneration system prototype

In order to assess the feasibility and performance of the new trigeneration system, a proof-of-concept prototype has been designed and built. The prototype involved the development and construction of some novel components as follows:

- Oil-free scroll expander lubricated by working fluid injection,
- Oil-heated vapor generator with micro-channel heat exchangers,
- Water-cooled condenser-resorber with micro-channel heat exchangers
- Ejector for cooling cycle with ammonia-water.

In addition, a custom-design oil heater has been built. All other components of the prototype trigeneration system were off-the-shelf elements and devices. The diagram of the trigeneration system prototype is shown in Figure 3.3. The testing system also includes a heating loop and a cooling circuit for the condenser.

Note that there are some slight differences between the conceptual design of the trigeneration system shown in Figure 3.1 and the built prototype shown in Figure 3.3. Namely, the prototype has incorporated only one single heat exchanger in the condensation/resorption loop (process 10-11 in Figure 3.3). Instead, the trigeneration system has two heat exchangers in series, which are 9-10 used for water heating and 10-11 used for heat rejection (Figure 3.1). The reason behind this is that the prototype's condensation/resorption loop includes one single heat exchanger to reduce cost. In addition to this, the cooling coil used for the cooling generation component of the system has a relatively small surface (0.02 m^2) and therefore is capable of producing cooling in the range of tens of watts up to $\sim 100 \text{ W}$. These simplifications do not affect the proof-of-concept.

The prototype is fully equipped with measurement devices for testing. In Figure 3.3, the state points are indicated which are required for data processing and thermodynamic analysis. The symbols used in the diagram are explained as given in Table 3.3. The prototype is equipped with many auxiliary components which are necessary for the proper operation for various procedures such as pressure testing, leak proofing, vacuuming, charging, draining, discharging, pressure release etc. The list of valves and their use for the prototype is given in Table 3.4.

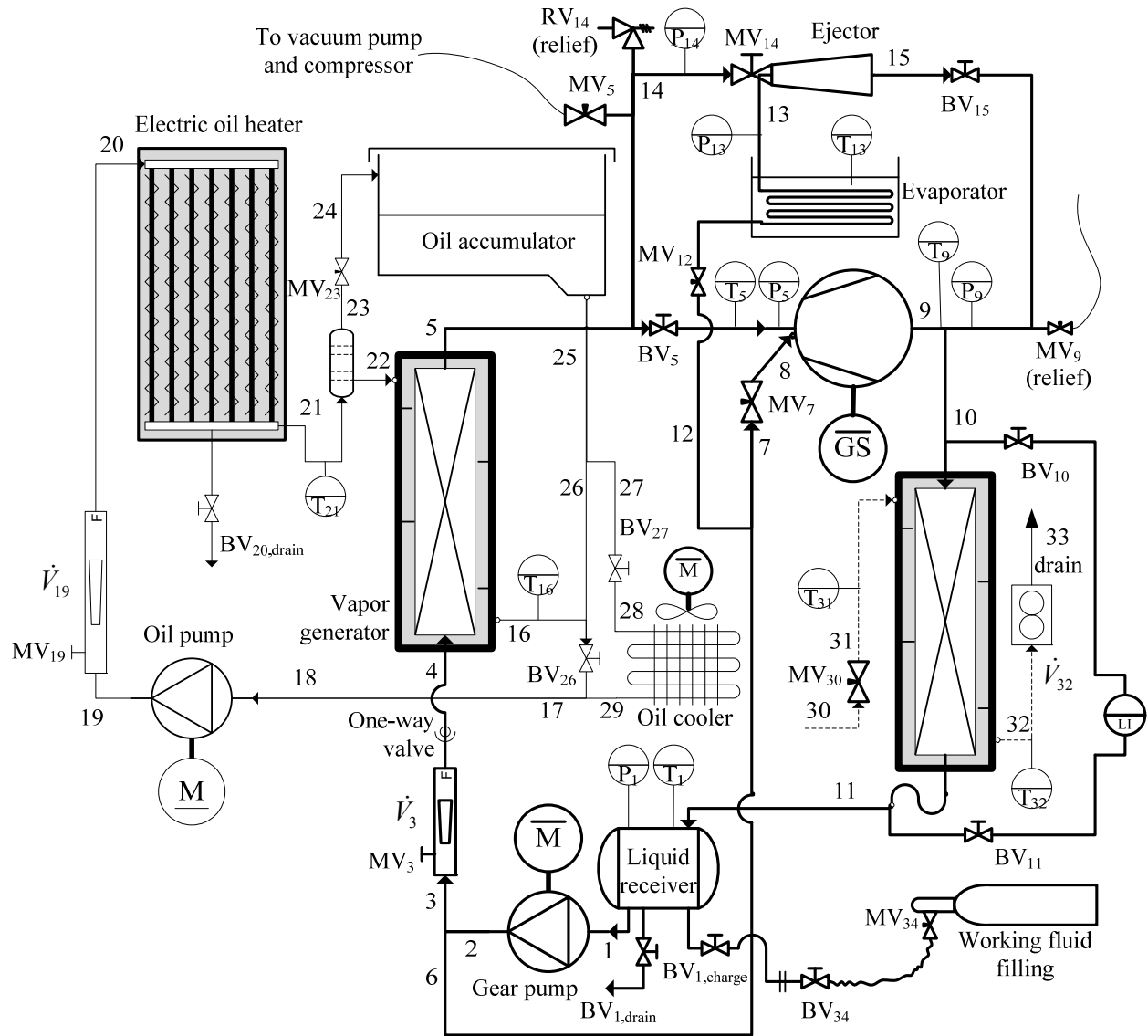


Figure 3.3: Ammonia-water based trigeneration system prototype, as built.

Some functional aspects of the system which are resolved by auxiliary components are described subsequently. The condenser/resorber has a liquid trap for the working fluid at the

exit. This will prevent any gas passing into the liquid receiver which must be flooded at all times. The vapor generator feed line has a non-return valve which impedes any tendency of the liquid inside to flow backwards. The oil line has a liquid-gas separator which allows for air or oil vapor separation and return via the metering valve MV₂₃ to the oil accumulator; so that the oil pressure is balanced hydrostatically.

Table 3.3: Significance of graphical symbols used in the system diagram from Figure 3.3.



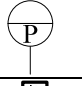
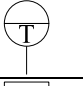
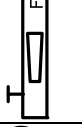
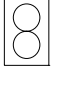
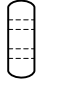
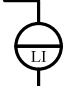
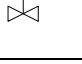
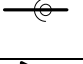


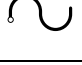
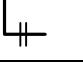
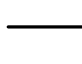

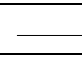
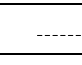
Symbol	Explanation	Symbol	Explanation
	DC motor; used to control the angular speed via electric potential adjustment		DC generator unit (consisting of an externally excited alternator and a rectifier)
	Pressure gage with its own digital indicator		Temperature sensor connected to data acquisition
	Flow meter (rotameter with incorporates a needle valve for flow rate regulation)		Volumetric flow meter
	Gas liquid separator used within the thermal oil circuit		Level indicator
	Ball valve (BV) used to open/close flow		One-way valve
	Metering valve (MV, for flow metering or throttling depending on the case)		Relief valve (RV, safety valve)
	Liquid trap (used after condenser)		Compression fitting for quick disconnect
	Working fluid line		Flexible line for working fluid charging
	Thermal oil line		Water line

Table 3.4: Valve functions for the prototype trigeneration system.

Valve	Function	Valve	Function
BV _{1,drain}	Safely drain the ammonia-water working fluid	BV _{1,drain}	Opens when working fluid is charged
MV ₃	Adjusts the flow rate of working fluid	BV ₅	Separates the expander from vapor generator
MV ₅	Connects the vacuum pump or compressor	MV ₇	Adjusts the flow rate of liquid injection
MV ₉	Allows for manual release of working fluid	BV ₁₀	Separates the liquid level indicator (gas phase)
BV ₁₀	Separates the liquid level indicator (liquid phase)	MV ₁₂	Throttles the liquid towards evaporator
MV ₁₄	Adjusts the primary flow through the ejector	BV ₁₅	Isolates the ejector from condenser
MV ₁₉	Adjusts the flow rate of thermal oil	BV _{20,drain}	Drains the thermal oil
MV ₂₃	De-aerates the oil circuit	BV ₂₆	When opens, by-passes the oil cooler
BV ₂₇	When opens, connects the oil cooler	MV ₃₀	Adjust water flow rate for condenser
MV ₃₄	Adjusts the flow rate during charging	BV ₃₄	Separates the charging line

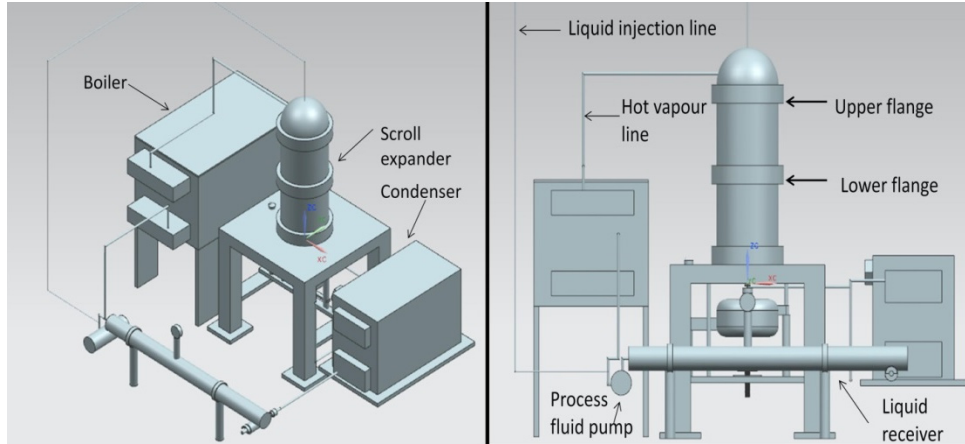


Figure 3.4: CAD drawing showing the relative placement of the main components of the trigeneration system.



Figure 3.5: Photograph of the trigeneration system.

The construction of the trigeneration system has been realized on a metallic structure designed such that it allows for working fluid circulation and drain through the gravitational field. In this respect, the expander is placed with the intake at a higher level, whereas the

condenser is below the expander outlet. The liquid receiver is placed below the condenser and the working fluid pump is placed at the lowest level on the supporting structure. Figure 3.4 shows a CAD drawing of the supporting structure. A photograph of the trigeneration system as built is shown in Figure 3.5. The prototype system is designed with the requirement of generating 1kW of power using a heat source of around 150°C. The amount of heat supply is estimated at 20-30kW. The heat exchanger on the heat source side is therefore designed on the basis of 30 kW heat transfer. The sink side heat exchanger has a similar duty.

The prototype includes the following subsystems having a custom design:

- Scroll expander which itself is developed as a prototype,
- Vapor generator which uses heat transfer oil for heating,
- Condenser-resorber,
- Oil heater which is of electric type with 30 kW duty,
- Ejector with adjustable nozzle throat.

All the other components of the prototype are off-the-shelf devices or elements. The ammonia-water (working fluid) pump is a gear pump with an internal bypass. The pump is driven by a 24 V DC motor of 4000 RPM which is connected through a magnetic coupling such that the pump is perfectly sealed. The pump is sized based on the required flow rate, system pressure, head and frictional losses within the piping system. In order to avoid problems with cavitations, a positive displacement pump with high suction head (24 inch) has been selected as an additional precaution, although the location of the pump is at the lowest level and in normal operation does not require priming. The characteristics of the working fluid pump are given in Table 3.5. A photograph showing the gear pump installed under the liquid receiver (left side) is shown in Figure 3.6.

Table 3.5: Working fluid pump characteristics.

Parameter	Specification	Parameter	Specification
Make	Cole Parmer 073003-4	Type	Gear pump with internal bypass
Capacity	1.17 ml/rev	ΔP_{\max}	4.1 bar
Drive	4000 RPM @ 24 V	Run dry	Up to 30s
Materials	316SS body, PPS gears, Viton seals	Duty cycle	Continuous from 150 to 5000 RPM



Figure 3.6: Photograph detail of the working fluid pump and liquid receiver.

For oil circulation, a diaphragm pump has been chosen with the maximum flow rate of 6.8 lpm and lower pressure differential of 3.1 bar. The pump type characteristics are given in Table 3.6. Duratherm 450 has been selected as thermal oil which is recommended for heat transfer application with temperature inferior to 235°C. The viscosity is around 1.3 cSt, thermal conductivity around 0.14 W/mK, heat capacity around 2.3 kJ/kgK, and density around 0.8 kg/l. However, the vapor pressure of oil is about 25 kPa at 235°C which indicates that evaporation occurs in the working condition when the presence of air in the oil cannot be avoided. Therefore, a special design and piping arrangement is made to allow for oil and gas expansion on one hand, and on the other hand to separate the gases and balance the circuit hydraulically.

Table 3.6: Characteristics of the circulation pump for thermal oil.

Parameter	Specification	
Make	Cole Parmer T-75420-07	
Type	Diaphragm pump	
Max flow	5.3 lpm @ 12 V drive	
ΔP_{\max}	3.1 bar	
Materials	Polypropylene (body), santoprene (diaphragm), valves (Viton)	
Priming	2.5 m H ₂ O suction	

An air-cooled oil cooler is integrated to cool the return oil from the boiler before supplying it to the pump as the pump cannot operate at high temperature. A by-pass line is installed to by-pass the flow while performing the experiments to vary the operating parameters. Figure 3.7 shows the photograph of the oil-cooler which is a fined surface heat exchanger to which an air blower is attached.



Figure 3.7: Detail photograph of the air-cooled oil cooler.



SS-4MG valve for liquid injection metering; the valve has a micrometer handle

Figure 3.8: The installation of the metering valve for liquid injection.

The piping elements of the prototype are made in carbon steel although stainless steel will be a better choice for longer durability. However, the use of carbon steel is cost effective and is acceptable provided that ammonia concentration is low and operating temperatures are mild. The majority of the connections and fittings are of NPT standard (NPT = National Pipe Thread).

All ball valves are coated with nickel except BV_1 and BV_{34} which are stainless steel compression fitting types. The metering valves are of needle valve type except MV_{30} which is a screw-down valve in brass as it is used for water flow rate adjustment for the condenser. Also the metering valve MV_7 which adjusts the flow rate of the injected liquid is in stainless steel

with compression fittings from Swagelok (type SS-4MG) featuring a flow coefficient of 0.03 for which the flow rate is about 0.01 lpm at 1 turn and 0.1 lpm at full open in the operating conditions.

3.3 Scroll expander development

The scroll expander is a new oil-free design which features injection of liquid working fluid for lubrication. The design evolved during several trial and error iterations during one and half years. The scroll wraps are taken from a scroll compressor from refrigerator, namely Bristol H20R483DBE featuring 65 ml per revolution. The scrolls are of compliant type and an Oldham coupling is used to insure the compliance. The height of the wrap is 29 mm and the thickness is 3 mm. The built-in volume ratio, representing the geometric expansion ratio of the expanding cavity must match approximately the volume expansion for the power cycle. The over expansion has to be avoided. The procedure of cycle design when a scroll compressor is converted into an expander without modifying the scroll has been previously elaborated and validated in Oralli et al. (2010), Tarique (2011), Tarique et al. (2014), Oralli et al. (2014). This procedure has been applied for the same scrolls and thermodynamic cycle parameters determined accordingly.

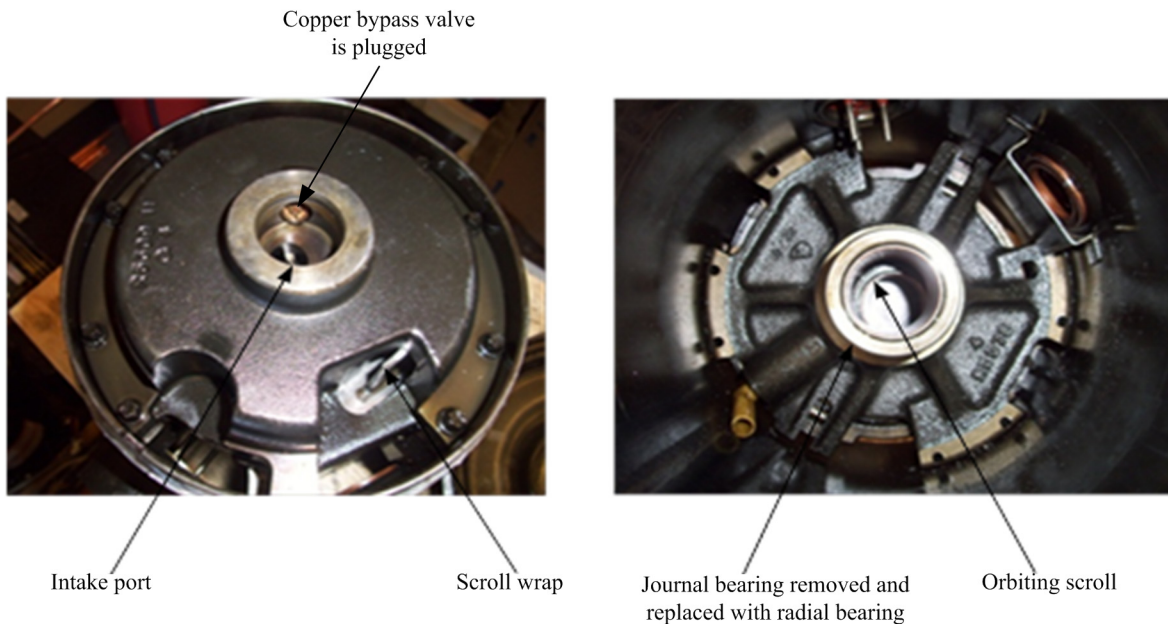


Figure 3.9: Removal of the bypass valve and journal bearing of the original Bristol H20R483DBE scroll module; the journal bearing was replaced with a radial roller bearing.

For constructive modifications, several adaptations were made. The copper by-pass valve previously existent on the fixed scroll has been removed and its channel blocked with a steel plug as shown in Figure 3.9 (left). Also, the original journal bearing of the orbiting scroll support has been completely removed. Instead, CNC machining was applied to install new parts and adaptations and a radial roller bearing has been inserted to support the upper part of the rotating shaft. Figure 3.9 (right) shows the original journal bearing of the scroll unit which has been replaced. In the figure, the position of the roller bearing can be observed.

As shown in Figure 3.10 the new expander-generator comprises the following elements:

- A vapor plenum which plays the role of pressure accumulator to dump short fluctuation,
- The liquid injection line transverses the plenum such that liquid can be injected at the right spot, that is above the intake port of the fixed scroll unit,
- The rolling bearing support structure is new and made robust to compensate for the eccentric forces due to orbiting movement,
- The shaft has been mechanically balanced by attaching a half ring in stainless steel weighting few hundred grams,
- The shaft has a flywheel,
- At the bottom support, a radial-axial roller bearing is inserted in a new supporting cage,
- The housing is completely new and comprises two sets of flanges,
- A magnetic coupling with contaminant barrier has been added to transmit power,
- A clutch has been designed and built to couple or decouple the generator.

The original scroll wraps were rectified. These are shown in Figure 3.11, where the fixed scroll is in the left and the orbiting scroll in the right.

The scrolls surface has been cleaned by sand blasting and the fixed scroll has been machined in order to reduce the leakage gap between the two mating scrolls. Through machining, the radial gap has been reduced four times from 300 μm to below 70 μm .

Figure 3.12 shows the fixed scroll after modification consisting of the elimination of the bypass valve and CNC rectification, the shaft with the eccentric, flywheel and its radial axial bearing at bottom, the new supporting part for the radial bearing at the top, the housing with upper flange and middle flange and O-rings. Figure 3.13 shows a detail photograph of the expander housing. The housing has three components: the upper cap (a), the top body (b) and the lower body (c).

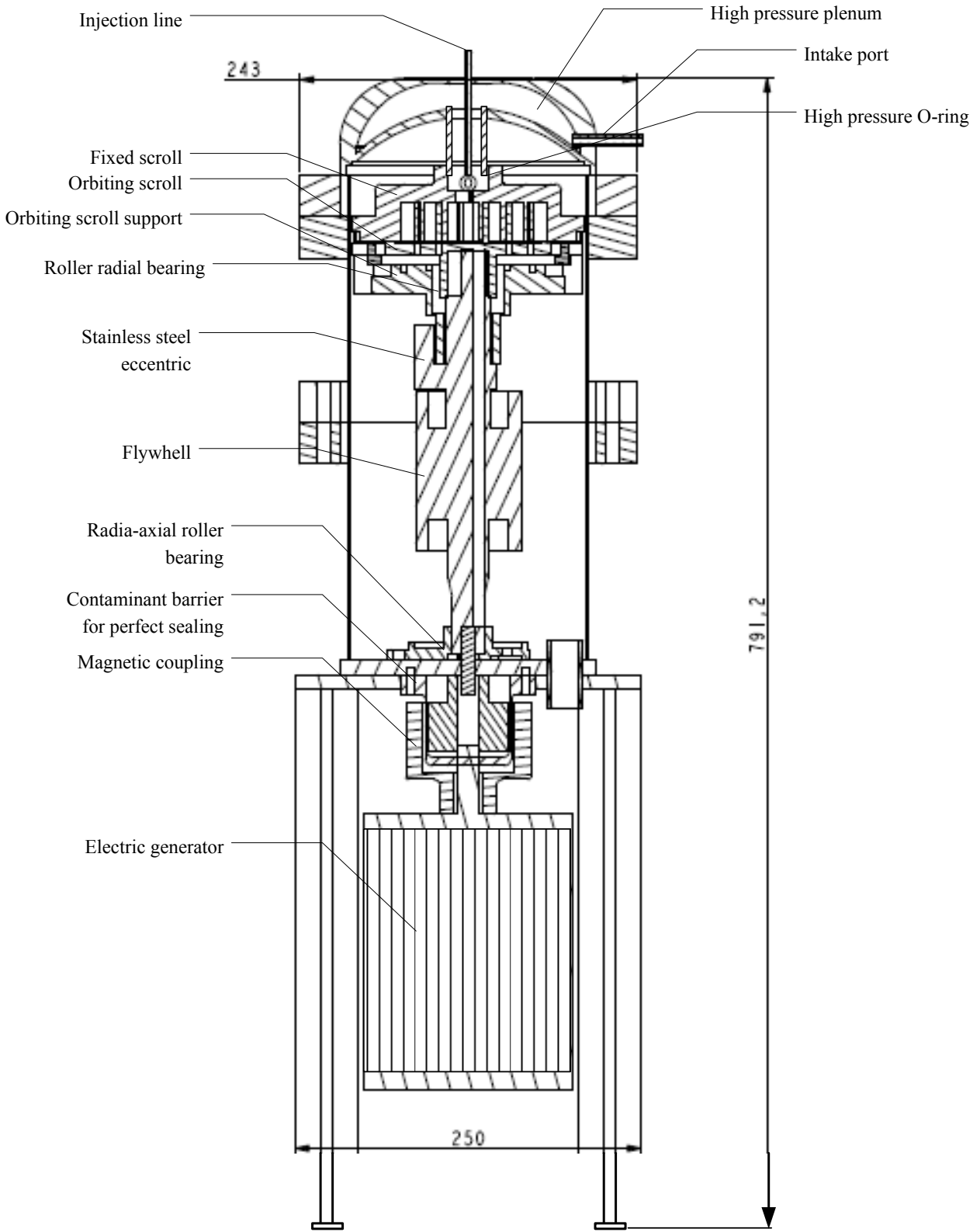


Figure 3.10: Novel scroll expander / generator assembly.

Only the expander cap, where hot working fluid enters, is thermally insulated. In the housing, the working fluid is at lower pressure (the same pressure as the pressure of the expanded working fluid).

The expander must work in very tight sealing conditions so that no ammonia can escape out of the system. In this respect a magnetic coupling has been selected and installed. The magnetic coupling has been selected based on the design angular speed and shaft power. The average angular speed is set to the order of 1000 RPM based on previous experience with scroll units. However, for the present expander it is expected that angular speed may reach over 3000 RPM. The torque-power relationship is:

$$\dot{W} = \mathcal{T} \omega$$

with $\omega = 2\pi\dot{N}/60$, where \dot{N} is the angular speed in RPM.



Figure 3.11: Scroll wraps of the scroll unit (fixed scroll – left side, orbiting scroll – right side).

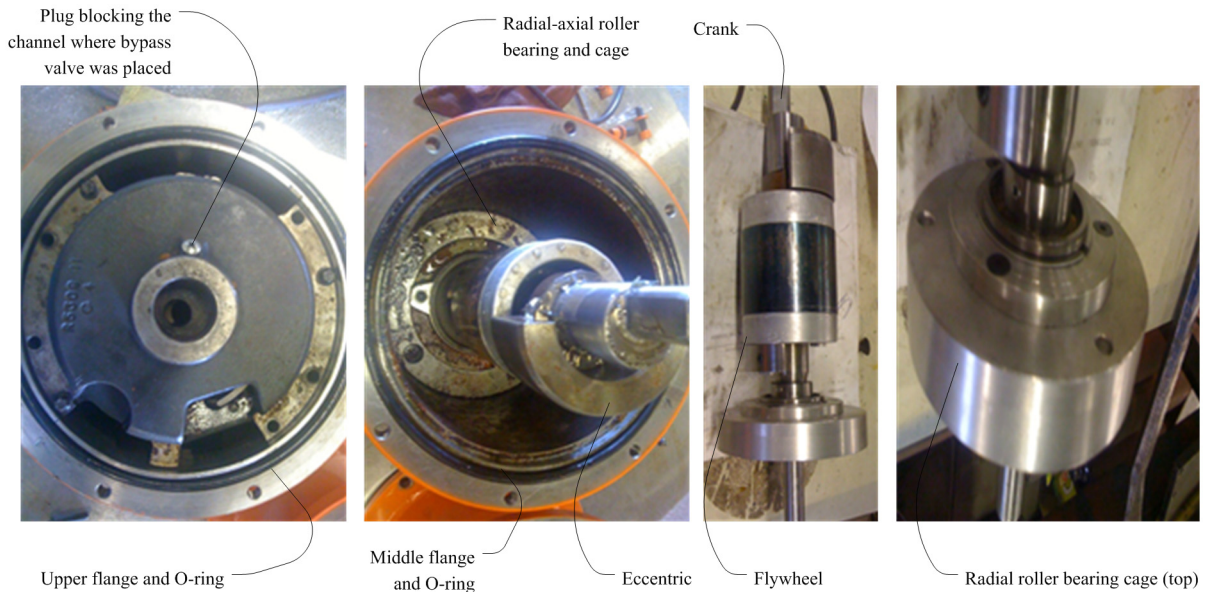


Figure 3.12: Modifications and additions to scroll unit and shaft.

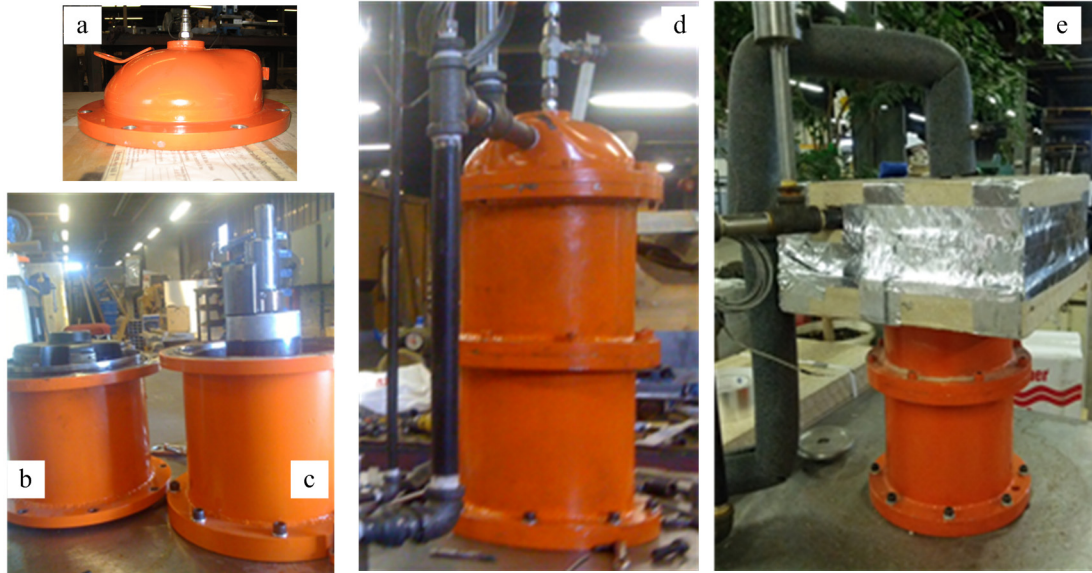


Figure 3.13: Detail photograph of the expander housing: a) upper cap, b) top body, c) bottom body, d) assembled expander, e) thermal insulation.



Figure 3.14: Expander-generator clutch arrangement.

Consider an estimated value of the power output of the expander as 1kW with an angular speed of 1000 RPM. Then τ becomes 10 Nm. This value of the estimated torque can be used in sizing the magnetic coupling. The shaft end is connected to the male part of a magnetic coupling. The magnetic coupling is used to transmit the shaft power to a generator without physical contact. This arrangement is used to confine the process fluid within the leak proof closed loop.

However, the contaminant barrier cup placed between the shaft-connected magnet and the external magnet which is connected to the generator is made of stainless steel and therefore dissipates power. According to the manufacturer of the magnetic coupling, the mechanical power losses due to magnetic dissipation are of the order of 20% of the transmitted shaft power. The selected magnetic coupling is MTC-10 of co-axial having the nominal torque of 10 Nm, peak torque of 12 Nm and maximum angular speed of 13,000 RPM. Thence, for our expected maximum angular speed of 3600 RPM the maximum transmitted power is about 3.7 kW.

It has been observed from preliminary tests with compressed air that idle start is sometimes better for the expander. Because of this reason, a clutch system has been designed and built. The clutch arrangement functions as a mechanism of disengaging the driven shaft from the power shaft during start-up of the engine. This unloads the shaft and reduces torque during starting the engine. Figure 3.14 shows a photograph with the clutch disengaged (left) and engaged (right). The clutch arrangement is composed of two sprockets entrained by a chain with the help of a crank.

3.4 Ejector development

The ejector dimensions were estimated based on the ejector cooling design methodologies as reviewed in Chunnanond and Aphornratana (2004). In this respect, the COP of the system has been assumed to a value within the known range for practical applications. Using the COP value and the targeted cooling duty the mass flow rates for the main flow and secondary flow are obtained. With these the diameter of the main throttle is calculated. The speed of sound in throttle has been determined for the ammonia-water with concentration in the range of 10-20% by weigh: this is $\sim 400 - 430$ m/s.

An ejector has been designed and built. The technical drawing of the ejector is shown in Figure 3.15. For simplicity of the construction the ejector has been made starting from a commercial Swagelok valve which has been modified. As seen in the figure, the main flow port is at the bottom. The main flow is directed toward a small plenum at the nozzle intake. A needle is used to control the nozzle throat cross section and thus the flow rate. The flow becomes supersonic at the nozzle exit and meets the secondary (entrained) flow in conditions of lower pressure. Further, the flow is choked somewhere at the end of the constant area section and increases the pressure in the diffuser.

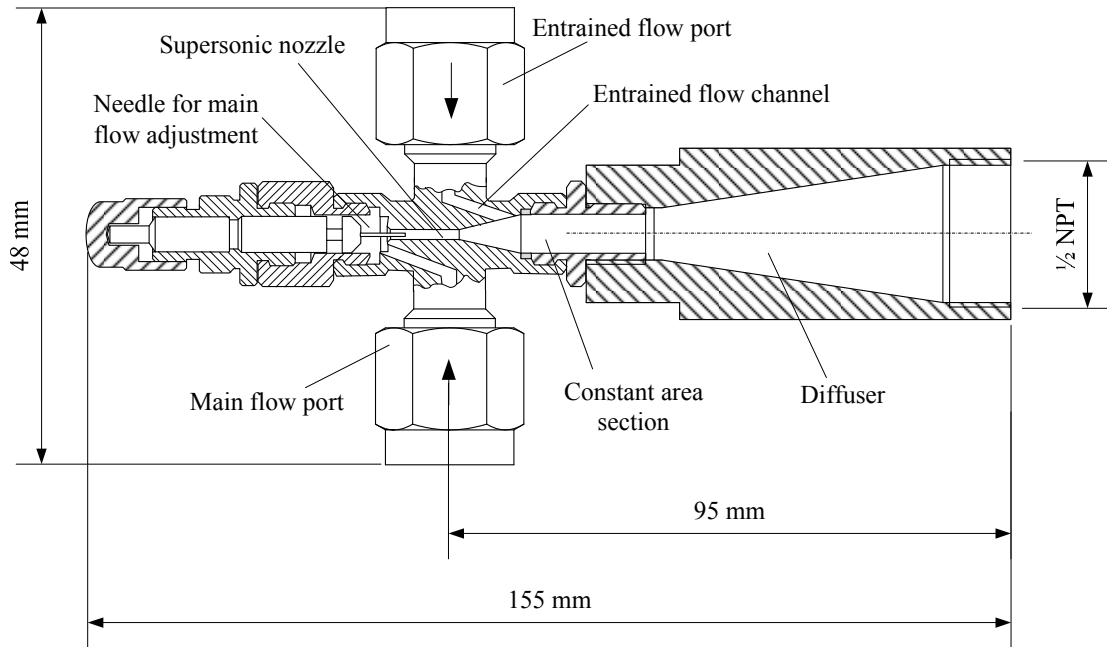


Figure 3.15: Ejector drawing “as-built”.



Figure 3.16: Photograph of the ejector as installed in the system.

Table 3.7: Constructive parameters of the custom-made ejector.

Parameter	Remark	Parameter	Remark
Throat diameter	0.87 mm	Nozzle length	10 mm
Nozzle's divergent section angle	60°	Nozzle end diameter	4 mm
Diameter of constant area section	4 mm	Length of constant area section	20 mm
Diffuser length	60 mm	Diffuser end diameter	18 mm



Figure 3.17: Immersed cooling coil setup connected to the ejector system.

The ejector parameters are given in Table 3.7. For the considered design conditions, the entrained flow factor has been 0.315. For a cooling duty of 100 W the estimated consumption of high pressure fluid is around 10-20 ml per minute. Figure 3.16 shows a photograph of the ejector as installed in the system. The needle valve which adjusts the main flow rate has a micrometer handle from Swagelok. The ejector is connected to a cooling coil shown in Figure 3.17 through which the secondary flow is circulated. In the photograph from the figure the throttling valve and an on-off ball valve are also visible. The cooling coil is immersed in a beaker of 1 liter capacity.

3.5 Heat exchangers

In this work two custom made heat exchangers were designed and built: the vapor generator and the condenser-resorber. The two heat exchangers have similar construction but the flows are circulated differently in each unit. Condensation and resorption occurs in a down flow in microchannels while the outer surface is cooled by a water stream circulated in counter-current, cross flow. The vapor generator has liquid supplied at the bottom side. The vapors are generated inside the microchannels while the stream flows upwards. The vapor generator is heated with thermal oil supplied from above in a counter-current, cross flow configuration.

The heat exchanger duty results from the cycle analysis as discussed in the Analysis and Results and Discussion sections. For power generation of the order of 1 kW under prototype

operation parameters the duty of the two heat exchangers is superior to 20 kW. Because of technical reasons, the vapor generator has duty to be higher: the thermal oil must be cooled below 100°C prior feeding into the pump, or otherwise the pump may be damaged. Considering also the heat losses, it is decided that the vapor generation duty is 30 kW. The duty of the condenser is slightly lower.

The design of the two heat exchangers assumed a LMTD of 10 K; thence the heat transfer area is estimated to 3 m². Both heat exchangers are custom made micro channel heat exchangers. The main features are counter cross flow fin-tube type heat exchanger with a pair of parallel vertical header tubes which distributes the process fluid. A number of extruded aluminum multi-port tubes are brazed to the headers. Multi-port extrusion (MPE) tubes are flat tubes with multiple small channels running across the length of the tube.

An aluminum multi-port extrusion (MPE) arrangement ensures high performance operation by creating a favorable heat transfer area to volume ratio. Also, the flat geometry of MPE tubes reduces the aerodynamic drag on the secondary fluid side of the heat exchanger. A number of baffles are positioned within the header to arrange for multi-pass operation.

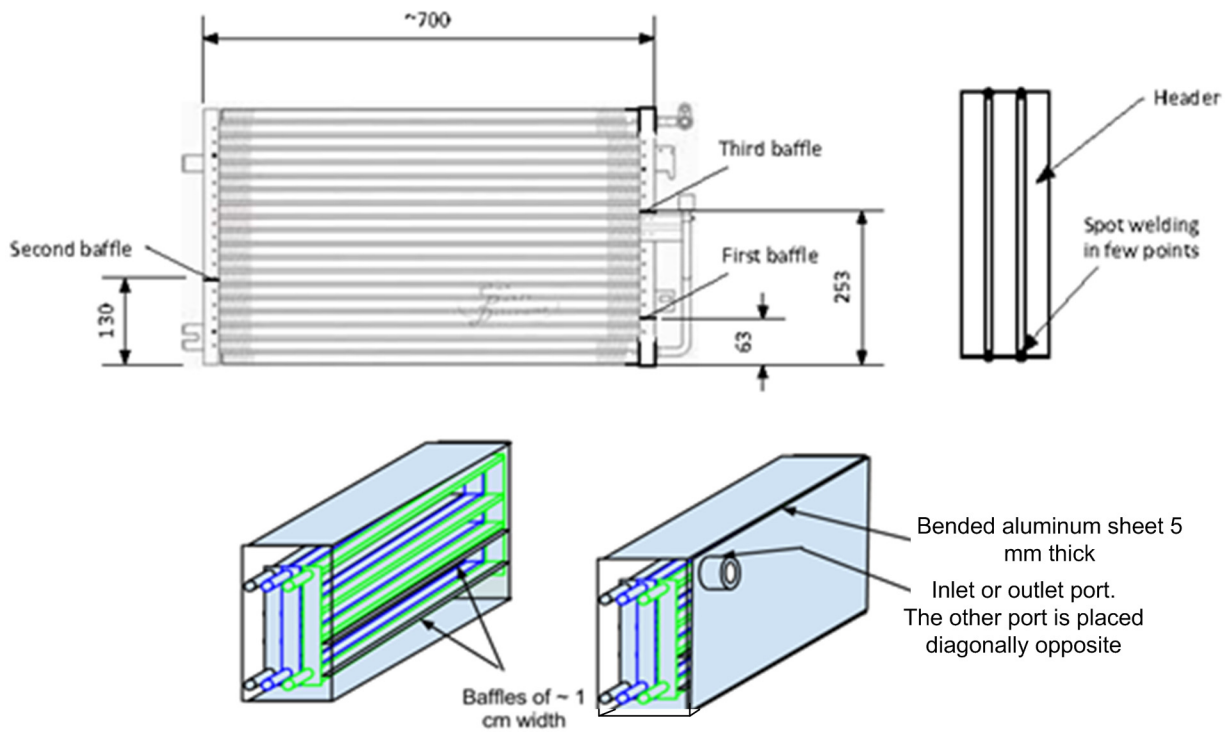


Figure 3.18: Heat exchanger design specification.

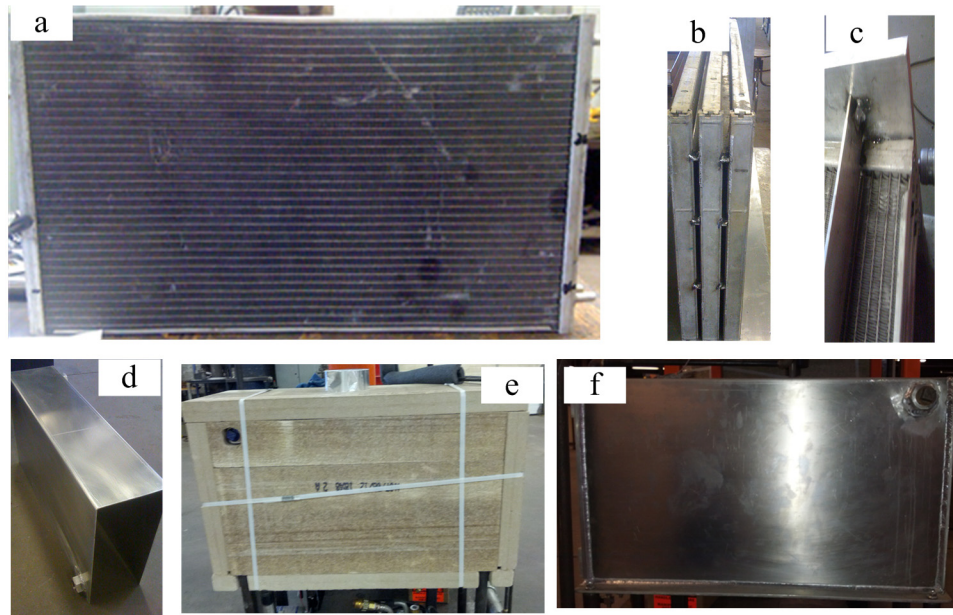


Figure 3.19: Photograph details of the realized heat exchangers: a) front view of inner circuit, b) side view of inner circuit, c) baffles detail for the shell side circuit, d) shell, e) thermally insulated vapor generator, f) condenser.

Six car refrigeration condensers are procured to build either heat exchanger for the desired purpose. A set of three heat exchangers are spot welded together as shown in the figure to serve the purpose of the system with the designed capacity. Figure 3.18 shows a technical drawing of the inner circuit and shell side arrangement for the heat exchangers.

The inner side has two headers with welded flow baffles so that at the top side many microchannel strips are connected in parallel, whereas at bottom only two parallel channels exist. The outer side of the microchannel strips has installed an extended surface with aluminum fins. The flow is circulated in a counter current, cross flow using a series of baffles. Figure 3.19 shows photographs illustrating the practical realization of the heat exchangers.

3.6 Oil heater

The oil heater is installed to the system to simulate a source of sustainable heat to heat the process fluid of the heat engine. The heater is designed by wrapping a nickel-chromium heating wire over the copper tube through which the oil will flow. Both the copper tube bundle and the wire are casted in a refractory brick (Kastite) that facilitates heat transfer, as shown in Figure 3.20. The heater is designed to supply 30 kW of thermal energy to oil heat transfer fluid.

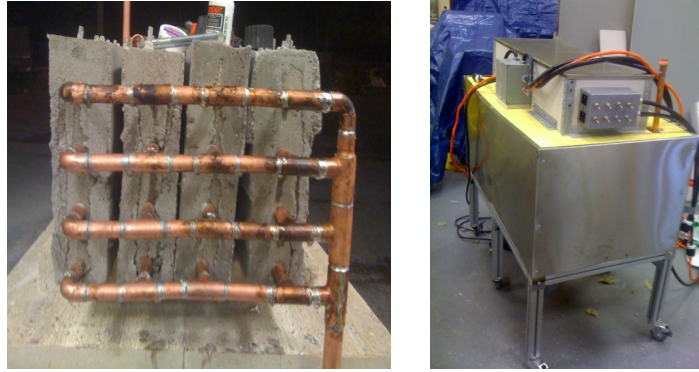


Figure 3.20: Heater construction

The electrical circuit of the oil heater comprises 11 switches which supply power to 28 electrical heating segments, each of them having 1.2 kW at 110 V. The heaters are connected in a series parallel scheme such that the user can switch on/off segments of 2.5 kW up to 4 kW. In this manner the desired thermal power can be generated.

The heater has a very high thermal inertia, estimated based on preliminary measurements to about 100 kJ/K. In many tests it has been observed that the oil temperature continues to increase even if the electrical current is switched off. The heat transfer surface consists of 16 copper tubes embedded in a casted structure. Inside the brick the temperature of the NiCr wire reaches around 1000 K and heat is transferred through conduction to the colder copper tube wall. The inner surface of the tube is cooled by oil circulated at high flow rate.

3.7 Closing Remarks

A novel ammonia-water based trigeneration system is proposed as shown in Figure 3.1. This system includes a regenerative Rankine cycle with heat recovery for heating generation. In addition the system includes an ejector cooling loop to generate useful refrigeration effect.

A prototype has been built aiming to test the proposed concept and to assess its performance and feasibility. The core system component is the expander which has been developed starting from a refrigeration scroll compressor. The system includes other custom made parts such as: ejector, heat exchangers and oil heater. As it will be described in the Results and Discussion chapter, the study identified a modified version of the trigeneration system which confers improved trigeneration performance which is worth for further development.

Chapter 4: Experimental Investigation

The main goal of the experimental investigation pursued in this work is to assess the system prototype based on energy and exergy efficiency. The exergy destructions at every component of the system are also to be determined. The experimental investigation is needed for concept proofing of the trigeneration system and to demonstrate its feasibility.

In this respect, the trigeneration system was instrumented with measurement devices and several test runs were performed. In addition, each component has been tested individually in separate experiments. In this chapter, the experimental investigation is described, the measurement devices are presented together with measurement error, and the analysis for uncertainty propagation is exposed. In this work, six types of experiments were performed as described subsequently. Each experiment had a number of runs with varied process parameters.

4.1 Experiment 1: Investigations with the prototype system

The objective of this experiment is to test the trigeneration system prototype in various running modes and to acquire sufficient measurement data with varied concentrations of ammonia such that the energy and exergy efficiencies and exergy destructions can be determined.

A manual start-up method has been established for the prototype shown in Figure 3.3 after several trials. In brief, the starting-up requires as first step the filling of the cold vapor generator with working fluid in liquid phase up to half volume. The volume of liquid that must enter the vapor generator at start-up must be 0.6 l which corresponds to approximately half of the inner volume of the microchannels. The amount of volume that enters the vapor generator at cold start-up can be determined using a timer and the reading from the flow meter \dot{V}_3 .

After filling the liquid, the valves MV₃, BV₅, MV₅ and MV₁₄ are locked. The pressure builds up gradually in the vapor generator due to heat addition. When sufficient pressure is observed, MV₃ is gradually opened to allow feeding of liquid process fluid to the vapor generator and BV₅ is opened such that the expander starts turning and generates power. When cooling generation is studied, the valve MV₁₄ is opened. Because of the fluctuation of vapor pressure a steady regime could not be maintained for long time. The “Experiment 1” has been complemented with several other types of experiments, including open loop (non-condensing mode), cooling-only mode and other related investigations as described in subsequent sections.

The following data was recorded during Experiment 1 using data loggers: T_{21} , T_{16} , T_1 , T_5 , T_9 , T_{13} , P_{13} . All other data have been recorded with “paper-and-pencil” as follows:

- The electric power provided to the boiler; this has been determined by previous measurements of voltage and current of the oil heater,
- The volume flow rate \dot{V}_3 and \dot{V}_{32} ,
- Pressures P_1 , P_5 , P_9 , P_{14} ,
- Temperatures T_{31} , T_{32} , lab temperature T_0 and temperature increase over oil cooler,
- Voltages and currents of all electrical drives,
- Indications such as liquid level in condenser (LI), and needle valve position at $MV_{7,12,14}$.

For Experiment 1 the following general procedure was established:

- The plant is checked for leaks using compressed air at 80 psi gage. The compressor is connected at MV_5 and air fills the plant and pressure increases to the desired value.
- Once the plant is leak proof the vacuum pump is connected to MV_5 and vacuum is generated down to 1 psi absolute or below. In this project a double stage diaphragm pump was used because it is corrosion resistant to the action of ammonia-water. In addition, the pump setup allows for the separation of liquid before pump suction. During the vacuuming, the working fluid canister is connected to the plant with its valve MV_{34} closed, but with valves $BV_{1,charge}$ and BV_{34} open.
- Once the plant is vacuumed and the vacuum is stable, then working fluid is filled by gradual opening of MV_{34} . After filling the desired amount of working fluid the isolation valve $BV_{1,charge}$ is closed and the working fluid tank lowered to allow as much emptying of the flexible hose as possible. Then BV_{34} is closed.
- If it is desired that the ammonia canister is removed, then the line between $BV_{1,charge}$ and BV_{34} is disconnected. Protection equipment and gas mask are used accordingly. Any liquid is drained back into the canister by holding up the flexible hose and shutting down MV_{34} . Any additional ammonia in the hose is spilled into a water bucket.
- The desired test session is performed.
- The ammonia-water working fluid is drained out in a water bucket via the valve $BV_{1,drain}$.
- The plant is blown with compressed air via valve MV_5 to remove any liquid.
- The plant is allowed to empty by opening valves $BV_{1,drain}$, MV_5 and MV_9 .

Table 4.1: Description of tests runs for Experiment 1.

Run	Working fluid
1	Ammonia-water with 30% concentration
2	Ammonia-water with 20% concentration
3	Ammonia-water with 10% concentration
4	Non-condensing test with steam only
5	Steam working fluid in closed loop cycle
6	Ammonia-water with 5% concentration
7	Ammonia-water with 28% concentration

For Experiment 1, 7 runs were made. The first 3 runs were made in 2013 and concluded that the expander scrolls must be rectified for obtaining better performance. The last 4 runs were made in June 2014 with the scrolls rectified for reducing the bypass leaks. Table 4.1 describes each run. In subsequent paragraphs the main aspects related to each run are described. The rough data for the experiments is given in Appendix A and processed as shown in the Results and Discussion chapter.

Run 1

For this run and also for runs 2 and 3, no cooling component has been installed into the cycle. The heat engine ran for power and heating production only. For working fluid charging water has been degassed first. Degassing water is necessary to reduce corrosion, since ammonia-water is extremely corrosive. In this respect, 2 liters of degassed water were prepared using an ultrasonic bath of 300 W while keeping water in vacuum condition. The degassed water has been transferred in a sealed plastic bag using a peristalting pump. The vacuum bag has been connected to the drain $BV_{1,drain}$ (Figure 3.3). The plant was put under vacuum and water moved inside after which the valve $BV_{1,drain}$ was closed.

An amount of ammonia has been added from the canister through the flexible hose. The canister has been weighted before and after feeding to determine the charge. Ammonia and water mixing has been observed by the heat released when the liquid receiver is touched with hand. After about 30 minutes, the pressure gage from liquid receiver and the room temperature are read. Since ammonia-water is at saturation, the pressure and temperature can be used to calculate the concentration according the equation of state.

The run started by circulating hot oil through the vapor generator. Pressure and temperature data have been recorded. The duration of the run has been of approximately three hours. After the test, a cooling down procedure has been conducted. Because the oil heater has

very high thermal inertia, the cooling process takes about two hours. After the run was concluded, the ammonia-water working fluid was removed out from the plant and the interior has been blown with compressed air for cleaning. The following aspects are noted for the experimental “Run 1”:

- Oil rose too high in the oil accumulator. This revealed that the oil circuit was not hydraulically balanced. Air in the oil circuit expanded too much and created a hydrostatic column of oil too high at the pump suction. At the time of “Run 1”, no oil-gas separator was installed in the circuit. Decision has been made to make the oil circuit more robust, to raise-up the oil accumulator and to insert the oil separator and to add the de-aeration valve MV₂₃ (Figure 3.3).
- The temperature at the oil pump suction has been too high although cooling has been applied by the oil cooler. This high temperature potentially can damage the oil pump. At the time of Run 1 test, no blower has been attached to the oil cooler, thence the cooling has been with natural convection. It was decided that blower will be added to the oil cooler for future experiments to generate forced air convection cooling to enhance the cooling rate for oil.
- The pressure was not building-up well in the pressure generator. Note that at the time when Run 1 was performed the flow meter \dot{V}_3 and ball valve BV₅ were not installed into the plant. The pressure in the vapor generator was maintained by applying a small voltage to the liquid pump such that few tens of ml/minute were fed to the vapor generator. It was decided that for future experiments, the ball valve BV₅ will be included in the plant and this will stay closed during the initial period for rapid building of pressure.
- The expander did not turn well as expected based on its known characteristics. Based on data processed from Run 1, it resulted that the expander had unacceptably high bypass leakages. It was decided that the expander has to be tested separately with compressed air. This has been done as reported in “Experiment 2” below, without removing the expander from the plant, but only by opening its discharge port to the atmosphere. Also, as mentioned earlier, the expander has been rectified by machining to reduce the built in leakage for compression operation. The Runs 4-7 were done with a rectified and improved scroll expander.

Run 2

This run is similar to Run 1 but has been done with lower concentration of ammonia in water. Also the oil circuit has been well improved according to the conclusions from Run 1. No changes were made yet on the ammonia-water circuit. In this experimental run more focus has been directed to the condenser and maintain appropriate condensation pressure. The system has been charged with ammonia-water solution of 20% concentration using a similar procedure. The following aspects are noted for the experimental “Run 2”:

- The condenser pressure has been higher than that which was believed to be correspond to saturation temperature. It was “guessed” that there may not be sufficient liquid in the plant. It was decided that a level indicator should be installed on the condenser and also that the volume of the liquid receiver, condenser and vapor generator should be tarred with water after the plant is emptied. These changes were actually applied latter.
- The pressure still not built as desired in the vapor generator. It was speculated that a pressure accumulator (in form of a pressure vessel) should be installed at the vapor generator discharge. This measure was not actually pursued.

Run 3

In this run the ball valve BV_5 was installed (Figure 3.3). Ammonia-water with 10% concentration has been charged this time. The flowing aspects are noted for the experimental “Run 3”:

- Although BV_5 was closed the pressure did not built much faster in the vapor generator. It was concluded that a check valve should be included at vapor generator fed line. Also the working fluid pump must be checked. Therefore, the pump has been dismantled at latter date and tested for calibration as presented below at Section 4.6 (Experiment 6).
- It was decided that flow meter \dot{V}_3 must be installed at vapor generator feed line.
- It was decided to test the vapor generator in open loop and assess it separately. This is done by opening the valve MV_5 to the atmosphere while using steam as working fluid, as reported in Section 4.4 (Experiment 4).
- Oil circulation and heating of the vapor generator performed very well.

Run 4

This run and the subsequent runs have been done after the scrolls of the expander have been rectified and improved. The run has been done with steam only in open circuit so that focus is made on pump, vapor generator and expander operation. The condenser has not been used. Therefore, the line between condenser and liquid receiver, and the line between the expander and condenser have been removed.

A bucket of de-ionized water was connected to the $BV_{1,charge}$. The flow meter \dot{V}_3 has been installed and as well the one way valve at the vapor generator feed line. There is no need of vacuum as there is no condenser connected. The vapor generator was charged half-volume with water. The valves MV_3 and BV_5 have been locked. Pressure increased in the system due to heat addition. When pressure increased sufficiently over the atmospheric pressure, the valve BV_5 has been opened and working fluid pump started. The valve MV_3 has been tuned to achieve proper flow rate of liquid in the feed line. The relief valve MV_9 was fully opened. Slightly superheated steam has been generated and passed through the expander. The low pressure steam was released outside. The expander turned well and steady. The following aspects are noted for the experimental “Run 4”:

- Adjustment of the liquid flow rate in the feed line of vapor generator is very important and has to correlate with the heat input
- It is better and more accurate to set the pump drive to a fixed voltage (e.g., 24 V) and adjust the flow rate through MV_3 rather than adjusting the flow rate through changing the voltage applied to the drive. This strategy has been used in all further experiments.
- The heat engine ran very well in open loop confirming a good operation of the pump, vapor generator and expander.
- Very reliable experimental data has been obtained.

Run 5

In this experiment, steam has been charged to the plant. Although ammonia-water gives better results for trigeneration, steam is a possible option for cogeneration with a similar setup. Steam imposes less safety issues than ammonia. In addition, for the purpose of a parametric study regarding the influence of ammonia concentration, the experiments with steam (or zero % ammonia-water concentration) become a reference. The experiments with steam are deemed to

confirm the good operation of the system. The experiments were performed with saturation temperature in the range of 100°C to 125°C and a slight superheating. The following aspects are noted for the experimental “Run 5”:

- Water lock has been observed which blocks the expander. When too much water enters in the expander intake port it locks into the expander cavity. Since the leakage paths are very narrow and water cannot flush easy, the expander brakes and stalls. If the expander is turned by hand, then the expansion cavity opens and the liquid is removed and the expander starts turning well. This observation teaches that the liquid amount entering the expander must be controlled. Liquid enters in the expander in two ways: i) if full saturation is not achieved, it enters together with vapor passing through valve BV₅; ii) through liquid injection valve MV₇, if this valve is opened too much.
- Because the manner in which vapor generator feed is changed (as discussed above, pump was supplied with constant voltage and needle valve MV₃ has been adjusted), the pressure at the vapor generator exit is much lower than the pressure at the pump discharge; thence, the injection valve must be closed more in these circumstances.
- It is difficult to correlate the liquid flow rate with the heat input; therefore, fluctuations occur frequently in vapor generator pressure. If water in the feed line is at too high flow rate, then the volumetric flow rate of vapor and their pressure decreases and so does the expander’s angular speed.
- Often fluctuation of water level in the condenser has been observed which probably created flow variation of the working fluid driven by the pump. Therefore it was decided that better the condensation is made in large volume outside the microchannels. In this way, it is hoped that fluctuation of hydrostatic pressure dumps since the reserve of working fluid is larger in that way.

Run 6

The condenser lines were reconfigured to study condensation outside the tubes. It has been planned to experiment with a concentration of ammonia of 22% for which the condensation at 45°C occurs at 1 atm. However, while changing the circuit some brass fittings were used. Therefore, lower concentration was planned of 5% which will not create problems with corrosion for short term. Deionised water has been used because degassing became not

anymore necessary (degassing is only an additional measure to impede corrosion). The following aspects are noted for the experimental “Run 6”:

- After changing the configuration of the condenser, this was leak tested under pressure at the shell side (20 psi) and broken. It was repaired by welding and further tested under vacuum. It gives sign that will deform at vacuum lower than 4 psi. However, with ammonia concentration at 5% as planned, the required vacuum is much high: -11.6 psi. In these conditions, the circuit has been redone with condensation in microchannel and the attempt to test condensation outside the microchannel abandoned. Ammonia-water with concentration at approx. 15% has been then charged into the plant.
- The test performed well and data was collected; however, there were many water locks in the expander this time, which made expander to stall. After some investigations, it was found that the inner circuit of the condenser has been damaged during the failure. Therefore, being under vacuum it sucked water from the outer circuit. A rough density measurement showed that due to water suction in the condenser, the ammonia water concentration reduced to approx. 5%.
- In order not to lose the data; an ad-hoc procedure has been performed during the experiment runtime. The relief valve MV₉ has been opened to release vapor and liquid into a bucket of water. In the same time the drain valve BV_{1,drain} was opened to release liquid into a bucket of water. The liquid level lowered in the condenser until it reached the liquid trap. Air entered in the condenser in this way, keeping the partial pressure of ammonia-water vapor lower. After closure of valves BV_{1,drain} and MV₉ air remained trapped into the condenser and the experiment continued.
- Good amount of data has been collected, although the condenser was full of air, but the expander turned well.

Run 7

In this run, ammonia at 28% concentration has been charged into the plant. The condenser outer section was flooded of water. Condensation process has been maintained at 30°C case in which the gage pressure in the condenser was maintained at 1 psi. Therefore, the leak into condenser was toward outside and has been minor due to the small pressure difference. The following aspects are noted for the experimental “Run 7”:

- Condenser performed very well and good deal of data was collected for it.
- Vapor generator performed very well. The working fluid has been heated up to 140°C.
- The expander was flooded several times due to wrong correlation of the feeding rate of the vapor generator with the heat input. This issue occurred because the adjustment has been made manually, based on pre-calculated flow rate data in correlation to vapor temperature and pressure. This issue can be resolved by implementing some automation procedure.
- The expander is not damaged by the water locks; it only stalls; when turned with hand for some time it starts turning provided that enough flow rate of vapor is provided.
- Sufficient data has been acquired and processed. However, more experiments would be beneficial with varied operating conditions for a parametric study.

4.2 Experiment 2: Expander performance determination with compressed air

This experiment has been performed in order to assess the expander performance under variable conditions in terms of pressure ratio and pressure difference. Compressed air has been obtained from a belt driven two stages compressor with 80 gallon of pressurized air tank.

The discharge flow rate, the intake pressure of the compressor has been measured for intake pressures in the range of 10 psi to 80 psi in conditions when the discharge pressure has been maintained to atmospheric. In the same time, a load is connected to the expander. The expander has set in its normal position as installed in the trigeneration system skid and an electric generator is connected to the shaft through a magnetic coupling and the clutch mechanism. The experimental setup for “Experiment 2” is shown in Figure 4.1.

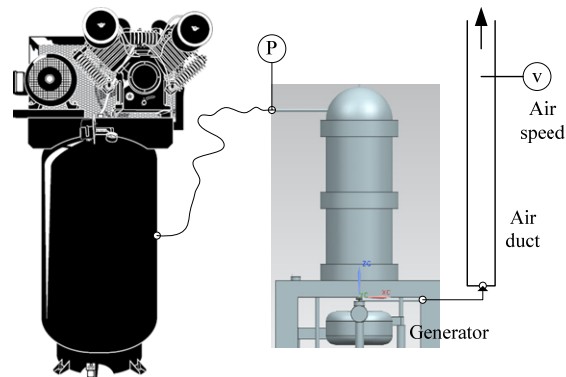


Figure 4.1: Setup for expander investigation with compressed air.

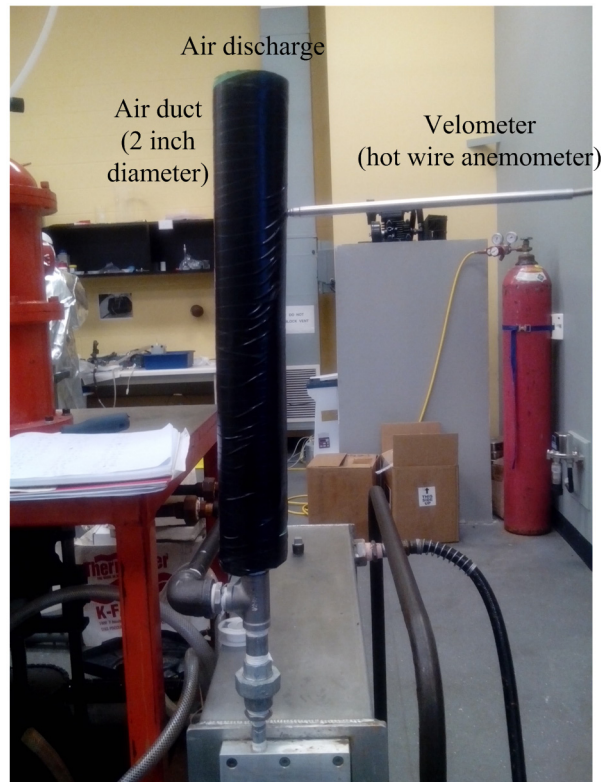


Figure 4.2: Photograph for air flow rate measurement system at expander discharge.

The exhaust air velocity is measured at the exhaust with a velometer. Once the air velocity has been determined, the air flow rate is calculated according to the equation: $\dot{V} = A v$, where cross sectional area of the duct results from its diameter which is of 2 inches. Figure 4.2 shows a photograph of the air duct which was of 1 m length. The rough data and data processing for Experiment 2 is presented in the Results and discussion section. Note that the angular speed of the expander has been also measured using a spot light meter.

4.3 Experiment 3: Ejector performance determination

In this experiment, the ejector cooling system has been tested separately under a special arrangement. Compressed air was used as the primary fluid. The refrigerant was water and ammonia water. A test set-up has been constructed by modification of an existing cooling system present in the lab which included a refrigerant recipient equipped with a glass tube and a ruler for level determination.

Figure 4.3 shows the test arrangement for Experiment 3. There is a buffer tank in which ammonia-water solution is prepared. The system comprises the anhydrous ammonia canister, the buffer tank with level indicator and ruler, vacuum pump with vacuum recipient, a throttling valve (TV), several ball valves (BV), an immersed cooling coil, the ejector, four pressure gages (P) and one temperature gage.

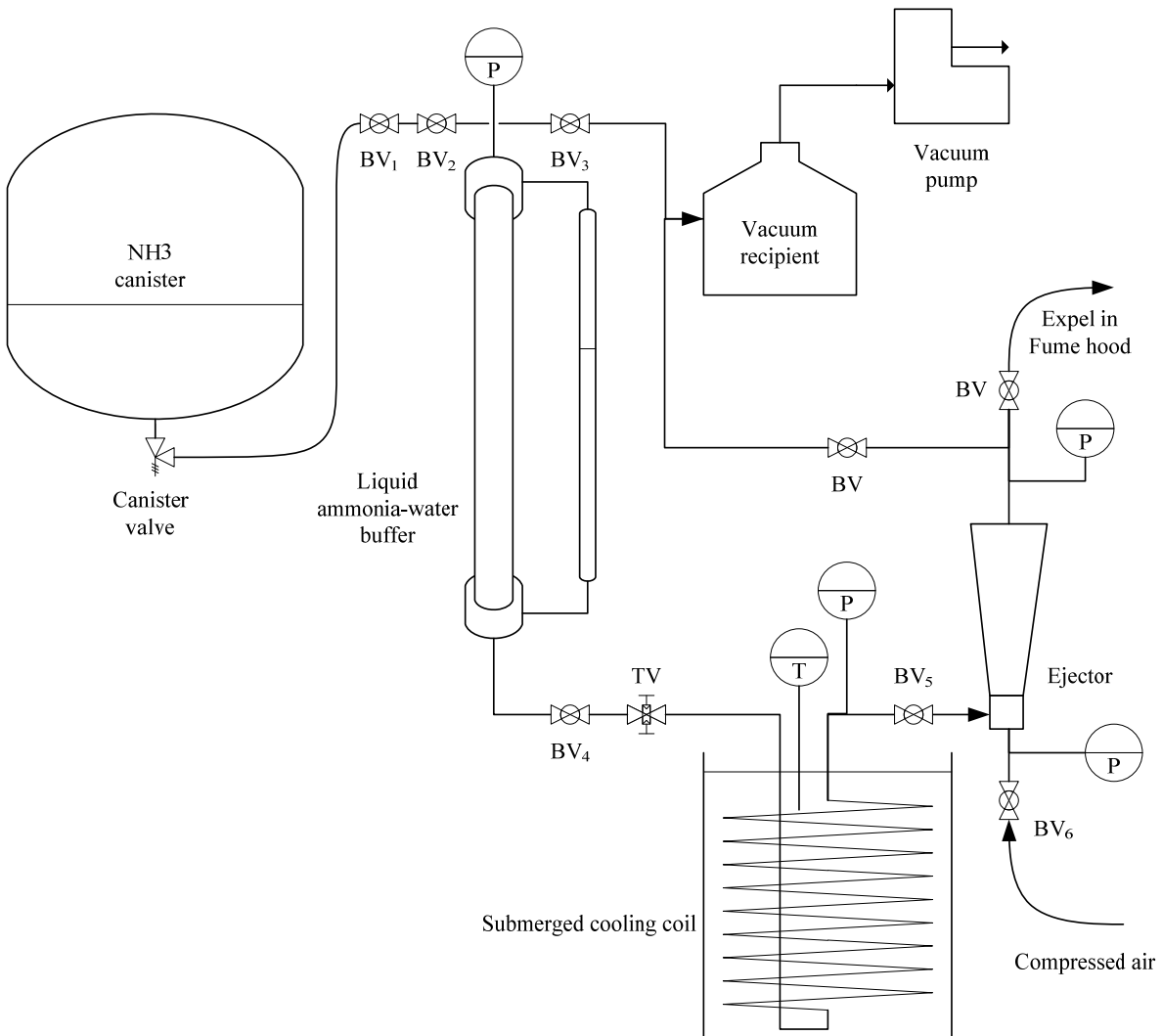


Figure 4.3: Setup for Experiment 3 – ejector performance determination.

The experimental procedure implied ammonia-water charging as a first step. In this respect BV₄ is locked, the buffer tank is opened and a quantity of water poured into it. Then the buffer tank is sealed and BV₁, BV₂, BV₃ opened. The vacuum pump is started and air eliminated out of the system. Then BV₂ is closed and then the ammonia canister valve is

opened. Ammonia is charged slowly to the desired amount and then the BV_2 is closed. The pressure in the buffer tank is monitored.

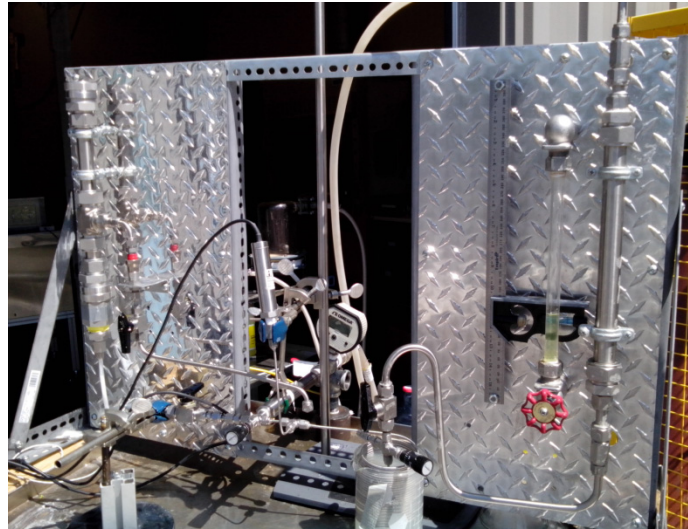


Figure 4.4: Photograph of the experiment 3 setup.

The experiment starts by running compressed air through the ejector. Further, BV_4 is opened and the refrigerant is allowed to pass through the throttling valve and through the coil while it is sucked into the ejector. Two options exist for the ejector discharge: to expel into the fume hood and to pass it through the vacuum pump and then to the fume hood. The photograph of the Experiment 3 setup is shown in Figure 4.4. This experiment has been performed both with pure water and with ammonia water.

4.4 Experiment 4: Vapor generator investigation

The Experiment 4 has been done with the trigeneration system from Figure 3.3 in a special configuration that focuses on vapor generator investigation. Deionized water was used as working fluid. A water recipient was connected to $BV_{1,drain}$. The condenser lines were physically disconnected from the system. The valve BV_5 was closed and the MV_5 was opened. Pump drive was run at 24 V and the water feed flow rate adjusted with valve MV_3 . The heater power was adjusted by connected various combinations of heating segments. The recorded data consist of:

- Volume flow rate of feed water,
- Vapor generator pressure,

- Vapor temperature at generator exit,
- Oil temperature at inlet and exit,
- Voltage and current of the oil pump.

4.5 Experiment 5: Working fluid pump calibration

The working fluid pump is of major importance. This is a gear pump as described in Chapter 3 (Cole Parmer 073003-4). The pump is driven by a d.c. motor and is capable to finely adjust the revolution speed (and thus the flow rate) through the applied voltage. The manufacturer gave the pressure curve for a rotation speed of 3450 rpm. However, more pressure vs flow rate curves are required for the present investigation. Therefore, the pump has been tested for calibration purpose for other three test points at smaller angular speeds.

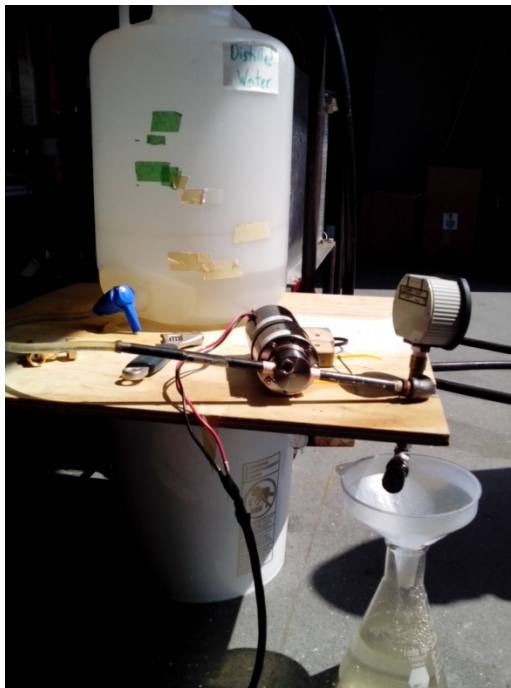


Figure 4.5: Photograph of the setup for Experiment 5.

The photograph from Figure 4.5 shows the experimental setup. The pump was connected with a metered recipient at suction, where water was placed. Water flows gravitationally and feeds the pump's suction port. At the discharge of the pump, a pressure gage is installed and a needle valve.

The procedure involved the application of a fixed voltage to the pump. The needle valve is constrained into a fixed position. Then the pressure and the current absorbed by the pump drive are read. The collected data and the data processing for this experiment are described in the chapter “Results and discussion”.

4.6 Experiment 6: Oil heater testing and calibration

The oil heater required thorough calibration in order to determine the electric power consumed by each of the electric heater segments and to determine the thermal inertia of the system. The electric heater power has therefore been determined with the measurement of the current and the voltage of the individual power supplies to the heaters. There were in total 11 circuits connected to 11 switches. The power for each circuit has been noted down. When the heaters were actually used, the power fed into the system was therefore known based on the number of switches which are set to the ON position.

The determination of the heater thermal inertia was obtained via a heating test for which the oil flow rate and the temperatures at oil heater inlet T_{16} and outlet T_{21} were monitored (Figure 3.3). The setup included the oil cooler used as a load for the electric heater. Balance equations and a heater model were elaborated to determine eventually the thermal inertia of the heater as shown in the chapter “Results and discussion”.

4.7 Measurement devices and accuracy

The following measurements were made in this experimental investigation: temperature, pressure, volumetric flow rate, level, time, current, voltage, angular speed. Here, we describe the instruments used and their accuracy. This data is required for uncertainty analysis which is presented in the “Results and discussion” chapter.

Two data acquisition systems were used here for temperature monitoring: the OMEGA DAQ Pro 5300 and VERNIER LabQuest Mini. The data acquisition systems are shown in Figure 4.6. The OMEGA system measures RTDs while VERNIER measures an NTC (thermistor).

The measurement accuracy of OMEGA system is 0.01°C ; this device was used to measure the RTD temperature probes attached to the trigeneration systems. From Figure 3.3, these probes are: T_1 , T_5 , T_9 , T_{16} , T_{21} . The accuracy of the VERNIER data acquisition is of

0.05°C. This system has been used to monitor the water temperature in the beaker with the immersed coil as shown in the setup in Figure 4.3.



Figure 4.6: Data acquisition systems for temperature monitoring: Omega DAQ-Pro (left) and Vernier LabQuest (right).

Table 4.2: Temperature and pressure sensors.

Sensor location	Photo	Description
T ₁ , T ₅ , T ₉ , T ₁₆ , T ₂₁ in Figure 3.3 (trigeneration prototype)		Pipe plug RTD sensor with 1/4 NPT Class A, 3-wire, high accuracy
T in Figure 4.3 the same as T ₁₃ in Figure 3.3		Low precision NPT sensor Range -15°C to 110°C Accuracy: 0.07°C
Pressure sensor on the cooling coil (P ₁₃ in Figure 3.3, P in Figure 4.3)		PX409-050GUSBH USB pressure transducer from OMEGA Accuracy 0.08% of full span Absolute pressure measurement.
Pressure sensors P ₅ (0-100 psi absolute), P ₉ (0-50 psi gage), P ₁₄ (0-100 psi gage)		OMEGA digital pressure sensor DGP1100B series Accuracy 0.5% of full span
Pressure sensor P ₁ (psi gage)		Dial pressure sensor from OMEGA. Vacuum to 50 psi. Accuracy 0.5 psi.

The temperature and pressure sensors are given in Table 4.2. The air velocity sensor has been a hot wire anemometer: HTF 1000 series from OMEGA. Figure 4.7 shows this sensor and measurement device. The sensor accuracy is of 1.5% of full scale, whereas the full scale is of 5000 fpm. The current and voltage has been measured for calibration of the electric heater 8

segments. The measurement devices were a multimeter and a clamp-on ammeter as shown in Figure 4.8. The accuracy of voltage measurement is of 0.05 V and the accuracy of current measurement is of 0.1 A. Two multichannel power sources were used to drive the d.c. motors in the system. Figure 4.9 shows these sources.



Figure 4.7: Hot wire anemometer used for air velocity measurement (left) and hand-held digital tachometer for angular speed measurement (right).



Figure 4.8: Clamp-on ammeter (left) and multi-meter (right) used for current and voltage measurement (respectively).

The power source PSU 505 from OMEGA is used to control the oil pump motor and the blower of the oil cooler. The oil pump motor is supplied normally with 12V nominal voltage. The current and the voltage of the pump are read because from this information the flow rate and pressure can be determined. The power source PSU 305 from OMEGA is used to control the working fluid pump. The accuracy of voltage measurement integrated with the power sources is 0.05 V whereas the accuracy of current measurement is of 0.05 A.



Figure 4.9: Power sources used to run the d.c. motors within trigeneration system.



Figure 4.10: Level gauge used as part of flow rate determination method for cooling coil.

The measurement system also included a level gauge which was used to determine the level of the liquid refrigerant supplied to the cooling coil. Implicitly, the flow rate has been determined because the time has been measured between two changes of the level. Figure 4.10 shows the gage used to measure the level. This system is part of the Experiment 3 setup as

presented in Figure 4.3. The level is measured with an accuracy of 0.5 mm. The level gauge has been calibrated so that the volume change is determined based on the change of level. The conversion factor is 0.46; therefore:

$$\Delta V[\text{ml}] = 0.46 \Delta z[\text{mm}]$$

Therefore, the accuracy of volume change reading is of 0.23 ml. The time is measured with accuracy of better than 1 second.

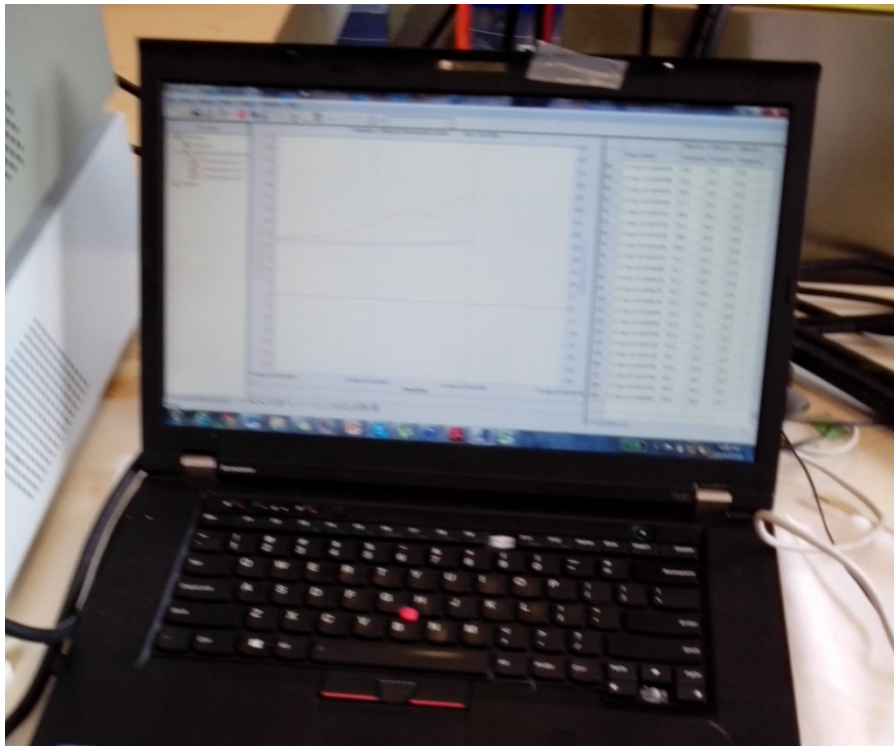


Figure 4.11: Laptop used for experimental data recording.

Two data acquisition software were used for recording the data read during experiments. OMEGA systems were logged using the DAQLAB Windows Software. VERNIER sensor used the LabQuest 2 software. Figure 4.11 shows a photograph of the laptop screen during the data acquisition process.

Chapter 5: Analyses

Several types of analyses were pursued with the trigeneration system proposed in Figure 3.1. In the first part of this chapter, the energy and exergy analyses of the system are presented. The scroll unit being the most important component of the system the second section of this chapter is dedicated to the geometrical analysis of the scroll machine. This type of analysis is deemed to determine the variation of the expanding cavity volume and that of the by-pass leakage gaps. The thermodynamic analysis of the expander follows the geometrical analysis results. Further vapor generator and the condenser/resorber are analyzed thermodynamically based on the sizing and geometrical characteristics. Lastly, the ejector is analysed thermodynamically.

5.1 Energy and Exergy analyses of the trigeneration system

The trigeneration system from Figure 3.1 is modeled based on balance equations for mass, energy, entropy and exergy. These equations are written for each component of the system. There are ten components: pump, vapor generator, expander, regenerator, water heating heat exchanger, condenser/resorber, throttling valve, evaporator, ejector and metering valve for liquid injection.

The balance equations are given in Table 5.1 for each of the component. The irreversibilities for each component are taken into account by considering isentropic efficiencies and average temperature differences at the heat exchangers. The isentropic efficiencies are:

- For the pump $\eta_{is,p} = \frac{h_{2s} - h_1}{h_2 - h_1} < 1$
- For the expander $\eta_{is,e} = \frac{h_6 - h_7}{h_6 - h_{7s}} < 1$

The average temperature differences at heat exchangers are imposed according to the following equations (see Figure 3.1):

$$\Delta T_{r,1} = T_7 - T_3 > 0; \Delta T_{r,2} = T_8 - T_2 > 0; \Delta T_{vg} = \bar{T}_{vg} - \frac{h_5 - h_3}{s_5 - s_3} > 0$$

$$\Delta T_{wh} = \frac{h_{10} - h_9}{s_{10} - s_9} - \bar{T}_{wh} > 0; \Delta T_c = \frac{h_{11} - h_{10}}{s_{11} - s_{10}} - \bar{T}_0 > 0; \Delta T_{ev} = \frac{h_{14} - h_{13}}{s_{14} - s_{13}} - \bar{T}_c > 0$$

For the ejector modeling an entrainment ratio is assumed:

$$ER = \dot{m}_{14}/\dot{m}_{15}$$

Table 5.1: Balance equations for the trigeneration system (Figure 3.1).

Comp.	Balance equations	Comp.	Balance equations
Pump	$\begin{aligned} MBE: \dot{m}_1 &= \dot{m}_2 \\ EBE: \dot{m}_1 h_1 + \dot{W}_p &= \dot{m}_2 h_2 \\ EnBE: \dot{m}_1 s_1 + \dot{S}_{g,p} &= \dot{m}_2 s_2 \\ ExBE: \dot{m}_1 ex_1 + \dot{W}_p &= \dot{m}_2 ex_2 + \dot{E}x_{d,p} \end{aligned}$	Rege- nerator	$\begin{aligned} MBE: \dot{m}_2 &= \dot{m}_3 + \dot{m}_{17} \text{ and } \dot{m}_7 = \dot{m}_8 \\ EBE: \dot{m}_3 h_2 + \dot{m}_7 h_7 &= \dot{m}_3 h_3 + \dot{m}_8 h_8 \\ EnBE: \dot{m}_3 s_2 + \dot{m}_7 s_7 + \dot{S}_{g,r} &= \dot{m}_3 s_3 + \dot{m}_8 s_8 \\ ExBE: \dot{m}_2 ex_3 + \dot{m}_7 ex_7 &= \dot{m}_3 ex_3 + \dot{m}_8 ex_8 \\ &+ \dot{E}x_{d,e} \end{aligned}$
Vapor genera- tor	$\begin{aligned} MBE: \dot{m}_3 &= \dot{m}_5 \\ EBE: \dot{m}_3 h_3 + \dot{Q}_{in} &= \dot{m}_5 h_5 \\ EnBE: \dot{m}_3 s_3 + \frac{\dot{Q}_{in}}{\bar{T}_{vg}} + \dot{S}_{g,vg} &= \dot{m}_5 s_5 \\ ExBE: \dot{m}_3 ex_3 + \dot{Q}_{in} \left(1 - \frac{T_0}{\bar{T}_{vg}}\right) &= \dot{m}_5 ex_5 + \dot{E}x_{d,vg} \end{aligned}$	Ex- pander	$\begin{aligned} MBE: \dot{m}_5 &= \dot{m}_6 + \dot{m}_{15} \text{ and } \dot{m}_6 + \dot{m}_{18} \\ &= \dot{m}_7 \\ EBE: \dot{m}_6 h_6 + \dot{m}_{18} h_{18} &= \dot{m}_7 h_7 + \dot{W}_{out} \\ EnBE: \dot{m}_6 s_6 + \dot{m}_{18} s_{18} + \dot{S}_{g,e} &= \dot{m}_7 s_7 \\ ExBE: \dot{m}_6 ex_6 + \dot{m}_{18} ex_{18} &= \dot{m}_7 ex_7 + \dot{W}_{out} \\ &+ \dot{E}x_{d,e} \end{aligned}$
Water heater	$\begin{aligned} MBE: \dot{m}_9 &= \dot{m}_{10} \\ EBE: \dot{m}_9 h_9 &= \dot{m}_{10} h_{10} + \dot{Q}_{heating} \\ EnBE: \dot{m}_9 s_9 + \dot{S}_{g,wh} &= \dot{m}_{10} s_{10} + \frac{\dot{Q}_{heating}}{\bar{T}_{heating}} \\ ExBE: \dot{m}_9 ex_9 &= \dot{m}_{10} ex_{10} + \dot{Q}_{heating} \left(1 - \frac{T_0}{\bar{T}_{heating}}\right) \\ &+ \dot{E}x_{d,wh} \end{aligned}$	Con- denser	$\begin{aligned} MBE: \dot{m}_{10} &= \dot{m}_{11} \\ EBE: \dot{m}_{10} h_{10} &= \dot{m}_{11} h_{11} + \dot{Q}_{out} \\ EnBE: \dot{m}_{10} s_{10} + \dot{S}_{g,c} &= \dot{m}_{11} s_{11} + \frac{\dot{Q}_{out}}{T_0} \\ ExBE: \dot{m}_{10} ex_{10} &= \dot{m}_{11} ex_{11} + \dot{E}x_{d,c} \end{aligned}$
Thro- tling valve	$\begin{aligned} MBE: \dot{m}_{11} &= \dot{m}_1 + \dot{m}_{12} \text{ and } \dot{m}_{12} = \dot{m}_{13} \\ EBE: \dot{m}_{12} h_{12} &= \dot{m}_{13} h_{13} \\ EnBE: \dot{m}_{12} s_{12} + \dot{S}_{g,tv} &= \dot{m}_{13} s_{13} \\ ExBE: \dot{m}_{12} ex_{12} &= \dot{m}_{13} ex_{13} + \dot{E}x_{d,tv} \end{aligned}$	Evapo- rator	$\begin{aligned} MBE: \dot{m}_{13} &= \dot{m}_{14} \\ EBE: \dot{m}_{13} h_{13} + \dot{Q}_{cooling} &= \dot{m}_{14} h_{14} \\ EnBE: \dot{m}_{13} s_{13} + \frac{\dot{Q}_{cooling}}{\bar{T}_c} + \dot{S}_{g,ev} &= \dot{m}_{14} s_{14} \\ ExBE: \dot{m}_{13} ex_{13} + \dot{Q}_{cooling} \left(1 - \frac{T_0}{\bar{T}_c}\right) &= \dot{m}_{14} ex_{14} + \dot{E}x_{d,ev} \end{aligned}$
Ejec- tor	$\begin{aligned} MBE: \dot{m}_{14} + \dot{m}_{15} &= \dot{m}_{16} \\ EBE: \dot{m}_{14} h_{14} + \dot{m}_{15} h_{15} &= \dot{m}_{16} h_{16} \\ EnBE: \dot{m}_{14} s_{14} + \dot{m}_{15} s_{15} + \dot{S}_{g,ej} &= \dot{m}_{16} s_{16} \\ ExBE: \dot{m}_{14} ex_{14} + \dot{m}_{15} ex_{15} &= \dot{m}_{16} ex_{16} + \dot{E}x_{d,ej} \end{aligned}$		

The trigeneration system designed as shown in Figure 3.3 has power generation, heating and in addition has an integrated cooling loop. Because the trigeneration system uses at least two thermal energy fluxes as input (these are the heat source thermal input and the heat flux associated with the cooling effect) the performance of trigeneration can be quantified by a coefficient of performance defined as follows:

$$\eta_{3gen} = \frac{\dot{W}_{net} + \dot{Q}_{heating} + \dot{Q}_{cooling}}{\dot{Q}_{in}} \quad (5.1)$$

Beside the assessment through the coefficient of performance, the trigeneration system can be assessed based on energy efficiency for power only generation and energy efficiency for power and heat generation. These factors can be defined as the net generated work divided to thermal energy input for power generation efficiency:

$$\eta = \frac{\dot{W}_{net}}{\dot{Q}_{in}} \quad (5.2)$$

and as energy utilisation factor for power and heat generation

$$\epsilon_u = \frac{\dot{W}_{net} + \dot{Q}_{heating}}{\dot{Q}_{in}} \quad (5.3)$$

Also the following ratios can be defined:

- Heating to work ratio: $HWR = \dot{Q}_{heating}/\dot{W}_{net}$
- Cooling to work ratio: $CWR = \dot{Q}_{cooling}/\dot{W}_{net}$

The exergy based assessment of the trigeneration system is made through the exergetic coefficient of performance efficiency defined with the following equation:

$$\psi_{3gen} = \frac{\dot{W}_{net} + \dot{E}x_{heating} + |\dot{E}x_{cooling}|}{\dot{E}x_{in}} \quad (5.4)$$

where one notes that the exergy of cooling is taken in absolute value because of its negative sign.

In addition, the power generation exergy efficiency is defined by

$$\psi = \frac{\dot{W}_{net}}{\dot{E}x_{in}} \quad (5.5)$$

and the power and heating co-generation exergetic efficiency is defined by:

$$\psi_{2gen} = \frac{\dot{W}_{net} + \dot{E}x_{heating}}{\dot{E}x_{in}} \quad (5.6)$$

5.2 Ammonia-water mixture

Ammonia-water is a zeotropic mixture which boils and condenses at increasing and decreasing temperatures, respectively with the change of concentration level of the fluid mix within the system. In fact, during boiling ammonia desorbs from liquid phase, whereas during condensation ammonia vapor resorbs into the liquid phase. This makes it possible to keep the temperature profile of the working fluid closer to a heat source of decreasing temperature in a vapor generator and a heat sink of increasing temperature in a condenser.

The variable temperature heat transfer process reduces the temperature mismatch between the hot and cold stream of the heat exchanger. During evaporation, the mixing ratio of the zeotropic working fluid changes because of the lower boiling temperature of ammonia which evaporates chiefly at the beginning.

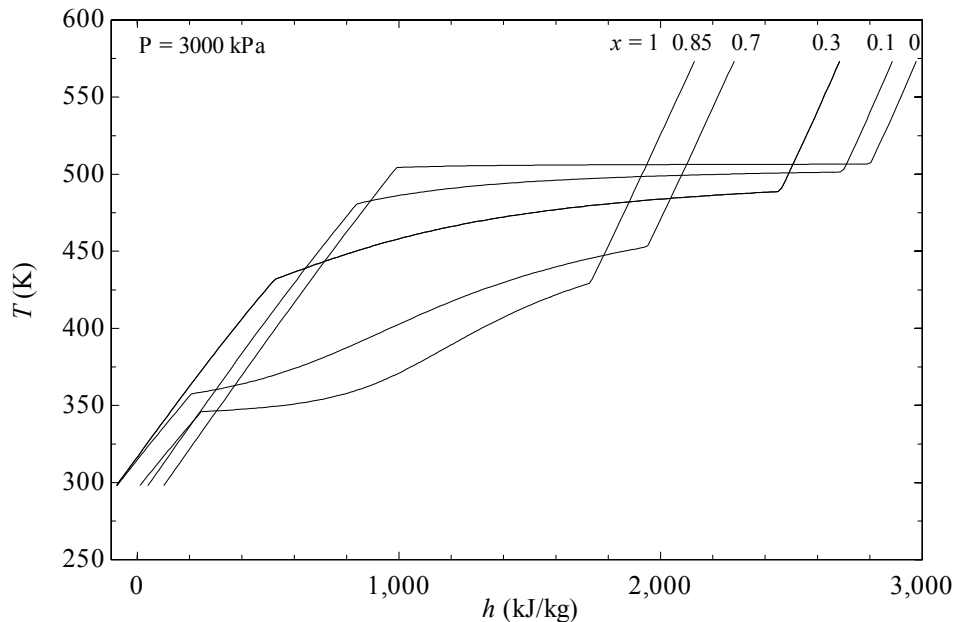


Figure 5.1: Temperature variation during liquid-vapor phase change of ammonia-water solution at 3000 kPa [data calculated with EES software].

In Figure 5.1, four different curves present the variable boiling temperatures of different ammonia–water mixtures against the isothermal evaporation of pure water at a pressure of 3000 kPa. The mixture of ammonia and water boils at a variable temperature depending on its

composition. The evaporation and condensation processes are not isothermal. The higher the fraction of ammonia in the mixture, the lower is its boiling temperature. With the increasing ammonia concentration, the specific enthalpy of steam decreases.

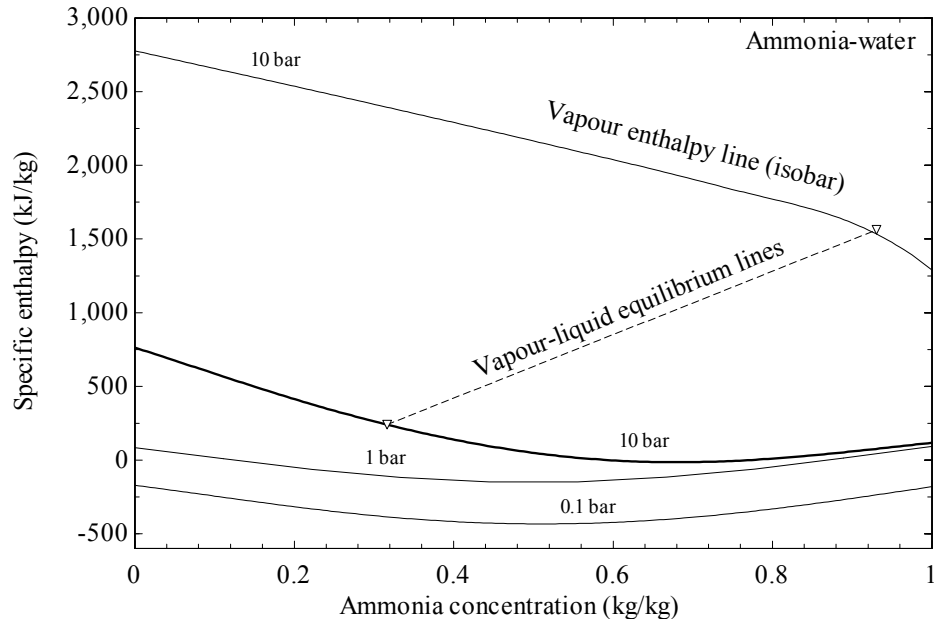


Figure 5.2: Vapor and liquid equilibrium lines for ammonia-water.

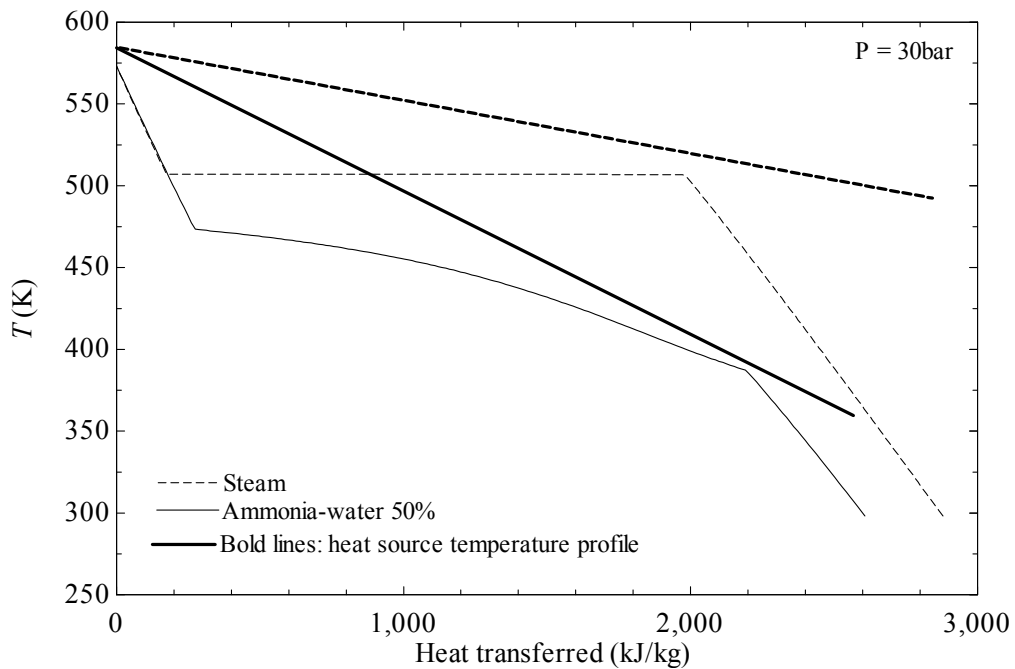


Figure 5.3: Comparison of heat transfer profile in a vapor generator working with steam vs with ammonia-water mixture at 50% concentration.

The boiling process for an ammonia-water mixture is illustrated in Figure 5.2. When the mixture boils, a separation of the components takes place. The vapor is richer with ammonia than the liquid. The starting point for the boiling is called the bubble point and the end point is called the dew point. The bubble point temperature for a mixture with a mass fraction of ammonia of 0.5 at a pressure of 11 MPa is 204 °C. During the boiling the temperature increases. When the temperature of the boiling mixture has reached 230°C, the mass fraction of ammonia in the liquid phase is 0.37, while it is 0.70, in the vapor phase. As can be seen, the difference in mass fraction of ammonia between the coexisting liquid and vapor is large. At the dew point, the mixture is completely vaporized and the mass fraction of ammonia in the vapor is 0.5.

The change in temperature during boiling and condensation of a mixture makes it possible to keep the temperature profile of a binary working fluid closer to a heat source of decreasing temperature or a heat sink of increasing temperature. This is illustrated in Figure 5.3 where the temperature profile in the vapor generator is shown for steam and for ammonia-water.

Ammonia and water are both strongly polar substances of about the same molecular structure and mass. Both substances also show hydrogen bonding, even though it is stronger in water than in ammonia. Despite many similarities, they have considerably different normal boiling points and critical points. When calculating the performance of an ammonia-water power cycle and designing the equipment such as heat exchangers, turbines and boilers, thermophysical properties of the ammonia-water mixture need to be known. The thermophysical properties are usually obtained from equations of state and other general equations. For mixtures, it is common to combine equations for the pure substances that the mixture consists of. However, the mixture of ammonia and water is non-ideal and has an advantageous heat transfer property.

The mixing effect is substantial, especially for the liquid. The liquid volume decreases in the order of up to 20 % when ammonia and water are mixed. The enthalpy of mixing can be as great as -4 kJ/mol (Tillner-Roth and Friend, 1998). This makes it difficult to predict the properties of the mixture from properties of the pure substances. Experimental data are therefore necessary for the development of correlations for describing the properties.

5.3 Geometrical analysis of scroll machine

The geometrical analysis of scroll machine is a prerequisite for its thermodynamic modeling. The intend of the geometric modeling is to obtain the expressions for areas and volumes of different working chambers formed within the scroll wraps and the leakage paths areas as a function of the orbiting angle. These expressions are required to analyze the compression or expansion process of the scroll unit when working as either of the two modes.

Because of the geometric complexity, it is very important to derive the expressions by performing a careful analysis of the geometric features. Some considerations may be made to limit the number of geometrical variables to deduce exact expressions.

The scroll unit consists of two identical intermeshing wraps. These wraps have geometrical parameters that determine the size of the scroll unit as a whole. As shown in the Figure 5.4, the orbiting scroll wrap always has conjugacy with the fixed scroll wrap at a number of points that depends on the length of the scroll wrap.

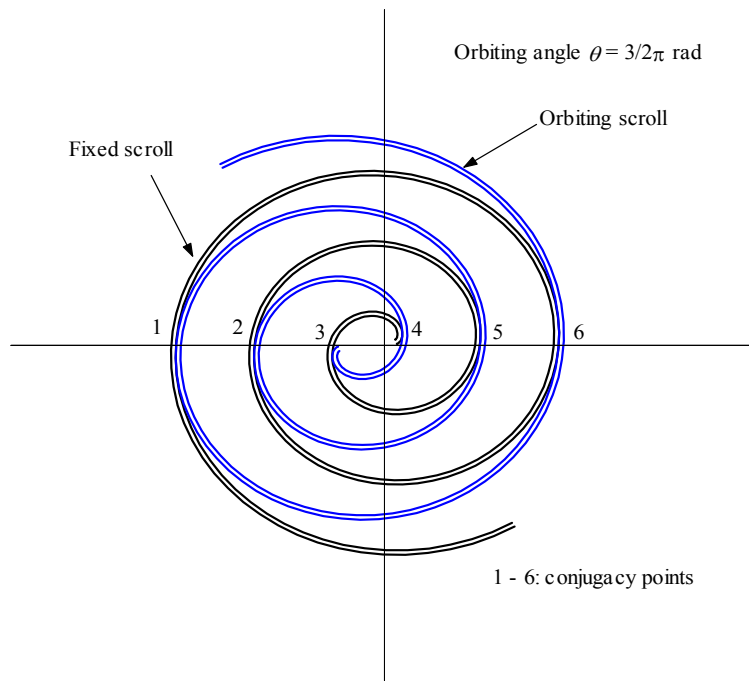


Figure 5.4: Representation of scroll wraps and conjugacy points.

The scroll geometry is defined with the following parameters: r_b radius of the basic circle of the scroll, h height of scroll vanes, φ_{e0} initial angle of the external involute curve, φ_{i0} initial angle of the internal involute, φ_{eS} starting angle of the external involute, φ_{iS} starting

angle of the inner involute. In addition, there is the maximum angle of the scroll (sometimes called the rolling angle) which gives the number of turnings.

Some other parameters exist in relation to the conjugacy of the two scrolls. The orbiting angle θ describes the number of turns that the orbiting scroll must do for a complete cycle of compression or expansion. The built-in volume ratio is defined as the ratio of the volume of the expansion chamber at the end of the expansion process to the volume of the intake chamber at the beginning of the process. The built-in volume ratio is the most important parameter of scroll machine because it directly influences the capacity and operation of a scroll machine.

As mentioned earlier, the basic geometrical features of the scroll dynamics are defined as two involutes that develop around a base circle. All the literature works on geometry modeling so far refer to scroll compressors. However, the scroll expander operation is similar, but in reverse, so the published results can be easily transposed for operation as expander.

A group of authors describe the geometry using the intrinsic equation that links the arc-length and the tangent direction (Bush and Beagle, 1992; Chen et al., 2002) while the others use parametric equations (Lee and Wu, 1995; Wang et al., 2005). Gravensen and Enriksen (2001), proposed an ortho-normal frame (t, n) where the geometry describes all the properties of the scroll very clearly. Two unit vectors $t(\varphi)$ and $n(\varphi)$ can be represented by the following expressions using complex algebra

$$t(\varphi) = (\cos \varphi, \sin \varphi) = \cos \varphi + j \sin \varphi \quad (5.7)$$

$$n(\varphi) = (-\sin \varphi, \cos \varphi) = -\sin \varphi + j \cos \varphi \quad (5.8)$$

The scroll is the involute of a circle with radius r_b and the center in ξ (where ξ is a complex number seen as a 2D vector) can be thus expressed as shown in Figure 5.5, namely:

$$S_{ab} = r_b t(\varphi) - r_b \left(\varphi - \varphi_{y_0} \right) n(\varphi) - \varepsilon \quad (5.9)$$

where φ is the involute angle, φ_{y_0} the internal or external involute initial angle with $a \in \{f, m\}$ and $b \in \{i, e\}$ and “f” stands for fixed scroll and “m” stands for orbiting scroll and “i” is inner and “e” is external (or outer). The first term on the right side of the Eq. (5.9) is known as centre of radius of curvature, the second term is radius of curvature and the third one (ε) is denoted eccentricity.

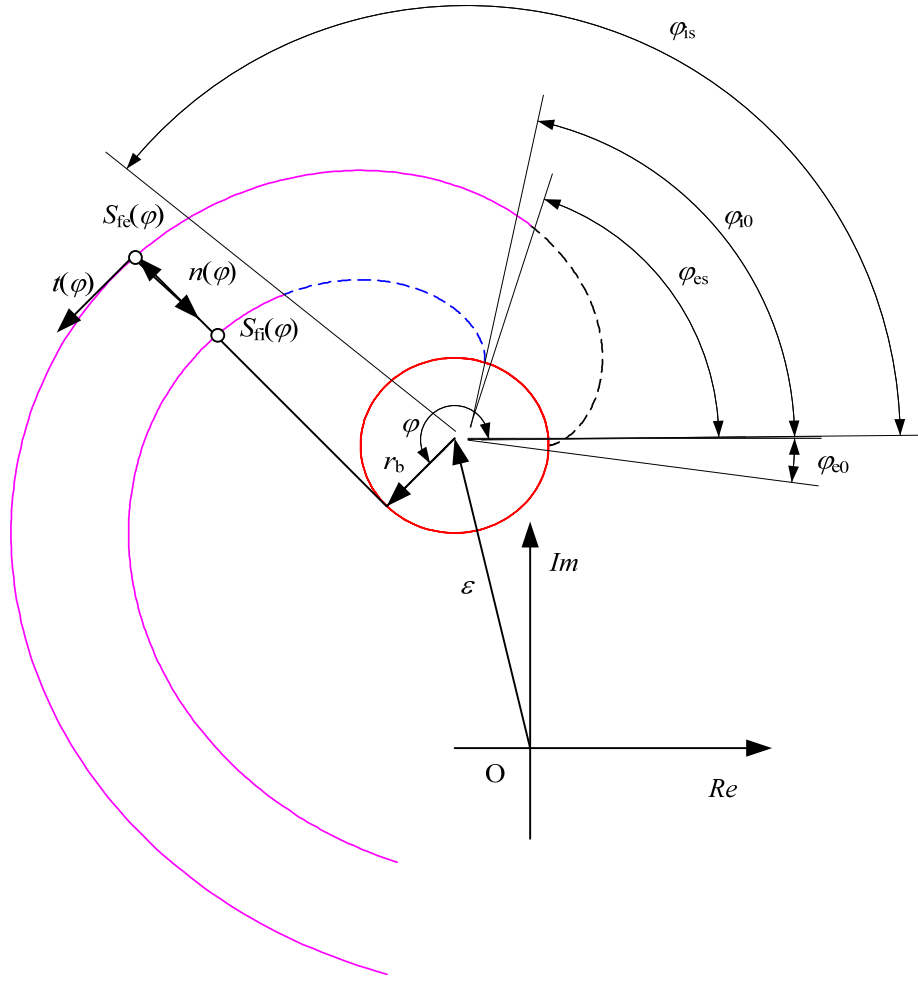


Figure 5.5: Representation of the scroll geometry in the complex plane (or polar coordinates).

The arc-length, l of the involute of a circle is given by the intrinsic equation (Gravensen and Henriksen, 2001):

$$\frac{dl}{d\varphi} = \rho(\varphi) = r_b(\varphi - \varphi_{a0}) \quad (5.10)$$

where $\rho(\varphi)$ is the radius of curvature of the involute. From the equation (3), we can write:

$$S_{fe}(\varphi) = r_b t(\varphi) - r_b(\varphi - \varphi_{e0})n(\varphi) \quad \forall \varphi \in I_e = [\varphi_{es}, \varphi_{\max}] \quad (5.11)$$

$$S_{fi}(\varphi) = r_b t(\varphi) - r_b(\varphi - \varphi_{i0})n(\varphi) \quad \forall \varphi \in I_i = [\varphi_{is}, \varphi_{\max}] \quad (5.12)$$

where S_{fe} and S_{fi} are the external (e) and internal (i) involutes respectively. The φ_{es} and φ_{is} are the external and internal starting angles, φ_{e0} and φ_{i0} the initial angles of the external and internal involutes and φ_{max} the involute ending angle (or rolling angle). The thickness of the scroll wrap is given by.

$$e = r_b (\varphi_{i0} - \varphi_{e0}) \quad (5.13)$$

The connection line between the external and internal involutes, which connects their starting point, is denoted as the interpolation curve. Blunier et al. (2009) represented the interpolation line by an arc of a circle which is tangent to the inner involute at the point of its start angle

$$C_{ci}(\alpha) = O_{ci} - r_c n(\alpha) \quad (5.14)$$

where O_{ci} and r_c are, respectively, the centre and the radius of the circle.

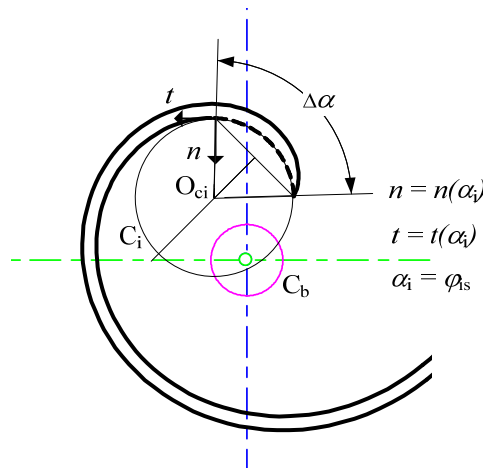


Figure 5.6: Definition of the interpolation circle between inner and outer scrolls.

By imposing that the arc of the circle is symmetric with respect to the cord which unites the starting points of the two involutes, Blunier et al (2009) derived the following equation for r_c considering C_i passing through $S_{fi}(\varphi_{is})$ and $S_{fe}(\varphi_{es})$ and no discontinuity of the derivative at $S_{fi}(\varphi_{is})$ between the spiral S_{fi} and the circle, C_i

$$r_c = \frac{r_b\{2 + \xi_1^2 + \xi_2^2 - 2(1 + \xi_1\xi_1)\cos\xi_3 - 2(\xi_2 - \xi_1)\sin\xi_3\}}{2(\xi_2 - \xi_1\cos\xi_3 - \sin\xi_3)} \quad (5.15)$$

where $\xi_1 = \varphi_{es} - \varphi_{eo}$, $\xi_2 = \varphi_{is} - \varphi_{io}$ and $\xi_3 = \varphi_{is} - \varphi_{es}$. The centre of the interpolation circle can be now deduced as follows:

$$O_{Ci} = r_b t(\varphi_{is}) + \{r_c - r_b(\varphi_{is} - \varphi_{io})\}n(\varphi_{is}) \quad (5.16)$$

The parameter α gives the domain for the interpolation for the circle, with $\alpha \in [\varphi_{is}, \varphi_{is} + \Delta\alpha]$. Here, $\Delta\alpha$ is given by the following expression from Blunier et al. (2009):

$$\Delta\alpha = \cos\left(1 - \frac{r_b}{r_c}(\xi_2 - \xi_1\cos\xi_3 + \sin\xi_3)\right) \quad (5.17)$$

The geometry of the orbiting scroll can be expressed as the fixed scroll except with a phase difference of π .

$$S_{me}(\varphi) = -S_{fc}(\varphi) - r_o n(\theta) \quad \forall \varphi \in I_e = [\varphi_{es}, \varphi_{max}] \quad (5.18)$$

$$S_{mi}(\varphi) = -S_{fi}(\varphi) - r_o n(\theta) \quad \forall \varphi \in I_i = [\varphi_{is}, \varphi_{max}] \quad (5.19)$$

where, $r_o = r_b(\varphi_{eo} - \varphi_{io} + \pi)$ is the orbiting radius.

In the scroll machine, the design feature is such that each point on one wrap's surface has one and only one contact point on the other wrap's surface. The two scrolls are in contact at their points of conjugacy at involute conjugate angles, φ_k .

The expansion process can be described by the four positions of the orbiting scroll shown in Figure 5.7. During the process, θ varies from 2π to 0. At each time instant during the expansion, three pair of chambers can be defined: Two intake chambers; two or a multiple of two expansion chambers; two discharge chambers.

Due to unique features of scroll geometry and dynamics, the volumes of each pair of chambers are equal. However, even the volumes of each pair of pockets are the same; the expansion process of the identical chambers cannot be considered as symmetrical because of the position of the discharge port. The discharge port is not connected at once with the two expansion chambers. Thus, pressure of the two expansion chambers differs.

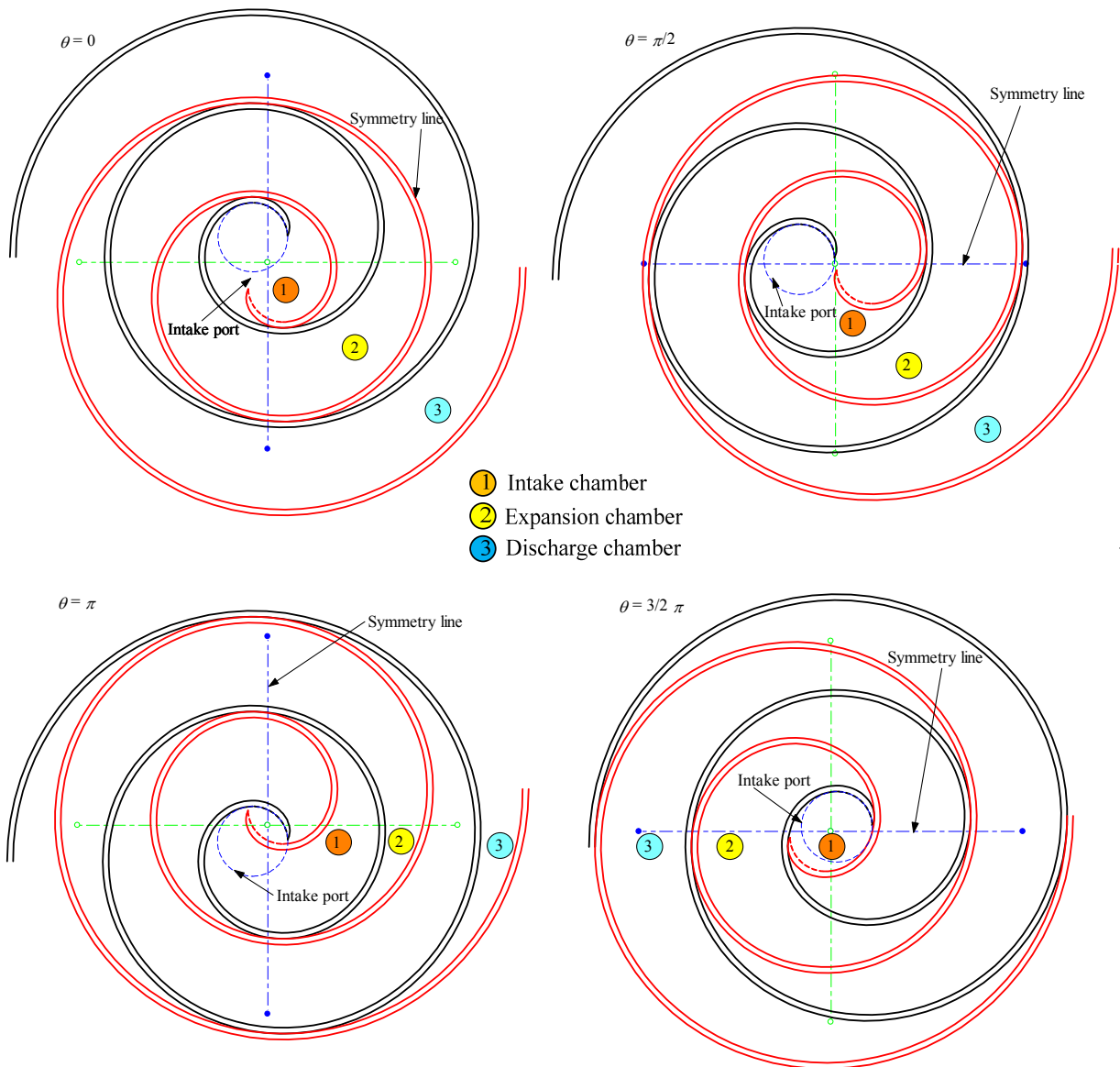


Figure 5.7: Expansion phases and gas chambers formed between the scrolls.

The compression process is considered as cyclic. One cycle consists of the following steps:

- 1) At the start of the intake, the volume of the suction chamber is zero and the volume of the discharge chamber is the maximum. The discharge chamber then opens and a contact point appears between discharge chamber and the adjacent expansion chamber.

Leakages occur between:

- a. Expansion chamber and the adjacent discharge chamber,
- b. The two intake chambers,

- c. The intake chambers and the discharge port.
- 2) The expansion chamber is enclosed between two contact points depending on the orbiting angle. Leakages occur between the:
 - a. Expansion chamber to discharge chamber,
 - b. Expansion chamber to intake chamber,
 - c. Intake to intake,
 - d. Intake chamber and intake port.
- 3) One of the expansion chambers, just before intake, has contact point with intake port and a leakage flow occurs.
- 4) Finally, the expansion chambers open to the intake port.
- 5) Thus, the process restarts with the building of the new discharge chamber, conversion of intake chamber to expansion chamber and opening of the intake chamber to the intake port.

The clearance volume of the scroll machine as depicted by Yanagisawa et al. (1990) is:

$$V_{cl} = \sigma r_c^2 \left(\pi - \sin \left(\frac{2r_b}{r_c} \right) - \frac{2r_b}{r_c} \right) \quad (5.20)$$

The volume of the intake chamber is given by the following equations from Blunier et al. (2009):

$$V_{int}(\theta) = \begin{cases} 0.5 V_0(\theta) & \text{if } (\theta \geq \theta^{dis}) \vee (\theta \geq \theta^{suc}) \\ 0.5 h r_c [r_c \beta(\theta) - (r_c - l_{dis}(\theta)) \sin \beta] & \text{elsewhere} \end{cases} \quad (5.21)$$

where

$$V_0(\theta) = \begin{cases} \sigma (f(\varphi_{i0}, \varphi_{is}, \theta) - f(\varphi_{e0}, \varphi_{es}, \theta - \pi, \theta) + V_{cl}) & \text{if } \theta \geq \theta^{dis} \\ \sigma (f(\varphi_{i0}, \varphi_{is}, \theta + 2\pi, \theta) - f(\varphi_{e0}, \varphi_{es}, \theta + \pi, \theta) + V_{cl}) & \text{elsewhere} \end{cases}$$

$$f(\varphi_{y0}, \varphi_1, \varphi_2, \theta) = \frac{r_b^2}{3} \left((\varphi_2 - \varphi_{y0})^3 - (\varphi_1 - \varphi_{y0})^3 \right) - \frac{r_b r_o}{2} [\cos(\theta - \varphi_2) - \cos(\theta - \varphi_1)] \\ - (\varphi_2 - \varphi_{y0}) \sin(\theta - \varphi_2) + (\varphi_1 - \varphi_{y0}) \sin(\theta - \varphi_1)]$$

The discharge chamber volume computation is computed with the formula given in Blunier et al. (2009), namely:

$$\frac{V_{dis}(\theta)}{\sigma} = \begin{cases} \frac{1}{2}(f(\varphi_{i0}, \theta + 4\pi, \varphi_{max}, \theta) - (f(\varphi_{e0}, \theta + 3\pi, \varphi_{max} - \pi, \theta))) + A, \theta \leq \theta^{suc} \\ \frac{1}{2}(f(\varphi_{i0}, \theta + 2\pi, \varphi_{max}, \theta) - (f(\varphi_{e0}, \theta + \pi, \varphi_{max} - \pi, \theta))) + A, \text{elsewhere} \end{cases} \quad (5.22)$$

with:

$$A = \frac{r_b r_o}{4} (2 - 2 \cos(\theta - \varphi_{max}) - (\varphi_{i0} + \varphi_{e0} + \pi - 2\varphi_{max}) \sin(\theta - \varphi_{max}))$$

The volume of the expansion chamber is defined as the area enclosed by the involutes of the orbiting and the fixed scrolls between two conjugate points, multiplied by the height of the scroll (σ):

$$V_{exp}(\theta) = \begin{cases} \sigma r_b r_o \pi (2\theta - \varphi_{ei} - \varphi_{ei} + \pi) & \text{if } \theta \geq \theta^{dis} \\ \sigma r_b r_o \pi (2\theta - \varphi_{eo} - \varphi_{eo} + 5\pi) & \text{if } \theta \geq \theta^{suc} \\ 0.5 [V_0(\theta) - h r_c [r_c \beta(\theta) - (r_c - l_{dis}(\theta) \sin \beta)] & \text{elsewhere} \end{cases} \quad (5.23)$$

The discharge port and leakages occur through paths S as shown in Figure 5.8. The discharge process becomes asymmetric.

In a scroll machine, ideally the orbiting scroll and the fixed scroll should contact each other perfectly while in operation. However, it is impractical to design and fabricate unit in perfect match. So, there always exist narrow gaps that lead two types of leakage known as (i) tangential leakage and (ii) radial leakages along the contact surfaces. The amount of leakage flow depends on the built in clearance but also varies on the properties of the process fluid, lubricant and on the operating parameters. Thus, actual pressure in the chambers differs from the ideal pressure. The leakage flow directs from high pressure chamber to lower pressure chamber. The leakage flow, drained to lower pressure chamber, accompanies the main flow stream again and recompresses to compression. The leakage flow, drained to lower pressure chamber, accompanies the main flow stream again and recompresses to higher pressure. This causes higher energy consumption and decrease in volumetric efficiency. The two types of leakage are illustrated in Figure 5.8.

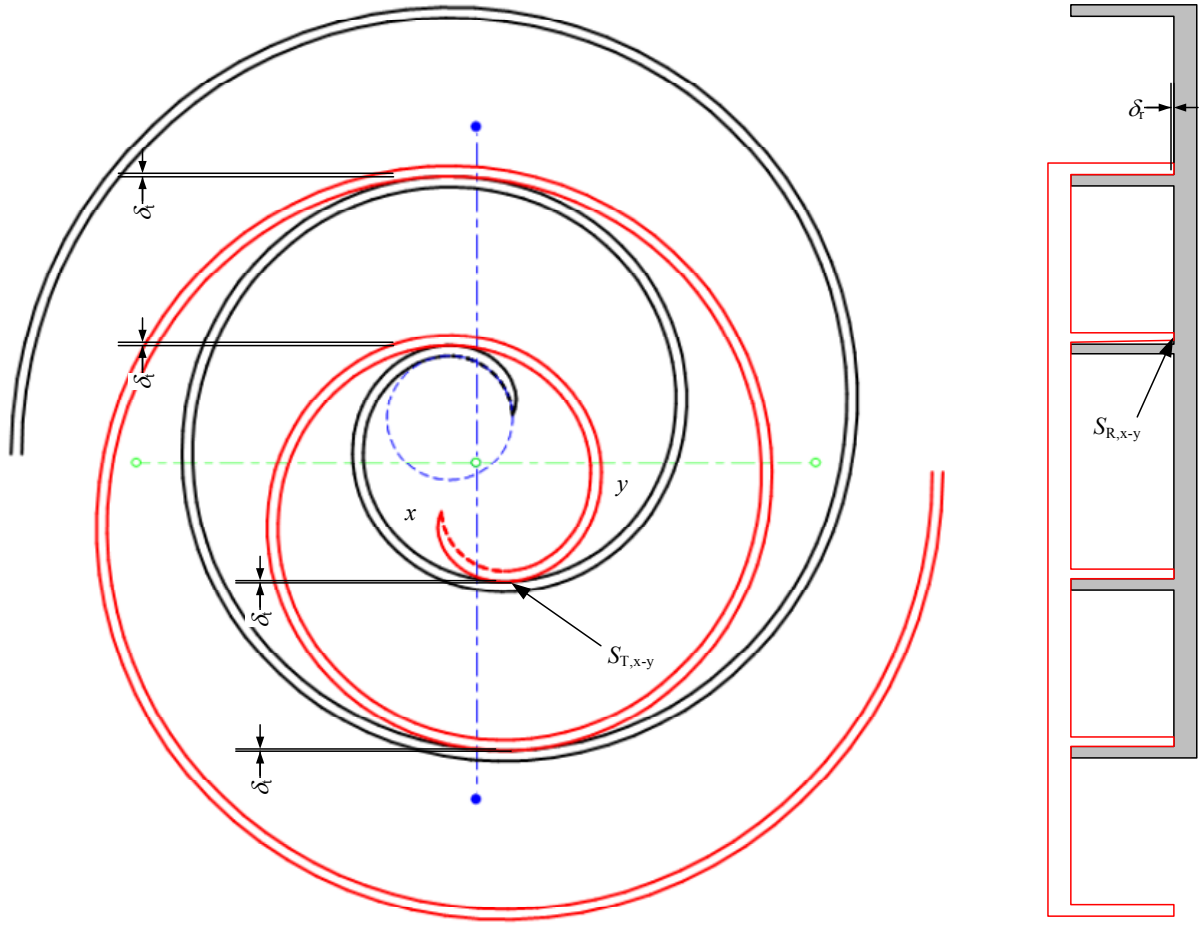


Figure 5.8: Leakage flow of a scroll compressor.

In the tangential leakage, the gas flows through the clearance, δ_T between the flanks of the two scrolls as shown in Figure 5.8 and the tangential leakages between the chambers x and y are noted $S_{T,x-y}$. These types of leakages occur through the contact points in all chambers but for modelling purpose, we shall consider only suction and discharge areas. In a contact point between two chambers x and y, the leakage can be computed as: $S_{T,x-y} = \delta_T h$ where h represents the height of the scroll wrap. The discharge leakage area derived by Tojo et al. (1986) is given as:

$$S_{T,amb-suc} = \sigma(r_o(1 - \cos(\theta - \theta^{suc})) + \delta_T) \quad (5.24)$$

Considering that there is negligible curvature, Tojo et al. (1986) depicted the leakage area as:

$$S_{T,exp-intake} = \begin{cases} \delta_T \sigma & \text{if } (\theta \geq \theta^{dis}) \vee (\theta \geq \theta^{suc}) \\ \sigma l_{dis}(\theta) & \text{elsewhere} \end{cases} \quad (5.25)$$

Also, the leakage area between two intake chambers is computed as:

$$\begin{aligned} S_{T,intake-intake} &= [4r_b^2(\varphi_{es}^2 - 2\varphi_{es}\varphi_{e0} + \varphi_{e0}^2 + 1) \\ &\quad - 4r_b r_o ((\varphi_{es} - \varphi_{e0}) \cos(\theta - \varphi_{es}) + \sin(\theta - \varphi_{es})) + r_o^2]^{1/2} \end{aligned}$$

In the radial leakage, the gas flows through the clearance δ_R formed between each base plate and corresponding wrap tip and the radial leakages between the chambers x and y are noted, $S_{R,x-y}$. In general, the radial leakage is considered more critical as the leakage flow is much higher than the tangential leakage because the length of radial leakage boundary is much longer. In a steady operating condition of a scroll compressor, the inner chamber pressure is higher than the outer chambers. In radial leakage, the direction of flow stream is from inner to outward. Also the arc length of the spiral is not exactly same due to the involvement of the thickness between internal and external spiral. However, for simplicity, we can consider the mean arc length l_{mean} . The expression for the mean fixed spiral can be given as:

$$\tilde{S}_{mean} = r_b t(\varphi) - r_b \left(\varphi - \frac{\varphi_{i0} + \varphi_{e0}}{2} \right) n(\varphi) + \frac{1}{2} r_o(\theta) \quad (5.26)$$

$$\frac{dl_{mean}(\varphi)}{d\varphi} = r_b \left(\varphi - \frac{\varphi_{i0} + \varphi_{e0}}{2} \right) = \rho(\varphi) \quad (5.27)$$

where ρ is the radius of curvature of the involute. Then, the mean arc length between the two angle φ_1 and φ_2 can be deduced as:

$$l_{mean}(\varphi_1 \rightarrow \varphi_2) = \frac{1}{2} r_b (\varphi_2 - \varphi_1) (\varphi_1 + \varphi_2 - \varphi_{e0} - \varphi_{i0})$$

The radial leakage that occurs in a scroll compressor can be listed as follows:

- (1) Leakage between discharge and compression chamber,
- (2) Leakage between two compression chambers,

- (3) Leakage between compression and suction chambers,
- (4) Leakage between compression chamber and outside, and
- (5) Leakage between suction chamber and outside.

Radial leakage between intake and expansion chambers between $\varphi_{ce,1}$ and $\varphi_{ci,1}$ or $\varphi_{ce,2}$ and $\varphi_{ci,2}$. Then as shown in Blunier et al. (2009) it can be deduced that:

$$S_{R,intake-exp} = \begin{cases} \frac{\delta R r_b \pi}{2} (2\theta - \varphi_{e0} - \varphi_{i0} - \pi) & \text{if } \theta \geq \theta^{dis} \\ \frac{\delta R r_b \pi}{2} (2\theta + 3\pi - \varphi_{e0} - \varphi_{i0}) & \text{if } \theta \geq \theta^{suc} \\ \frac{\delta R r_b \pi}{2} (\theta - \varphi_{es})(\theta - \varphi_{e0} + \varphi_{es} - \varphi_{i0}) & \text{elsewhere} \end{cases}$$

The radial leakage between the two expansion chambers may occur when there is a pressure difference between the two and till the pressure balances. In the case, when $\varphi_{ce,3}$ exists, it can be computed as:

$$S_{R,exp-exp} = \begin{cases} \frac{\delta R r_b \pi}{2} (2\theta - \varphi_{e0} - \varphi_{i0} + 5\pi) & \text{if } \theta \geq \theta^{suc} \\ \frac{\delta R r_b \pi}{2} (2\theta - \varphi_{e0} - \varphi_{i0} + \pi) & \text{elsewhere} \end{cases}$$

The radial leakage between the two compression chambers and the suction chambers are computed when there exists $\varphi_{ce,3}$:

$$S_{R,com-suc} = \begin{cases} \frac{\delta R r_b \pi}{2} (\varphi_{max} - 4\pi - \theta)(\theta + 2\pi + \varphi_{max} - \varphi_{e0} - \varphi_{e0}) & \text{if } \theta \geq \theta^{suc} \\ \frac{\delta R r_b \pi}{2} (\varphi_{max} - 4\pi - \theta)(\theta + \varphi_{max} - \varphi_{e0} - \varphi_{i0}) & \text{where} \end{cases}$$

Leakage between compression chamber and outside exists only when the expansion chambers are in contact with outside:

$$S_{R,com-suc} = \begin{cases} \frac{\delta R r_b}{2} (\theta + 5\pi - \varphi_{max})(\theta + 3\pi + \varphi_{max} - \varphi_{e0} - \varphi_{i0}) & \text{if } (\theta \leq \theta^{suc}) \wedge (\varphi_{max} - 5\pi \leq \theta) \\ \frac{\delta R r_b}{2} (\theta + 3\pi - \varphi_{max})(\theta + \pi + \varphi_{max} - \varphi_{e0} - \varphi_{i0}) & \text{if } \varphi_{max} - 5\pi \leq \theta \\ 0 & \text{elsewhere} \end{cases}$$

Though at the onset of discharge, the pressure at the discharge chamber is lower than the ambient, the discharge chamber pressure builds up with the conversion of discharge chamber

towards expansion chamber. Even the leakage flow is minute at this condition, an expression can be written as:

$$S_{R,com-suc} = \begin{cases} \frac{\delta R r_b}{2} (\varphi_{max} - \theta - 4\pi) * (\theta + 4\pi + \varphi_{max} - \varphi_{e0} - \varphi_{i0}) & \text{if } (\theta \leq \theta^{suc}) \wedge (\varphi_{max}) \\ \frac{\delta R r_b}{2} (\theta + 3\pi - \varphi_{max}) * (\theta + \pi + \varphi_{max} - \varphi_{e0} - \varphi_{i0}) & \text{if } \varphi_{max} - 3\pi \leq \theta \\ \frac{\delta R r_b}{2} (2\varphi_{max} - \pi - \varphi_{e0} - \varphi_{i0}) & \text{elsewhere} \end{cases}$$

5.4 Energy and exergy analyses of scroll machine

As the geometry of the scroll component and scroll operation is known, a thermodynamic modelling is required to compute the performance of the scroll machine as a compressor. The modeling as a expander is somehow similar, but it works in reverse. Blunier et al. (2009) defined the scroll operation consisting of two components. The control volume component and the leakage component both are the function of the orbiting angle. Separate modelling is required for each of the component.

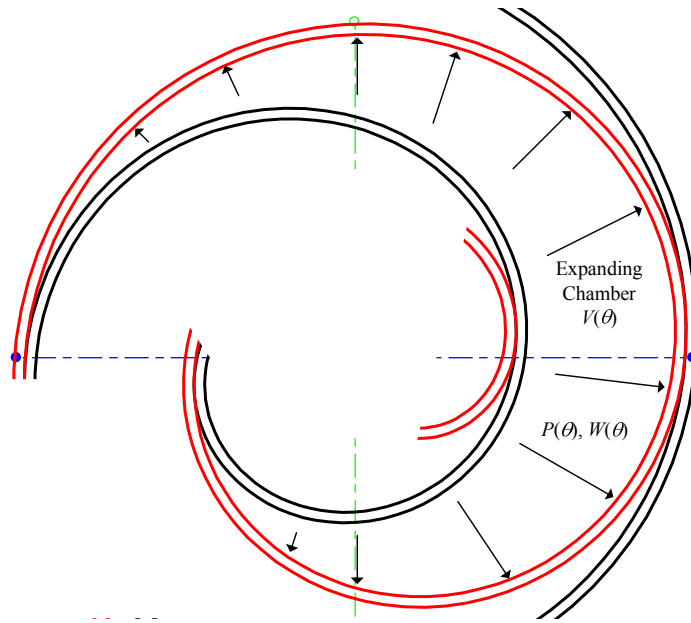


Figure 5.9: Expanding chamber generating boundary work due to pressure forces and orbiting movement.

Assume for simplicity, the operation of a scroll expander without leakages. Then a known amount of working fluid is enclosed in the expanding chamber which increases its

volume according to the function $V(\theta)$ determined from the expander's geometrical analysis. In this case, the specific volume of the working fluid inside changes according to the equation:

$$v(\theta) = \frac{V(\theta)}{m}$$

where $m = V_{\text{intake}}/v_{\text{intake}}$.

The energy balance equation for the expanding cavity is:

$$0 = m \frac{du}{dt} + \dot{W}$$

where the boundary work is:

$$\dot{W} = P \frac{dV(\theta)}{dt}$$

Assume that the scroll orbits at fixed angular velocity; thence $d\theta = \omega dt$. Therefore, the energy balance equation becomes:

$$\frac{du}{d\theta} = -\frac{P}{m} \frac{dV(\theta)}{d\theta} \quad (5.28)$$

If the concentration of ammonia-water mixture is specified, then the pressure in the above equation can be determined based on internal energy and specific volume $P = P(x, u, v)$. Therefore, the above equation can be integrated from $\theta = 0$ to $\theta = \theta_{\text{max}}$. When this equation is solved, the pressure change with angle θ is determined and thus the generated work. Of course, the total boundary work is the double of the boundary work of a single chamber.

If the angular speed of the expander is reasonably high, then a thermodynamic model which considers the average flow through the expander can be considered. In Oralli et al. (2011) a thermodynamic model of scroll expander is described. This model is shown in Figure 5.10. In this model, the many by-pass leakages in a scroll expander are averaged and an orifice flow model is used. As shown in Figure 5.10, due to leakage path, a part of the high pressure working fluid bypasses the expander and leaks directly to suction port. Once a leakage coefficient is known, the leakage flow rate of bypass leaks can be calculated based on thermodynamic states 1 and 2 shown in Figure 5.10 as follows:

$$\dot{m}_{leak} = \zeta \sqrt{P_1/v_1 - P_2/v_{2,h}} \quad (5.29)$$

where $v_{2,h}$ is the specific volume of the flow having the same specific enthalpy as in state 1 but a pressure equal to that of state 2.

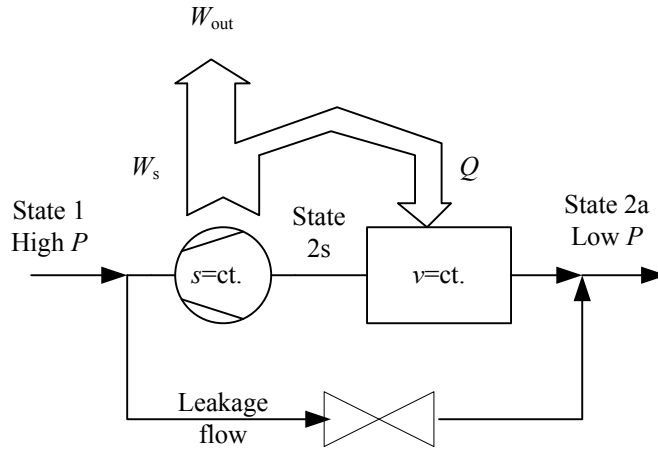


Figure 5.10: Thermodynamic model for scroll expander.

The mass flow rate through the expander can be determined based on the angular speed and the intake chamber volume, V_1 . This mass flow rate through the expander is therefore:

$$\dot{m}_{2s} = \frac{V_1 \omega}{2\pi v_1}$$

Assume that flow \dot{m}_{2s} expands isentropically then it generates the work rate as follows:

$$\dot{W}_s = \dot{m}_{2s}(h_1 - h_{2s})$$

where h_{2s} is the flow enthalpy at the same specific entropy as in 1 and a specific volume higher than in 1 with a factor equal to the built in volume ratio of the expander.

Due to various irreversibilities, a part of the reversible work \dot{W} is wasted and eventually converted into heat. In fact, the flow will adapt to the external conditions at discharge. As

justified also in Oralli et al. (2011), the flow adaptation to external condition occurs at constant specific volume. Therefore in state 2a, the pressure is equal to the pressure in the discharge line and the specific volume of the flow is $v_{2s} = v_1$ BVR. The mass and energy balance equation at the discharge port, which require that $\dot{m}_1 = \dot{m}_{\text{leak}} + \dot{m}_{2s}$ and $\dot{m}_{\text{leak}}h_1 + \dot{m}_{2s}h_{2v} = \dot{m}_1h_2$, where $h_{2v} = h(P_2, v_{2s})$, will determine the actual discharge state of the expander.

The output work generated by the expander is therefore

$$\dot{W}_{\text{out}} = \dot{W}_s - \dot{m}_{2s}(h_{2s} - h_{2v})$$

Eventually, the isentropic efficiency can be determined with:

$$\eta_s = \frac{\dot{W}_{\text{out}}}{\dot{m}_1 (h_1 - h_2)} \quad (5.30)$$

5.5 Heat exchangers analysis

To select the vapor generator and condenser, a careful analysis of the heat exchangers is performed. The basic function of the heat exchanger is to transfer heat from one fluid to another or from or to a fluid and the environment. Broadly heat exchangers can be categorized as direct contact heat exchangers where there is no intervening surface between fluids and indirect contact heat exchangers, where there exist a partition between the fluids.

Shell-and-tube heat exchangers are fabricated with round tubes mounted in cylindrical shells with the tube axis parallel to that of the shell. One fluid flows inside the tubes, the other flows across and along the tubes. The major components are tube bundles, front and rear end head, tube sheets and baffles. The differences between the several variations of this basic type of heat exchanger lie mostly in their construction features depending on the desired heat transfer and the provisions made for handling differential thermal expansion between tubes and shell.

Plate heat exchangers consist of a stack of parallel thin plates that lie between heavy end plates. Each fluid stream passes alternately between adjacent plates in the stack, exchanging heat through the plates. The plates are normally corrugated for strength and to enhance the heat transfer by directing the flow and increasing the turbulence. These exchangers have very high

effectiveness due to high heat transfer coefficients and area. But they have low pressure capability.

Recuperators are direct-transfer heat exchangers in which heat transfer occurs between two fluid streams at different temperature levels in a space that is separated by a thin solid wall (a parting sheet or tube wall). Heat is transferred by convection from the hot (hotter) fluid to the wall surface and by convection from the wall surface to the cold (cooler) fluid.

In this project, two main heat exchangers are used; one for the vapor generator and one for the condenser. Careful analysis is made in selection of heat exchanger for those purposes. The selection of heat exchanger involves rating and sizing based on the requirement and optimization of the heat transfer process. In the rating problem, we used the principle of heat transfer rate and outlet temperature and pressure drop performances of the already designed heat exchanger.

In the consideration of boiler design, it is required to heat ammonia-water with hot oil preheated in an electrical heater. The thermodynamic governing relationship can be used in calculation of design parameters. Assume a hot stream flowing with a capacity rate $C_h = \dot{m}_h c_{ph}$ and a cold stream flowing with a capacity rate $C_c = \dot{m}_c c_{pc}$. Then, applying conservation of energy in the form of enthalpy balance, we obtain:

$$\dot{Q} = C_h(T_{hi} - T_{ho}) = C_c(T_{ci} - T_{co}) \quad (5.31)$$

where the subscripts i and o refer to the inlet and outlet of the heat exchanger and T_h and T_c denote hot and cold fluid temperature.

Eq. (5.31) represents the rate of heat flow based on the fluid flow and temperature conditions. Another equation can be described based on the convection-conduction phenomena of the two fluid heat exchanger. The heat transfer rate is proportional to the heat transfer area A and the mean temperature difference ΔT_m between the fluids:

$$\dot{Q} = UA\Delta T_m$$

The entire heat exchange process can be represented by:

$$\dot{Q} = U_h \eta_{f,h} A_h \Delta T_m = U_c \eta_{f,c} A_c \Delta T_m = C_h(T_{hi} - T_{ho}) = C_c(T_{ci} - T_{co}) \quad (5.32)$$

where $\eta_{f,h}$ and $\eta_{f,c}$ are the fin efficiencies for the hot and cold side respectively.

For heat transfer surface without fins, the term η_f bears the value 1. Consider the bare tube of length L shown in Figure 5.11 and observe that because of the tube wall thickness δ_w , the inner diameter will be smaller than the outer diameter and the surface areas will be different $A_i = \pi d_i L$, $A_o = \pi d_o L$. In the case of the finned tube, shown with one fin on the inside and outside of the tube wall, the fin surface areas will be $A_{fi} = 2n_i b_i L$ and $A_{fo} = 2n_o b_o L$, where n_i and n_o are the number of fins on the inside and outside of the tube wall, respectively, and it is presumed that no heat is transferred through the tip of either of the inner or outer fins. In this case, the prime or base surface areas $A_{bi} = (\pi d_i - n_i \delta_{fi})L$, $A_{bo} = (\pi d_o - n_o \delta_{fo})L$. The total inside surface will then be $A_i = (\pi d_i + n_i(2b_i - \delta_{fi}))L$.

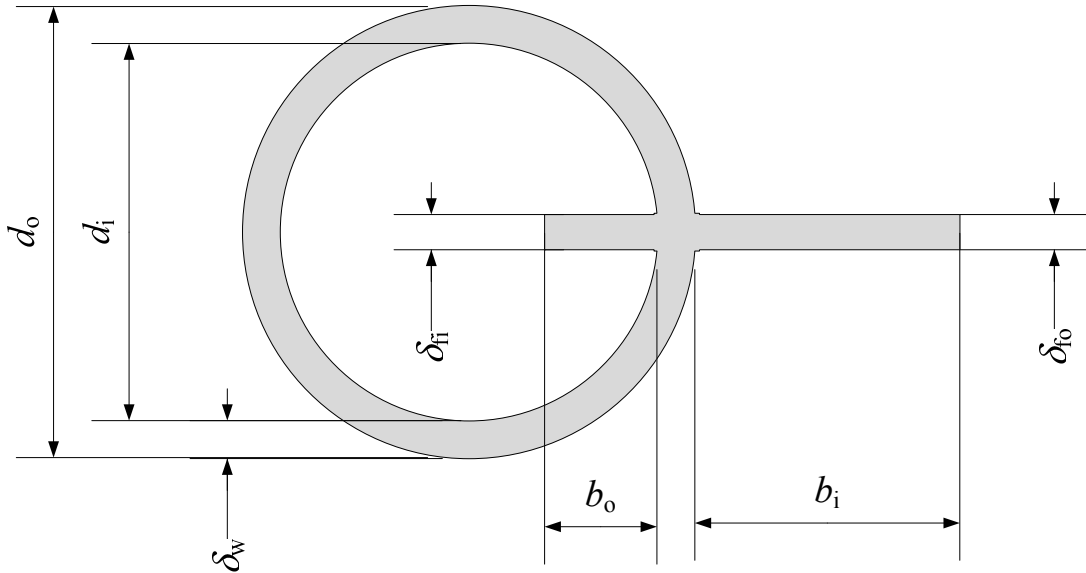


Figure 5.11: Extended surfaces for heat transfer.

Similarly, outside surface is $A_o = (\pi d_o + n_o(2b_o - \delta_{fo}))L$. The ratio of the finned surface to the total surface is:

$$\frac{A_{fi}}{A_i} = \frac{2n_i b_i}{\pi d_i + n_i(2b_i - \delta_{fi})}$$

and:

$$\frac{A_{fo}}{A_o} = \frac{2n_o b_o}{\pi d_o + n_o(2b_o - \delta_{fo})}$$

The overall surface efficiencies $\eta_{ov,h}$ and $\eta_{ov,c}$ are based on the base surface operating at an efficiency of unity and the finned surface operating at fin efficiencies of η_{fi} and η_{fo} . Hence

$$\eta_{ov,i}A_i = A_{bi} + \eta_{fi}A_{fi} = A_i - A_{fi} + \eta_{fi}A_{fi} = 1 - \frac{A_{fi}}{A_i}(1 - \eta_{fi})$$

The overall heat transfer coefficient of the boiler can be determined by analyzing the thermal resistances occurring in the between hot and cold stream. The vapor generator design configuration is shell and tube arrangement and five types of resistances can be involved. The individual heat transfer resistance/coefficients depend on the nature of the heat transfer process, the stream properties and the heat transfer surface arrangements.

- Hot side convective layer resistance:

$$R_h = \frac{1}{h_h \eta_{ov,h} A_h}$$

- Hot side fouling resistance due to the accumulation of foreign material on the hot side surface of the tube:

$$R_{dh} = \frac{1}{h_{dh} \eta_{ov,h} A_h}$$

- Resistance of the tube material.

Resistance of the exchanger material, which has a finite thermal conductivity, depends on the shape of the heat transfer surfaces. The configuration of the boil is shell and tube but the tubes are flat type. So the heat transfer surface can be considered as plane tube:

$$R_m = \frac{\delta_w}{k_m A_m}$$

- Cold side fouling resistance.

$$R_{dc} = \frac{1}{h_{dc} \eta_{ov,c} A_c}$$

- Cold side convective layer resistance.

$$R_h = \frac{1}{h_c \eta_{ov,c} A_c}$$

The above resistances are in series and the total resistances for the heat flow can be represented a generalized equation:

$$\frac{1}{UA} = \frac{1}{h_h \eta_{ovh} A_h} + \frac{1}{h_{dh} \eta_{ovh} A_h} + \frac{\delta_w}{k_m A_m} + \frac{1}{h_{dc} \eta_{ov,c} A_c} + \frac{1}{h_c \eta_{ov,c} A_c}$$

In the boiler, the thickness of the flat tube is very small and the thermal conductivity of the metal is high. So the metal resistance can be neglected. The equation then becomes:

$$U = \frac{1}{\frac{A}{h_h \eta_{ovh} A_h} + \frac{A}{h_{dh} \eta_{ovh} A_h} + \frac{A}{h_{dc} \eta_{ov,c} A_c} + \frac{A}{h_c \eta_{ov,c} A_c}} \quad (5.33)$$

The ΔT_m in Eq. (5.32) is the logarithmic mean temperature difference, which can be written as follows:

$$\Delta T_m = LMTD = \frac{\Delta T_1 - \Delta T_2}{\ln(\Delta T_1 / \Delta T_2)} = \frac{\Delta T_2 - \Delta T_1}{\ln(\Delta T_2 / \Delta T_1)} \quad (5.34)$$

The heat exchanger configuration for boiler is chosen as a cross-flow/counter-flow multi-pass type. The LMTD method is not applicable directly to this system rather the true mean temperature difference in multi-pass cross-flow exchanger. The ΔT_m will be the counter-flow logarithmic mean temperature difference and expressed as:

$$\Delta T_m = F(LMTD_c)$$

where the correction factor

$$F = \frac{\Delta T_m}{LMTD_c}$$

A micro channel heat exchanger (MCHEX) is composed of many microchannel tubes that are attached to the two ducts known as headers. The inlet and output streams of flows are connected to the headers in a position as per the requirement of the flow stream heat transfer. The microchannel tubes are placed horizontally in a parallel arrangement and brazed to the headers. To configure the system to several passages a number of partition walls are mounted inside the headers. The number of tubes in each passes varies depending on the phase change procedure of the fluid. In boiler fluid flows through the lower portion of the shell and vapour exists from the top portion of the shell. So, to accommodate the higher volume of the fluid upper passes are required to have more tubes. A set of wavy fins are normally connected to the

external surface of the tubes to increase the heat exchange surface. MCHEX have attracted attention because they have a high heat transfer area per operational volume unit, and thus, high heat transfer coefficients. For a very small dimension, they provide a very large heat flux transfer.

Microchannel Heat Exchangers (MCHEX) have, according to the classification proposed by Kandlikar and Grande (2003), a hydraulic diameter $h D = 0.2 \dots 0.01 \text{ mm}$ involving the advantage maximum thermal performance with the minimum volume. Also, at very small sizes, the processes of heat and mass transfer occurring in the dynamic and thermal boundary layers are very effective. Considering r_d is the ratio between characteristic dimensions of microchannel, it can be written:

$$r_d = L_d / l_d$$

According to Kandlikar and Grande (2003) for $r_d = 0.5 \dots 2$, one has $l_d = \sqrt{A_t / (n_{mc} \cdot r_d)}$, where A_t is the cross sectional flow area for all microchannels/microtube n_{mc} . Accordingly, thickness of the partition wall between two microchannels is:

$$\delta_d = (W_t - n_{mc} \cdot r_d \cdot l_d) / (n_{mc} + 1)$$

and upper and lower wall thickness, considering equal is:

$$\delta_h = (H_t - l_d) / 2$$

where W_t is the width of the tube and H_t is the height of the tube with microchannels.

The equivalent diameter of the flow through a microchannel can be written as:

$$d_{eq} = \frac{4A_{mc}}{P_{wet}} = \frac{2L_{d_{opt}}l_{d_{opt}}}{(L_{d_{opt}} + l_{d_{opt}})}$$

where A_{mc} and P_{wet} are the cross section and the wetted perimeter of one microchannel respectively. The expression for the total inner heat exchanger surface of the microchannel tube can be written as:

$$A_{in}^{mt} = n_{mc} \cdot P_{wet} \cdot L_t \cdot n_t = 2n_{mc}(L_{d_{opt}} + l_{d_{opt}}) \cdot L_t \cdot n_t$$

where L_t is the length of the tube and n_t is the number of microtube. The inner surface of two collector of height H and cross-sectional dimension $w_h \times l_h$ is:

$$A_{in}^h = 2H \cdot 2(w_h + l_h)$$

The total inner heat transfer surface may be written as:

$$A_{in} = A_{in}^{mt} + A_{in}^h = 2n_{mc} (L_{d_{opt}} + l_{d_{opt}}) \cdot L_t \cdot n_t + 2H \cdot 2(w_h + l_h)$$

The total inside volume of the micro-channel heat exchanger is:

$$V_{in} = V_{in}^{mt} + V_{in}^h = A_t \cdot L_t \cdot n_t + 2H \cdot w_h \cdot l_h$$

where A_t is the cross sectional flow area for all microchannels/microtubes.

5.6 Ejector analysis

The theory for ejector analysis is generally based on the assumption of two discrete streams-the motive stream and the evaporated vapor-maintaining their identity down the converging duct of the diffuser. It is postulated that the secondary vapors reach sonic velocity and are therefore effectively choked at some cross section of the ejector. Standard calculations of nozzle flow enable the capacity of the ejector to be found, and in turn a prediction of steam jet refrigerator performance.

The ejector is a mechanically simple mixing device which may be analysed using compressible flow theory. The ejector is comprised of the converging-diverging (CD) nozzle at the primary inlet, the suction chamber housing the secondary inlet, the constant-area mixing chamber and the recovery diffuser. Following compressible gas theory, the flow expands isentropically and accelerates through the CD nozzle to reach supersonic velocity resulting in the low pressure region in the suction chamber. The secondary flow is entrained and undergoes choking due to the hypothetical converging duct formed between the primary flow stream and the ejector wall. The primary and secondary flows mix during the constant pressure process. A shock wave forms in the constant area chamber if the ejector is operating under choked conditions (critical operation). The resulting stream regains pressure in the diffuser.

High pressure steam generated in the boiler passes through the nozzle. As per the nozzle theory this creates a low pressure in the throat of the converging-diverging nozzle. Due to low pressure at the throat fluid from the evaporator sucks into the throat area creating an action of evaporation of water in the evaporator. The remaining water in the evaporator thus cooled which ultimately cools the fluid passing through the evaporator coil. The primary steam and the secondary steam then mix together to flow to the diffuser section. It then attains a higher pressure to flow finally to the condenser. The condenser water may flow back to the evaporator again or discharged elsewhere in an open loop.

In the evaporator, the cooling action may be gained using the evaporator water directly as a cooling fluid or else heat transferred from a secondary stream. The advantages of the steam jet compression cycle for cooling are the relatively low capital cost, simplicity of operation, reliability and very low maintenance costs. Particular advantages are the ability to eliminate heat transfer surfaces and the ability to use very low pressure motive steam. The disadvantages of the system are the limitation of lowest temperature that is to be above zero and the cost of water.

In practice, two choking phenomena exist in the ejector performance: one in the primary flow through the nozzle and the other in the entrained flow. In addition to the choking in the nozzle, the second choking of an ejector results from the acceleration of the entrained flow from a stagnant state at the suction port to a supersonic flow in the constant-area section. The ejector performance can then be divided into three operational modes, according to the back pressure P_c :

- 1) double-choking or critical mode as $P_c < P_c^*$, while the primary and the entrained flows are both choking and the entrainment ratio is constant;
- 2) single-choking or subcritical mode as $P_c^* < P_c < P_{co}$, while only the primary flow is choked and entrainment ratio changes with the back pressure P_c ; and
- 3) back-flow or malfunction mode as $P_c > P_{co}$, while both the primary and the secondary flow are not choked and the entrained flow is reversed (malfunction).

The following assumptions can be made for the ejector analysis:

- 1) The working fluid is an ideal gas with constant properties C_p and γ .
- 2) The flow inside the ejector is steady and one dimension.

- 3) The kinetic energy at the inlets of primary and suction ports and the exit of diffuser are negligible.
- 4) The isentropic relations are used as an approximation. But to account for non-ideal process, the effects of frictional and mixing losses are taken into account by using some coefficients introduced in the isentropic relations. These coefficients are related to the isentropic efficiency and need to be determined experimentally.
- 5) After exhausting from the nozzle, the primary flow fans out without mixing with the entrained flow until reaching the hypothetical throat which is inside the constant-area section.
- 6) The two streams start to mix at hypothetical throat with a uniform pressure.
- 7) The entrained flow is choked at the hypothetical throat.
- 8) The inner wall of the ejector is adiabatic.

For a given inlet stagnant pressure P_g and temperature T_g , the mass flow through the nozzle at choking condition follows the gas dynamic equation:

$$\dot{m}_p = \frac{P_g A_t}{\sqrt{T_g}} \sqrt{\frac{\gamma}{R}} \left(\frac{2}{\gamma + 1} \right)^{(\gamma+1)/(\gamma-1)} \cdot \sqrt{\eta_p}$$

where η_p is a coefficient relating to the isentropic efficiency of the compressible flow in the nozzle. The gas dynamic relations between the Mach number at the exit of nozzle M_{p1} and the exit cross section area A_{p1} and pressure P_{p1} are, using isentropic relations as an approximation:

$$\frac{A_{p1}}{A_t} \approx \frac{1}{M_{p1}^2} \left[\frac{2}{\gamma + 1} \left(1 + \frac{(\gamma - 1)}{2} M_{p1}^2 \right) \right]^{(\gamma+1)/(\gamma-1)}$$

$$\frac{P_g}{P_{p1}} \approx \left(1 + \frac{(\gamma - 1)}{2} M_{p1}^2 \right)^{\gamma/(\gamma-1)}$$

The Mach number M_{py} of the primary flow at the y-y section follows the isentropic relations as an approximation:

$$\frac{P_{py}}{P_{p1}} \approx \frac{(1 + ((\gamma - 1)/2)M_{p1}^2)^{\gamma/(\gamma-1)}}{(1 + ((\gamma - 1)/2)M_{py}^2)^{\gamma/(\gamma-1)}}$$

For the calculation of the area of the primary flow core at the y-y section, we use the following isentropic relation, but an arbitrary coefficient is included to account for the loss of the primary flow from section 1-1 to y-y:

$$\frac{A_{py}}{A_{p1}} = \frac{(\phi_p/M_{py})[(2/(\gamma + 1))(1 + ((\gamma - 1)/2)M_{py}^2)]^{(\gamma+1)/(2(\gamma-1))}}{1/M_{p1}[(2/(\gamma + 1))(1 + ((\gamma - 1)/2)M_{p1}^2)]^{(\gamma+1)/(2(\gamma-1))}}$$

The loss may result from the slipping or viscous effect of the primary and the entrained flows at the boundary. The entrained flow reaches choking condition at the y-y section. For a given inlet stagnant pressure P_e , we have:

$$\frac{P_e}{P_{sy}} \approx \left(1 + \frac{\gamma - 1}{2} M_{sy}^2\right)^{\gamma/\gamma-1}$$

The entrained flow rate at choking condition then follows:

$$\dot{m}_s = \frac{P_e \times A_{sy}}{\sqrt{T_e}} \sqrt{\frac{\gamma}{R}} \left(\frac{2}{\gamma + 1}\right)^{(\gamma+1)/(\gamma-1)} \cdot \sqrt{\eta_s}$$

where η_s is the coefficient in regards to the isentropic efficiency of the entrained flow.

The temperature and the Mach number of the two stream at hypothetical throat follows:

$$\frac{T_g}{T_{py}} = 1 + \frac{\gamma - 1}{2} M_{py}^2$$

$$\frac{T_g}{T_{sy}} = 1 + \frac{\gamma - 1}{2} M_{sy}^2$$

The two streams starts to mix from the hypothetical throat onwards. A shock then takes place with a sharp pressure rise. A momentum balance relation thus can be derived as:

$$\phi_m [\dot{m}_p V_{py} + \dot{m}_s V_{sy}] = (\dot{m}_p + \dot{m}_s) V_m$$

where V_m is the velocity of the mixed flow and ϕ_m is the coefficient accounting for the frictional loss. Similarly, an energy balance relation can be derived as:

$$\dot{m}_p \left(C_p T_{py} + \frac{V_{py}^2}{2} \right) + \dot{m}_s \left(C_p T_{sy} + \frac{V_{sy}^2}{2} \right) = (\dot{m}_p + \dot{m}_s) \left(C_p T_m + \frac{V_m^2}{2} \right)$$

where V_{py} and V_{sy} are the gas velocities of the primary and entrained flow at the section y–y:

$$V_{py} = M_{py} \times a_{py}; \text{ where, } a_{py} = \sqrt{\gamma R T_{py}}$$

$$V_{sy} = M_{sy} \times a_{sy}; \text{ where, } a_{sy} = \sqrt{\gamma R T_{sy}}$$

The Mach number of the mixed flow also can be expressed as:

$$M_m = \frac{V_m}{a_m}; \text{ where, } a_m = \sqrt{\gamma R T_m}$$

A supersonic shock will take place at with a sharp pressure rise. Assuming that the mixed flow after the shock undergoing an isentropic process, the mixed flow between section m–m and section 3–3 inside the constant area section has a uniform pressure P3. Therefore, the following gas dynamic relations exist:

$$\frac{P_3}{P_m} = 1 + \frac{2\gamma}{\gamma + 1} (M_m^2 - 1)$$

$$M_3^2 = \frac{1 + ((\gamma - 1)/2)M_m^2}{\gamma M_m^2 - ((\gamma - 1)/2)}$$

5.7 Optimization

In this research work one of the goals is to minimize the heat rejected into the environment, thus maximizing the end-product: power, heating and cooling. Optimization can be applied with the objective function to maximize the system efficiency. Some trade-offs may be considered such as maximizing the efficiency while minimizing the cost. Therefore, multi-objective optimization can be formulated for improved system design and operation. Genetic algorithms are in general used for multi-objective optimization problems. Figure 5.12 shows the schematic description of a genetic algorithm for multi-objective optimization.

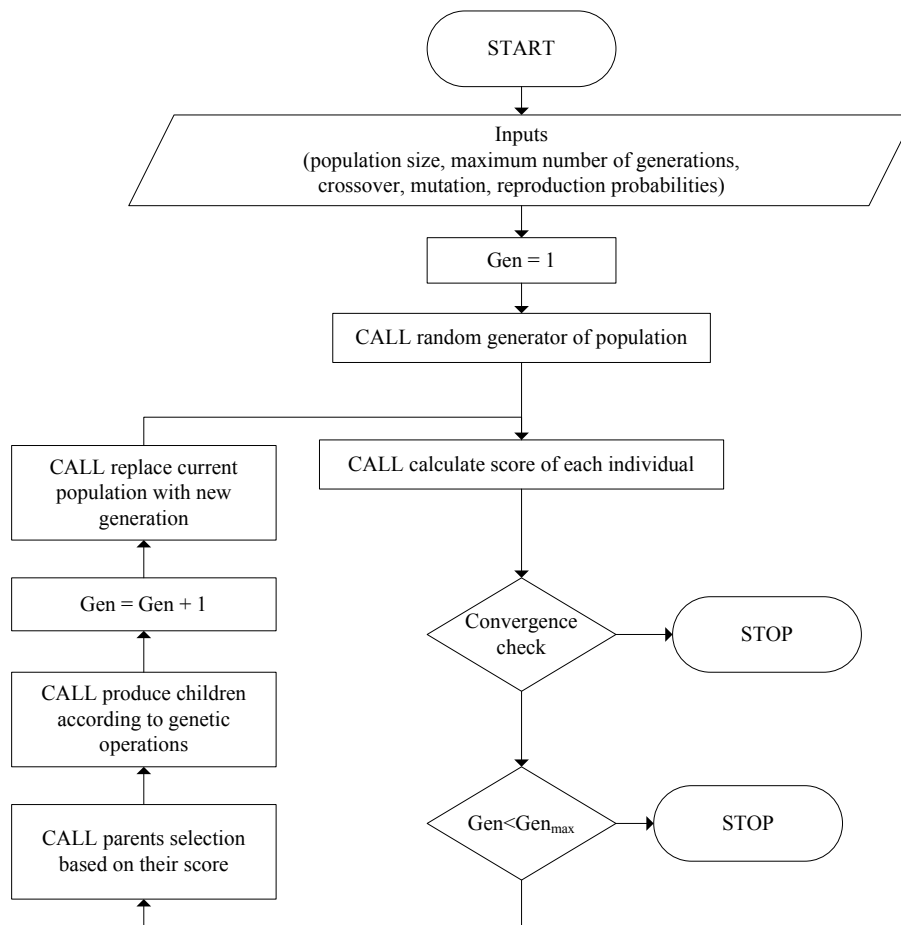


Figure 5.12 Genetic algorithm for optimization.

The performance indicator of trigeneration system can be expressed as energy efficiency and exergy efficiency. In mathematical expression these are reproduced as mentioned in Chapter 5 as:

- Energy efficiency

$$\eta_{3gen} = \frac{\dot{W}_{net} + \dot{Q}_{heating} + \dot{Q}_{cooling}}{\dot{Q}_{in}}$$

- Exergy efficiency

$$\psi_{3gen} = \frac{\dot{W}_{net} + \dot{E}x_{heating} + |\dot{E}x_{cooling}|}{\dot{E}x_{in}}$$

Exergetic specific emission of pollutants per unit of power, cooling and heating generation can be defined as indicated in Dincer and Zamfirescu (2014)

$$SE_{ex} = \frac{\dot{m}_{pollutant}}{\dot{W} + \sum \dot{Q}_H \left(1 - \frac{T_0}{T_H}\right) + \sum \dot{Q}_C \left(\frac{T_0}{T_C} - 1\right)} \quad (5.35)$$

Payback period as defined is the number of years required to return the investment cost (IC), if the products are to be sold at the market price. It depends on the annual operational costs (AOC) and annual rate of income from multiproduct regeneration:

$$PBP = \frac{IC}{\sum c_H \dot{Q}_H + \sum c_C \dot{Q}_C + \sum c_{el} \dot{W}_{net} - AOC} \quad (5.36)$$

where c_H is the selling price of heating, c_C is the selling price of cooling, c_{el} is the selling price of electric power.

Levelized product cost can be defined as the selling price of unit of product to balance the investment cost (IC) and the operational costs (OPC) for the lifetime (LT). The operational cost are proportional to the energy consumption $OPC = LT \sum c_{source} \dot{E}_{source}$, where c_{source} is the specific cost of energy supply, per kind

$$LPC = \frac{IC + LT[\sum c_{source} \dot{E}_{source} - \sum c_H \dot{Q}_H - \sum c_C \dot{Q}_C - \sum c_{el} \dot{W}_{net}]}{LT (\sum c_H \dot{Q}_H + \sum c_C \dot{Q}_C + \sum c_{el} \dot{W}_{net})} \quad (5.37)$$

Total exergetic cost rate is defined based on exergoeconomic balance equation (see Dincer and Rosen, 2013). It depends on fuel cost rate (\dot{C}_f), cost of exergy destruction (\dot{C}_d), cost of environmental impact (\dot{C}_{ei}) and capital cost rate (\dot{Z}_{tot})

$$\dot{C}_{tot} = \dot{C}_f + \dot{C}_d + \dot{C}_{ei} + \dot{Z}_{tot} \quad (5.38)$$

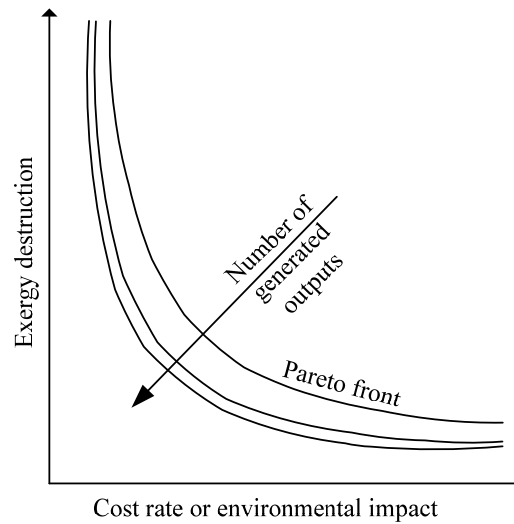


Figure 5.13: Multiobjective optimization of multigeneration systems [modified from Dincer and Zamfirescu (2014)].

As mentioned above, the design of trigeneration systems requires the application of multiobjective, multivariable optimization methods. The goal is to maximize efficiency and to minimize payback period, levelized electricity cost, exergoeconomic cost rate, specific emission factor. The best design selection must be made based on a trade-off analysis.

The Pareto front indicates the best solutions. The optimization variables are the parameters that influence the system performance: the design and the operational parameters. Integrated and multigeneration systems bring an additional dimension to multiobjective optimization because intrinsically these systems are aimed to improved system configuration

(architecture). Systems configurations with more outputs generated; such as trigeneration tend to perform better than single generation ones.

Pareto fronts of multigeneration systems are shown in Figure 5.13 with incrementally at higher performance as the number of outputs increases. Trigeneration systems increase the profitability due to increase of the number of generated outputs. Because of more freedom to morph, the Pareto surface expands toward better systems.

There are several analytical and numerical methods for optimization of complex systems as reviewed in Dincer and Rosen (2012). The multiobjective problem can be reduced to single objective by formulating a compounded objective function or by applying constraints. For example, if the objective function to minimize are the sustainability index $SI = 1 - \psi$ (introduced in Dincer and Rosen, 2013) and the levelized product cost LEC (defined by Eq. 5.37) and both these parameters depend of a number of variables $x_i, i = 1 \dots n$, then the multiobjective optimization problem can be formulated mathematically as follows:

$$\min\{SI(x_i), LPC(x_i), i = 1 \dots n | N = \text{fixed}, \text{other constraints}\} \quad (5.39)$$

where N represents the number of outputs of the multigeneration system.

As shown in Dincer and Zamfirescu (2014), the multiobjective optimization problem (5.39) can be transformed in k single-objective optimizations as follows:

$$\min\{SI(x_i), i = 1 \dots n | LEC(x_i) = LEC_j, j = 1 \dots k, n = \text{fixed}, \text{other constraints}\} \quad (5.39)$$

Depending on the nature of the constraints Lagrange multiplier or other methods of optimization can be applied such as evolutionary algorithms with random but educated search. With these evolutionary algorithms the search progresses according to the natural selection theory of the fittest. These methods can be applied to discontinuous functions which is a great advantage when complex systems are optimized.

5.8 Closing Remarks

In this chapter various analyses are presented which are relevant to system modeling, design and optimization. The chapter starts with the energy and exergy analyses of the trigeneration

system, where balance equations and efficiencies are introduced. In order to be able to perform energy and exergy analyses, several other aspects must be considered as detailed in the chapter.

These are as follows:

- Modeling of the ammonia-water mixture with appropriate equation of state,
- Geometric modeling of the scroll machine such that the volume of the intake, expanding and discharging cavity as well as leakage path areas can be determined,
- Energy and exergy analysis and modeling of the scroll expander itself,
- Heat exchanger analysis with emphasis of heat exchangers modeling methods and heat transfer correlations in meso-channels and extended surfaces,
- Ejector analysis and modeling.

In top of these aspects, the optimization methods especially multi-objective optimization and genetic algorithms are analysed as they are relevant to system optimization according to some indicators such as efficiency, specific emissions, payback period etc. The analysis presented here is extensively used in Results and Discussion chapter to solve modeling and simulation aspects as well as optimization problems.

Chapter 6: Results and Discussion

In this chapter, the results and discussion of the work are presented. The chapter consists of three parts. In the first part, the experimental work is presented. The aim of the experimental work is to prove the concept of trigeneration with the integrated ammonia-water and ejector cycles and to determine the achievable performance parameters. Parameters such as isentropic efficiency of the expander, the entrainment ratio of the ejector, the efficiency of power generation and the COP of the cooling cycle are determined and correlated with input parameters. This data is further used in the second part in modeling and simulation of the trigeneration system which is made for a parametric study. Some optimization, economic and environmental assessments with the system are shown for specific applications in the third part.

6.1 Experimental results

The experimental data has been processed according to a procedure which is presented subsequently. The uncertainty analysis is provided here. This section is structured in a similar manner as Chapter 4, where the experimental investigations are presented.

6.1.1 Uncertainty propagation

The rough experimental results are collected and the measurement error is known based on the measurement devices calibration sheets and data. Further, data is used for processing and other quantities of interest are derived. Due to measurement error, the uncertainty propagates when other quantities of interest are calculated.

The measurement error of the instruments is denoted as the “accuracy of the measurement”. Here, the accuracy is given either as an absolute value or as a relative with respect to the instrument span. The propagated uncertainties associated with the calculated results are based on the uncertainties associated with the measurements.

Assume that x_i represent the primary measurements and a quantity R is determined as follows: $R = R(x_1, x_2, x_3, \dots, x_n)$. Denote $\sigma_1, \sigma_2, \sigma_3, \dots, \sigma_n$ the absolute measurement errors. Then, the uncertainty of R determination becomes:

$$\sigma_R = \left[\left(\frac{\partial R}{\partial x_1} \sigma_1 \right)^2 + \left(\frac{\partial R}{\partial x_2} \sigma_2 \right)^2 + \left(\frac{\partial R}{\partial x_3} \sigma_3 \right)^2 + \dots + \left(\frac{\partial R}{\partial x_n} \sigma_n \right)^2 \right]^{0.5} \quad (6.1)$$

In this thesis, the uncertainty propagation has been calculated using the EES software which has implemented the standard calculation of uncertainty from NIST according to the guidelines by Taylor and Kuyatt (1994).

6.1.2 Experiment 1

Here, the data acquired during Run 1 is presented; afterwards data interpretation and processing is explained and finally the processed results are given. The first data refers to the charging process. Table 1 gives the pressure increase in the system, after ammonia has been added into water. The pressure inside the plant has been stabilised at 10 psi absolute, which is an indication that a concentration of 30% has been achieved for Run 1 and 5.3 psia in Run 2. Note that the plant has been in vacuum during this process.

The initial vacuum in the system has been 1 psi absolute. This is extracted from the pressure reading before calculating the ammonia concentration. The ammonia is fed in liquid phase through the liquid receiver at the bottom. Therefore, during charging ammonia vapor desorbs from the liquid and increase the pressure in the gas space of the plant.

Table 6.1: Pressure increase during charging and the concentration in liquid phase (Run-1).

Time	16:18*	16:20**	16:30	16:40	16:50	17:15
Pressure read (psia)	1.0	5.94	5.8	6.4	5.5	5.4
y (kg/kg)	0	0.948	0.946	0.954	0.942	0.940
x (kg/kg)	0	0.213	0.210	0.22	0.203	0.199

* before charging (no ammonia inside); ** end of charging.

The calculation of the concentration in vapor and liquid for the data given in Table 6.1 has been done based on the read pressure and ambient temperature using EES software. The pressure was determined by extracting 1 psi from the pressure reading, since the initial pressure after vacuuming has been 1 psi. The code for calculation is as follows:

For vapor concentration y: CALL NH3H2O(128,20+273.15,P,q=1:T,P,y,h,s,u,v,q)

For vapor concentration x: CALL NH3H2O(128,20+273.15,P,q=0:T,P,y,h,s,u,v,q)

The uncertainty of ammonia concentration determination has been calculated based on two types of measurements: 1) starting from weight determination; 2) based on pressure and temperature determinations at equilibrium. The determination 1) is used for the “double-check”

because it actually determines the overall ammonia concentration (in vapor and liquid altogether). Considering that the ammonia in vapor phase has a negligible weight, the overall ammonia concentration and the ammonia concentration in liquid phase should be close. This in fact can be observed from the data given in Table 6.2 where the uncertainty of ammonia concentration from weight measurement resulted a little higher.

Table 6.2: Uncertainty of ammonia-water concentration determination (Run 1).

Uncertainty from weight measurement (overall conc.)	Uncertainty from pressure and temperature measurement
Initial ammonia mass: 30.84 ± 0.01 kg Final ammonia mass: 29.9 ± 0.01 kg Ammonia mass charged: 0.944 ± 0.014 kg Ammonia concentration: 0.32 ± 0.00344	Measured pressure: 0.648 ± 0.05 bar Measured temperature: 293.2 ± 1 K Ammonia concentration: 0.292 ± 0.011 Pressure measurement error influence: 76%

Table 6.3: Temperature readings and calculated input heat flux

Time	T_{21} (°C)	T_{16} (°C)	\dot{Q}_{in} (kW)
18:00	25	25	0 ± 21.68
18:10	28	27	153.3 ± 23
19:00	68.8	50	2883 ± 145.8
19:10	80	34	7053 ± 353.3
19:27	88	34	8280 ± 414.6
20:15	95	35	9200 ± 460.5
20:18	107	39.8	10304 ± 515.7
20:33	109.5	46.1	9721 ± 486.6
20:46	113	44	10580 ± 529.4
20:52	127	61.9	9982 ± 499.6

Note: Sensors notations T_{16} and T_{21} correspond to the diagram from Figure 3.3.

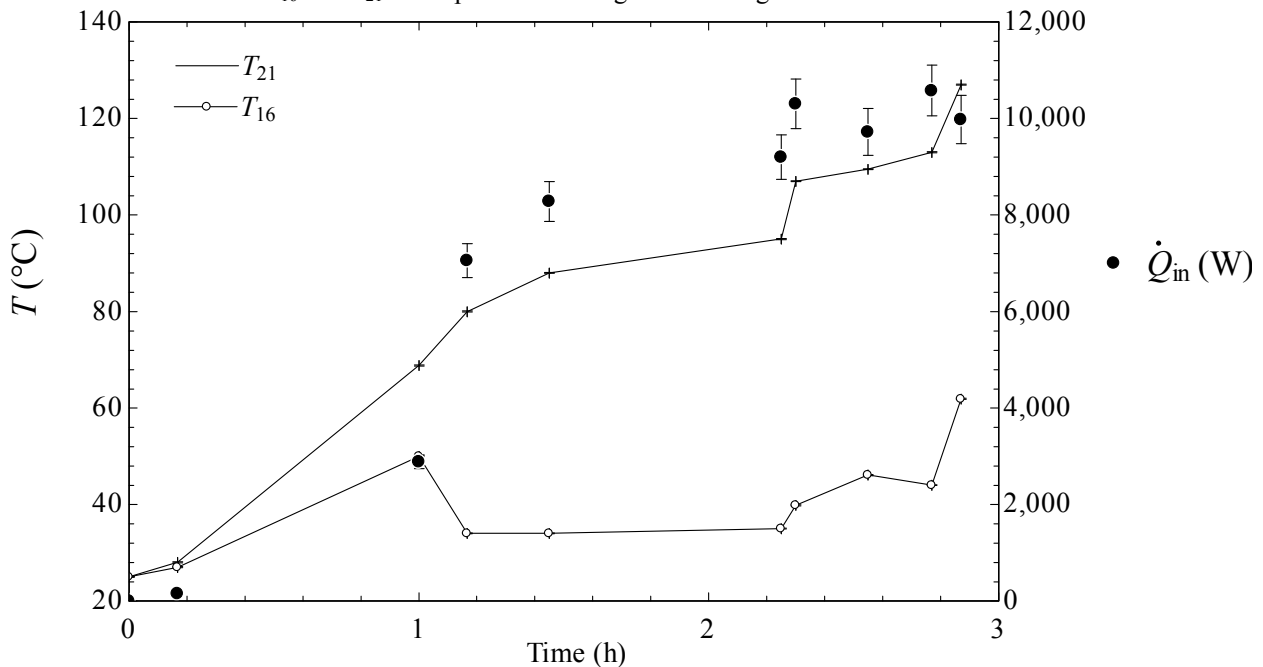


Figure 6.1: Selection of the period of relative steady-state for data processing.

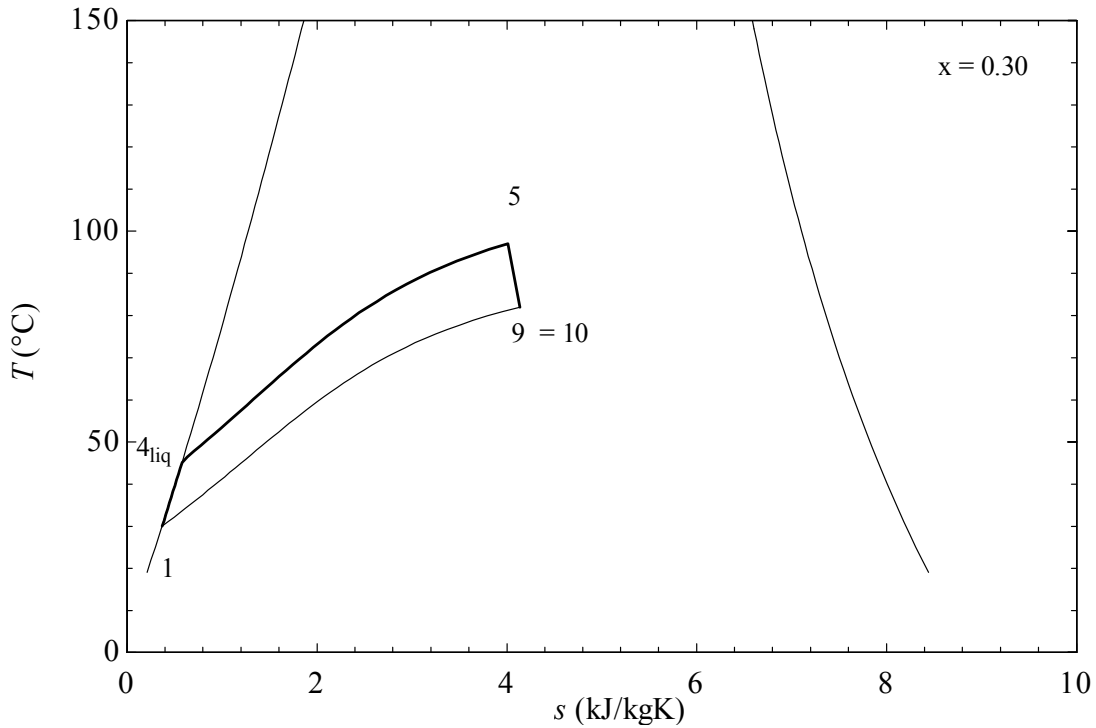


Figure 6.2: Thermodynamic cycle determined for Experiment 1, Run 1.

In the Run 1, the heat input has been maintained at about 10 kW. The expected work output in this condition is of the order of few hundreds of Watt. The start-up heating process is indicated by the data given in Table 6.3. The steady regime has been achieved in the interval approx. 20:30 to 21:00. The achievement of the steady-state regime can be observed from the plot in Figure 6.1 which indicates a minor variation of the heat flux input.

During the steady state, the condensation process evolved at 15.08 psi absolute which corresponds to a saturated liquid temperature of 30°C. With a measured flow rate of water of $\dot{V}_{32} = 34$ lpm and the measured $T_{31} = 18^\circ\text{C}$ and $T_{32} = 21.8^\circ\text{C}$, the condensation heat is $\dot{Q}_{\text{out}} = 10,414$ W. The balance equation on the plant reads:

$$\dot{Q}_{\text{in}} + \dot{W}_{\text{p}} = \dot{Q}_{\text{out}} + \dot{W}_{\text{exp}}$$

where \dot{W}_{exp} is the expander power and \dot{W}_{p} is the pump power.

The pump power is calculated based on measured voltage and current of the power which are 3 V and 0.27 A. The pressure at vapor generator has been $P_5 = 26.9$ psi absolute and temperature $T_5 = 97^\circ\text{C}$, whereas the measured temperature at expander exit has been $T_{10} =$

81.7°C. These values conclude the thermodynamic cycle as given in Table 6.4. The cycle power generation efficiency is around 0.31% while the expander isentropic efficiency is 0.078 ± 0.015 .

Table 6.4: Main results and uncertainty propagation for Experiment 1, Run 1.

$\eta = 0.0031 \pm 0.001$	$\eta_E = 0.078 \pm 0.015$	$h_1 = -60.55 \pm 4.952 \text{ kJ/kg}$	$h_{10} = 1,201 \pm 78.53 \text{ kJ/kg}$
$\dot{V}_3 = 0.56 \pm 0.029 \text{ lpm}$	$\dot{Q}_{in} = 10,580 \pm 529 \text{ W}$	$\dot{Q}_{out} = 10,414 \pm 377 \text{ W}$	$\dot{W}_E = 32.8 \pm 6.5 \text{ W}$

Also, Figure 6.2 shows the thermodynamic cycle constructed based on the data for Experiment 1, Run 1. It is clear that the expansion occurred in two phase, at a vapor quality of about 0.5. Two-phase expansion is well tolerated by the scroll expander. However, one can remark that the flow rate of working fluid was too high. If the pump would be turned at lower voltage, and the flow rate would be low, then higher vapor quality can be obtained and more work produced. Another aspect refers to the very low isentropic efficiency of the expander which reveals some problems with it. As mentioned already in Chapter 4, the expander will be improved after rectification, and better results will be shown for Runs 4 and onwards.

Run 2

This experiment has been similar to Run 1, but with lower ammonia concentration in the process fluid. In this case, ammonia concentration was set to 20% and the same procedure is used for charging. Table 6.5 shows how the pressure and thence the concentration stabilise during the charging procedure. This time, the working fluid pump has been reduced to approx. 1.7 lpm.

The temperature of hot oil has been maintained around 127°C, whereas the colder oil exited the vapor generator at 82°C. The temperature at the expander inlet was 110°C and at expander exit was 71.6°C. The water temperature at condenser exit was 20.5°C. In these conditions, the cycle efficiency has been 1.7% and isentropic expander efficiency 18%.

Table 6.5: Pressure increase during charging and the concentration in liquid phase.

Time	20:28*	20:31**	20:32	20:45	20:57	21:10	21:30
Pressure read (psia)	1.0	5.94	5.8	6.4	5.5	5.4	5.4
y (kg/kg)	0	0.948	0.946	0.954	0.942	0.940	0.940
x (kg/kg)	0	0.213	0.210	0.22	0.203	0.199	0.199

* before charging (no ammonia inside); ** end of charging.

Table 6.6: Main results and uncertainty propagation for Experiment 1, Run 2.

$\eta = 0.017 \pm 0.007$	$\eta_E = 0.18 \pm 0.08$	$h_1 = -7.118 \pm 6.72 \text{ kJ/kg}$	$h_{10} = 1,545 \pm 117 \text{ kJ/kg}$
$\dot{V}_3 = 0.28 \pm 0.014 \text{ lpm}$	$\dot{Q}_{in} = 6,900 \pm 346 \text{ W}$	$\dot{Q}_{out} = 6,783 \pm 377 \text{ W}$	$\dot{W}_E = 118.1 \pm 51 \text{ W}$

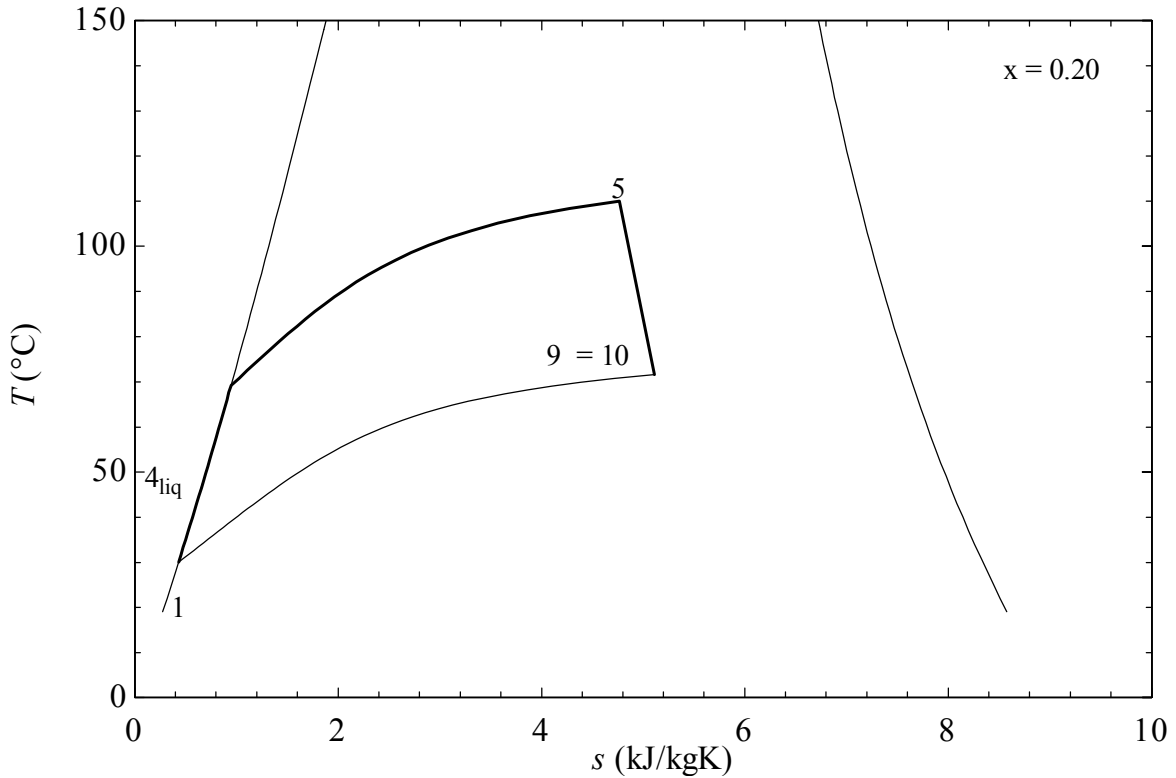


Figure 6.3: Thermodynamic cycle determined for Experiment 1, Run 2.

The thermodynamic cycle determined for Experiment 1, Run 2 is shown in Figure 6.3. The vapor quality at vapor generator outlet is increased to 60%. However, the reduction of flow rate of working fluid correlated with the increase of phase change enthalpy for Run 2 with respect to Run 1 led to a lower performance of the vapor generator which absorbed only 6,783 W as compared to Run 1 when \dot{Q}_{in} was slightly over 10 kW. These aspects show that the heat engine is difficult to tune. Thence, in order to increase the heat input while keeping a low flow rate of working fluid, either the surface area or the LMTD should be increased; however, one should recall that the surface area of the vapor generator is quite high (3 m²).

Run 3

In this experiment, the ammonia-water concentration was only 10%. The procedure of data reduction is similar as for previous ones. Table 6.7 gives the processed data.

Table 6.7: Main results and uncertainty propagation for Experiment 1, Run 3.

$\eta = 0.0249 \pm 0.0069$	$\eta_E = 0.15 \pm 0.04$	$h_1 = 58.43 \pm 7.37 \text{ kJ/kg}$	$h_{10} = 1,694 \pm 117 \text{ kJ/kg}$
$\dot{V}_3 = 0.28 \pm 0.014 \text{ lpm}$	$\dot{Q}_{in} = 7,667 \pm 383 \text{ W}$	$\dot{Q}_{out} = 7,477 \pm 377 \text{ W}$	$\dot{W}_E = 191.1 \pm 53 \text{ W}$

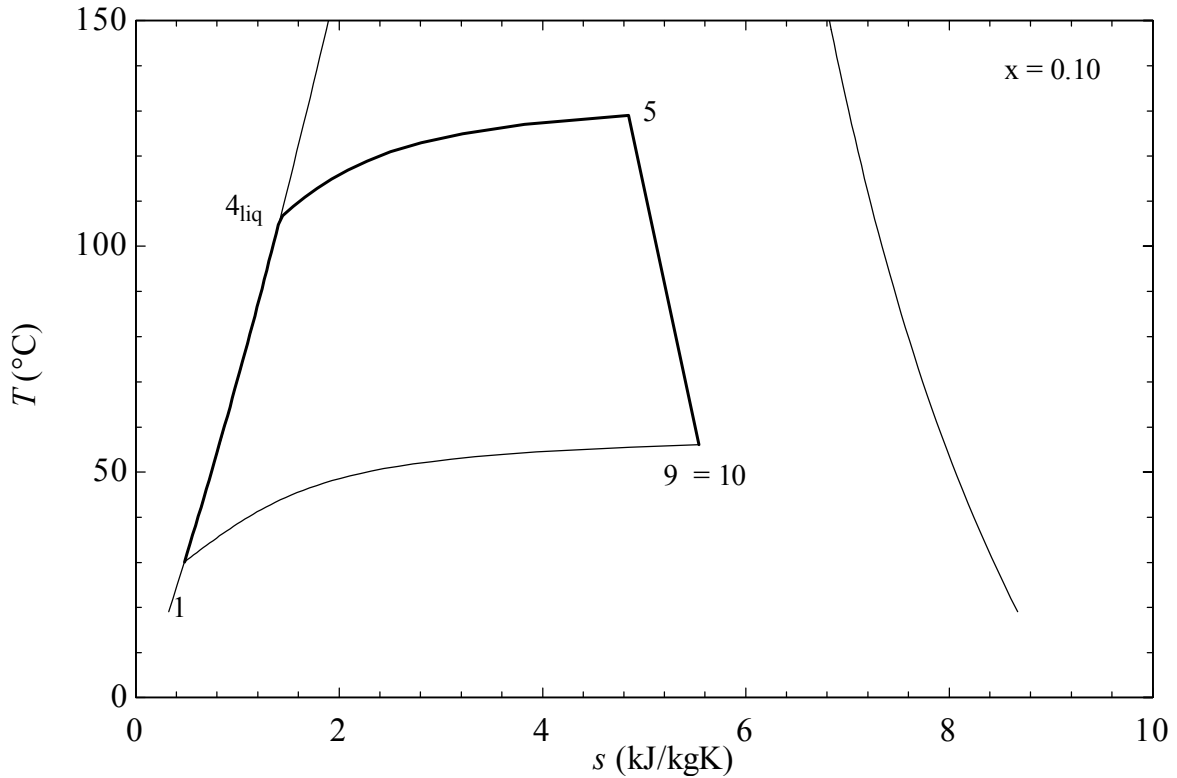


Figure 6.4: Thermodynamic cycle determined for Experiment 1, Run 4.

In Figure 6.4, the thermodynamic cycle determined for Run 3 is shown. The cycle efficiency is much better: 2.49%. However, the expander isentropic efficiency has been lower than before; now it is 15%. The vapor generator absorbs more heat, but still not as much as in the case of the first run. Note that oil heater is constructed such that is able to accumulate very high heat. In fact, it has been observed that even if the heating elements were off, the oil continues to raise the temperature. In fact, in many instances, manual shutting off of the heater has been done such that the temperature of the hot oil could be maintained quasi constant.

Run 4

In this experiment, the condenser has not been used; instead water was feed from a larger vessel, continuously to the vapor generator. The working fluid has been steam. The flow rate of working fluid was adjusted using the needle valve MV₃, as also explained in Chapter 4. Some

fluctuations were observed, related to the improper correlation of the heat input with feed flow rate and expander load.

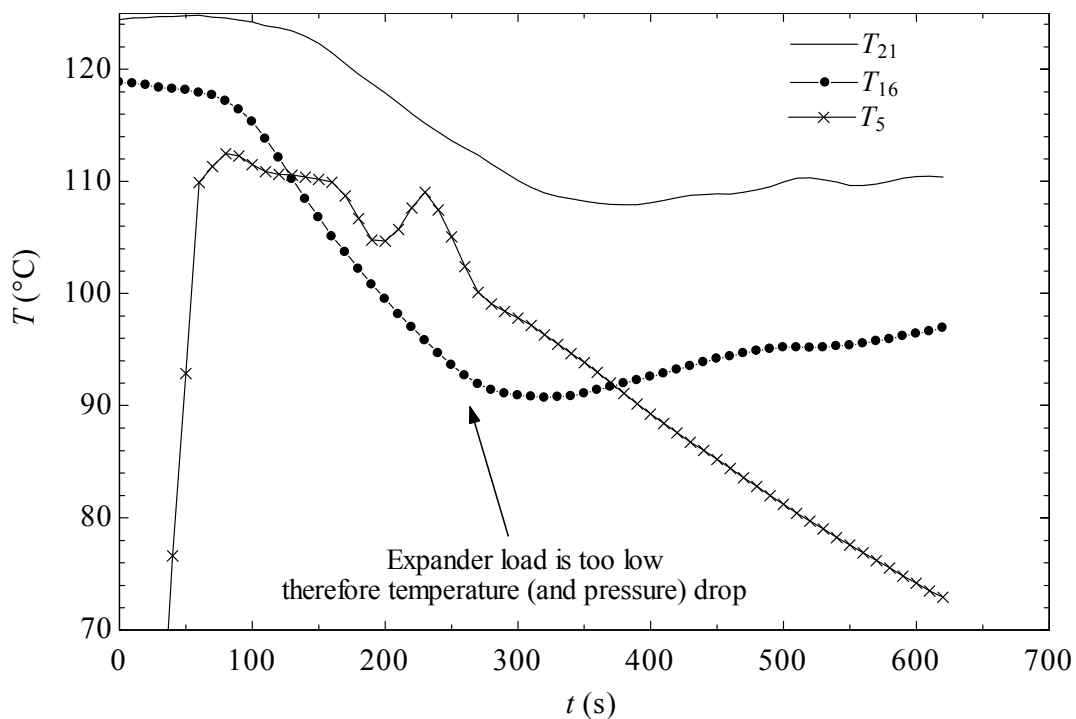


Figure 6.5: One subset of recorded temperature data for Run 4.

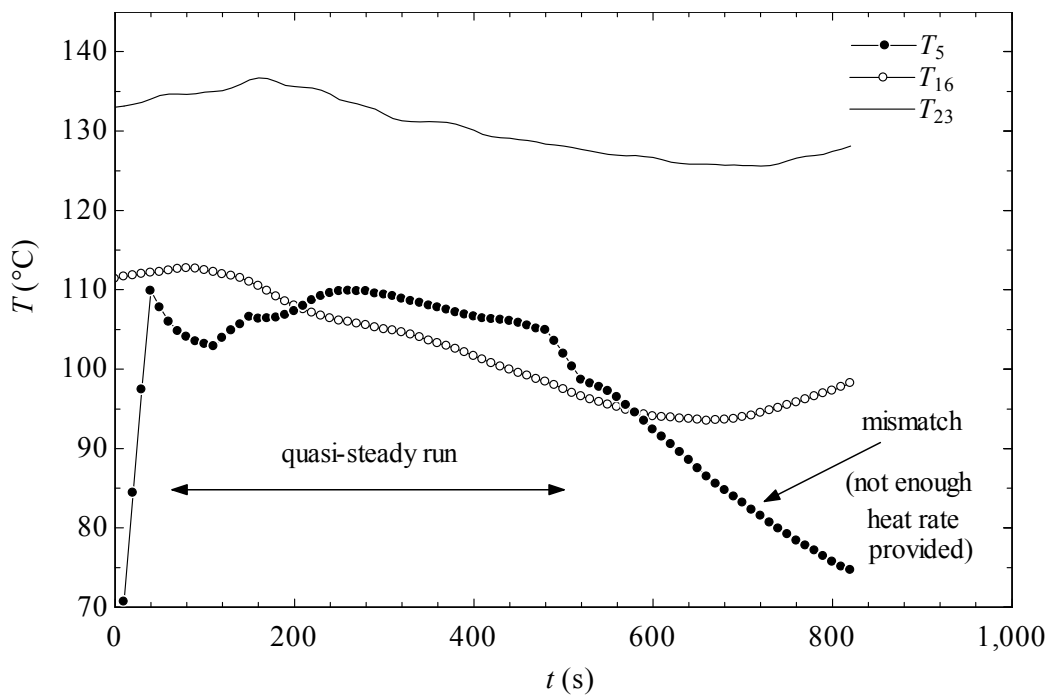


Figure 6.6: Identification of a period of quasi-stable operation for Run 4.

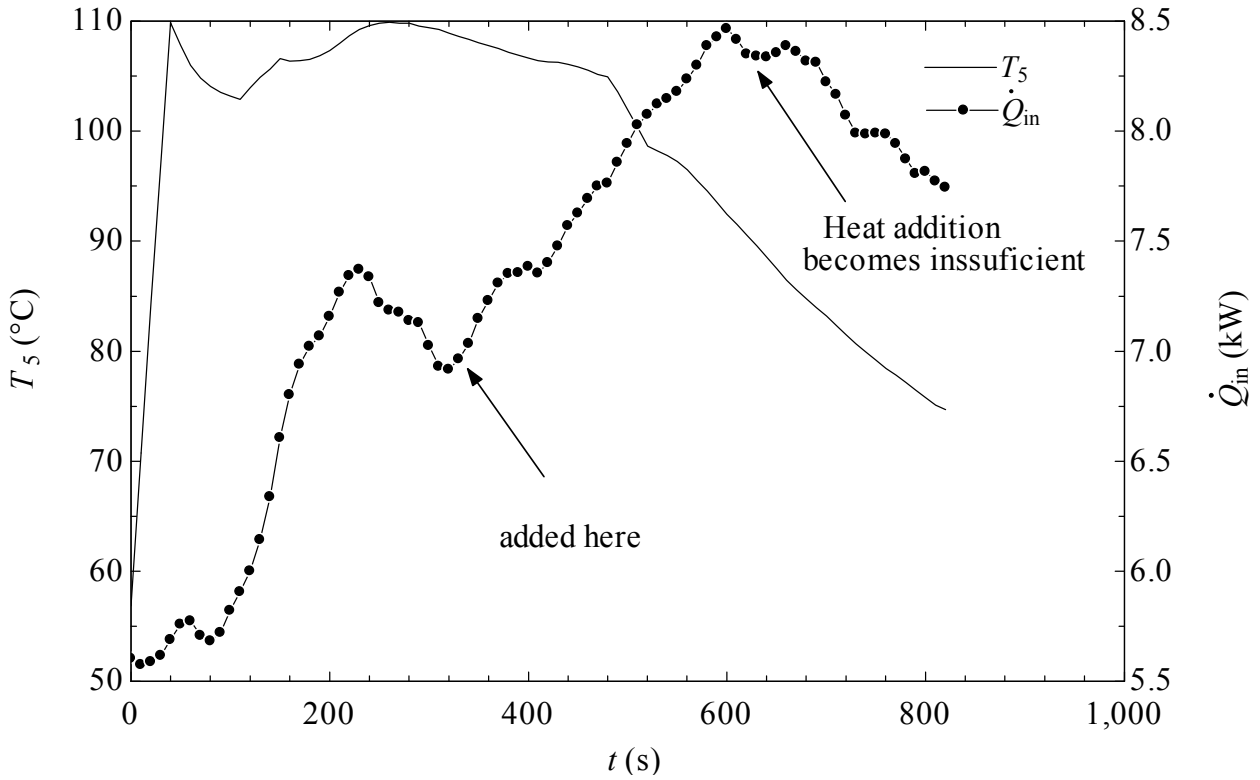


Figure 6.7: Heat input supplementation manoeuvre to maintain steam generation.

If expander load is too low, then pressure decreases and so does the vapor specific enthalpy; eventually vapor become too moist and vapor quality decreases too much. Figure 6.5 shows a situation when the mismatch between expander load, pump flow rate and heat input rate happens. Here, when temperature of generated steam falls close or below 100°C, expander cannot turn because pressure is too low.

Figure 6.6 shows another data record for same experiment. This time, the period when the engine ran was stable it is longer. Figure 6.7 shows a data record which illustrated the heat input supplementation. This manoeuvre has been done to compensate for the demand of heat input needed to maintain stable steam generation. It also shows that if heat input is not sufficient, according to the demand, the vapor generation rate reduces and so does the power generation.

Table 6.8: Main results and uncertainty propagation for Experiment 1, Run 4.

$\eta = 0.0153 \pm 0.0066$	$\eta_E = 0.571 \pm 0.025$	$h_1 = 418.6 \pm 4.33 \text{ kJ/kg}$	$h_{10} = 1,777 \pm 92 \text{ kJ/kg}$
$\dot{V}_3 = 0.38 \pm 0.019 \text{ lpm}$	$\dot{Q}_{in} = 8,433 \pm 422 \text{ W}$	$\dot{Q}_{out} = 8,305 \pm 377 \text{ W}$	$\dot{W}_E = 128.8 \pm 57 \text{ W}$

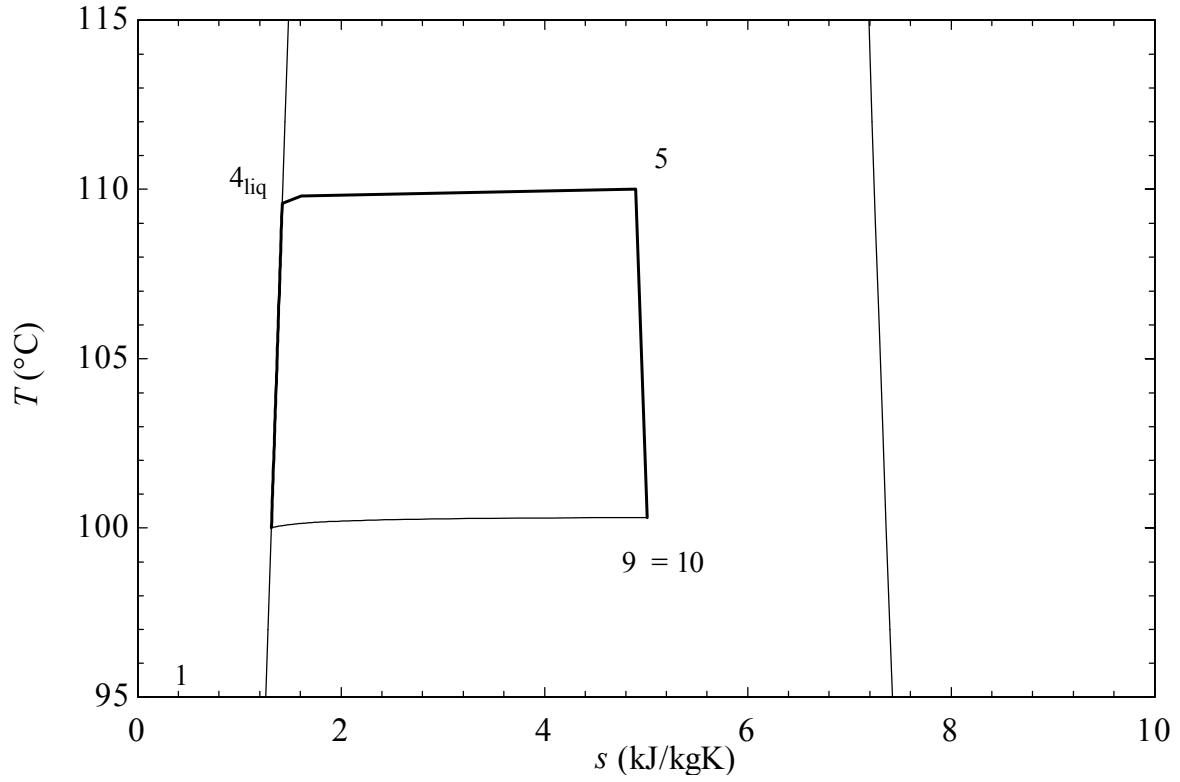


Figure 6.8: Thermodynamic cycle obtained in open loop operation (Run 4).

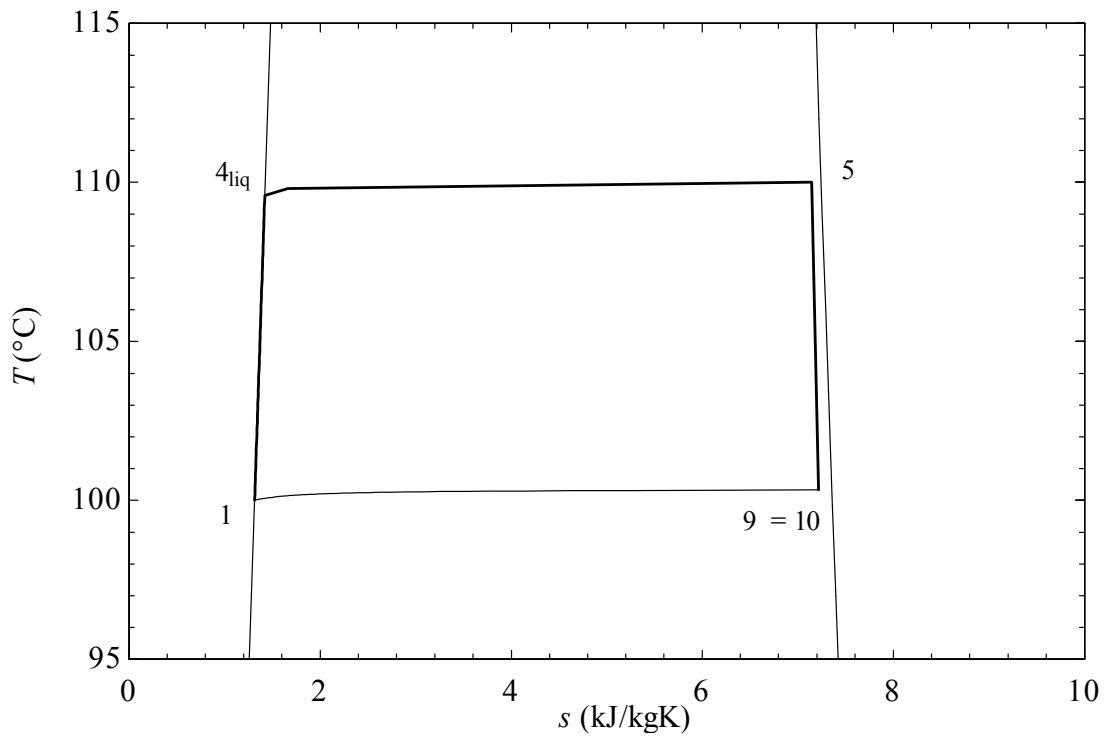


Figure 6.9: Thermodynamic cycle with lower working fluid flow rate and expansion of vapors close to saturation (Run 4).

Table 6.9: Main results and uncertainty propagation for Experiment 1, Run 4.

$\eta = 0.0184 \pm 0.0066$	$\eta_E = 0.68 \pm 0.0241$	$h_1 = 418.6 \pm 4.33 \text{ kJ/kg}$	$h_{10} = 2,626 \pm 150 \text{ kJ/kg}$
$\dot{V}_3 = 0.23 \pm 0.0112 \text{ lpm}$	$\dot{Q}_{in} = 8,433 \pm 422 \text{ W}$	$\dot{Q}_{out} = 8,278 \pm 378 \text{ W}$	$\dot{W}_E = 155.4 \pm 57 \text{ W}$

Table 6.10: Angular speed correlated with pressure drop and pressure ratio for Run 3.

Pressure difference (kPa)	98	70	28
Pressure ratio	1.98	1.70	1.28
Angular speed (RPM)	1300	1000	200

From this experimental run it results that – although the expander performed excellent (with an isentropic efficiency close to 60%) – the cycle has not been at satisfactory efficiency. The reason is due to the fact the heat input was insufficient. When the flow rate at the working fluid pump has been reduced, the cycle conditions became better and the efficiency reached 1.8% as shown in Table 6.8; the cycle corresponding to these data is shown in Figure 6.8. Also, in Table 6.10 the correlation between pressure difference and pressure ratio and expander angular speed is given, for Run 3.

Run 5

In this experiment, the condenser is used but the working fluid is steam. Better efficiency is obtained in this way. Also the heat input was higher because a larger temperature difference on oil side was possible. The power transmitted to the shaft has been 1,251 W. However, there are 20% magnetic field dissipations and also the frictional losses were 20%.

In total, the expander work was 2,086 W. The heat engine efficiency reached 16% and the expander isentropic efficiency 81% as shown in Table 6.11. The angular speed measured was 1707 RPM for a torque of 7 Nm (close to the nominal value of the magnetic coupling, 10 Nm). As seen, the heat input rate this time was about 13 kW. The thermodynamic cycle for this case is presented in Figure 6.10.

Table 6.11: Main results and uncertainty propagation for Experiment 1, Run 5.

$\eta = 0.16 \pm 0.05$	$\eta_E = 0.81 \pm 0.16$	$h_1 = 125.1 \pm 4.17 \text{ kJ/kg}$	$h_{10} = 2,278 \pm 131 \text{ kJ/kg}$
$\dot{V}_3 = 0.23 \pm 0.0112 \text{ lpm}$	$\dot{Q}_{in} = 13,033 \pm 652 \text{ W}$	$\dot{Q}_{out} = 10,948 \pm 378 \text{ W}$	$\dot{W}_E = 2,086 \pm 753 \text{ W}$

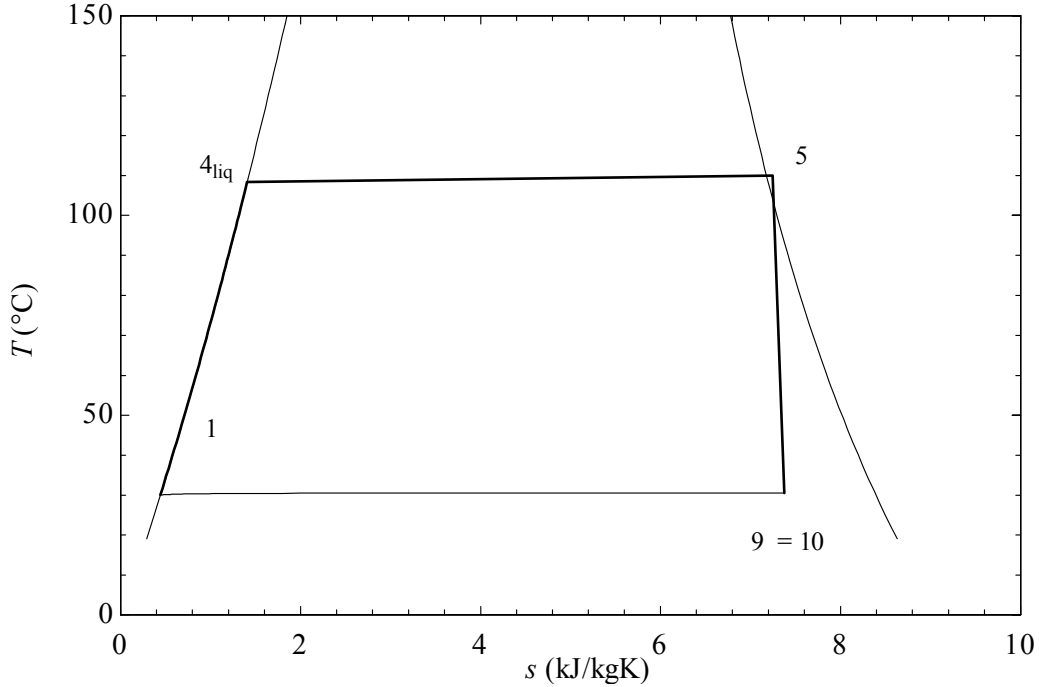


Figure 6.10: Determined thermodynamic cycle for Run 5 (only slight superheating obtained).

Run 6

In this experiment, air has been present into the condenser, such that condenser pressure was of around 0.9 atm. However, the partial pressure of ammonia-water (5%) vapor into the condenser was at vacuum level of 1.6 psi absolute. Although the water vapor condenses at a vacuum partial pressure, the expander discharges to 1 atm. Therefore, the cycle efficiency has been lower since the expander discharged at higher pressure as shown in Figure-6.11. The cooling system primary flow is shown as 5-15-10 whereas secondary flow as 12-13-15.

Table 6.12 gives the processed results for the Run 6. Cycle efficiency was 3% and expander performed well under the imposed conditions with an isentropic efficiency of about 80%. In fact, it has been observed that the expander turns very smoothly even at low pressure differences. For this run, the pressure difference across the expander was only 8.7 psi and the pressure ratio was 1.7. The cooling cycle has been run, but not simultaneously with the power cycle.

Table 6.12: Main results and uncertainty propagation for Experiment 1, Run 6.

$\eta = 0.031 \pm 0.005$	$\eta_E = 0.82 \pm 0.15$	$h_1 = 305.8 \pm 7.45 \text{ kJ/kg}$	$h_{10} = 2,558 \pm 132 \text{ kJ/kg}$
$\dot{V}_3 = 0.355 \pm 0.017 \text{ lpm}$	$\dot{Q}_{in} = 13,033 \pm 652 \text{ W}$	$\dot{Q}_{out} = 12,631 \pm 378 \text{ W}$	$\dot{W}_E = 402 \pm 75.3 \text{ W}$

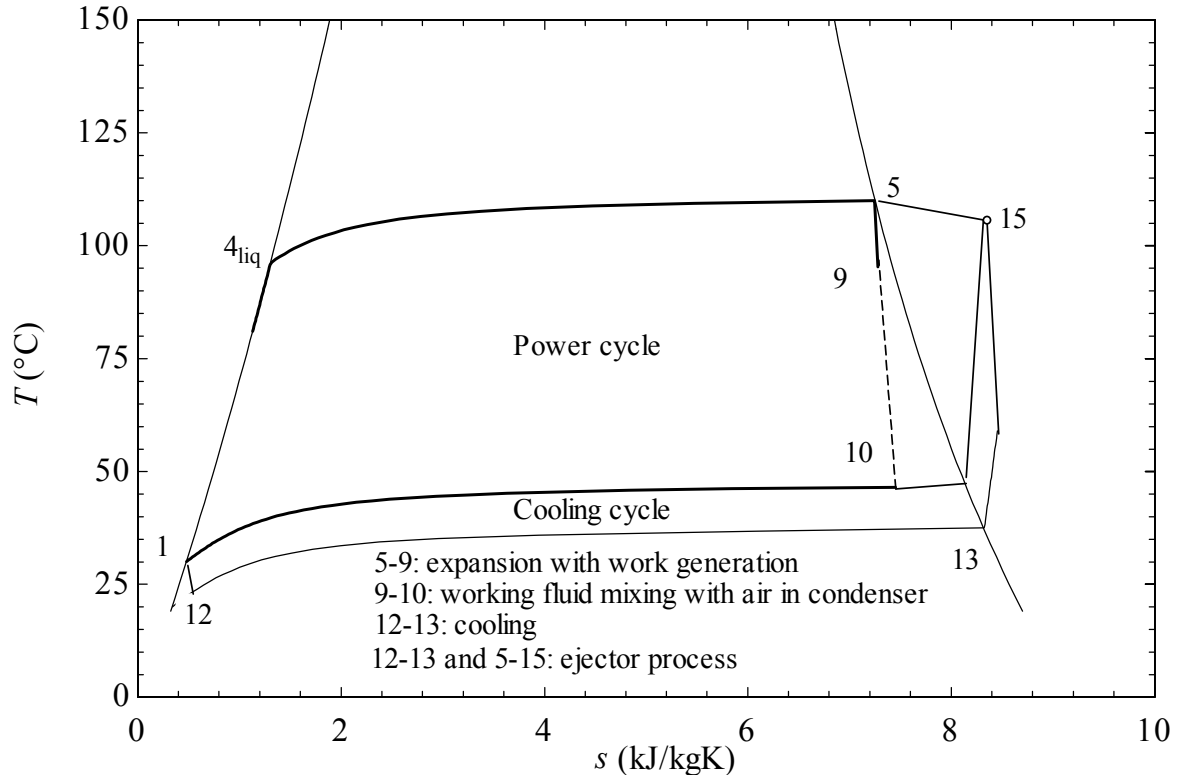


Figure 6.11: Thermodynamic cycle for Run 6 when the condenser had air penetration.

The ejector for cooling cycle worked in an operating condition such that the discharge pressure has been the atmospheric. This is why the cooling was not too deep. The obtained temperatures for evaporation were around 24°C.

Run 7

This experimental run has been done with 28% concentrated ammonia-water. The results for this test are presented in Table 6.13 and Figure 6.12. Only power mode of operation was tested. However, the conclusions of this experiment can be extrapolated for trigeneration mode. Here the cogeneration efficiency is also calculated. Assume that heat is recovered from the condensation/resorption process until the temperature of the working fluid decreases to 60°C. This heat is used therefore for generating hot service water at 45°C.

Table 6.13: Main results and uncertainty propagation for Experiment 1, Run 7.

$\eta = 0.042 \pm 0.0055$	$\eta_E = 0.63 \pm 0.08$	$h_1 = -51.23 \pm 5.4 \text{ kJ/kg}$	$h_{10} = 1,418 \pm 85.5 \text{ kJ/kg}$
$\dot{V}_3 = 0.602 \pm 0.03 \text{ lpm}$	$\dot{Q}_{in} = 13,800 \pm 690 \text{ W}$	$\dot{Q}_{out} = 13,218 \pm 378 \text{ W}$	$\dot{W}_E = 583 \pm 78 \text{ W}$

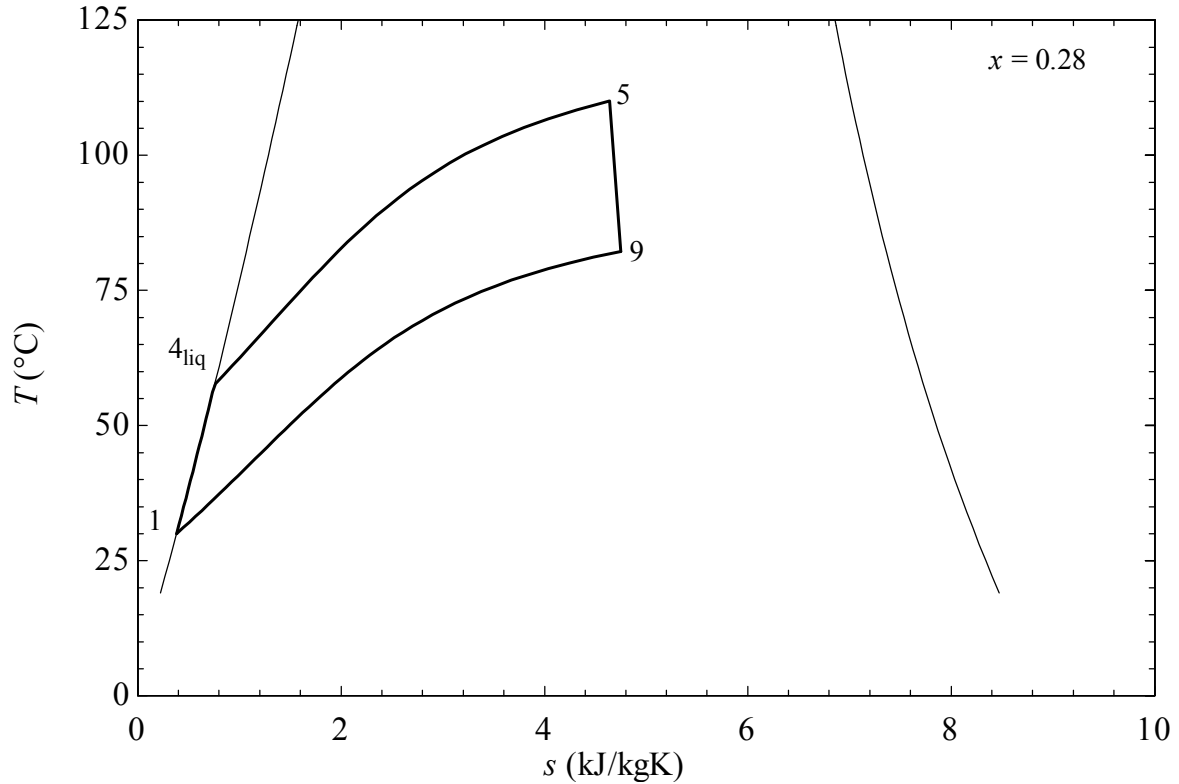


Figure 6.12: Trigeneration cycle data for Run 7.

In these assumed conditions it is determined that the cogenerated heat is $8,336 \pm 452$ W. Therefore, the energy utilisation factor (or energy efficiency of cogeneration) is calculated as follows:

$$\eta_{\text{cog}} = \frac{\dot{W} + \dot{Q}_{\text{wh}}}{\dot{Q}_{\text{in}}} = 0.65 \pm 0.003$$

Looking to the nonlinear temperature profile for condensation in Figure 6.12, it can be concluded that a concentration as high as 0.28 is not a good choice for trigeneration, although, it is an excellent choice for cogeneration.

6.1.3 Experiment 2

The data processing for Experiment 2 involved the determination of the volumetric flow rate of air, the pressure ratio and the pressure difference across the expander as a first step. The area of the duct for measurement of flow rate is 31.18 cm^2 . The flow rate results from multiplication of the measured velocity with the cross sectional area of the duct.

Table 6.14: Expander run with compressed air.

Before rectification					
P_5 (kPa)	AS (RPM)	V_{air} (m/s)	ΔP (kPa)	PR	\dot{V}_{air} (l/min)
222±1.1	641±32	4.1±0.2	120.7±1.1	2.191±0.01	542.4±29.21
194±0.9	403±20	2.66±0.1	92.68±0.9	1.915±0.01	351.9±18.95
192±0.9	381±19	2.41±0.1	90.68±0.9	1.895±0.01	318.8±17.17
188±0.9	377±18	2.43±0.1	86.68±0.9	1.855±0.01	321.5±17.31
179±0.9	347±17	2.33±0.1	77.68±0.8	1.767±0.01	308.2±16.6
176±0.8	322±16	2.31±0.11	74.68±0.88	1.737±0.01	305.6±16.46
172±0.8	293±14	2.15±0.10	70.68±0.86	1.698±0.01	284.4±15.32
170±0.8	274±13	2.05±0.10	68.68±0.85	1.678±0.01	271.2±14.6
166±0.8	262±13	1.95±0.09	64.68±0.83	1.638±0.01	258±13.89
162±0.8	226±11	1.9±0.095	60.68±0.81	1.599±0.01	251.3±13.54
160±0.8	214±10	1.77±0.08	58.68±0.8	1.579±0.01	234.1±12.61
After rectification					
P_5 (kPa)	AS (RPM)	V_{air} (m/s)	ΔP (kPa)	PR	\dot{V}_{air} (l/min)
301±1.5	1295±64	5.58±0.2	199.7±1.5	2.971±0.01	738.2±39.75
285±1.4	1254±62	5.35±0.2	183.7±1.4	2.813±0.01	707.7±38.11
275±1.3	1240±62	5.27±0.2	173.7±1.3	2.714±0.01	697.1±37.54
259±1.2	1165±58	4.54±0.2	157.7±1.2	2.556±0.01	600.6±32.34
253±1.2	1130±56	4.24±0.2	151.7±1.2	2.497±0.01	560.9±30.2
248±1.2	869±435	4.14±0.2	146.7±1.2	2.448±0.01	547.7±29.49
243±1.2	816±40	3.85±0.1	141.7±1.2	2.398±0.01	509.3±27.43
230±1.1	762±38	3.47±0.1	128.7±1.1	2.27±0.01	459±24.72

Table 6.14 gives the data processing for the expander test, before and after scrolls rectification. The test has been done using the set-up described in Chapter 4. The uncertainty propagation due to measurement error has been calculated with EES software. For all the experiments, the temperature in the air is assumed 22°C (temperature in the lab) and the pressure is the standard atmospheric pressure. In the table, PR signifies the pressure ratio, that is P_5/P_0 with P_5 being the pressure at the expander intake.

The isentropic efficiency of the expander is calculated based on the measured data which allow for determination of the reversible work as a first step. In this respect, the working fluid is assumed to be dry air and modeled as a real gas using the equation of state implemented in EES software. Then, the reversible work is calculated as follows:

- the enthalpy and entropy of air at intake is determined:

$$h_5 = \text{Enthalpy}(\text{air}_{ha}, P = P_5, T = 22^\circ\text{C})$$

$$s_5 = \text{Entropy}(\text{air}_{ha}, P = P_5, T = 22^\circ\text{C})$$

- the enthalpy of air after isentropic expansion:

$$h_{9s} = \text{Enthalpy}(\text{air}_{ha}, P = P_0, s = s_5)$$

- the specific volume of air at discharge:

$$v_9 \cong \text{Volume}(\text{air}_{ha}, P = P_0, T = 21^\circ\text{C})$$

- the mass flow rate of air through the expander:

$$\dot{m} = \frac{\dot{V}_{\text{air}}}{v_9}$$

- the reversible work:

$$\dot{W}_{\text{rev}} = \dot{m} (h_5 - h_{9s})$$

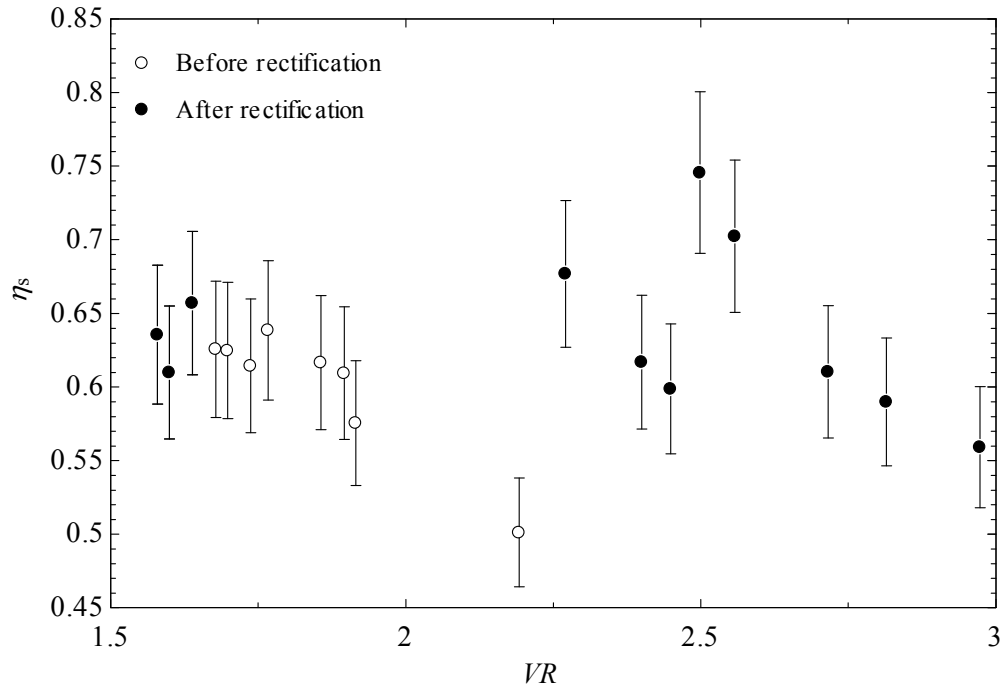


Figure 6.13: Isentropic efficiency before and after rectification.

For calculation of the actual work, the load connected to the expander has to be considered. The actual load consists of the electric generator and all the mechanical system connected to the shaft which produces losses, including magnetic losses and frictional losses. The torque is a consequence of those losses. The torque has been lower after rectification because less friction within the scrolls has been obtained. The maximum torque transmitted by the magnetic coupling is 10 Nm. The actual work has been calculated as follows:

- the angular speed has been determined from AS [RPM]:

$$\omega = 2\pi \frac{AS}{60}$$

- the actual work results from the torque (\mathcal{T}):

$$\dot{W}_{\text{act}} = \omega \mathcal{T}$$

The isentropic efficiency becomes:

$$\eta_s = \frac{\dot{W}_{\text{act}}}{\dot{W}_{\text{rev}}}$$

Figure 6.13 shows that isentropic efficiency of the expander improved after rectification, as correlated with the volume ratio (VR) across expander. The improvement is mainly due to reduction of the friction. In addition to this, the volumetric efficiency has been much improvement. The volumetric efficiency expresses the amount of flow rate which actually generates work with respect to entire flow rate that passes through the expander.

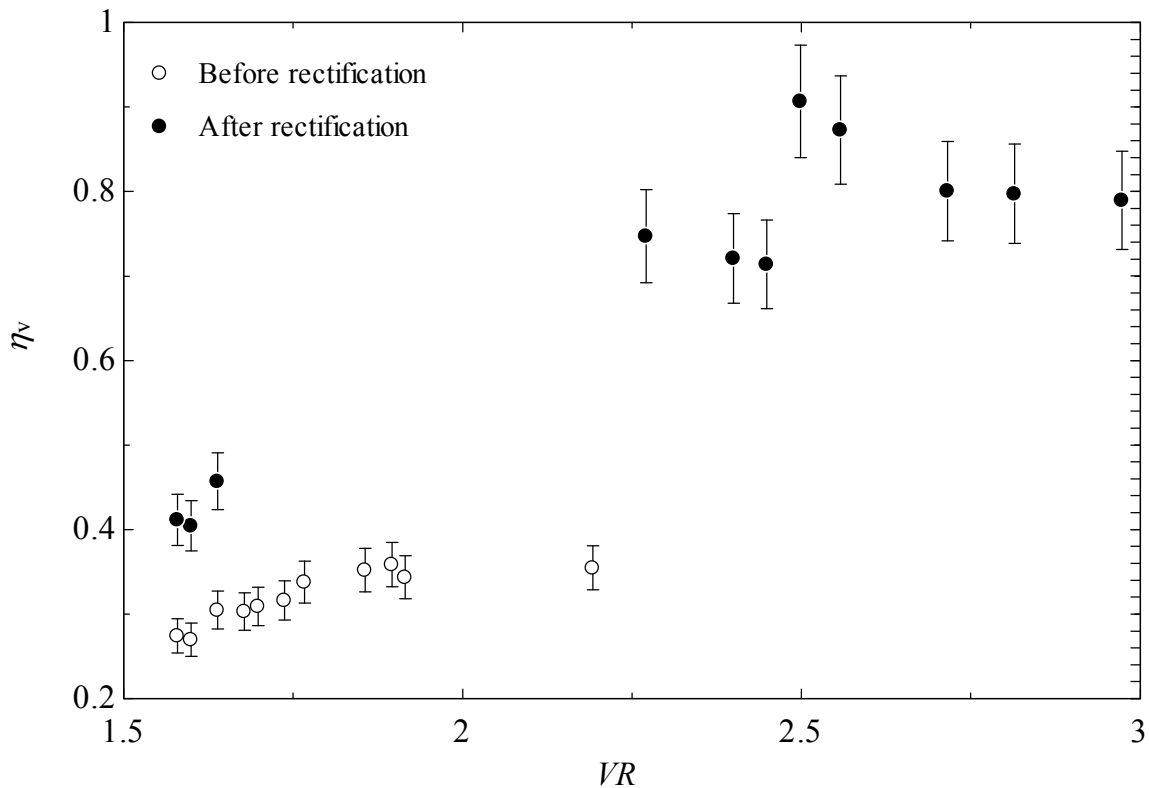


Figure 6.14: Volumetric efficiency before and after rectification.

The volumetric efficiency represents the ratio between the volume of the expansion cavity at discharge and the actual discharged volume at each rotation. The calculations with the data

from Table 6.14 demonstrate that the volumetric efficiency of the expander has been much improved after rectification. The improvement is definitely due to the lower gaps that were obtained. Figure 6.14 compares the volumetric efficiency of the expander before and after rectification.

6.1.4 Experiment 3

The aim of this experiment is two-fold; to determine the entrainment ratio of the ejector under some relevant operating conditions and to study the assembly of throttling valve, cooling coil and ejector. Two working fluids are used, namely pure water and ammonia-water.

Run 1

In this run water is the working fluid. The purpose of the test is to determine the entrainment ratio only. In this respect, water at ambient temperature and pressure is added into the metering cylinder of the setup shown in Figure 4.3.

Compressed air pressure higher than 50 psi gage is provided as the main flow. This flow is choked because the discharge pressure is kept in vacuum. The pressures at the secondary port and at the discharge port of the ejector are measured. The level of water is recorded and plotted against the time to determine the water consumption rate and thence the flow rate of the secondary flow and further the entrainment ratio (ER).

Figure 6.15 shows the data record of level readings for the experiment. This data have been fitted linearly and the rate of level drop determined as 0.19 mm per minute. There is a calibration coefficient of the level meter which is 0.4 ml/min; therefore the flow rate in ml/min has been 0.076 ml/min.

The data processing scheme used to determine the entrainment ratio is as follows:

- the main flow rate is determined based on the known flow coefficient of the ejector. The flow coefficient is $C_v = 0.006$. The flow coefficient is known from the ejector design which has been manufactured from a Swagelok valve with Catalogue flow coefficient of 0.003. The valve modification involved modification of the nozzle with enlargement of the throat area at the exit. The equation used to determine the flow through the choked nozzle is also mentioned in Chapter 5, Section 5.6. Here, we used an equivalent form of it which gives the volume flow rate (state 6 as in Figure 4.3, P_6 and T_6 [K]):

$$\dot{V}_{\text{main}}[\text{lpm}] = 3273 C_v \frac{P_6}{\sqrt{T_6}}$$

- The mass flow rate of primary flow is calculated using air specific volume at discharge conditions and the volume flow rate of main flow calculated as above.
- The liquid water is flashed through the throttling valve (TV in Figure 4.3) via an isenthalpic process; under this assumption the specific volume of the expanded flow is calculated with EES as follows:

$$v_{\text{sec}} = \text{Volume}(\text{steam}, P = P_{\text{sec}}, h = \text{Enthalpy}(\text{water}, P = P_0, T = 22^\circ\text{C}))$$

- The evaporation coil is maintained in vacuum through the ejector which itself discharges in vacuum. The mass flow rate of secondary flow is determined based on the experimental data regressed as shown in Figure 6.15. This gives the volume flow rate which is then divided to the water density.
- The entrainment ratio is therefore determined with the equation:

$$ER = \frac{\dot{m}_{\text{sec}}}{\dot{m}_{\text{main}}}$$

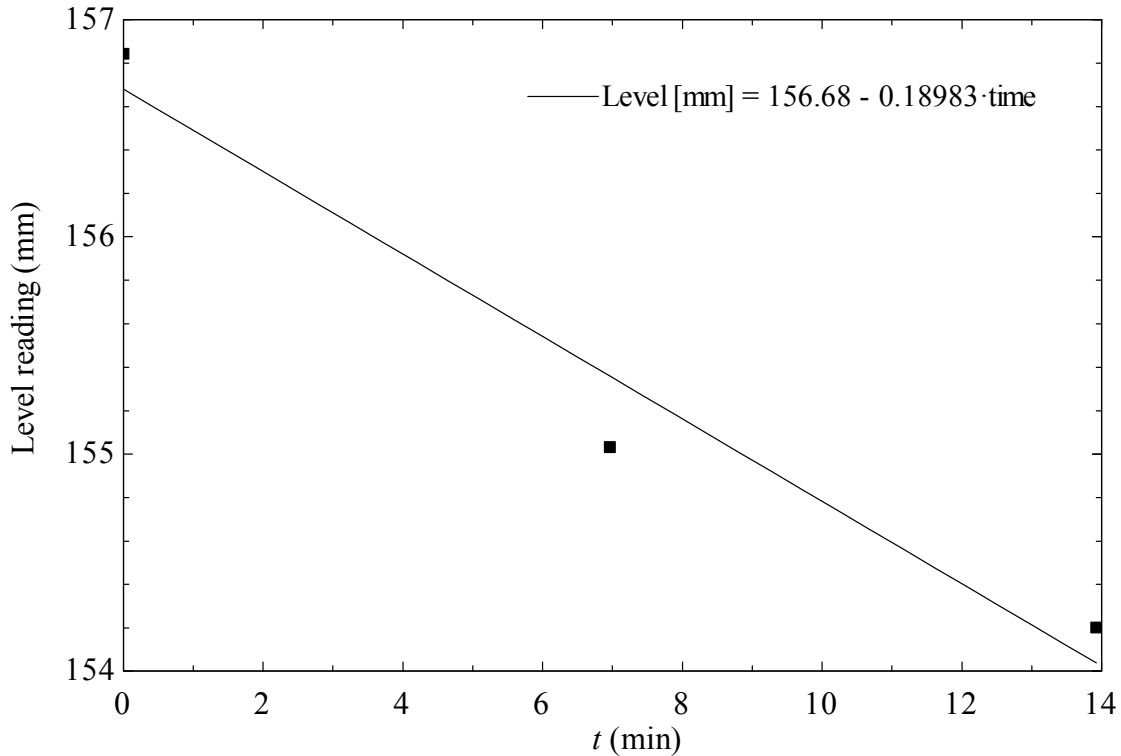


Figure 6.15: Level reading and liner data fitting for Experiment 3, Run 1.

Table 6.15: Calculated data and uncertainty propagation for Experiment 3, Run 1.

Reading or input data	Calculated data
$\frac{dz}{dt} = 0.189 \pm 0.72 \frac{\text{mm}}{\text{min}}$	$ER = 0.175 \pm 0.02$
$P_{\text{sec}} = 1.379 \pm 0.0689 \text{ kPa}$	$\dot{V}_{\text{main}} = 6.676 \pm 0.33 \text{ lpm}$
$P_{\text{discharge}} = 28.96 \pm 1.45 \text{ kPa}$	$\dot{V}_{\text{sec}} = 0.66 \pm 0.003 \text{ lpm}$
	$\dot{V}_{\text{liq}} = 0.42 \pm 0.055 \text{ ml/min}$

Table 6.15 gives the data processing for Run 1. The entrainment ratio has been of 0.175 which is in a reasonable practical range.

Run 2

A second run has been done with the ejector testing, in which ammonia-water is used as working fluid. In this case the test has been done outside the laboratory with the coil exposed under solar radiation. In these conditions, although there was clearly observed heat input, the coil cooled the water in the beaker; the volume of water was approx. 800 ml.

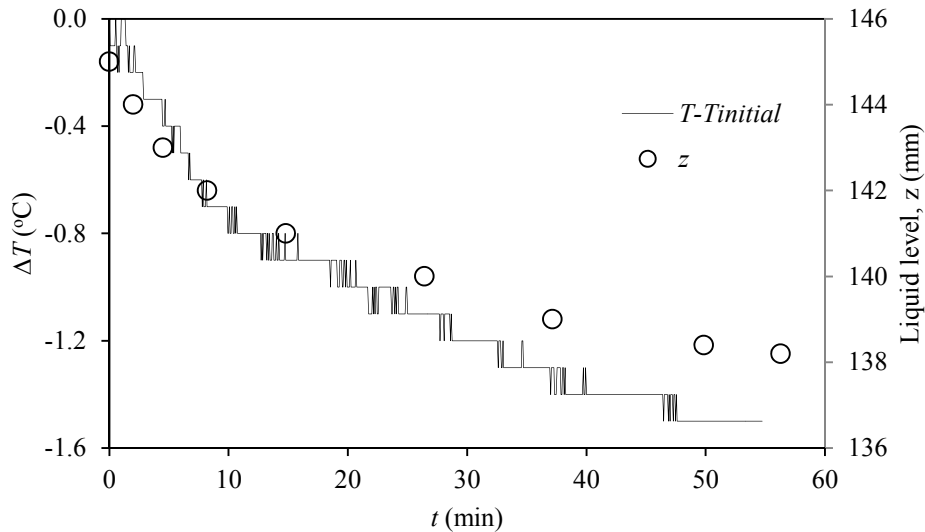


Figure 6.16: Temperature drop and liquid level data recorded for Run 2.

Figure 6.16 shows the experimental records of water temperature in the beaker. Ammonia-water at approx. 40% concentration has been prepared directly into the liquid accumulator of the setup shown in Figure 4.3. The level of liquid refrigerant read in level meter is indicated as the secondary y-axis of the plot.

Table 6.16: Calculated data and uncertainty propagation for Experiment 3, Run 2.

Measured parameter or input data	Calculated data
$\frac{dz}{dt} = 0.367 \pm 0.026 \frac{\text{mm}}{\text{min}}$	$ER = 0.069 \pm 0.001$
$P_{\text{sec}} = 94.46 \pm 0.4 \text{ kPa}$	$\dot{V}_{\text{main}} = 6.676 \pm 0.33 \text{ lpm}$
$P_{\text{discharge}} = 101.4 \pm 0.2 \text{ kPa}$	$\dot{V}_{\text{sec}} = 0.56 \pm 0.005 \text{ lpm}$
	$\dot{V}_{\text{liq}} = 0.81 \pm 0.057 \text{ ml/min}$

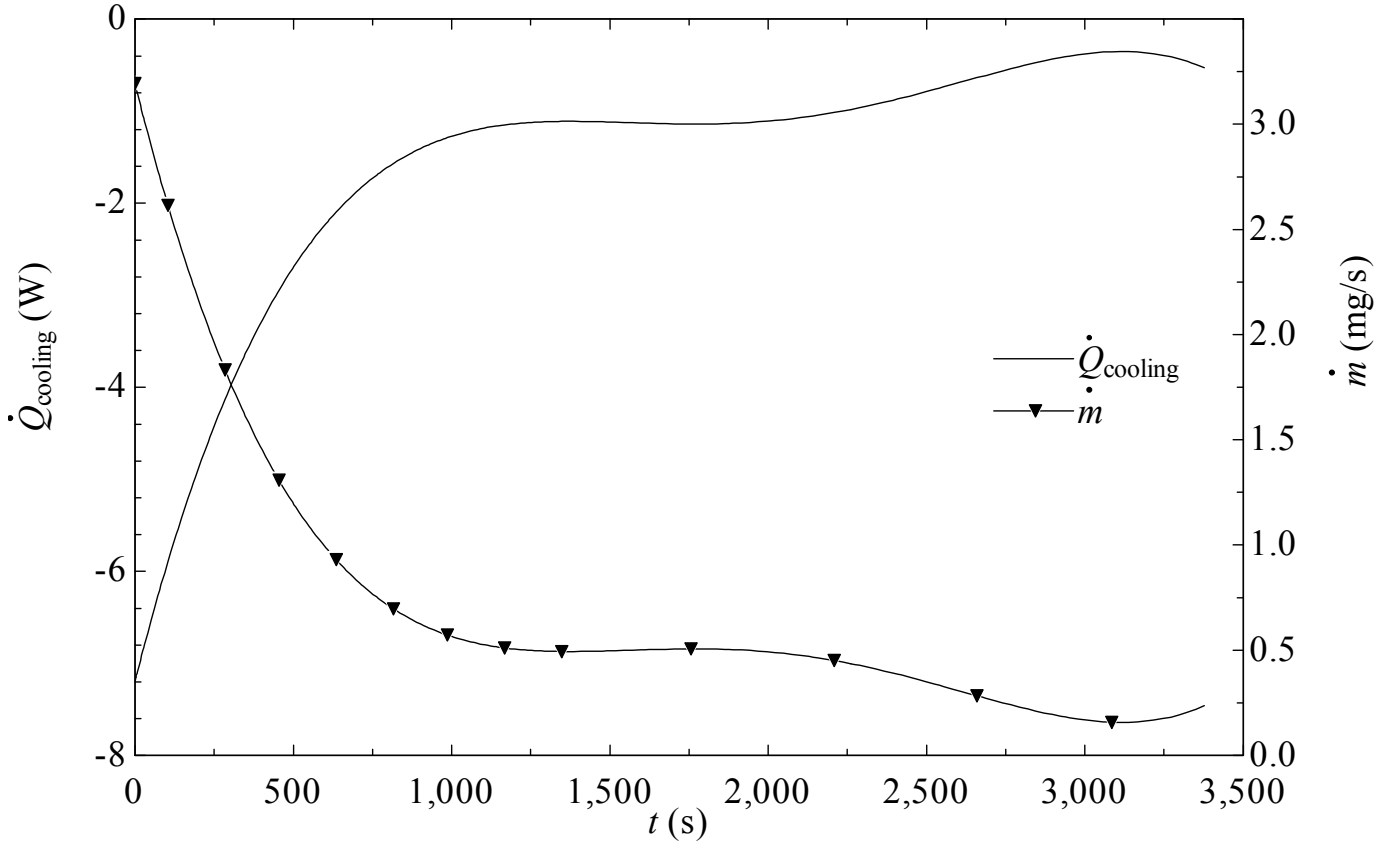


Figure 6.17: Cooling rate and refrigerant mass flow rate determined for Run 2.

The data processing has been made in a similar way as presented for Run 1. Although the level did not varied linearly in time, an approximation is made to regress $z(t)$ as linear. Table 6.16 shows the results. The entrainment ratio of the ejector has been about 0.07. More that processing has been obtained from the curve showing temperature variation in time. Assuming that the heat sink is only the coil, the following energy balance can be written for the cooling process:

$$\dot{Q}_{\text{cooling}} = \frac{dQ}{dt} = m C_p \frac{dT}{dt}$$

Further, the mass flow rate of refrigerant results from the following equation:

$$\dot{Q}_{\text{cooling}} = \dot{m} (h_5 - h_4)$$

where the indexes 4 and 5 correspond to the state points numbered in Figure 3.4 and the enthalpies represent the enthalpy of the throttled fluid (h_4) and of the saturated vapor at the exit of the cooling coil (h_5).

Numerical data has been interpolated with fifth degree polynomials and then integration has been performed to determine the cooling and the mass flow rates. The results are shown in Figure 6.17 and illustrate that the cooling rate was of order of few watts. Although the cooling rate is low (due to the operating conditions), the ejector operates well and its entrainment ratio is in the usual range for cooling applications.

6.1.5 Experiment 4

In this experiment, steam was used as working fluid as described in Chapter 4. The purpose of the experiment is to determine the vapor generator performance and observe the requirements of vapor generator control. In this experiment after sufficient pressure has been achieved in the vapor generator the needle valve MV₅ has been opened to release steam. The measured parameters were:

- Volumetric flow rate of water,
- Temperatures of primary and secondary circuit for the vapor generator,
- Volumetric flow rate of oil.

Three sets of readings were made, corresponding to three positions of the valve MV₅: opened, more opened, even more opened. The results for the vapor generation process were plotted in the T - s diagram as shown in Figure 6.18. The data recorded for this experiment is given in Table 6.17.

The temperature at the hot oil input has been 147°C for Run 1, 135°C for Run 2, and 119°C for Run 3. These runs were performed successively. Due to valve opening the vapor pressure decreased from 204 kPa at Run 1 to 120.8 kPa at Run 3. Of course, the decrease of pressure has been due to an increased consumption of steam. The vapor generator has been operated manually, without controls. Controls are not really necessary at this first phase of testing, however, they have to be implemented in the future.

Table 6.17: Calculated data and uncertainty propagation for Experiment 4.

Run	Measured parameter	Calculated parameter
1	$\dot{V}_3 = 0.243 \pm 0.0168$ lpm $T_5 = 131.4 \pm 0.5^\circ\text{C}$ $T_{16} = 77 \pm 2.3^\circ\text{C}$	$LMTD = 15.27 \pm 0.051^\circ\text{C}$ $\dot{Q} = 10,733 \pm 741$ W $UA = 703 \pm 48.9\text{W/m}^2\text{K}$
2	$\dot{V}_3 = 0.139 \pm 0.0144$ lpm $T_5 = 119 \pm 0.5^\circ\text{C}$ $T_{16} = 98.33 \pm 2.3^\circ\text{C}$	$LMTD = 16.28 \pm 0.06^\circ\text{C}$ $\dot{Q} = 5622 \pm 583$ W $UA = 345 \pm 35.7\text{W/m}^2\text{K}$
3	$\dot{V}_3 = 0.16 \pm 0.0198$ lpm $T_5 = 105 \pm 0.5^\circ\text{C}$ $T_{16} = 89 \pm 2.3^\circ\text{C}$	$LMTD = 16.25 \pm 0.12^\circ\text{C}$ $\dot{Q} = 4600 \pm 560$ W $UA = 283 \pm 36 \text{W/m}^2\text{K}$

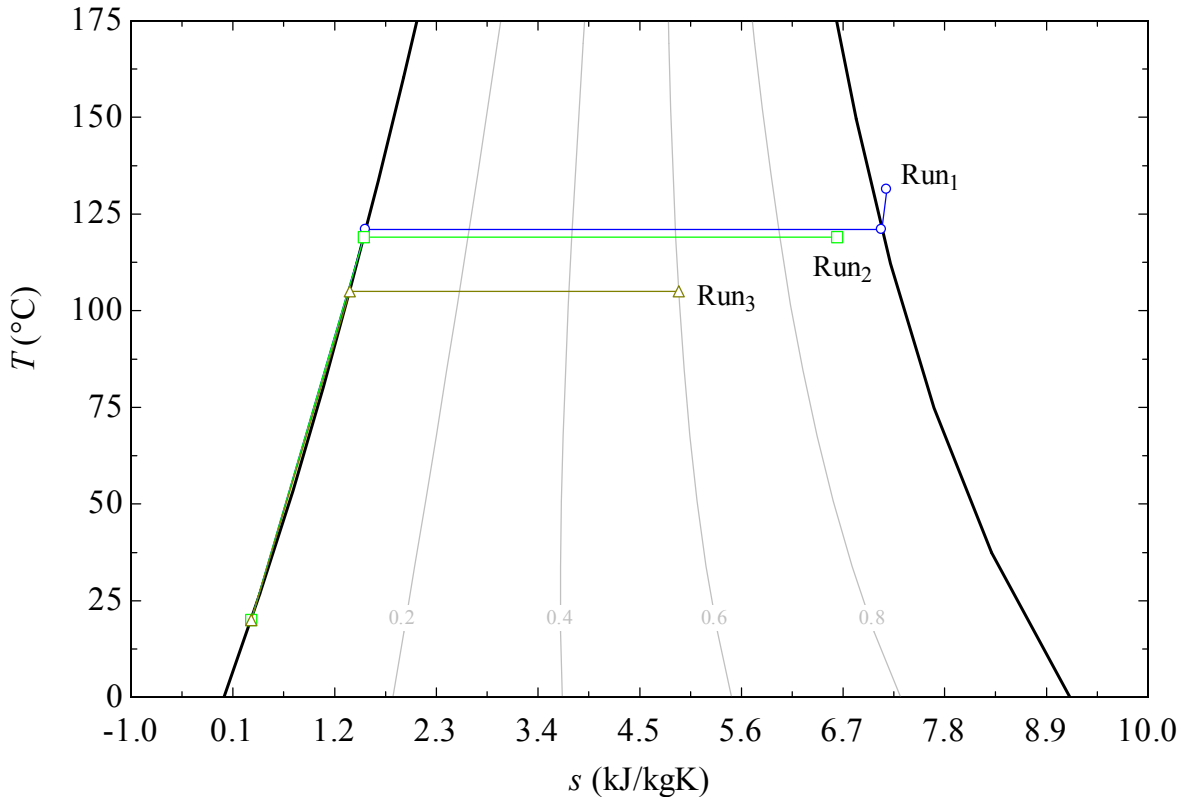


Figure 6.18: Results for vapor generator testing – Experiment 4.

Nevertheless, the main remark from the present experiment is that pressure regulators and controls are a must if the system is further developed. This test also revealed that the surface of heat transfer is sufficient for the vapor generator. The LMTD has been low, approx. 15°C.

6.1.6 Experiment 5

In this experiment, the working fluid pump is tested. This has been needed because in several instances, the pump did not build pressure and in addition, the pump diagram is not provided in

manufacturer's catalogues for the specific operating conditions of the heat engine. The parameters that were measured in this experiment were:

- Pump head,
- Volumetric flow rate,
- Voltage,
- Current.

Table 6.18: Data collected for pump calibration.

ΔP (psi)	\dot{V} (lpm)	V (Volt)	I (Amp)	\dot{W} (W)
15	0.6	24	0.06	1.48
17	0.093	24	0.011	0.26
21	0.051	24	0.010	0.24

Table 6.18 gives the measured and calculated data from this test. From this pump, calibration data it results that the pump energy efficiency (electrical to hydraulic) is approximately 0.7. The table from Table 6.18 is used in EES codes developed here to determine pump operation parameters by using interpolation.

6.1.7 Experiment 6

Oil heater is a custom made unit and requires calibration. As described in Chapter 4, the Experiment 6 objective is to determine the power input to the oil heater for each of the heating segments. The second objective, is to determine the thermal inertia parameters of the oil heater.

Table 6.19: Results from heaters calibration.

Switch	Current	Voltage	Power
1	14.7	110	1617±11.02
2	11	210	2310±21.01
3	20	120	2400±12.04
4	22.5	120	2700±12.05
5	23	120	2760±12.05
6	23.5	120	2820±12.06
7	10.8	210	2268±21.01
8	11	110	1210±11.01
9	22.2	215	4773±21.53
10	10.5	215	2258±21.51
11	30	215	6450±21.55

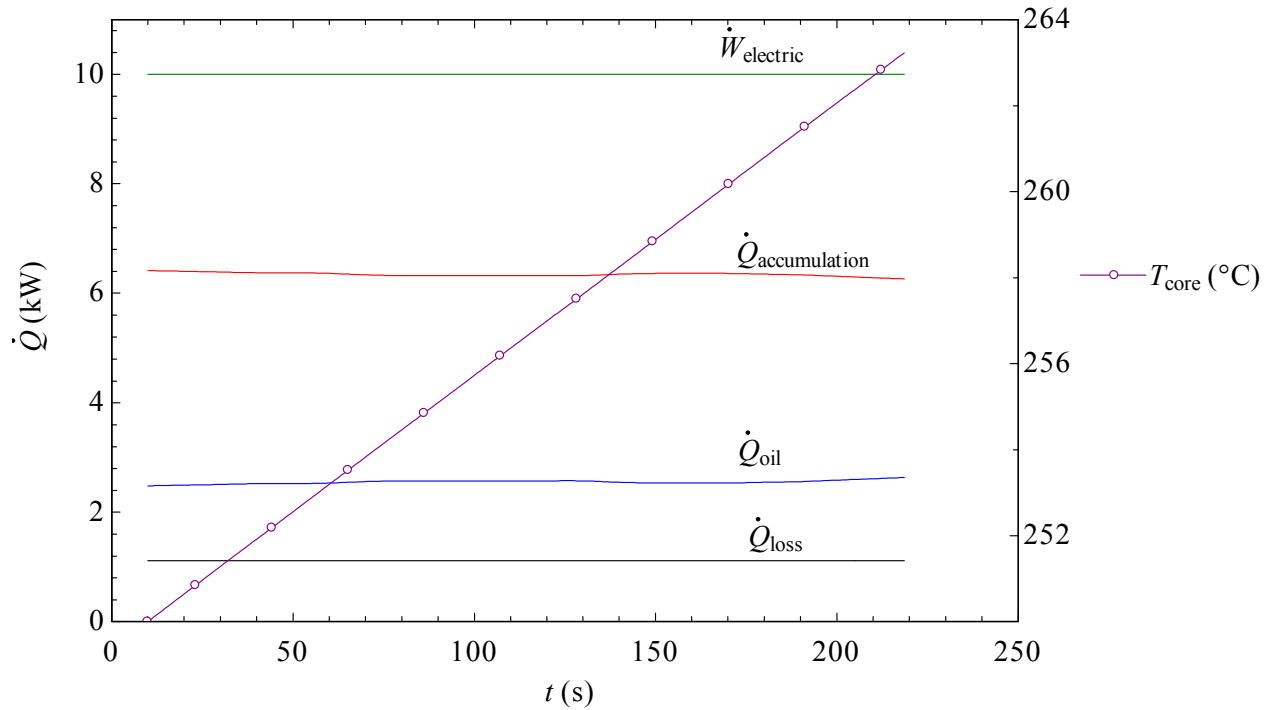


Figure 6.19: Recorded and calculated data for oil heater calibration experiment; the temperature in the ceramic core of the heater is also shown

Table 6.19 gives measured and calculated data for heating elements including the propagated uncertainty for heating rate (\dot{W}). Regarding the thermal inertia, a lumped capacity model is assumed for the oil heater. Denote the thermal inertia parameter for the oil heater with MC_p which represents the product between the mass of ceramic blocks and the specific heat. In this case, the energy balance for the oil heater is (see Figure 3.3 for temperature indexes):

$$\dot{W}_{\text{in}} = MC_p \frac{dT}{dt} + \dot{m}_{\text{oil}} c_{p,\text{oil}} (T_{16} - T_{21}) + h_{\text{tr}} A (T_{\text{surf}} - T_0)$$

The outer heat transfer surface of the oil heater has been determined by area measurements and it is 3.078 m^2 . Based on practical experience with the oil heater, it is remarked that its outer surface temperature is approx. 35°C to 45°C . For the heat transfer coefficient in natural convection a value of $20 \text{ W/m}^2\text{K}$ is assumed.

Figure 6.19 shows calibration data curves for the oil heater. The thermal inertia parameter has been determined and it is $MC_p \cong 100 \text{ kJ/K}$. A sequence of data has been measured giving

the oil flow rate and inlet/outlet oil temperatures. Based on this data and the assumptions introduced above, the energy balance equation for the oil heater has been integrated.

From the results, it is clear that the thermal inertia of the boiler is high. In addition, the temperature of the ceramic bricks is much higher than that of the oil. This reflects the fact observed during the experimentations that oil temperature may increase even if the heating elements are all switched off.

6.1.8 Discussion

This section concludes the Experimental Results chapter of the thesis. The trigeneration system prototype shows that the process is feasible and helped to relax several important assumptions as various important parameters are determined. However, in this work, the prototype was operated manually, without any automated control. This is why the trigeneration system did not show stable operation and often fluctuates. The following aspects resulted from the experimental investigation:

- The newly developed expander operates satisfactory; no lubrication is required as it can be easily lubricated with process working fluid. Moreover, the liquid helps sealing the gaps and improving the volumetric efficiency of the expander. The isentropic efficiency as high as 0.7-0.8 is obtained. The volumetric efficiency is reached 0.8. If too much liquid is provided to the expander through the vapor port, due to incomplete boiling in the vapor generator, the expander stalls, because it cannot flush the liquid at low pressure. However, it does not damage the wrap or other parts and when the liquid drains out it turn again.
- The vapor generator is well sized and operates well. It has a small charge of working fluid as the internal volume is about 0.6 l. However, the vapor generator is difficult to control. Back flow must be prevented by adding a one-way valve. Also, there must be installed a pressure regulator in the vapor line. Many times during the experiment the vapor generator feed was not been correlated with heat input and with vapor consumption. Therefore, in some situations, the vapor generator produced too moist vapors, and in other situations there were not sufficient heat input. The UA factor of the vapor generator was determined experimentally in the range of 300 W/K to 800 W/K.

- The condenser run well, but after some operation failure occurred in the form of a small leakage which could not be repaired. It is recommended that in the future the condenser is redesigned to allow condensation outside the microchannels and cooling from the inside of the microchannels. This will allow for a more effective heat transfer.
- The working fluid pump had an issue with its internal bypass which opened at lower pressure than needed. This problem was partially resolved.
- The ejector has the entrainment ratio of 0.1. However, the ejector in this system has been sized for a small flow rate, which generates cooling of tens of watts; this is done for demonstration only. The prototype allows for a larger size ejector to produce more cooling effect. The ammonia concentration is also very important. The cooling generation works well with ammonia concentration of 5%. Also, it is good to implement ejector cooling with ammonia concentration higher than 8%. In the intermediate range, the direct application of ejector cooling is not effective because the working fluid temperature increases too sharply with heat additions. Special schemes can be applied to investigate this case.
- The energy efficiency for power generation is of few percentages and increases to 60% when cogeneration is applied; also, trigeneration improve the system efficiency.

6.2 Modeling and numerical simulations

In this section, modeling results for expander and the trigeneration systems is presented. Based on these models, several codes for numerical simulations were elaborated for further use in system design, parametric studies and optimisations.

6.2.1 Expander geometrical simulation

A geometrical processor has been elaborated to simulate the scrolls geometry and determine volumes and leakage gaps for the expander. The code is written in EES software in complex algebra programming mode. The analysis theory presented in Section 5.3 is completely applied. The most parts of the code are based on the analytical formulations of Blunier et al. (2009).

The first use of the code is for identification of the geometrical parameters of the actual scrolls that are used in the expander. As explained above, these scrolls originate from a Bristol

scroll compressor. The scroll geometry is defined completely when the following parameters are known:

- The base circle radius,
- The inner involute initial angle,
- The exterior involute initial angle,
- The inner involute starting angle,
- The exterior involute starting angle,
- The maximum angle (or the rolling angle).

Table 6.20: Determined geometrical parameters of the scroll wrap.

Parameter	Value
Initial angle of the external involute	$\varphi_{e0} = 0.78635$ rad
Initial angle of the interior involute	$\varphi_{i0} = 2.035$ rad
Starting angle of the external involute	$\varphi_{es} = \varphi_{e0} + 2\pi(140/360)$ rad
Starting angle of the internal involute	$\varphi_{is} = \varphi_{i0} + 2\pi(80/360)$ rad
Rolling angle	$\varphi_{max} = 20.5867$ rad
Vane thickness	$e = 3.25$ mm
Pitch	$p = 16.35$ mm
Base circle radius	$r_b = 2.602$ mm
Orbiting circle radius	$r_o = 4.925$ mm
Height of the vane	$h = 28.1432$ mm
Radial gap	$\delta_R = 0.076$ mm

None of the above parameters are measurable. Therefore, a procedure has to be established to determine these parameters based on other measurable parameters. In fact, an image superposition using computer graphical tools is also required to determine the starting angles of the scroll. The following geometrical parameters can be measured from a scroll

- Vane thickness, e ,
- Pitch, p , or the distance between two vanes after a complete turn of 360° .

The procedure elaborated here for geometry identification of the scrolls starts as follows:

- The radius of the orbiting cycle r_o is determined right away from $p = 2(r_o + e)$,
- Introduce the parameter $\Delta\varphi = \varphi_{i0} - \varphi_{e0}$,
- The following equation relates $\Delta\varphi$ to base circle radius $e = r_b \Delta\varphi$,
- The following equation also relates $\Delta\varphi$ and r_b : $r_o = r_b(\pi - \Delta\varphi)$,
- When the above equations are solved the unknown $\Delta\varphi$ and r_b are determined,

- Now the initial angle of the external involute and the starting angles must be determined; this is done by image superposition.

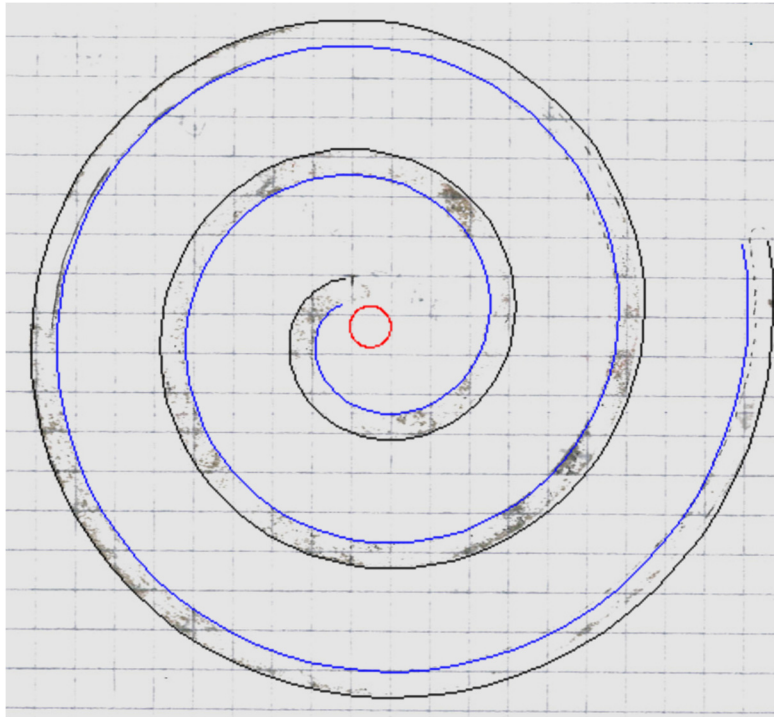


Figure 6.20: Superposition of the actual scroll vane with the modeled scroll.

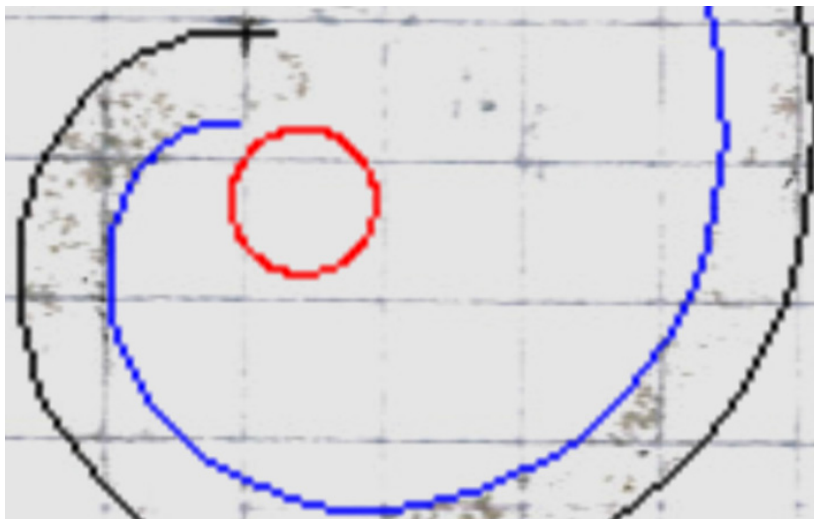


Figure 6.21: Zoom showing the superposition of the actual and modeled scroll for determination of starting angles.

The determinations made according to the procedure explained above are summarized in Table 6.20. The superposition results are shown in Figures 6.20 and 6.21. The computer code generated the spiral shown in Figure 6.20. The actual scroll impregnated with oil has been printed on a paper. The two scrolls are superimposed. In order to achieve the superposition, one single parameter has been varied, namely the initial angle of the external involute.

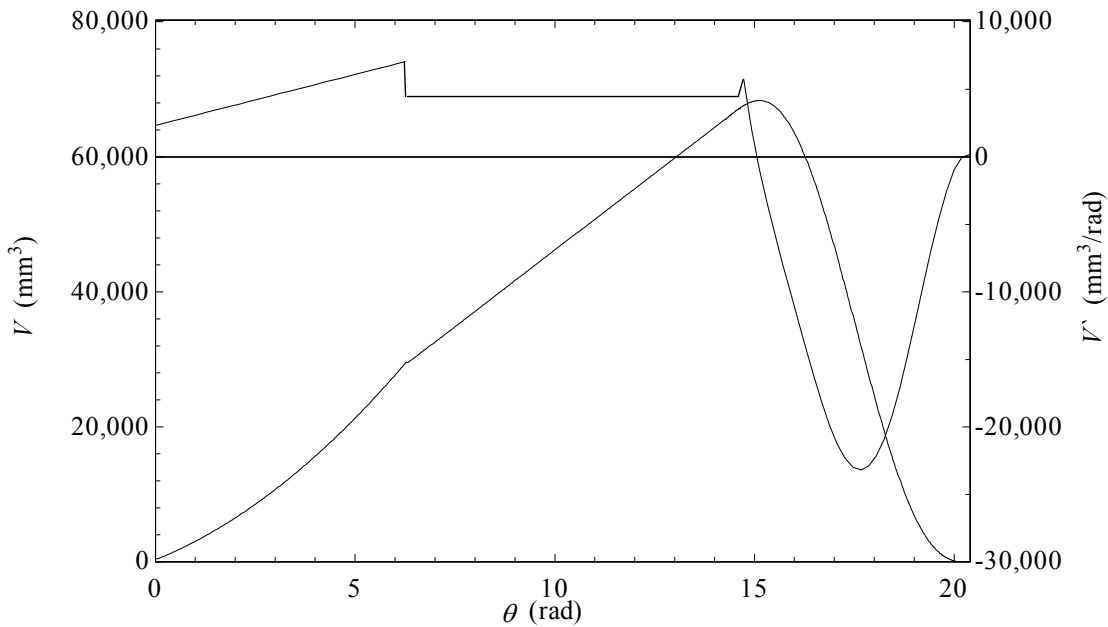


Figure 6.22: The chamber cavity volume and the derivative $V'(\theta)$ of the actual expander, determined based on numerical simulation of the expander geometry.

Table 6.21: Expander functional parameters resulted from the geometry simulation.

Parameter	Value
The chamber volume at the beginning of the expansion	27.191 ml
The chamber volume at the end of expansion (total)	65 ml
Built-in volume expansion ratio	2.4
Angle at the beginning of expansion	6.287 rad
Angle at the end of expansion	14.187 rad

After the initial angles were determined, the starting angles are found as shown in the zoom from Figure 6.21. Once the geometry of the actual expander is known, then the volumes of the chamber during the intake, expansion and discharge are determined using the appropriate algebraic equations implemented in the code, according to the theory presented in the Analyses section. The main result of the geometric simulation is represented by the variation profile of

chamber volume with the rotation angle θ ; this is $V(\theta)$. In addition, the derivative of $V(\theta)$ with respect to θ is required for a thermodynamic modeling of the expansion, that is $V'(\theta)$ as indicated in Figure 6.22.

6.2.2 Expander thermodynamic simulation

The volume chamber data variations derived and the parameters from Table 6.21 are used now as inputs in the thermodynamic model for expander simulation. The thermodynamic model is explained with the help of Figure 5.10 from the Analyses chapter.

Here, the experiments with compressed air are used to validate the thermodynamic model. In these simulations, the discharge pressure is the atmospheric and two pressure ratio were considered as:

- A pressure ratio of 2.6 that corresponds to the built-in volume ratio,
- A smaller pressure ratio of 1.2 which corresponds to over-expansion inside the chamber.

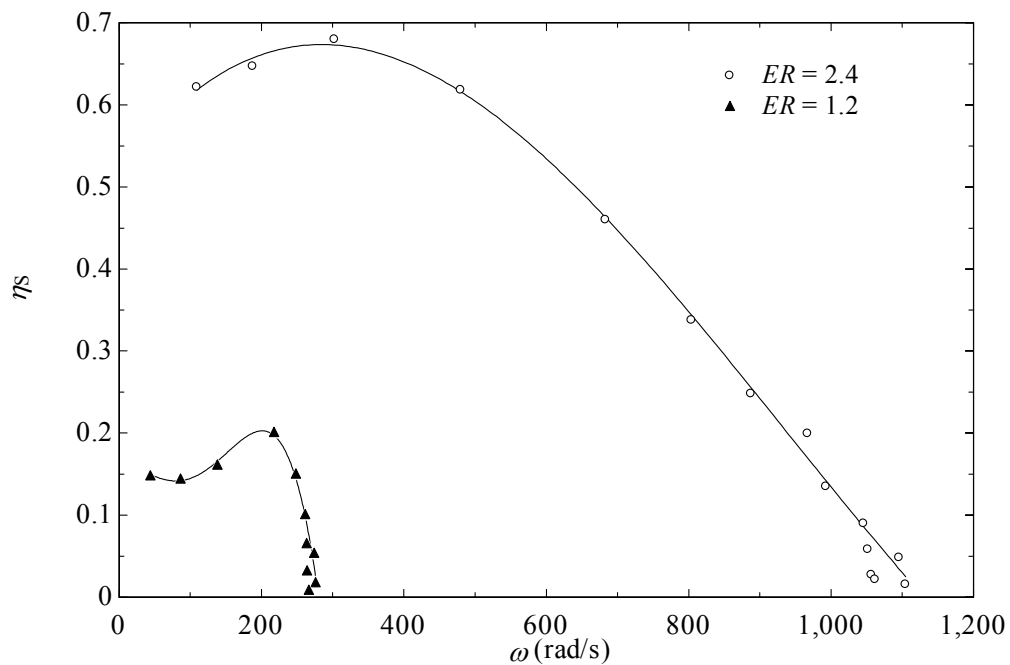


Figure 6.23: Results of expander simulation with air and validation with experimental data.

Figure 6.23 shows the results of expander simulation when working fluid is air. Data from experimental tests with air is used to validate the results. If the expansion ratio departs from the built-in volume ratio, the expander isentropic efficiency degrades much. Nevertheless,

the isentropic efficiency of the expander decreases very much if the expander operates in under expanded or over expanded condition.

6.2.3 Trigeneration cycle simulations

The experiments were successful in providing the working parameters of the vapour generator, the expander, and the condenser. Mainly, the temperatures and pressures that were achieved with the custom made boiler and expander. From these values, a working model was created to show the performance of the engine under ideal conditions. However, the isentropic efficiencies were considered to better approximate the results. The modeling assumed a mass flow rate of 1 kg/s for ease of understanding, however proportionally lower results should be expected in reality, the system was successful with about 0.0017 kg/s, meaning that about 0.17% of the values determined here would be used as a reference in a complete working prototype as the one which was built. During the experiments, the main findings were that the temperature at the boiler exit could reach a maximum of about 135 °C, the steady run pressure at the expander inlet could reach 47 psi, also the room temperature remained at about 22°C.

Figure 6.24 shows the cogeneration efficiency as a baseline, the efficiency of the system in the working conditions found from experiments, was approximately 67%. This is by using the steam to generate power completely. In the figure, the mass flow rate represents a percentage of flow diverted into the ejector, for example at 0.4, 40% of the steam is diverted to the ejector while the other 60% is supplied to the expander. The amount of new useful energy coming from the trigeneration system is in the form of cooling which has a significant value because steam from a common source is directly used to generate cooling, here cooling is provided directly from heat without the use of a compressor or other expensive machines used in cooling. When all the steam is diverted to the ejector the COP approximates 1, where almost all of the energy input from the heat and the pump is converted into cooling.

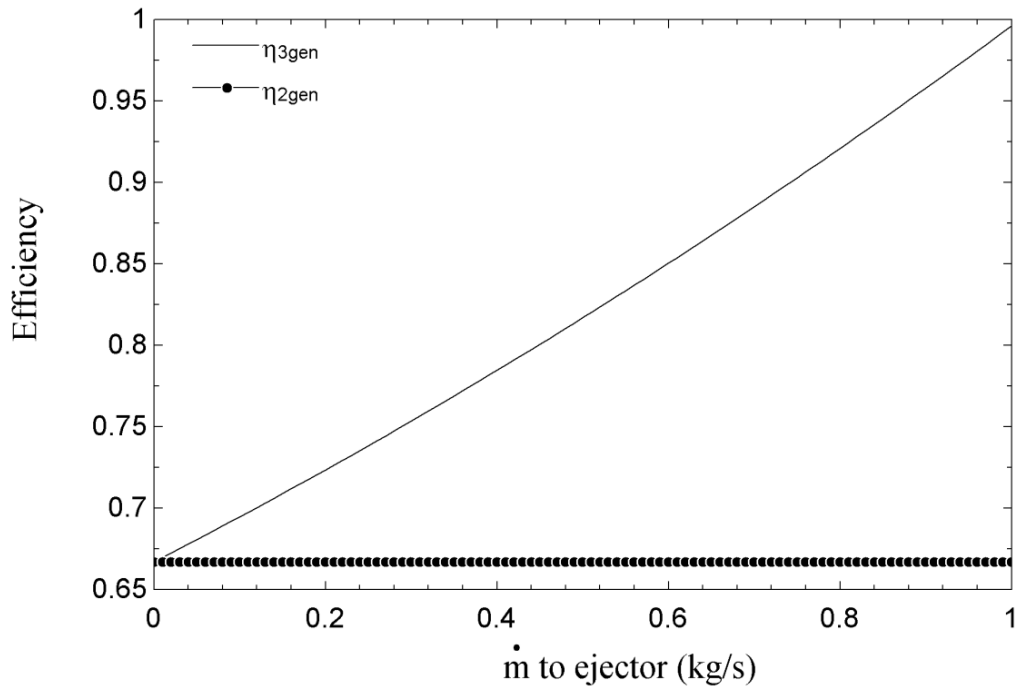


Figure 6.24 Efficiency comparisons between cogeneration and trigeneration

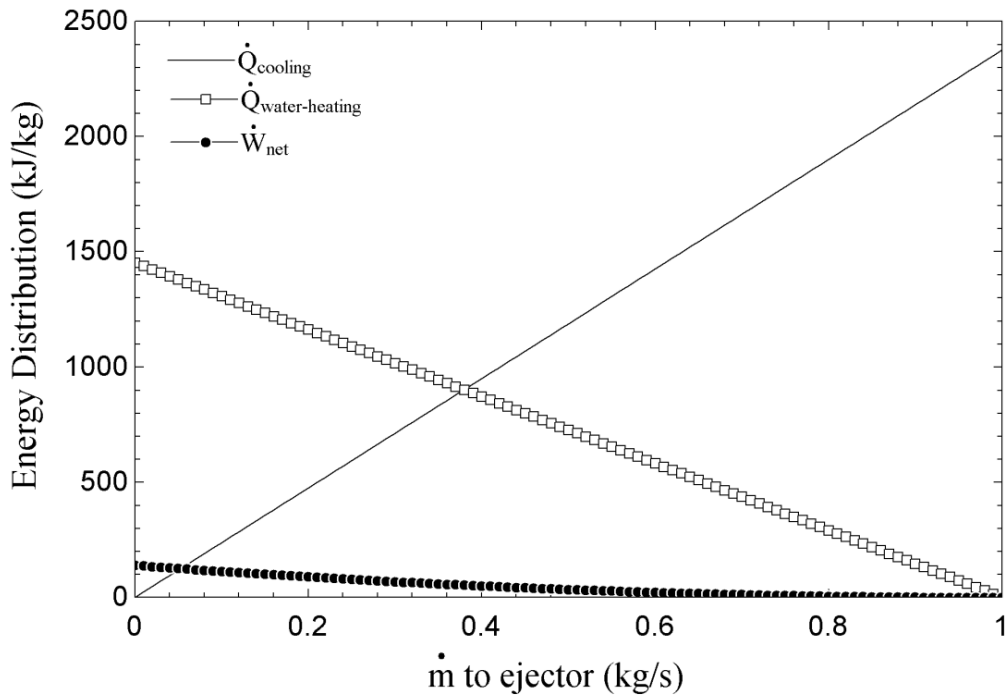


Figure 6.25: Energy distribution dependant on the mass flow diverted to the ejector

The operation of the trigeneration system can be adjusted depending on the most valuable resource of our requirement. For example; during winter heating is of most importance, cooling becomes primary in summer, and power dominates during peak hours. Figure 6.25 shows how the energy can be divided and controlled by simply varying the percentage of flow into the ejector. The system is cogenerating at 0% and only cooling is then generating at 100%, in between the system becomes trigenerating. The useful power output, although relatively low, decreases very slowly across the trigeneration region which proves to be viable in terms of being able to cool without sacrificing much electricity supply. In addition to this the heat output and cooling vary inversely which is very useful as was previously stated when using the system during winter versus summer. There is also a point of interest at about 40% flow diversion, where vast amount of cooling and heating are generated while working with 36% of the original power output from the expander. The dominant disadvantage is that great amounts of cooling higher than 1000 kW when working with 1 kg/s main mass flow rate will result in a big sacrifice in power output. Note that the values can be appreciated as specific heats and specific power since a total of 1 kg/s was used and the diversions to the ejector were represented in percentages.

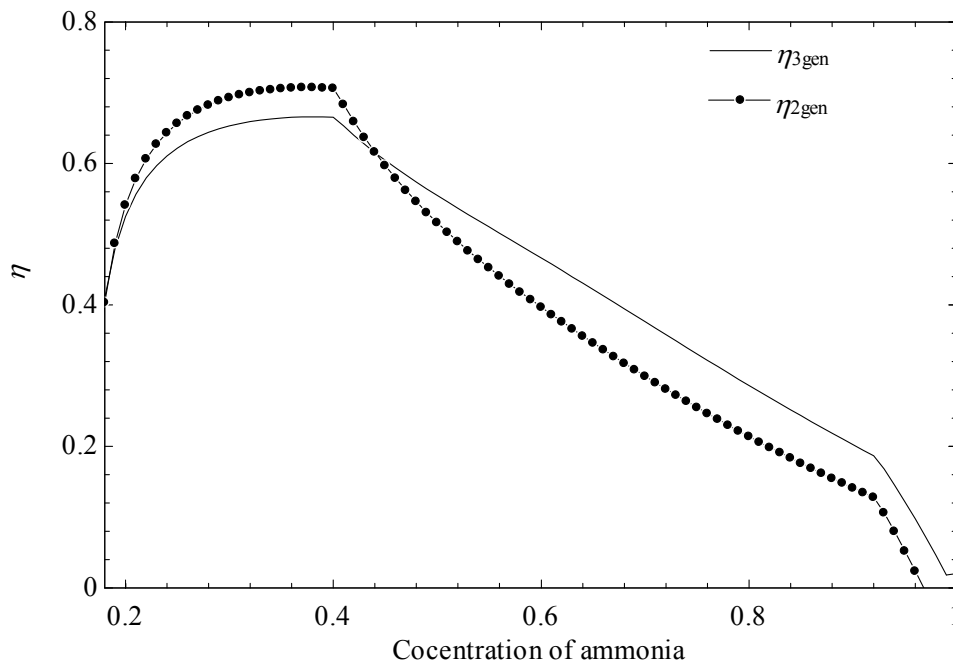


Figure 6.26: Energy efficiency over the ammonia concentration spectrum

The trigeneration combined efficiency which is represented as the COP which is the ratio of useful energy output over energy input, is higher than the cogeneration efficiency throughout the whole spectrum of ammonia concentration combinations. From this model in Figure 6.26, the optimum concentration is found to be 40%. There is also a wider gap between the efficiencies at higher concentrations, thus the trigeneration system is significantly better in that region.

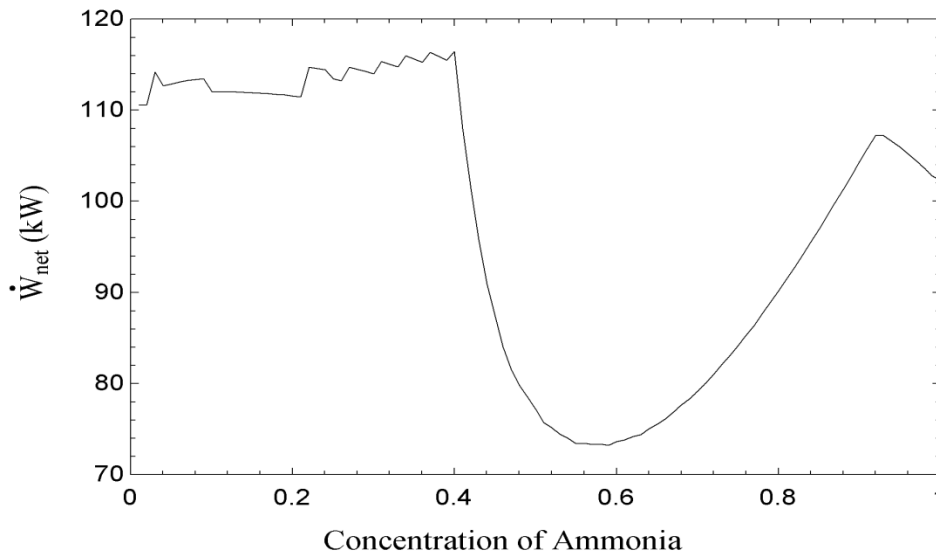


Figure 6.27: Power output trend based on ammonia concentration.

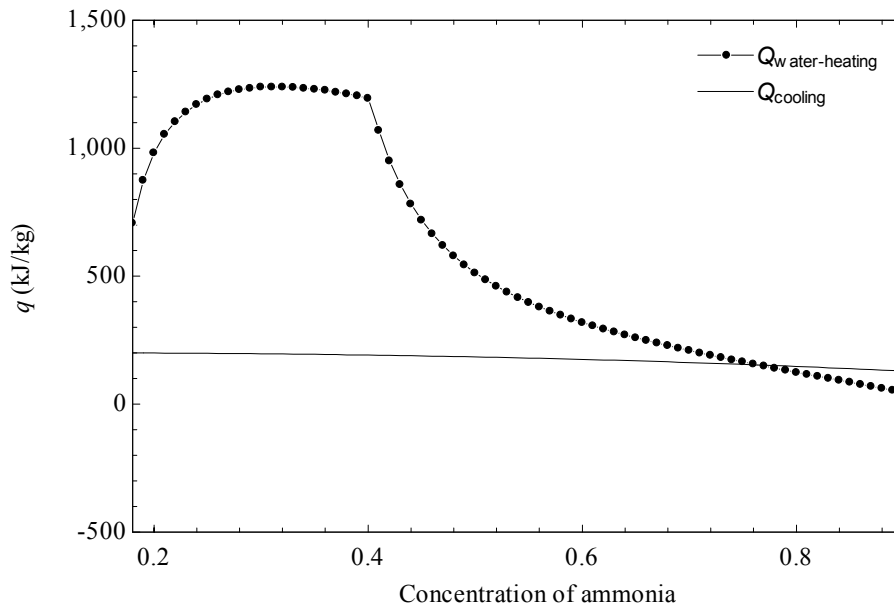


Figure 6.28: Water heating and ambient cooling trend based on ammonia concentration

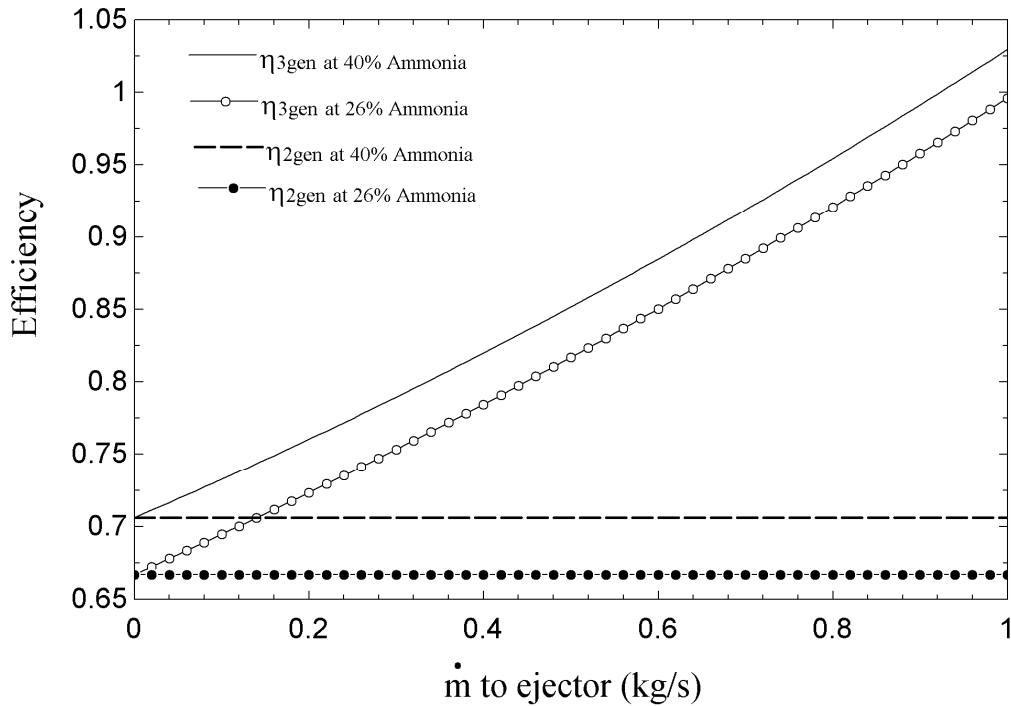


Figure 6.29: Optimum ammonia concentration versus an arbitrary base

The power output over low concentrations of ammonia up to about 0.4% is at the optimum amounts as is shown in Figure 6.27. When compared to the heating and cooling shown in Figure 6.28, it is noticeable that there is a similar trend and that the highest values tend to be at the lower end of the spectrum, where at higher concentration amounts they sharply decrease.

By comparing the system to different ammonia- water concentrations that are possible, a comparison such as the one made in Figure 6.29 can be used to prove that more investment in ammonia is worthwhile in a trigeneration system. The efficiency increases by 4%, this increase would be higher when comparing to lower concentrations or very high concentrations.

However in a cogeneration system both the work output and the amount of useful heating both decreases at higher concentration (more than 40%) as noted in Figure 6.30. This feature explains that at higher concentration ammonia vapour carries much less latent heat of evaporation, a portion of which is used for heating. Also at higher concentration more ammonia vapour generates and since ammonia has much less liquid to vapour ratio than water, the power

output drops. This feature is also reflected in Figures 6.26 to 6.29. In Figure 6.31 and Figure 6.32 the work and heat flow rate trends are shown respectively against ammonia concentration. Both trigeneration and cogeneration follows similar trend with ammonia concentration change however trigeneration being lower value in each cases. This is because in trigeneration system the heat input being same as cogeneration but a portion (here 10%) of the heat goes to ejector cooling system. In practical case the heat input can be increased to compensate the cooling portion of heat and the trend of power and heating should merge to cogeneration system for the same parameter. This additional heat input to increase the parameters are quite justified as the system is to be run by renewable energy which are available abundance in nature. This added heat input will not affect much on the overall efficiency of the system rather maximise the power output and heat input.

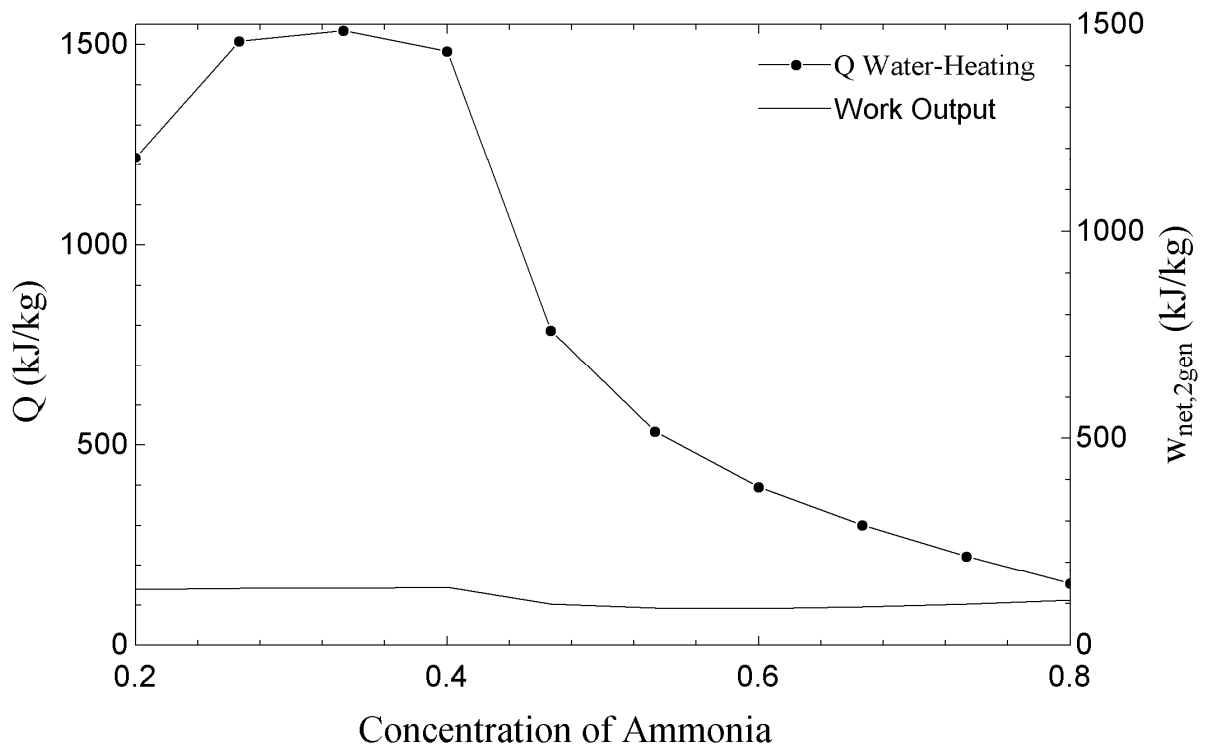


Figure 6.30: Cogeneration power output and water heating trends based on concentration of ammonia

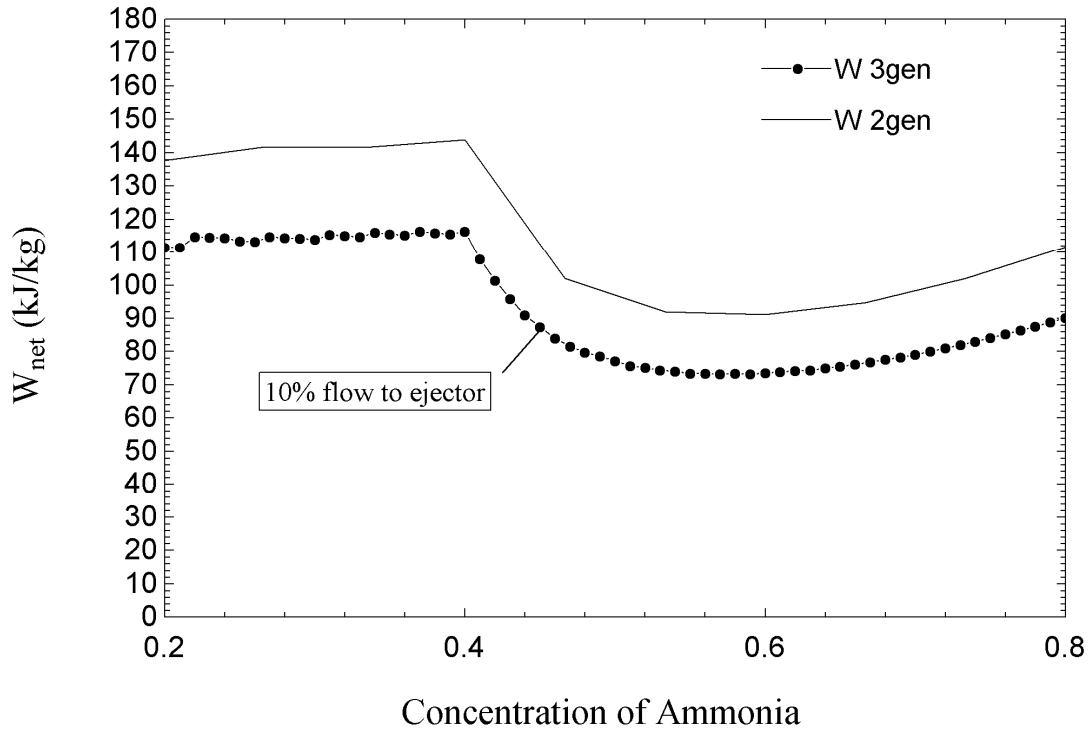


Figure 6.31: Trigeneration and cogeneration power output trends based on concentration of ammonia

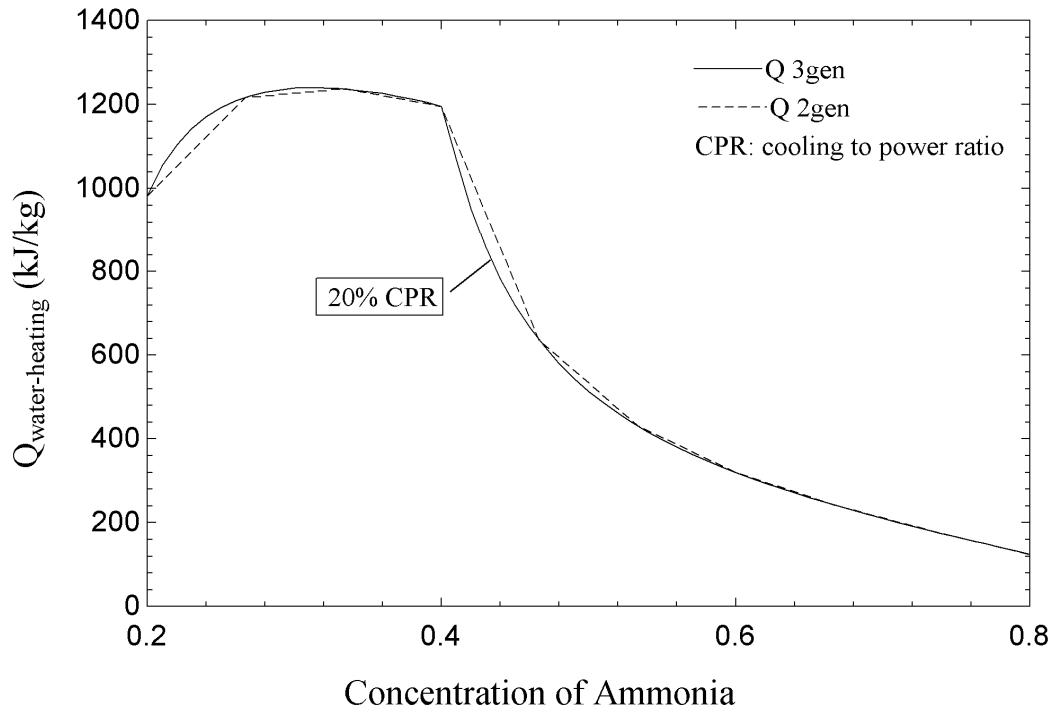


Figure 6.32: Trigeneration and cogeneration water heating trends based on concentration of ammonia

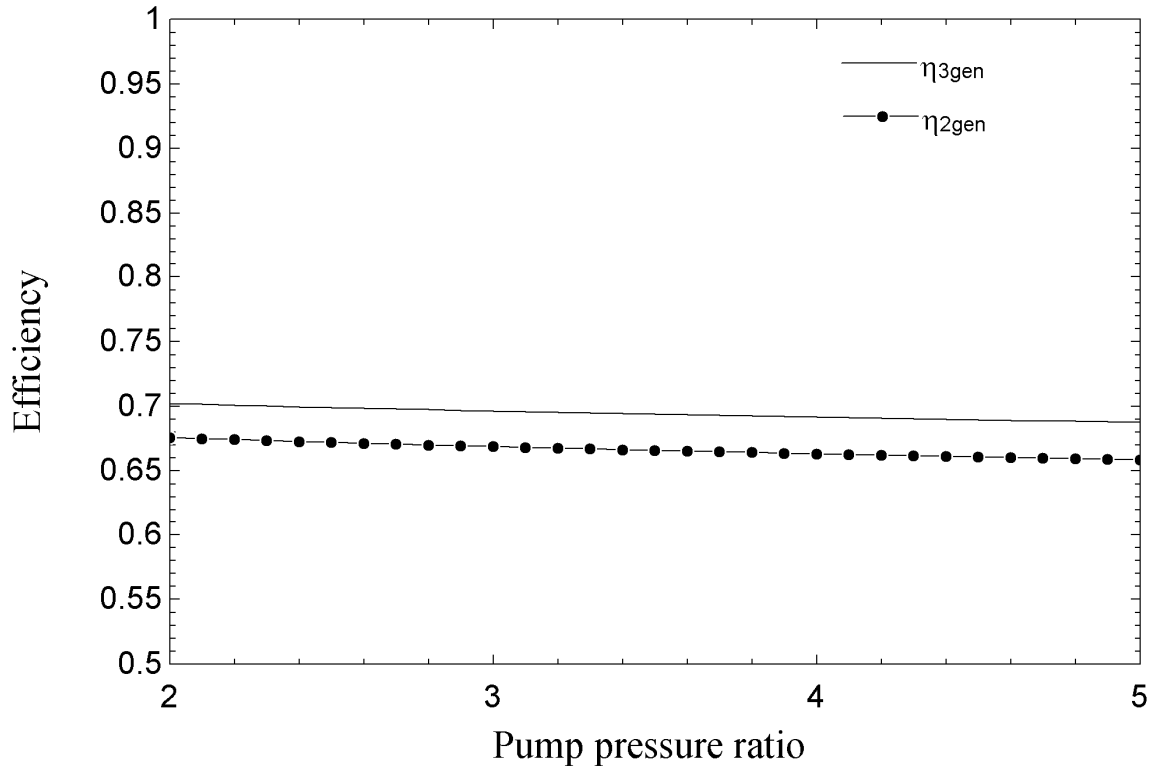


Figure 6.33: Effect of pump pressure ratio on the efficiency

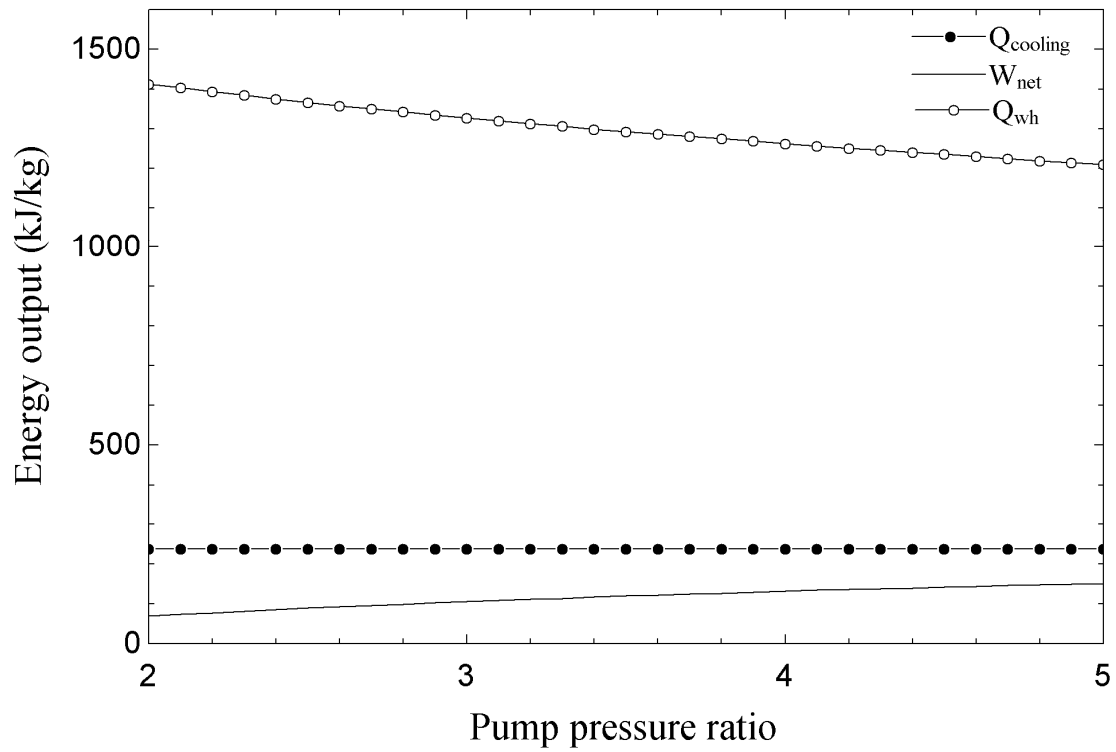


Figure 6.34: Effect of pump pressure ratio on energy outputs

Figure 6.33 shows the overall efficiency variation of the trigeneration system against process fluid pump pressure ratio. At higher pump pressure ratio the efficiency decreases. This is quite normal as at higher pump pressure ratio the rate of electrical energy input to the pump increases. It may be required to maintain a desired fluid flow rate by increasing the pump pressure ratio. However Figure 6.34 shows that it might be worth to sacrifice efficiency by using the pump power as an adjustment of the outcomes. By increasing the pump ratio the power output is increased and the water heating is decreased which may be useful since electric power is more valuable and optimizing the power output is of greater importance.

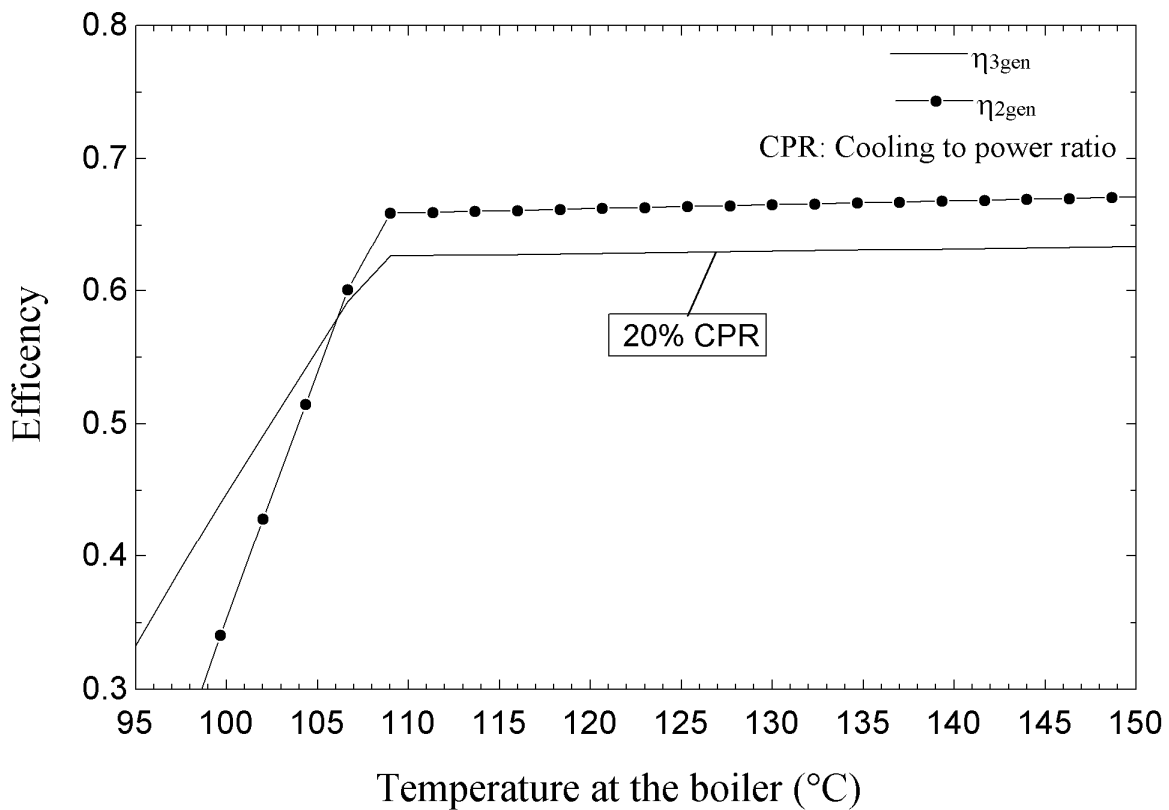


Figure 6.35: Boiler temperature effect on efficiency

In contrast to the pump effect, the outlet temperature of the vapour generator does not have the similar trend i.e. by increasing this temperature the efficiency does not increase much, even though it matters. This is depicted in Figure 6.35 however this does not significantly affect the composition of the outputs of the system as is shown in Figure 6.36

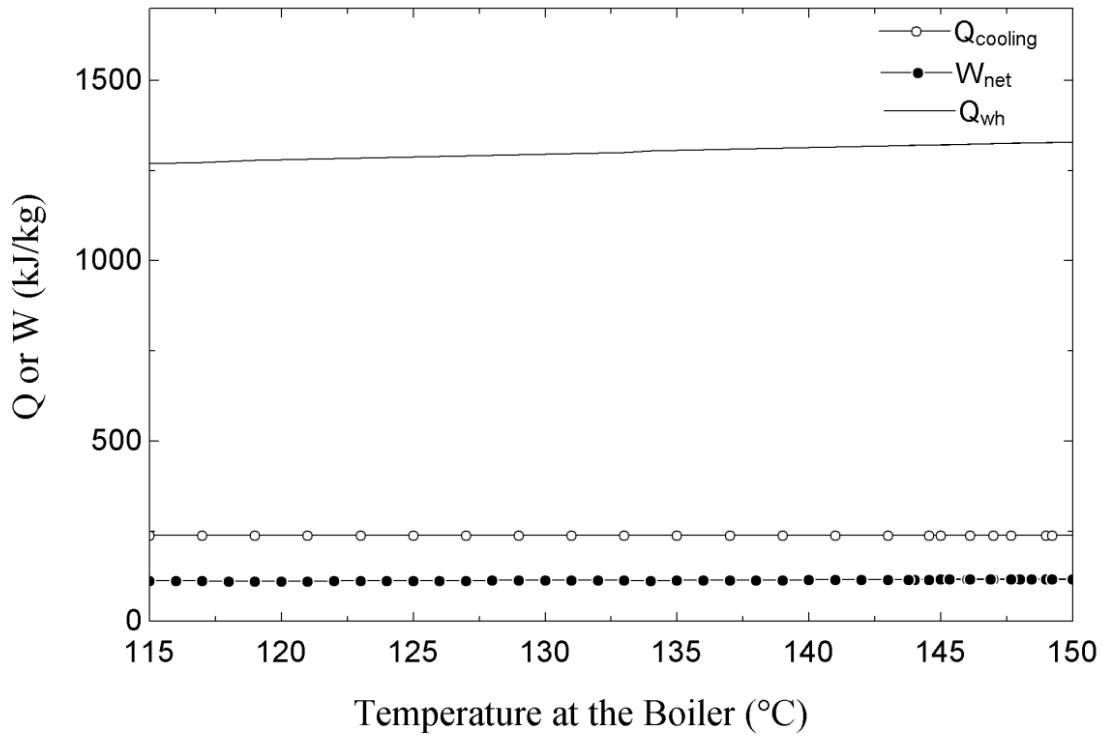


Figure 6.36: Boiler temperature effect on energy outputs

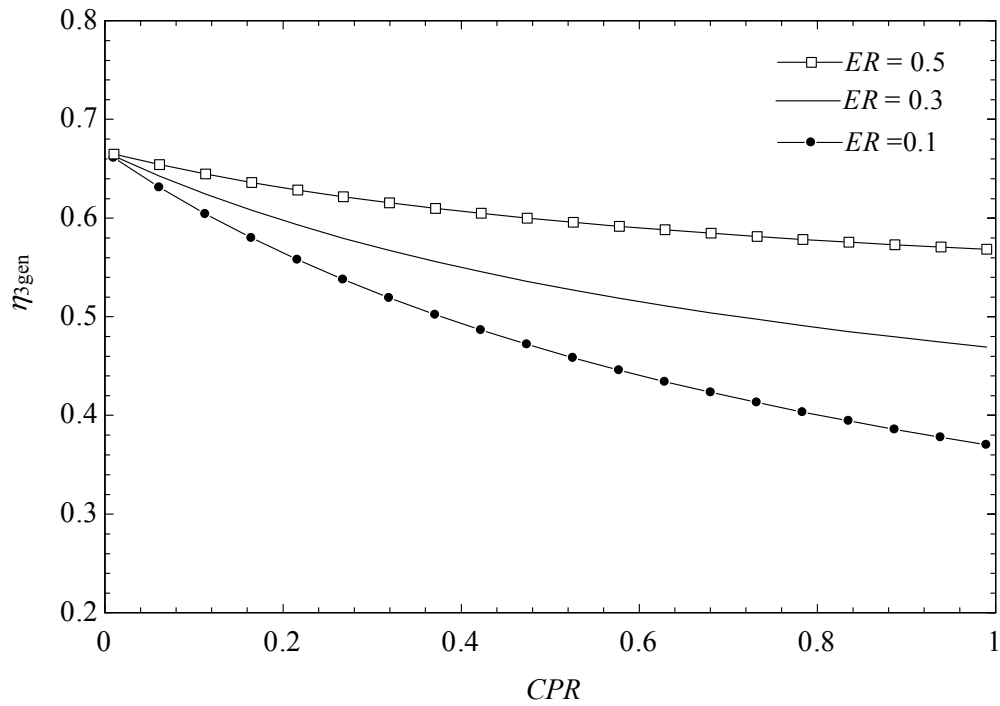


Figure 6.37: COP trend curve as a function of CPR for 2 main entrainment ratios.

Entrainment ratios of 0.3 and 0.1 are examined separately and render very different COP curves as shown in Figure 6.37, the higher ratio operates at a much higher efficiency and is preferable, however this is adjusted with the flow stream to the expander.

6.3 Comparative assessment of trigeneration systems

In this section, the ejector-based trigeneration system is compared with a compression refrigeration based trigeneration system with regards to energy and exergy efficiencies for assessment purpose. In this respect, an integrated vapor compression/expansion trigeneration cycle diagram has been elaborated. The cooling cycle uses a compressor, while the power cycle uses an expander. The compressor of the cooling cycle utilizes a portion of the power generated by the expander.

This definitely allows less power to be available from the system as the expander generator has limitations of maximum rated power. Even with the increase of heat input the expander power cannot be increased. The trigeneration system used for comparative assessment is represented schematically in Figure 6.38.

Ideally, the vapor compression-expansion trigeneration system must operate with weak ammonia-water solution in power generation section and very strong ammonia-water solution in cooling generation section. The proposed compression-expansion trigeneration system follows this remark: in power generation section, the ammonia concentration is around 0.25 whereas in cooling generation section the ammonia concentration is around 0.75. This feature is maintained in the system by introducing a vapour separator at state point 8-9-15. After the first water heater at state point 7-8 the low concentrated ammonia water enters the vapour generator where the vapour separates at higher concentration of ammonia and directs towards the second expander to generate further work. This expansion procedure acts as an expansion valve of the conventional compression refrigeration system. The low concentrated ammonia water liquid in the separator on the other hand flows back to the through the mixture where it mixes with the other stream of the cooling cycle.

The integration of compression refrigeration system has some advantages of higher coefficient of performance but the compressor has to share substantial amount of power from the expander or acquire from external grid.

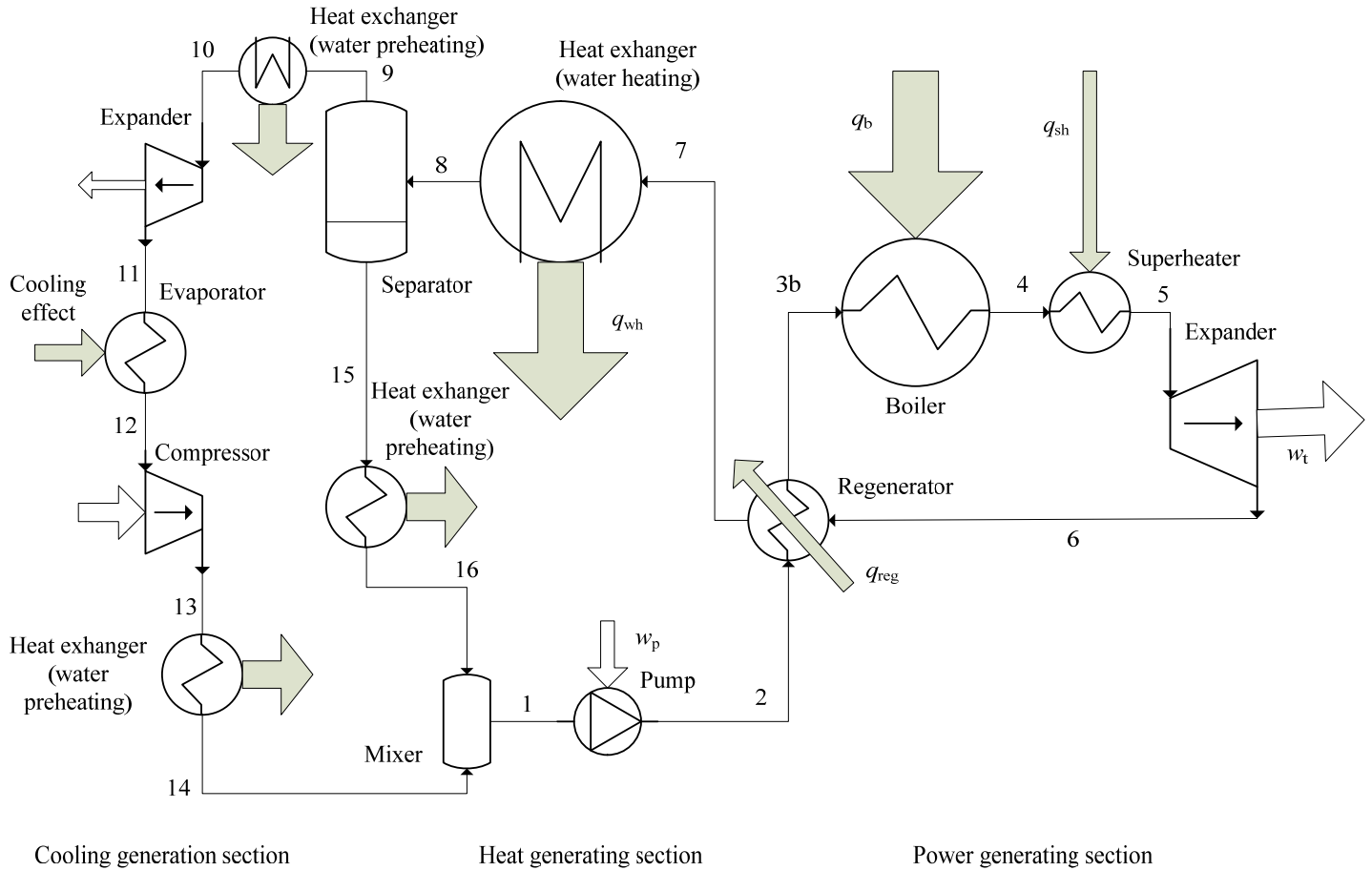


Figure 6.38: Trigeneration system with ammonia-water compression-expansion.

According to the diagram from Figure 6.38 the trigeneration system comprises a power generation, a heating generation and a cooling generation section. The power generation is based on a regenerative Rankine cycle 1 – 2 – 3 – 4 – 5 – 6 – 7 – 8 represented in Figure 6.39.

In this cycle, the temperature and enthalpy of the expanded stream at 6 is high enough to cover the thermal energy needed for preheat and a part of boiling/desorption process. Hence, in the regenerative heat exchanger the heat 6 – 7 is transferred to the process 2 – 3 – 3b. Further, of state 7, the working fluid is cooled and condenses/resorbs until a two-phase mixture in state 8 consisting of saturated vapor 9 become in equilibrium with saturated liquid at 15.

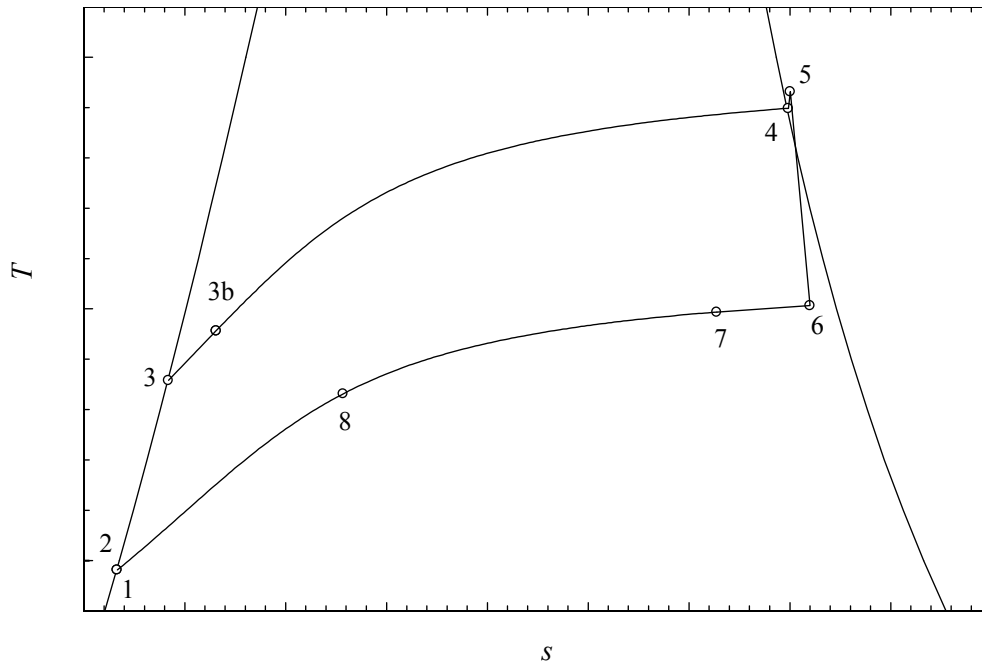


Figure 6.39: Qualitative representation of the thermodynamic cycle of the power generating section of the trigeneration system.

Since vapor is much more concentrated with ammonia than in liquid, they are extracted in a vapor-liquid separator and cooled by heat transfer with thermal sink until it reaches the temperature $T_{10} = T_1$. The refrigeration cycle operating with high concentration ammonia-water solution can be followed on the $T - s$ diagram from Figure 6.40. The two-phase mixture from state 10 is expanded in a scroll expander (able to operate in two-phase) until it reaches low temperature and pressure in 12. It follows the evaporation process 12 – 13, where the heat for cooling effect is absorbed. Further, there is a two-phase compression process with parameters selected such $T_{13} = T_9$ and in state 13 it becomes saturated vapor. Cooling is applied thereafter to the saturated vapor until they reach state 14 with $T_{14} = T_1$. The weak ammonia-water solution separated at state 15 is cooled to $T_{16} = T_1$. When the streams at state 14 and 16 are adiabatically mixed a saturated liquid is formed in state 1 at the suction of the pump. The net generation of work by the system is given by the work of the turbine and refrigeration expander (process at 11 – 12) minus the work consumed by the refrigeration compressor and the pump. There is heat rejected by the cycle with temperature decreasing from T_8 to T_1 . This heat can be recovered from heat exchangers 9 – 10, 13 – 14 and 15 – 16 which can work in parallel; the recovered heat can be used for water preheating or for other useful heating process depending on the application.

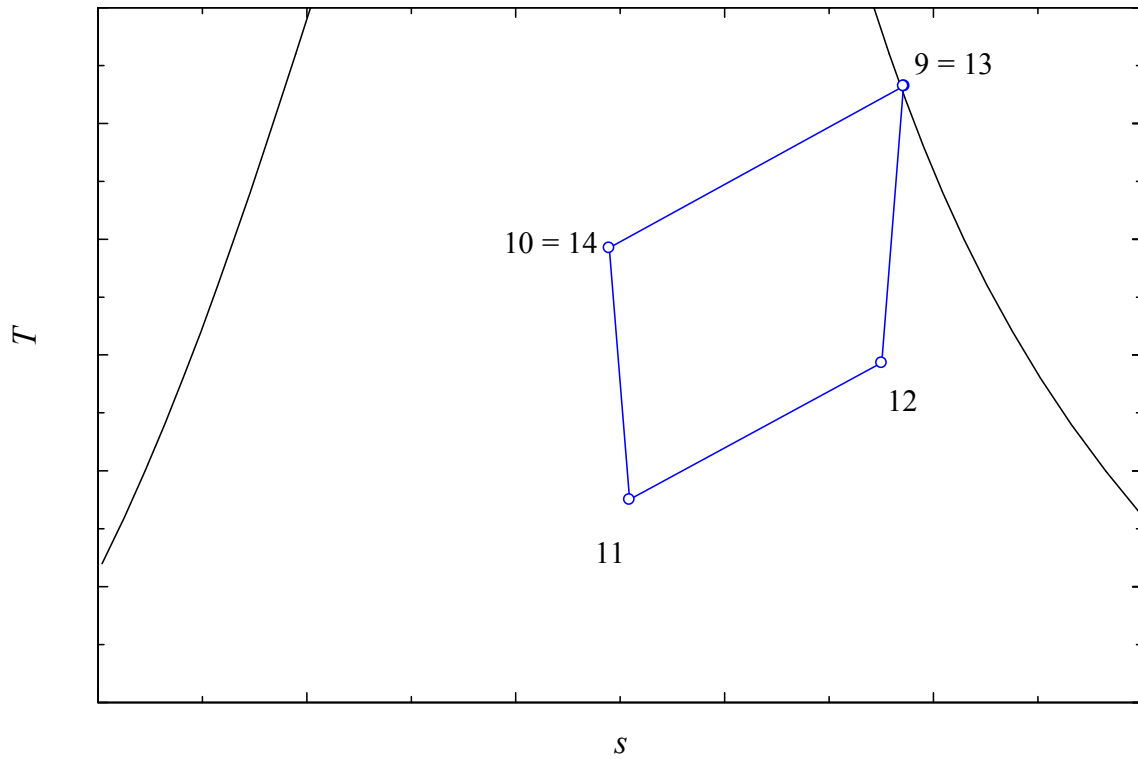


Figure 6.40: Qualitative representation of the thermodynamic cycle of the refrigeration section of the trigeneration system.

The trigeneration system as developed in this proposal is designed to integrate a cooling system to the previously described co-generation system. Likewise of a cogeneration system, the fluid after exiting the heat exchanger of the hot water system at state 8 has a quality of 0.2746 as given in Table 6.22. A separator is used to separate the ammonia water vapor of high concentration of ammonia to pass through a compression refrigeration cycle integrated with the system. The temperature at state 9 being 333K, a heat-exchanger is used to extract some heat to preheat the main hot water system.

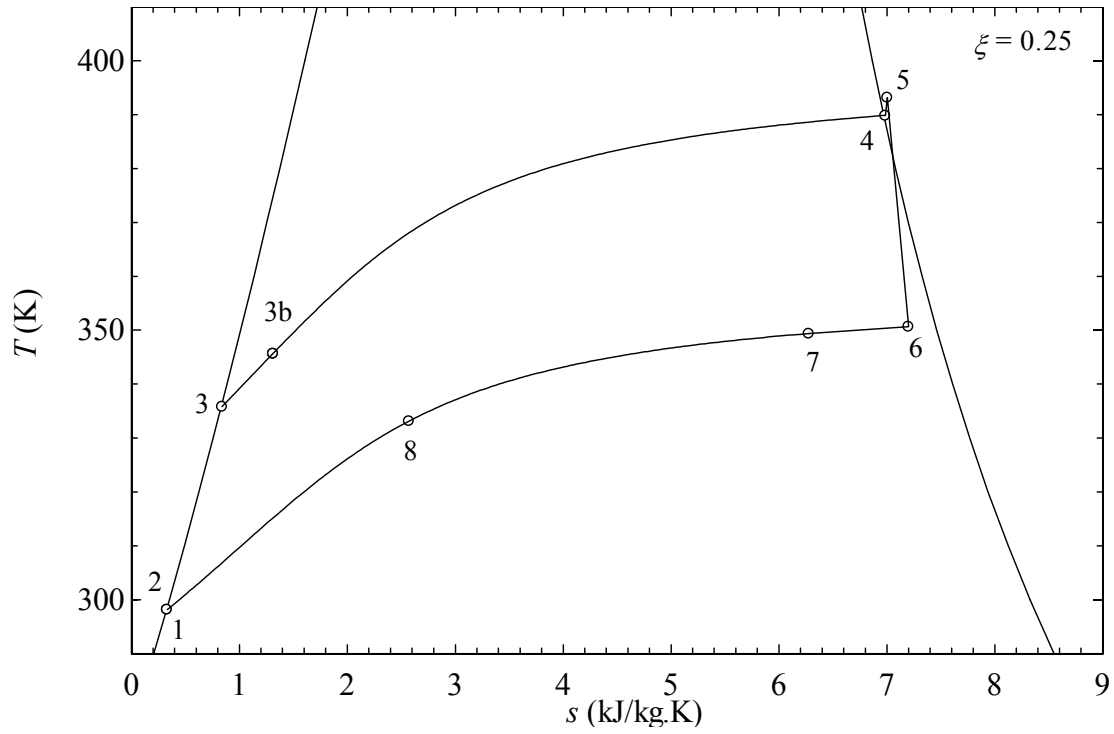


Figure 6.41: Predicted T-s diagram of Ammonia-water heat Rankine cycle trigeneration system (power generation subsystem cycle).

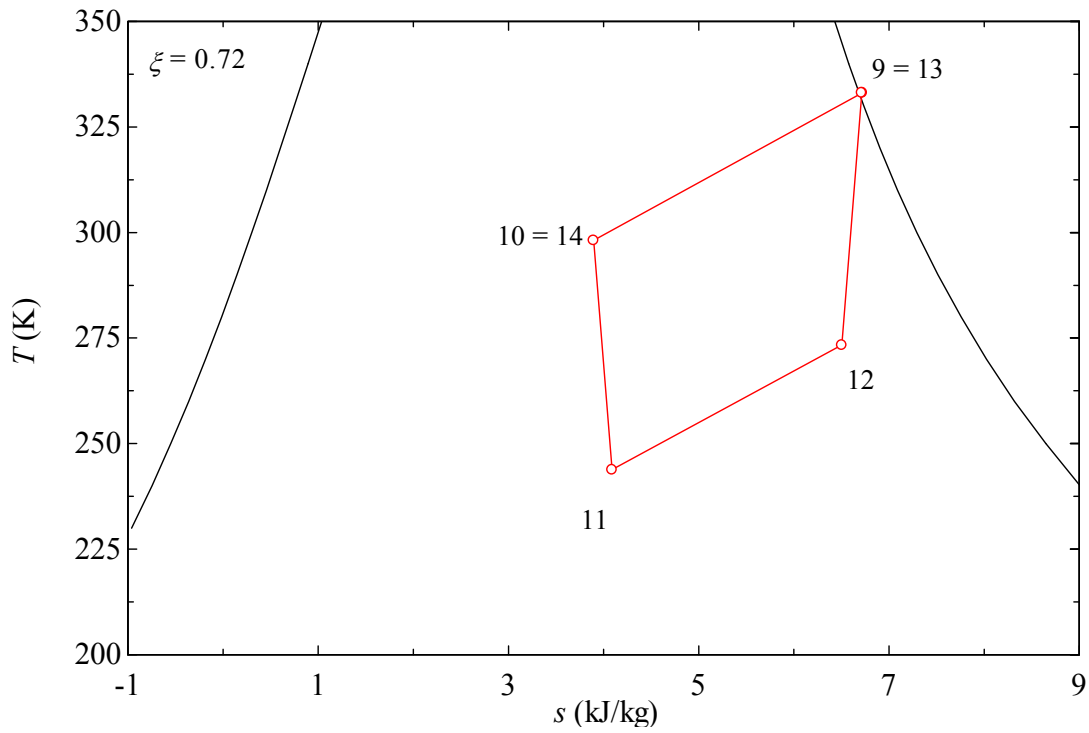


Figure 6.42: Predicted T-s diagram of Ammonia-water heat Rankine cycle Trigeneration system (Refrigeration subsystem cycle)

Table 6.22: State point parameters for the compression-expansion trigeneration system.

State	T (K)	P (kPa)	v (m ³ /kg)	Q	h (kJ/kg)	s (kJ/kgK)	ex (kJ/kg)
1	298.2	64.73	0.001106	0	-65.21	0.319	-0.04405
2	298.2	265.4	0.001106	-0.001	-64.88	0.3193	0.1813
3	336.4	265.4	0.001137	0	99.17	0.8366	9.999
3b	348.1	265.4	0.0514	0.08083	291.5	1.396	35.46
4	393	265.4	0.6744	1	2395	6.929	489.6
5	393.2	265.4	0.6747	1.001	2396	6.931	490.2
6	353.1	64.73	2.423	0.9577	2234	7.13	268.5
7	351.5	64.73	2.03	0.8039	1878	6.119	213.6
8	333.2	64.73	0.6741	0.2746	620.5	2.478	41.93
9	333.2	64.73	2.453	1	1767	6.723	-77.51
10	298.2	64.73	1.417	0.6362	861.8	3.896	-139.5
11	240.2	3.236	21.86	0.6041	3.9	3.9	-998.6
12	273.3	3.236	34.95	0.8571	1298	6.501	-479.4
13	333.1	64.73	2.448	0.9981	1762	6.71	-77.98
14	298.2	64.73	1.417	0.6362	861.8	3.896	-139.5
15	333.2	64.73	0.001061	0	186.8	0.8718	87.14
16	298.2	64.73	0.001042	-0.001	40.41	0.4075	79.17

Note: reference state ammonia-water at $T_0, P_0 = \xi = 0.25$

Table 6.23: Energy destruction in the compression-expansion trigeneration system.

Component	ex_d (kJ/kg)	ex_d (%)
Pump	0.097	0.04
Regenerator	19.56	7.71
Boiler	82.4	32.5
Superheater	0.006	0.002
Expander 5 – 6	59.36	23.4
Water heater	32.4	12.77
Water preheater 9 – 10	7.46	2.94
Water preheater 13 – 14	8.83	3.48
Water preheater 15 – 16	3.29	1.30
Expander 10 – 11	15.95	6.28
Cooler 11 – 12	9.25	3.64
Compressor	15.14	5.97
Total	253.7	100

The fluid after passing through the preheat heat exchange is routed through an scroll based expander which may be considered a substitute of an expansion valve of a compression refrigeration cycle. The fluid at this state has a temperature of 240K with a pressure of 3 kPa. This low pressure, low temperature fluid is passed through an evaporator to cool a media around freezing point of water. The ammonia-water refrigeration cycle is shown in Figure 6.42 in the $T - s$ diagram. The exergy destruction within the trigeneration system is given in Table 6.23 whereas the performance parameters are listed in Table 6.24.

Table 6.24: Performance of the compression-expansion trigeneration system

Quantity	Definition equation	Value
Net generated work	$w_{\text{net}} = w_{e1} + w_{e2} - (w_p - w_c)$	69.1 kJ/kg
Generated heat	$q_h = q_{wh} + q_{wph}$	1,930 kJ/kg
Generated cooling	$q_{\text{cool}} = q_8 (h_{12} - h_{11})$	226 kJ/kg
Heat input	$q_{\text{in}} = q_b + q_{sh}$	2,105 kJ/kg
Energy input	$ex_{\text{in}} = ex_b + ex_{sh}$	537.1 kJ/kg
Generated heat exergy	$ex_h = ex_{wh} + ex_{wph9-10} + ex_{wph13-14} + ex_{wph15-16}$	176 kJ/kg
Exergy of cooling effect	$ex_{\text{cool}} = q_{\text{cool}}(1 - T_0/\bar{T}_{15-16})$	-19.13 kJ/kg
COP	$COP_{3\text{gen}} = \frac{\dot{W}_{\text{net}} + \dot{Q}_{\text{heating}} + \dot{Q}_{\text{cooling}} }{\dot{Q}_{\text{in}}}$	1.06
Exergetic efficiency	$\psi_{3\text{gen}} = \frac{\dot{W}_{\text{net}} + \dot{E}x_{\text{heating}} + \dot{E}x_{\text{cooling}} }{\dot{E}x_{\text{in}}}$	0.49

The total exergy destruction is 253 kJ/kg which is little higher than co-generation system because of the involvement of more processes. From Table 6.24 it can be realized that the cooling effect of this system is 224 kJ/kg and the coefficient of performance is 1.06, whereas the trigeneration exergetic efficiency is 0.49.

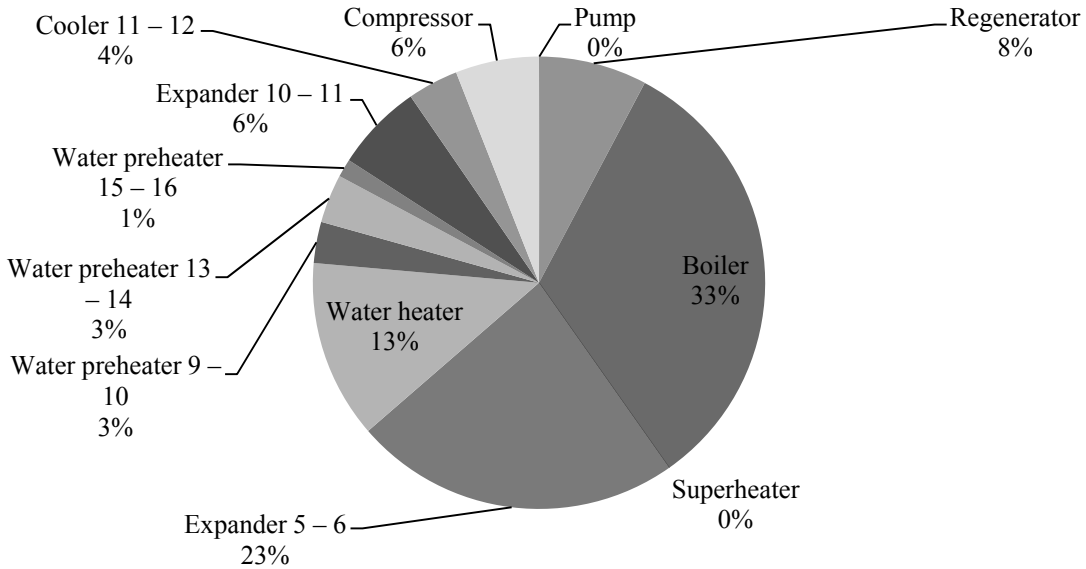


Figure 6.43: Exergy destructions of the compression-expansion trigeneration system.

The exergy destruction of the complex (Figure 6.43) system can be contrasted with the exergy destruction of the original system (Figure 6.44) used for modeling and simulation in the previous section. Although small, the exergy destruction is reduced significantly as a whole. This is a step further in the design of viable trigeneration system.

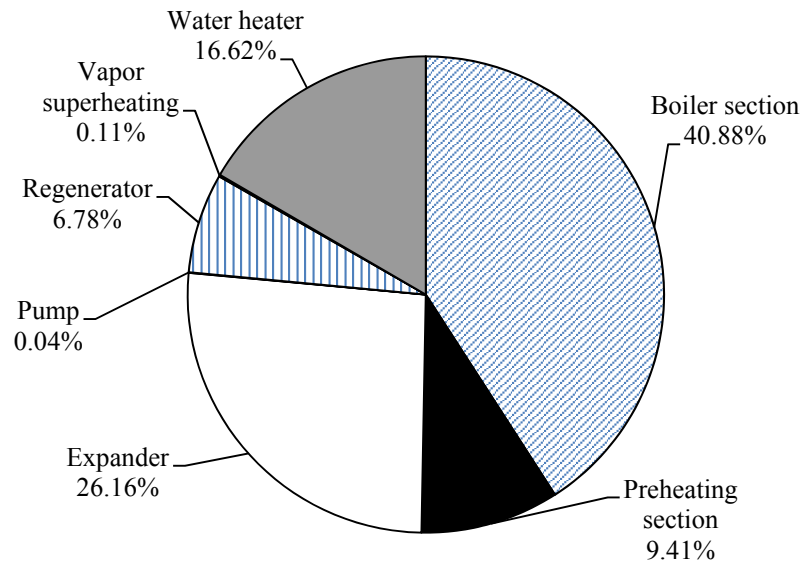


Figure 6.44: Exergy destruction of the ejector-expander based trigeneration system.

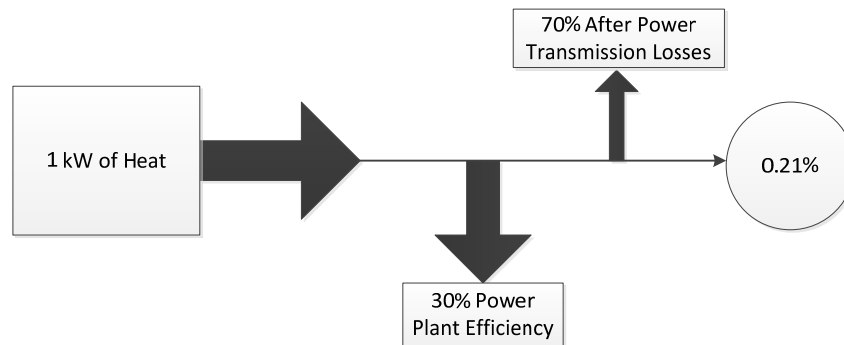


Figure 6.45: Cooling performance of a refrigeration system with COP of 1 using electricity from the grid which is assumed to be from a simple heat power plant

To compare the cooling value of the refrigeration side of the trigeneration system, it is necessary to compare it with existing refrigeration systems. The base for the comparison is shown in Figure 6.45 which has a simple refrigeration system with a COP of 1 powered by the electricity grid assumed to be supplied by thermal energy through a series of power plants. The assumptions made are very general to find a ball park in order to compare. The operation of the trigeneration plant is shown in Figure 6.46 where it is compared to the value found previously, it is evident that the operation of the refrigeration side matches accordingly and is even improved with a higher entrainment ratio or cooling to power ratio which is controlled by the mass flow rate as shown in the figure.

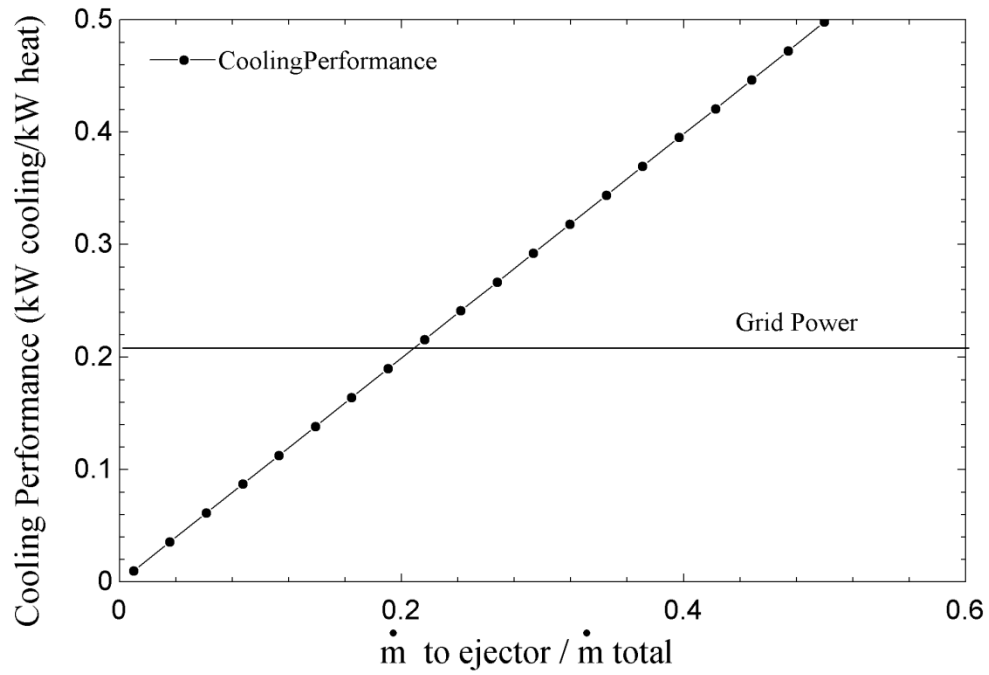


Figure 6.46: Cooling performance comparison between trigeneration and conventional refrigeration systems in terms of cooling unit per energy input in form of heat.

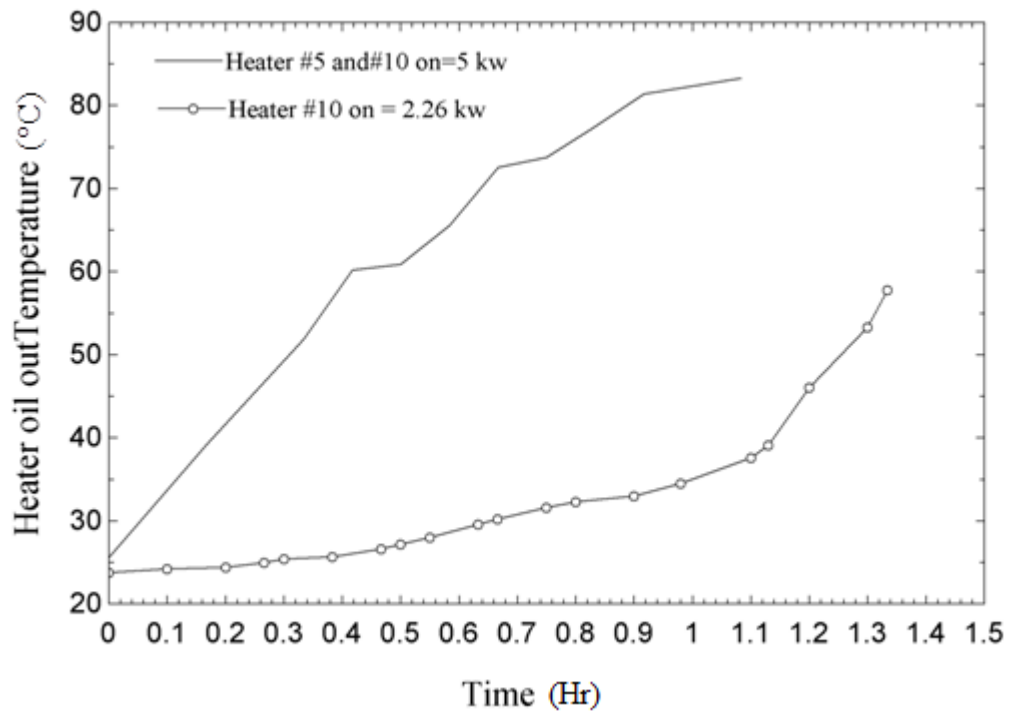


Figure 6.47: Temperature of the oil in two scenarios with different power inputs

Another comparison that can be noted is the amount of control that the electric power has on the rate of heating, even though it was previously discussed; the amount of power input as accumulation, lost to the surroundings, and transferred to the oil can be considered. This shows that there is still quite some control that can be achieved through the power supply in order to control the temperature at the boiler. This piece of insight can be used for controlling as well as to understand the role of thermal inertia in the system. The thermal inertia pattern may be viewed from the Figure 6.48, where the oil outlet temperature from the heater represents the heat accumulation in the refractory after all heaters have been switched off.

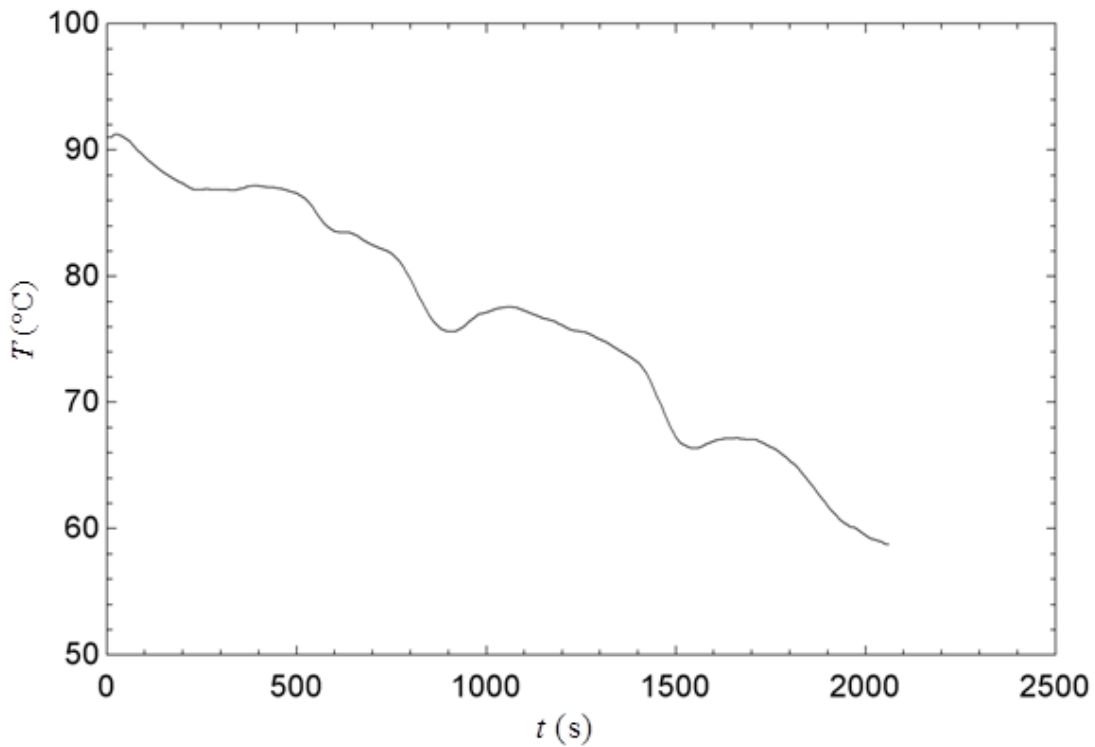


Figure 6.48: Representation of thermal inertia of heater determined by oil cooling

The thermal inertia therefore plays an important role in the heat transfer capability to the oil during heater operation.

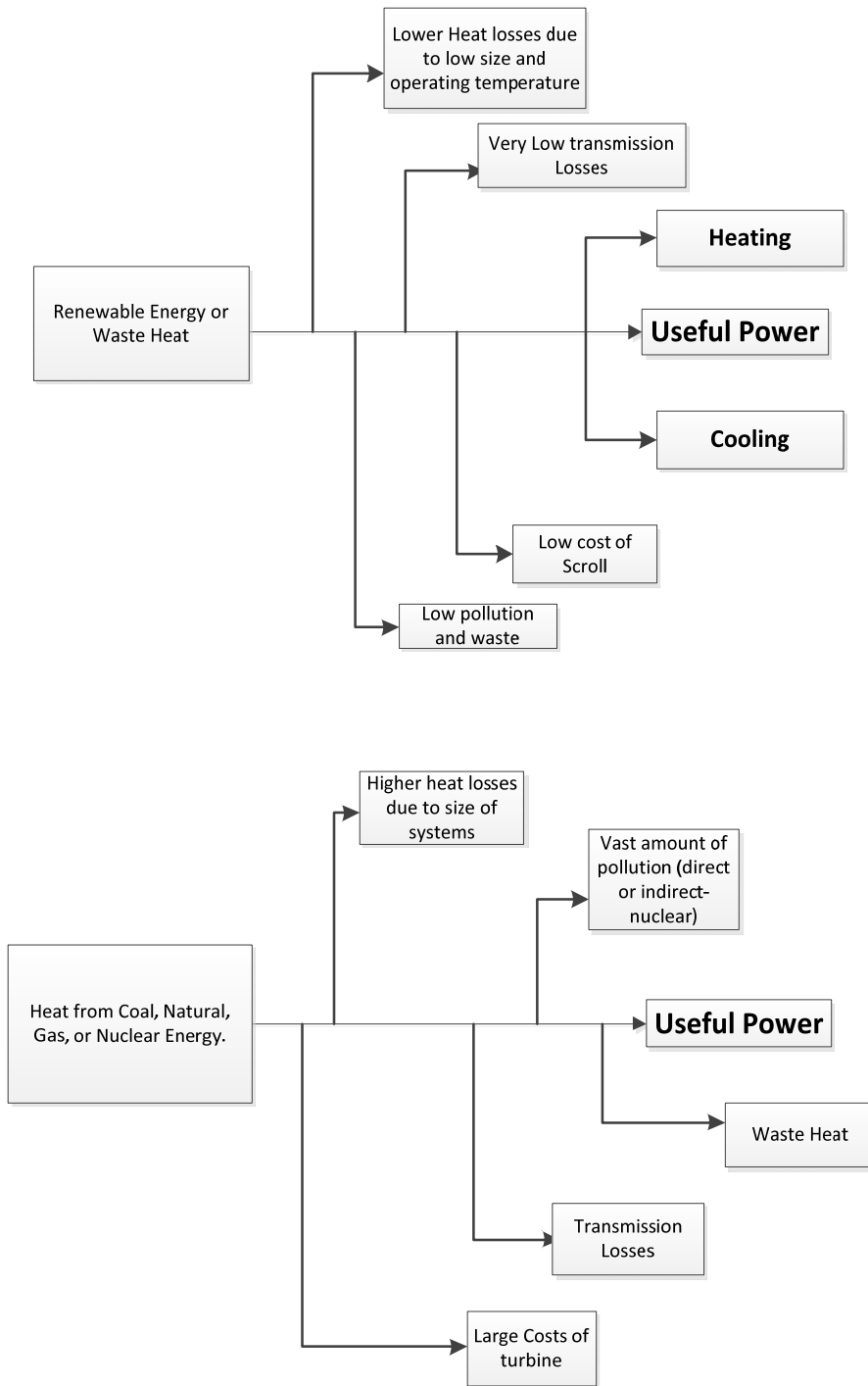


Figure 6.49: Comparative assessment of proposed (top) and conventional (bottom) systems.

The proposed system for its viability has to be in the vicinity of residential buildings which can make full use of the generated services. At this scale, it is possible for it to be powered by solar energy. Assuming the system becomes stable under the conditions specified, a comparison can then be made with existing conventional power plants as shown in Figure 6.49.

Table 6.25: Mass balance equations for the improved trigeneration system.

Component	Mass balance equation
Pump	$\dot{m}_1 = \dot{m}_2 = \dot{m}$
Regenerator	$\dot{m}_3 = \dot{m}_2 = \dot{m}, \dot{m}_8 = \dot{m}_9, \dot{m}_{18} = \dot{m}_{17}$
Vapor generator	$\dot{m}_5 = \dot{m}_3$
Valve 5-6-14 (3-ways)	$\dot{m} = \dot{m}_5 = \dot{m}_6 + \dot{m}_{14}, \dot{m}_{14} = f \dot{m}, f \in [0,1]$
Expander	$\dot{m}_6 = \dot{m}_7$
Liquid separator	$\dot{m}_7 = \dot{m}_8 + \dot{m}_{16}, \dot{m}_8 = (1 - q_7)\dot{m}_7, \dot{m}_{16} = q_7\dot{m}_7$
Valve 15-16-17 (3-ways)	$\dot{m}_{15} + \dot{m}_{16} = \dot{m}_{17}$
Heat exchanger for heating	$\dot{m}_9 = \dot{m}_{10}, \dot{m}_{18} = \dot{m}_{19}$
Condenser/desorber (heat rejection)	$\dot{m}_{11} = \dot{m}_{10}, \dot{m}_{19} = \dot{m}_1$
Throttling valve	$\dot{m}_{12} = \dot{m}_{11}$
Evaporator	$\dot{m}_{13} = \dot{m}_{12}$
Ejector	$\dot{m}_{13} + \dot{m}_{14} = \dot{m}_{15}; \dot{m}_{13}(1 - ER) = \dot{m}_{14} ER, ER \in (0,1)$

Table 6.26: Energy balance equations for the improved trigeneration system.

Component	Energy balance equation
Pump	$\dot{m}_1 h_1 = \dot{m}_2 h_2 + \dot{W}_p; h_{2s} - h_1 = \eta_{s,p}(h_2 - h_1)$
Regenerator	$\dot{m}_2 h_2 + \dot{m}_8 h_8 + \dot{m}_{17} h_{17} = \dot{m}_3 h_3 + \dot{m}_9 h_9 + \dot{m}_{18} h_{18}$
Vapor generator	$\dot{m}_3 h_3 + \dot{Q}_{in} = \dot{m}_5 h_5$
Valve 5-6-14 (3-ways)	$h_5 = h_6 = h_{14}$
Expander	$\dot{m}_6 h_6 = \dot{m}_7 h_7 + \dot{W}_e; h_6 - h_7 = \eta_{s,e}(h_6 - h_{7s})$
Liquid separator	$\dot{m}_7 h_7 = \dot{m}_8 h_8 + \dot{m}_{16} h_{16}$
Valve 15-16-17 (3-ways)	$h_{15} = h_{16} = h_{17}$
Heat exchanger for heating	$\dot{m}_9 h_9 + \dot{m}_{18} h_{18} = \dot{m}_{10} h_{10} + \dot{m}_{19} h_{19} + \dot{Q}_{heating}$
Condenser/desorber (heat rejection)	$\dot{m}_{11} h_{11} + \dot{m}_{19} h_{19} = \dot{m}_{10} h_{10} + \dot{m}_1 h_1 + \dot{Q}_{out}$
Throttling valve	$h_{12} = h_{11}$
Evaporator	$\dot{m}_{12} h_{12} + \dot{Q}_{cooling} = \dot{m}_{13} h_{13}$
Ejector	$\dot{m}_{13} h_{13} + \dot{m}_{14} h_{14} = \dot{m}_{15} h_{15}$

Table 6.27: Exergy balance equations for the improved trigeneration system.

Component	Energy balance equation
Pump	$\dot{m}_1 ex_1 = \dot{m}_2 ex_2 + \dot{W}_p + \dot{E}x_d$
Regenerator	$\dot{m}_2 ex_2 + \dot{m}_8 ex_8 + \dot{m}_{17} ex_{17} = \dot{m}_3 ex_3 + \dot{m}_9 ex_9 + \dot{m}_{18} ex_{18} + \dot{E}x_d$
Vapor generator	$\dot{m}_3 h_3 + \dot{Q}_{in} \left(1 - \frac{T_0}{\bar{T}_{source}}\right) = \dot{m}_5 ex_5 + \dot{E}x_d$
Expander	$\dot{m}_6 ex_6 = \dot{m}_7 ex_7 + \dot{W}_e + \dot{E}x_d$
Liquid separator	$\dot{m}_7 ex_7 = \dot{m}_8 ex_8 + \dot{m}_{16} ex_{16} + \dot{E}x_d$
Heat exchanger for heating	$\dot{m}_9 ex_9 + \dot{m}_{18} ex_{18} = \dot{m}_{10} ex_{10} + \dot{m}_{19} ex_{19} + \dot{Q}_{heating} \left(1 - \frac{T_0}{\bar{T}_{heating}}\right)$
Condenser/desorber (heat rejection)	$\dot{m}_{11} ex_{11} + \dot{m}_{19} ex_{19} = \dot{m}_{10} ex_{10} + \dot{m}_1 ex_1 + \dot{E}x_d$
Throttling valve	$\dot{m}_{11} h_{11} = \dot{m}_{12} h_{12} + \dot{E}x_d$
Evaporator	$\dot{m}_{12} ex_{12} + \dot{Q}_{cooling} \left(\frac{T_0}{\bar{T}_{cooling}} - 1\right) = \dot{m}_{13} ex_{13} + \dot{E}x_d$
Ejector	$\dot{m}_{13} ex_{13} + \dot{m}_{14} ex_{14} = \dot{m}_{15} ex_{15} + \dot{E}x_d$

The ammonia-water vapour thus being separated has much more concentration of ammonia and flows to the condenser via the regenerator. On the other hand, liquid with much

less concentration of ammonia goes through the evaporator as a secondary fluid for cooling. Doing this the evaporator performance increases and it enhances the cooling process.

The mass balance equations for the improved system are given in Table 6.25. The energy balance equation is given in Table 6.26. The exergy balance equation is given in Table 6.27. The calculated state points for the considered case study are given in Table 6.28. The thermodynamic cycle represented in the T - s diagram is shown in Figure 6.51 for a considered case study the highest temperature in the cycle is 165°C and the superheating degree is 15°C.

Table 6.28: State point parameters of the improved and optimized trigeneration system.

State	T (K)	P (bar)	h (kJ/kg)	s (kJ/kgK)	v (m ³ /kg)	x (kg _{NH₃} /kg)	q (vapor quality)
1	303.2	0.4738	-7.118	0.4305	0.001084	0.2	0
2	303.2	5.885	-6.393	0.431	0.001084	0.2	subcooled
3	337.4	5.885	138.4	0.8835	0.001109	0.2	subcooled
4v	423.1	5.885	2513	6.722	0.3195	0.2	1
5	438.2	5.885	2548	6.802	0.3332	0.2	superheated
6	438.2	5.885	2548	6.802	0.3332	0.2	superheated
7	347.4	0.4738	2234	7.096	3.154	superheated	0.9291
8	347.4	0.4738	300.5	1.032	0.001031	0.01607	0
9	347.6	0.4738	307.8	1.053	0.01091	0.01607	0.002912
10	338.1	0.4738	261.7	0.9188	0.001025	0.01607	subcooled
11	303.1	0.4738	115.4	0.4621	0.001009	0.01607	subcooled
12	278.8	0.01185	115.4	0.4794	4.753	0.01607	0.04322
13	282.4	0.01185	2498	8.931	110	0.01607	1
14	438.2	5.885	2548	6.802		superheated	superheated
15	409.5	0.4738	2543	7.907	4.011	0.1823	superheated
16	347.4	0.4738	2381	7.559	3.394	0.214	1
17	374.8	0.4738	2453	7.72	3.668	0.2	superheated
18	347.6	0.4738	2307	7.306	3.261	0.2	0.9606
19	338.1	0.4738	880.1	3.164	1.188	0.2	0.3534

Table 6.29: Assumptions considered for the improvement system optimization.

Parameter	Assumption
Isentropic efficiency of the pump	$\eta_{s,p} = 0.8$
Isentropic efficiency of the expander	$\eta_{s,e} = 0.75$
Entrainment ratio of the ejector	$ER = 0.1$
Temperature of superheated vapor	$\Delta T_{sup} = 165^\circ\text{C}$
Lowest temperature of working fluid	$T_1 = 30^\circ\text{C}$; saturated liquid in #1
Heat source temperature	$T_{so} = 175^\circ\text{C}$ (constant heat source temperature)
Heat sink temperature	$T_0 = 20^\circ\text{C}$ (the same as the reference temperature)
Lowest working fluid temperature in water heater	$T_{19} = 65^\circ\text{C}$
Temperature of the generated hot water	$\bar{T}_{wh} = 55^\circ\text{C}$ (assumed constant)
Highest working fluid temperature at evaporator	$T_{13} = 4.85^\circ\text{C}$
Temperature for cooling (air conditioning)	$\bar{T}_{ac} = 15^\circ\text{C}$ (delivery temperature of cold air)

The cycle parameters are determined and optimized based on an EES code elaborated for cycle modeling, which is based on the equations given in Tables 6.25-6.27. A number of assumptions are considered as given in Table 6.29.

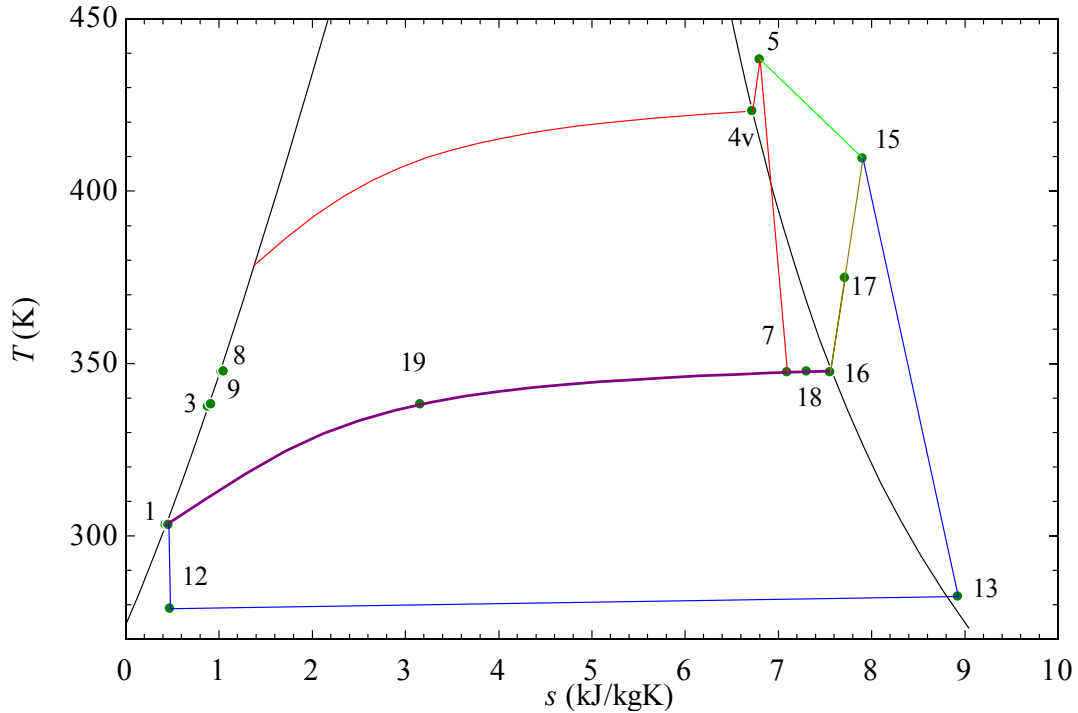


Figure 6.51: Predicted T - s diagram of the improved and optimized the trigeneration system.

Table 6.30: Performance parameters of the optimized system.

Parameter	Value
Work generated by the expander	188.3 kJ/kg
Work consumed by the pump	0.72 kJ/kg
Back work ratio	0.38%
Work generated (net)	187.6 kJ/kg
Generated heating	1492 kJ/kg
Generated cooling	101.3 kJ/kg
Heat input	2409 kJ/kg
Heat to power ratio	7.6
Cooling to power ratio	0.54
Power generation efficiency	7.8%
Cogeneration efficiency	67.1%
Trigeneration efficiency	71.3%
Exergy input (at heat source)	833.2 kJ/kg
Exergy delivered as heating	152.4 kJ/kg
Exergy delivered as cooling	1.7 kJ/kg
Power generation exergy efficiency	22.5%
Cogeneration exergy efficiency	40.8%
Trigeneration exergy efficiency	41.0%

Table 6.31: Exergy destructions for each component of the improved trigeneration system.

Component	Exergy destruction	Component	Exergy destruction
Pump	0.14 kJ/kg	Condenser/desorber	86.43 kJ/kg
Regenerator	11.65 kJ/kg	Throttling valve	0.21 kJ/kg
Vapor generator	159 kJ/kg	Evaporator	2.3 kJ/kg
Expander	51.76 kJ/kg	Ejector	116.9 kJ/kg
Water heating heat exchanger	60.28 kJ/kg	Total destructions	488.67 kJ/kg

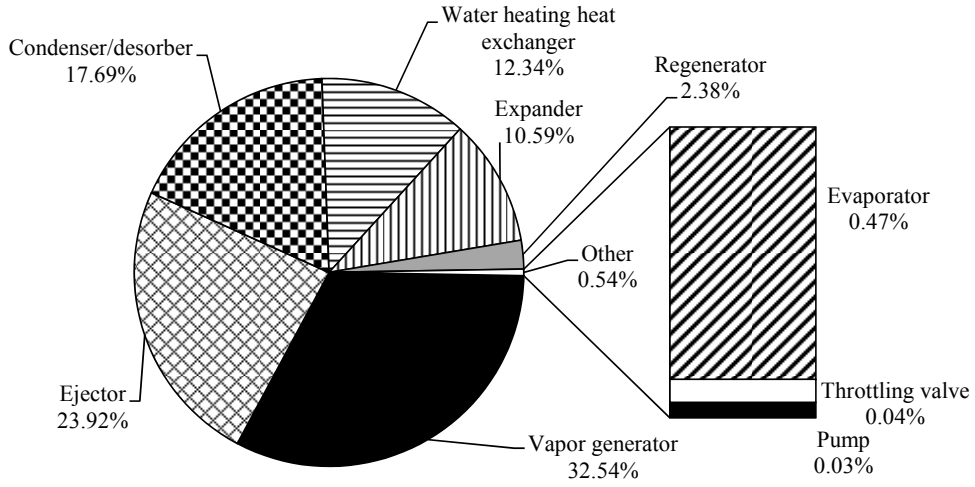


Figure 6.52: Exergy destruction in the components of the improved and optimized trigeneration system (in percentages from total).

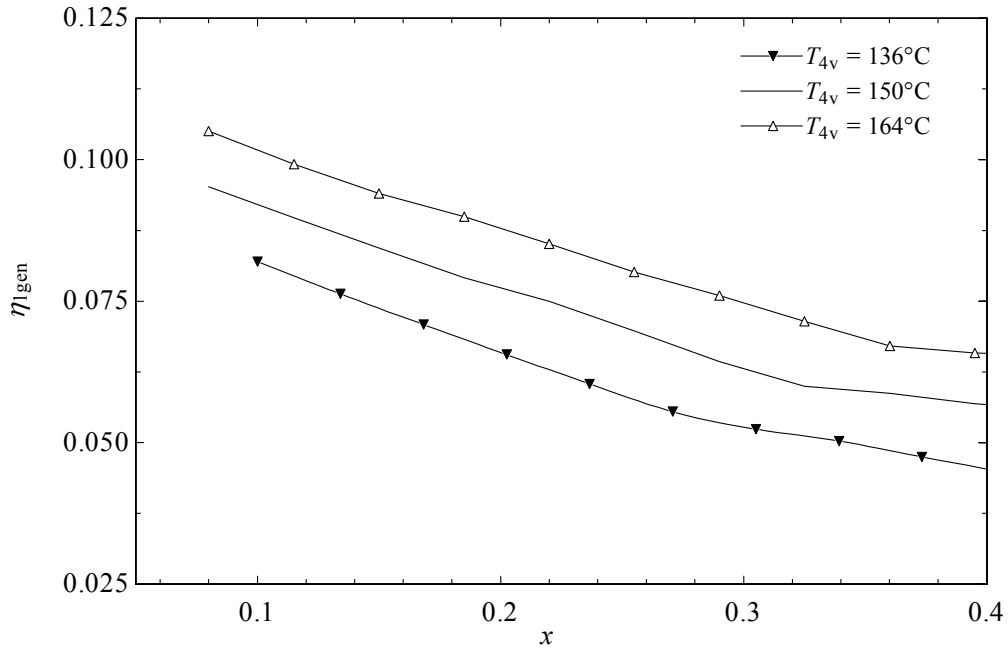


Figure 6.53: Influence of ammonia concentration and temperature of the saturated vapor (T_{4v}) on power generation efficiency (η_1).

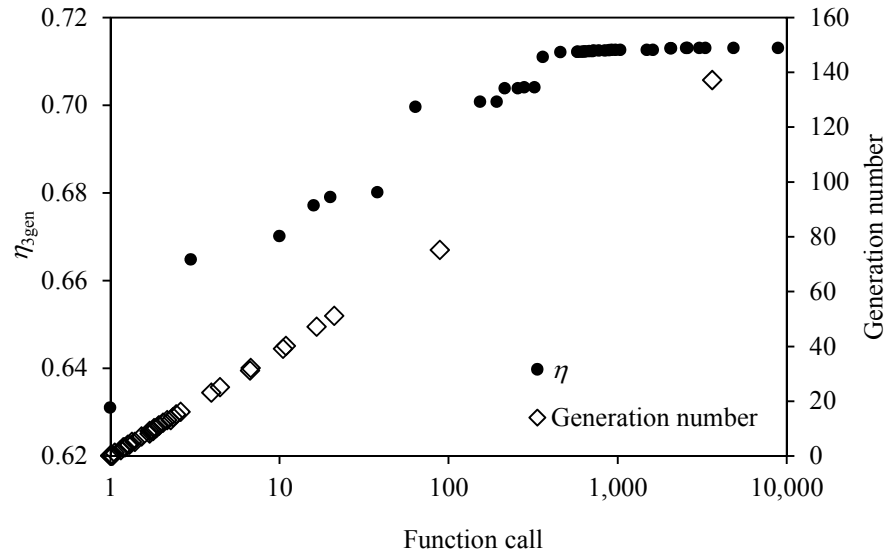


Figure 6.54: Genetic algorithm optimization process: the convergence for trigeneration energy efficiency (left axis) and the increase of the number of generations (right axis).

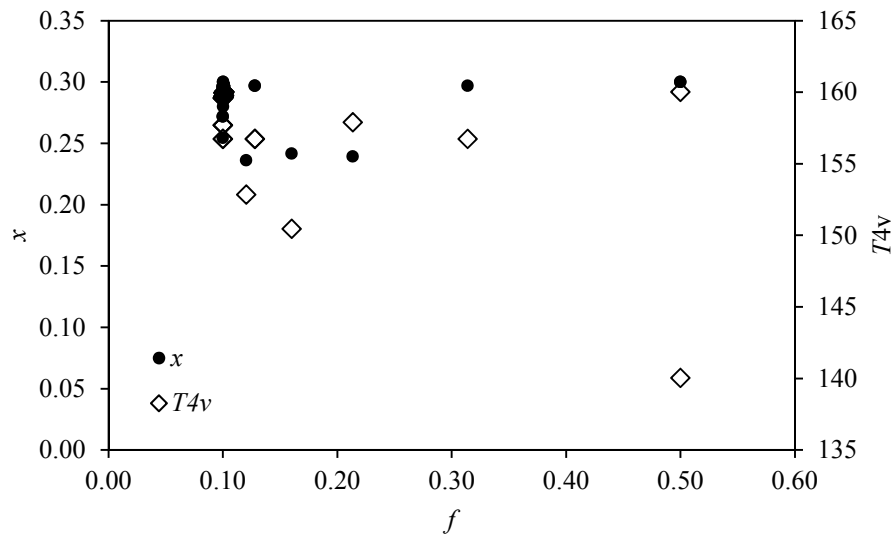


Figure 6.55: Genetic algorithm optimization process: change of the ammonia concentration (x) and of the temperature of the saturated vapor at heat source (T_{4v}) with the flow fraction diverted to the ejector (f).

The performance parameters of the system are given in Table 6.30. The energy efficiency of the improved trigeneration system is 71.3%. If only power and heating are generated then the energy efficiency drops to 67.1%. The power generation only efficiency is 7.8%. The exergy efficiency of power generation is 22.5%. When heat and power are

cogenerated, then the exergy efficiency becomes 40.8%. If power, heating and cooling are generated then the exergy efficiency of the trigeneration system becomes 41%. The exergy destructions in each component of the optimized trigeneration system are given in Table 6.31. The exergy destructions in percentages are represented in a pie-chart as shown in Figure 6.52. The improved trigeneration system has been optimized for maximum energy efficiency using a genetic algorithm.

Since the code for system modeling is elaborated in EES software, the genetic module of the same software has been used to optimize the systems. A multi-variable optimization has been performed with respect to the following variables:

- The flow fraction for vapors diverted to the ejector (f),
- The overall ammonia concentration in the working fluid (x),
- The saturation temperature of the vapor for the pressure condition existent in the vapor generator (T_{4v}).

There are a number of constraints for this optimization. These are as follows:

- The temperature at the expander inlet is maintained constant to 160°C,
- The temperature of the working fluid at condenser outlet is maintained constant to 30°C,
- The working fluid condition at condenser outlet is of saturated liquid,
- The isentropic efficiency of the pump is assumed to 0.8,
- The isentropic efficiency of the expander is assumed 0.75,
- The evaporation temperature is maintained in the range of 4-10°C.

In these conditions, the genetic algorithm is set 64 individuals and maximum 256 generations. The optimization run concluded after 8903 function calls with 137 generations. The evolution of the optimized trigeneration efficiency is shown in Figure 6.54 with respect to the function calls. It is clearly observed that the trigeneration energy efficiency reached 84.6% at the end of the optimization process. Figure 6.55 shows details of the genetic optimization process where the optimum values for x and T_{4v} are plotted against the flow fraction of vapors diverted to the ejector (f). The optimized system variables are as follows:

- Ammonia concentration 20%,
- Vapor flow fraction toward the ejector 0.4,
- Temperature of the saturated vapor inside the vapor generator 150°C.

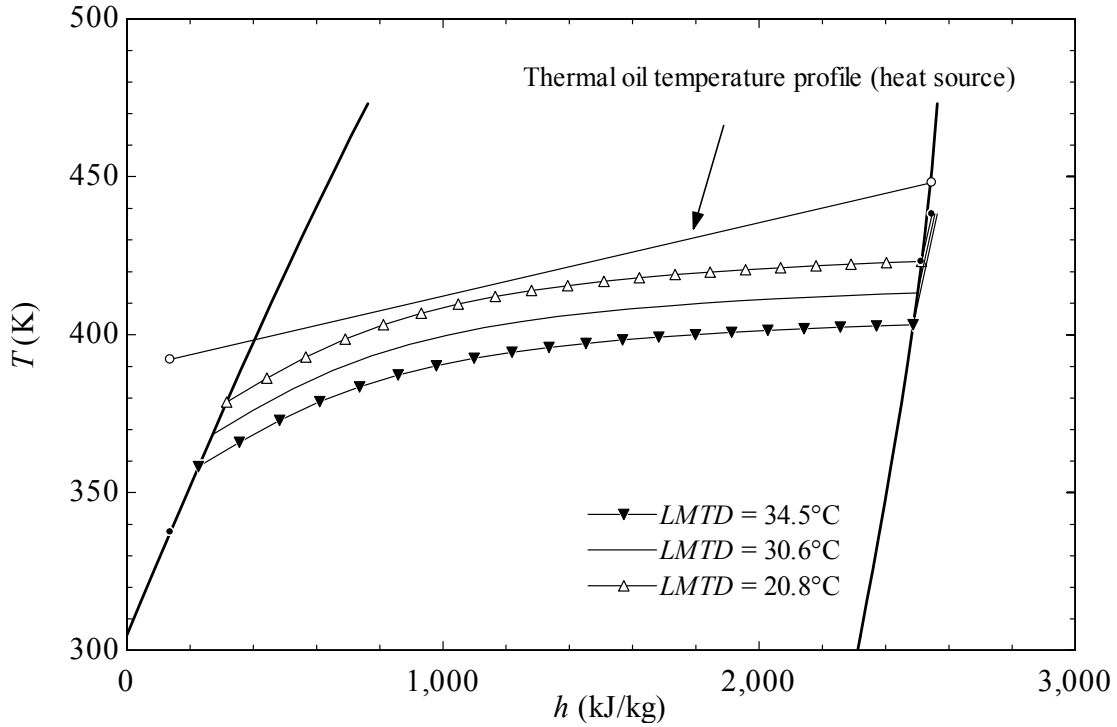


Figure 6.56: Temperature profiles at vapor generator for three values of LMTD.

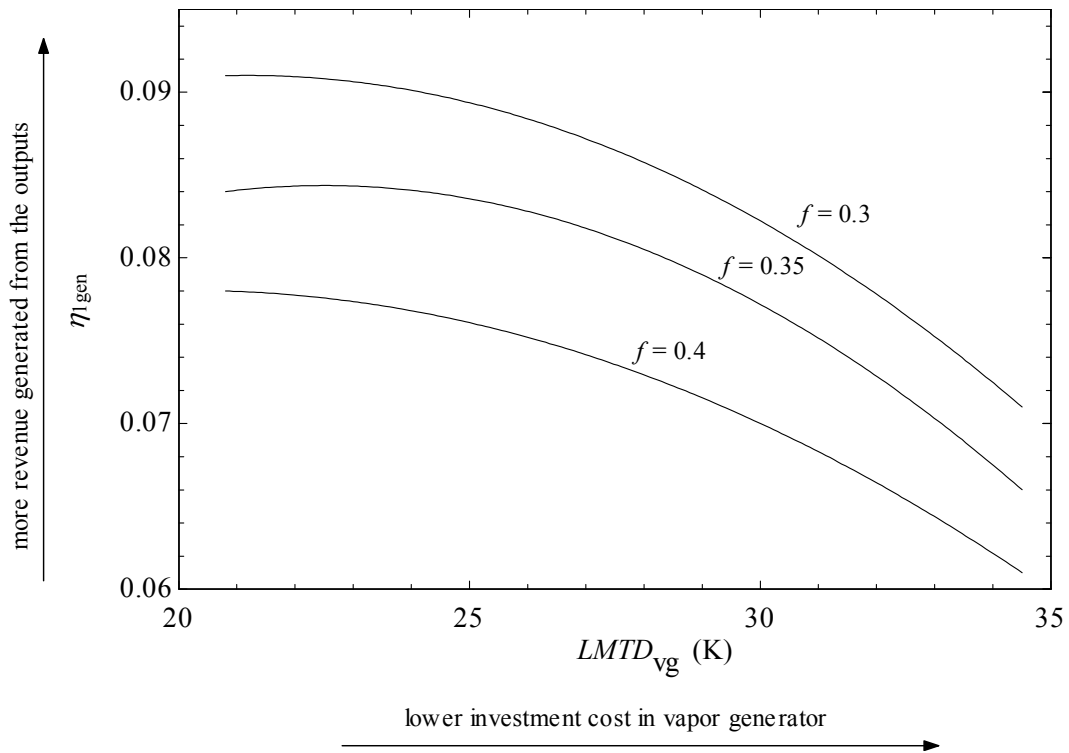


Figure 6.57: Pareto frontiers of two-objective optimization for the trigeneration system when vapor generator cost minimization and the revenue from power generation are the objective functions to be maximized.

Further, multi-objective optimization can be conducted with the improved system for various relevant scenarios. Here, we assume that the system generates power in the range of 1 kW and in addition it generates water heating and air conditioning in amounts that are determined such that the demand of 1 kW power is satisfied first. The heat source is solar energy supplemented with natural gas combustion. Thermal oil is used to transfer the heat from the heat source (solar collector and/or natural gas combustor) to the heat engine. Here the selected thermal oil is Duratherm 240 having a specific heat of 2.4 kJ/kg. So, the vapor generator operates with thermal oil. We fix the inlet and outlet temperature of the thermal oil in the vapor generator as optimization constrains. The temperatures are:

- 448.15 K at inlet
- 392.15 K at outlet.

A parametric study shown in Figure 6.56 illustrates the effect of the LMTD on the vapor generator on the temperature profiles of the thermal oil and working fluid. Here, the ΔT_{pinch} is taken as the ΔT_{min} for the *LMTD* calculation. According to this parametric study it results that the minimum LMTD is approx. 20 K; lower LMTD than this is not practical since the temperature at the pinch point will tend to zero. With the restriction that the minimum LMTD is 20 K at vapor generator a two-objective optimization of the trigeneration system is performed for three assumed vapor flow fraction diverted to the ejector: $f = 0.3, 0.35, 0.4$. The entrainment ratio of the ejector is set in the practical range of 0.05 to 0.15.

The results of the two-objective optimization are shown in Figure 6.57 which illustrates the Pareto frontiers. Observe that when the power generation efficiency is high, then $LMTD_{\text{vg}}$ must be low, therefore the investment cost in the vapor generator is high. However, in such a case the revenues from the power generation product are higher because more power is produced with a more efficient system. The flow fraction f cannot be reduced more than approx. 0.3 because then higher entrainment ratios more than 0.15 are required for the ejector, which becomes unpractical.

In order to optimize the system with respect to the investment cost in vapor generator and the power generation efficiency, the heat transfer surface area has to be determined. Table 6.32 shows the main equations used to determine the heat transfer area in the vapor generator. Recall, that the vapor generator is the most crucial component within the system which must be

optimized as, according to Figure 6.52, it destroys exergy the most. The equations for heat transfer calculation were detailed in Chapter 5, Section 5.

Table 6.32: Equations and assumptions used for determination of the heat transfer area.

Equations	Assumptions and remarks
$\dot{Q}_{vg} = \dot{m}_{oil} \bar{c}_{oil} (T_{in} - T_{out})$ $\dot{Q}_{vg} = \dot{m}_3 (h_5 - h_3)$ $\dot{Q}_{vg} = \bar{U}_{vg} A_{vg} LMTD_{vg}$	\bar{c}_{oil} is assumed fixed to 2.4 kJ/kgK. The LMTD is based on pinch point temperature difference, ΔT_{pinch} . The maximum temperature difference is at oil exit side, $\Delta T_{max} = T_{out} - T_3$. $LMTD = (\Delta T_{max} - \Delta T_{pinch}) / \ln(\Delta T_{max} / \Delta T_{pinch})$
$\frac{1}{\bar{U}_{vg}} = \frac{1}{h_{oil} \eta_f} + \frac{\delta_w}{k_{Al}} + \frac{1}{\bar{h}_{vg}}$	Wall thickness of the meso-channel assumed $\delta_{Al} = 0.5$ mm. Thermal conductivity of the wall taken for pure aluminum k_{Al} . The heat transfer coefficient inside the meso-channel is taken as averaged value
$h_{oil} = 0.023 Re^{0.8} Pr^{0.3}$	The fin efficiency equation used for oil side is taken from Bejan and Kraus (2003)
$\bar{h}_{tp} = \frac{\theta h_v + (2\pi - \theta) \times h_l}{2\pi}$	Here \bar{h}_{tp} is the average transfer coefficient in the two-phase region; θ is the dry channel angle, h_v, h_l are the laminar heat transfer coefficient for liquid and vapor.
$\bar{h}_{vg} = \chi_1 h_l + \chi_{tp} \bar{h}_{tp} + \chi_v h_v$	Where $\chi_{1,2,3}$ are the fractions of the total heat transfer area for liquid flow, two phase, and superheated vapor flow $\chi_1 + \chi_2 + \chi_3 = 1$.

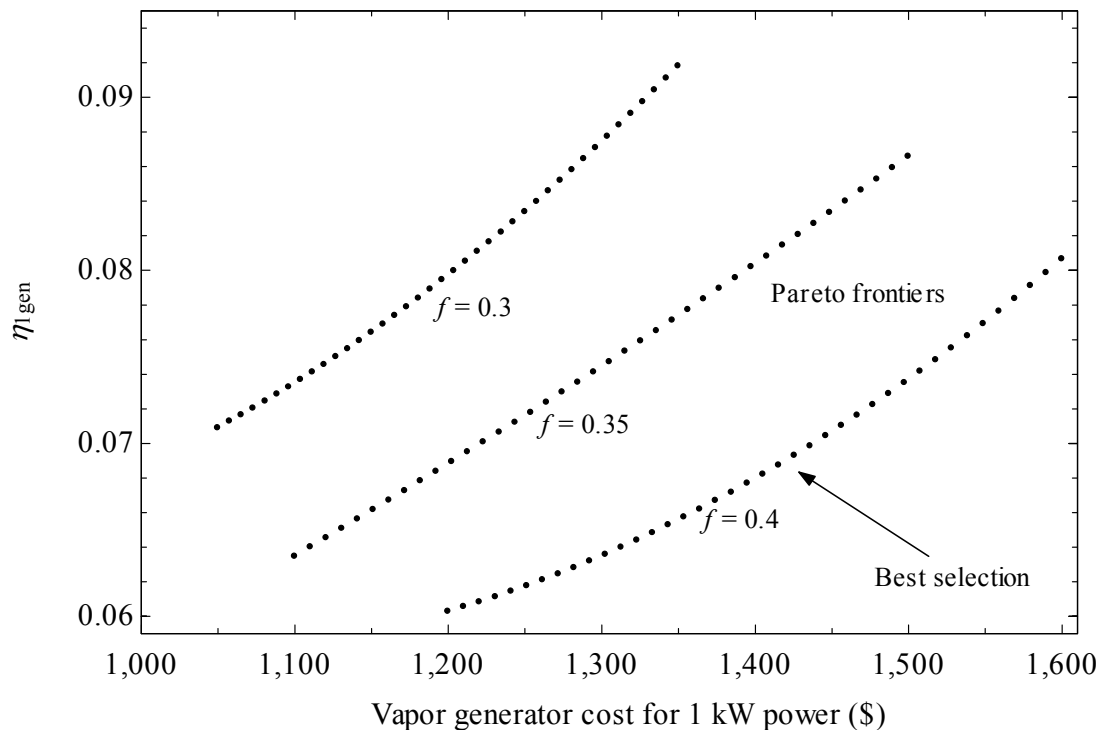


Figure 6.58: Pareto frontier for two-objective optimization considering the cost of vapor generator and the power generation efficiency as objective functions.

Note that the averaging procedure for the heat transfer coefficient is detailed elsewhere in Hogerwaard et al. (2013). The other assumption made here regards the heat exchanger cost. Namely, it is assumed that the cost of the vapor generator is \$1000 per square meter. Under this

assumption, a multi-objective optimization is conducted considering the cost of the vapor generator and the power generation efficiency as objective functions.

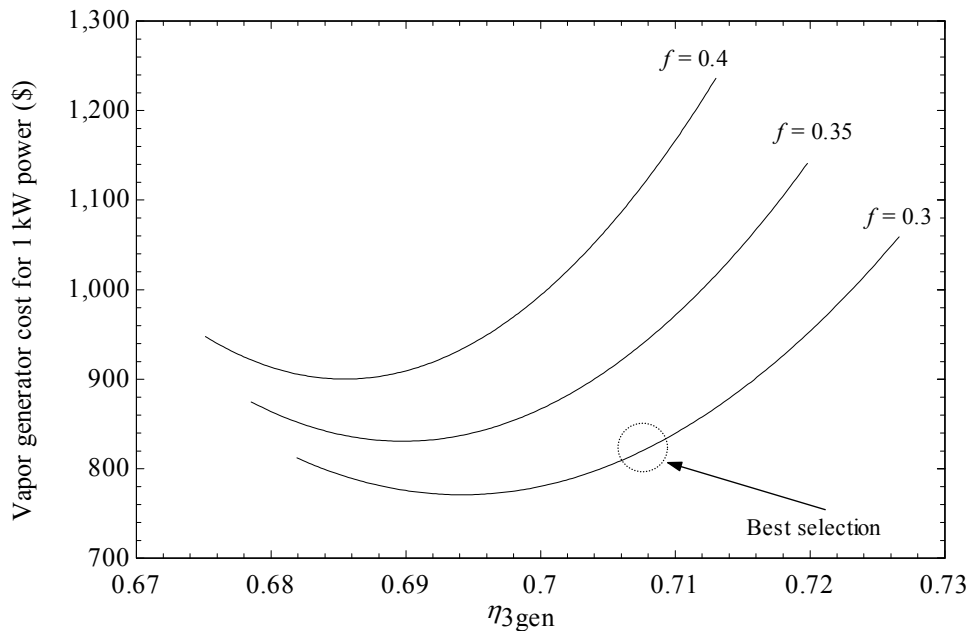


Figure 6.59: Pareto frontiers for two-objective optimization considering the cost of vapor generator and the trigeneration efficiency as objective functions.

The results are shown in Figure 6.58. Here, three Pareto frontiers are obtained for three flow rate ratios: 0.3, 0.35, 0.4. The trade-off is that in order to increase the system power generation efficiency the vapor generator cost (thence the system cost) increases. The Pareto frontiers help in selecting the best system configuration. From the figure, results that for enhanced power generation, fewer vapors must be diverted to the ejector and therefore more vapor go to the expander (f should be smaller). The systems with cost of \$1200 to \$1400 for the vapor generator give reasonable energy efficiency for generation of 1 kW power.

Regarding the trigeneration efficiency, the two-objective optimization gives somehow similar results, namely, when the objective functions are the cost of vapor generator and the trigeneration energy efficiency. From Figure 6.59, the results can be obtained. Here, it is observed that there is minimum vapor generator cost for efficiencies in the range of 0.68 to 0.7. A proposed best selection system is shown in the figure in terms of trigeneration efficiency and vapor generator cost for a system that generates 1 kW power and the system in addition produces water heating and air conditioning as valuable commodities.

7. Conclusions and recommendation

7.1. Conclusions

The experimental investigation of the scroll expander based trigeneration system has been performed in a number of test bench set-ups. This facilitated to acquire a set of well-defined experimental data for performance analysis. Starting with a preliminary experimental run of expander with compressed air, 6 other experimental run have been performed. After each run, some modifications of the system or components were performed to achieve better performance of the system. The following points are required to highlight as an important findings of the experiments.

- 1) Scroll expander used in the trigeneration system was modified and redesigned from refrigeration scroll compressor. Initially modification was done by removing check valve and pressure relief valve and installing two thrust bearing. By preliminary test with compressed air, the scroll expander RPM reached to a maximum 600, which is much lower to develop useful work. However, for compressor operation as it is designed, this leakage does not have much adverse effect because high pressure gas from the outer pocket leaks towards suction side pockets and forced back to merge with the high pressure side. On the other hand, for expander operation fluid from the high pressure intake side bleeds out toward low pressure exhaust side through the leakage area and never contribute to work generation. This reduces the energy conversion within the expander. After analysis, the radial gap between the scroll wrap and hub of both scroll was reduced by machining the scroll wrap. Finally, a maximum of 2000 RPM is achieved with compressed air of 40 psi.
- 2) The nozzle section of the ejector is used from a modified needle valve due to cost constraint and gave less cooling effect due to manual adjustment of throat area. However, for experimental analysis, the operation was within satisfied limit.
- 3) During run of the experiments, problem faced controlling the boiler fluid feed. It should match the vapour supply of the system. But, due to manual control initially, fluid supply to the boiler was not perfect and sometimes the boiler was over filled and caused ammonia-water vapour generation disruption. However, in the subsequent experiments with experience, the flow control was much precise

Despite the above issues, the heat engine prototype integrated in a trigeneration system, facilitated to perform the experimental analysis successfully. The scroll expander which has an unique characteristic of working with two phase fluid validated the feature as described in the result section. By experimental investigation, it is found that the expander operation is influenced by the inlet temperature, inlet pressure, mass flow rate and condenser pressure of the system. The experimental result shows a maximum isentropic efficiency of 67% and an overall energy efficiency of maximum 7% at 120°C source temperature, while the exergy efficiency is about 30%. In the trigeneration facility, the cooling and heating can be adjusted without affecting power generation. Also, the experimental result shows that the concentration of ammonia is a dominant factor in determining the optimum efficiency with a range of ammonia-water mixture. 40% ammonia concentration found optimum, however higher concentration drastically reduces the work output.

7.2 Recommendations

Based on the experimental analysis, a further research is recommended to improve the performance of the system by integrating additional components and through automation. The suggested areas for future studies, as summarized below:

- 1) Like a steam boiler, the ammonia-water boiler in this trigeneration system needs precise control of ammonia-water feed to the boiler. This feed system mainly depends on supply of the vapour out of the boiler and the level of the liquid within the boiler. An automatic control system of the liquid pump or the flow control valve in the feed line may be used. There are ‘two element’ and ‘three element’ liquid feed control systems are popular for the vapour generating boiler. Whatever be the system, it is recommended that in future an automatic liquid feed control mechanism should be incorporated to the system.
- 2) As the experimental result shows, a continuous vapour flow is required for the steady operation of the expander a boiler with adequate steam space is required to operate the system practically.
- 3) Proper size of check valve in the ammonia-water feed line and automatic vapour flow control valve in the supply line need to be installed in the future experimental set-up or for practical use.
- 4) For desired cooling demand, cascading of the ejectors can be integrated.

REFERENCES

- Abdulateef J.M., Sopian K., Alghoul M.A. Sulaiman M.Y. 2008. Review on solar-driven ejector refrigeration technologies. *Renewable and Sustainable Energy Reviews* 13:1338-1349.
- Aghahosseini S., Dincer I. 2013. Comparative performance analysis of low-temperature Organic Rankine Cycle (ORC) using pure and zeotropic working fluids. *Applied Thermal Engineering* 54:35-42
- Ahmadi P., Dincer I., Rosen MA. 2013. Development and assessment of an integrated biomass-based multi-generation energy system. *Energy* 56:155–166.
- Ahmadi P., Rosen M.A., Dincer I. 2011. Greenhouse gas emission and exergo-environmental analyses of a trigeneration energy system. *International Journal of Greenhouse Gas Control* 5:1540–1549.
- Al-Sulaiman F.A., Dincer I., Hamdullahpur F. 2010. Energy analysis of a trigeneration plant based on solid oxide fuel cell and organic Rankine cycle. *International Journal of Hydrogen Energy* 35:5104–5113.
- Al-Sulaiman F.A., Hamdullahpur F., Dincer I. 2011. Trigeneration: A comprehensive review based on prime movers. *International Journal of Energy Research* 35:233-258.
- ASHRAE 1979. Steam-jet refrigeration equipment. In: 1979 AHRAE Equipment Handbook, Atlanta, GA.
- Badr O., O'Callaghan P.W., Hussein M., Probert S.D. 1984. Multi-vane expanders as prime movers for low-grade energy organic Rankine-cycle engines. *Applied Energy* 16:129-146.
- Bejan A., Kraus A.D. 2003. *Heat Transfer Handbook*. John Wiley and Sons: New York.
- Bloomquist R.G. 2003. Integrating small power plants into agricultural projects. *Geothermics* 32:475-485.
- Blunier B., Pucci M., Cirrincione G., Cirrincione M., Miraoui A., 2008. A scroll compressor with a high performance sensorless induction motor drive for the air management of a pemfc system for automotive applications. *IEEE Transaction on Vehicular Technology* 57:3413–3427.
- Bombarda P., Invernizzi C.M., Pietra C. 2010. Heat recovery from Diesel engines: A thermodynamic comparison between Kalina and ORC cycles. *Applied Thermal Engineering* 30:212-219.
- Borsukiewicz-Gozdur A., Nowak W. 2007. Comparative analysis of natural and synthetic refrigerants in application to low temperature Clausius–Rankine cycle. *Energy* 32:344-352.
- Brasz J.J., Biederman B.P., Holdman G. 2005. Power production from a moderate-temperature geothermal source. GRC Annual Meeting, Reno NV, September 25-28

- Bush J.W., Beagle W.B. 1992. Derivation of general relationship governing the conjugacy of scroll profiles. Proceedings of International Compressor Engineering Conference at Purdue 1079-1088.
- Bush J.W., Beagle W.B. 1992. Derivation of general relationship governing the conjugacy of scroll profiles. Proceedings of International Compressor Engineering Conference at Purdue 1079-1088.
- Cardona E., Piacentino A. 2003a. A measurement methodology for monitoring a CHCP pilot plant for an office building. *Energy and Buildings* 35:919–925.
- Cardona E., Piacentino A. 2003b. A methodology for sizing a trigeneration plant in Mediterranean areas. *Applied Thermal Engineering* 23:1665–1680.
- Cardona E., Piacentino A. 2004. A validation methodology for combined heating cooling and power (CHCP) pilot plant. *Journal of Energy Resources Technology—Transactions of the ASME* 126:285–292.
- Cengel Y.A., Boles M.A. 2010. Thermodynamics: An engineering approach. McGraw-Hill: New York.
- Cetinkaya E. 2013. Experimental Investigation and Modeling of Integrated Trigeneration Systems. PhD Thesis, University of Ontario Institute of Technology, pp. 214.
- Chang, Y.J., Chen Y.M. 2000. Enhancement of a steam-jet refrigerator using a novel application of the petal nozzle. *Experimental Thermal and Fluid Science* 22: 203-211
- Chen Y., Halm N.P., Groll E.A., Braun J.E. 2002. Mathematical modeling of scroll compressors-part I: compression process modeling. *International Journal of Refrigeration* 25:731-750.
- Chen, Y., Lundqvist, P., Johansson, A., Platell, P. 2006. A comparative study of the carbon dioxide transcritical power cycle compared with an organic Rankine cycle with R123 as working fluid in waste heat recovery. *Applied Thermal Engineering* 26:2142-2147.
- Chunnanond K., Aphornratana S. 2004. Ejectors: applications in refrigeration technology. *Renewable and Sustainable Energy Reviews* 8:129-155.
- Colonna P., Nannan N.R., Guardone A., Lemmon E.W. 2006. Multiparameter equations of state for selected siloxanes. *Fluid Phase Equilibria* 244:193–211.
- Corman J.C., Bjorge R.W., Kalina A. 1995. Kalina cycle looks good for combined cycle generation. *MPS Review* 19-22.
- Dai Y., Wang J., Gao L., 2009. Parametric optimization and comparative study of organic Rankine cycle (ORC) for low grade waste heat recovery. *Energy Conversion and Management* 50:576–582.
- Decker L.O. 1993. Consider the cold facts about steam-jet vacuum cooling. *Chemical Engineering Progress* 89:74-77.

- Delgado-Torres M.A., Garcia-Rodriguez L. 2010. Analysis and optimization of the low-temperature solar organic Rankine cycle (ORC). *Energy Conversion and Management* 51:2846-2856.
- Desideri U., Bidini G. 1997. Study of possible optimization criteria for geothermal power plants. *Energy Conversion and Management* 38:1681–1691.
- Dincer I., Rosen M.A. 2012. Exergy, energy, environment and sustainable development. Elsevier: New York.
- Dincer I., Zamfirescu C. 2012. Renewable-energy-based multigeneration systems. *International Journal of Energy Research* 36:1403-1415.
- Dincer I., Zamfirescu C. 2014. Advanced Power Generation Systems. Elsevier: New York.
- DiPippo R. 2004. Second law assessment of binary plants generating power from low-temperature geothermal fluids. *Geothermics* 33:565-586.
- European Commission 2006. World Energy Technology Outlook – 2050. WETO-H₂. European Commission: Brussels.
- Gajewski W., Lezuo A., Nürenberg R., Rukes B., Vesper H. 1989. The Kalina cycle – thermodynamic principle and feasibility. *VGB Kraftwerkstechnik* 69:411-417.
- Garris Jr., Charles A. 2005. Exchange refrigeration system with steam. U.S. Environmental Protection Agency. Washington, D.C. 20460
- Gosney W.B. 1982. Principle of refrigeration. Cambridge: Cambridge University Press.
- Gravensen, J., Henriksen, C. 2001. The geometry of the scroll compressor. *Society for Industrial and Applied Mathematics* 43:113–126.
- Harada K. 2007. Development of a small scale scroll expander. Master of Science Thesis. Oregon State University.
- Harinck J., Turunen-Saaresti T., Colonna P, van Buijtenen J. 2010. Computational study of a high-expansion ratio radial ORC turbine stator. *Journal Engineering of Gas Turbines and Power* 132:054501.
- Hasan A.A., Goswami D.Y., Vijayaraghavan S. 2002. First and second law analysis of a new power and refrigeration thermodynamic cycle using a solar heat source. *Solar Energy* 73:385–393.
- Hettiarachchi H.D., Golubovic M., Worek W.M., Ikegami Y. 2007. The Performance of the Kalina Cycle System 11(KCS-11) With Low-Temperature Heat Sources. *Journal of Energy Resources Technology* 129:243.
- Hogerwaard J., Dincer I., Zamfirescu C. 2013. Analysis and assessment of a new organic Rankine cycle based heat engine system with/without cogeneration. *Energy* 62:300-310.
- Hoque S.Md.E. 2011. Experimental investigation of an R134a based organic Rankine cycle. MSc Thesis, University of Ontario Institute of Technology: Oshawa.

- Huang B.J., Petrenko V.A., Chang J.M., Lin C.P., Hu S.S. 2001. A combined-cycle refrigeration system using ejector cooling cycle as the bottomcycle. *International Journal of Refrigeration* 24:391–399.
- Huangfu Y., Wu Y., Wang R., Xia Z. 2007. Experimental investigation of adsorption chiller for Micro-scale BCHP system application, *Energy and Buildings* 39:120–127.
- Hung B.J., Chang J.M., Wang C.P., Petrenko V.A. 1999. A 1-D analysis of ejector performance. *International Journal of Refrigeration* 22:354-364.
- Hung T. 1997. A review of organic Rankine cycles (ORCs) for the recovery of low-grade waste heat. *Energy* 22:661-667.
- Hung T. 2001. Waste heat recovery of organic Rankine cycle using dry fluids. *Energy Conversion and Management* 42: 539-553.
- Husband W.W., Beyene A. 2008. Low-Grade Heat-Driven Rankine Cycle, A Feasibility Study. *International Journal of Energy Research* 32:1373-1382.
- Ibrahim O.M., Klein S.A. 1993. Thermodynamic Properties of Ammonia-Water Mixtures. ASHRAE Transaction: Symposia 21(2):1495.
- Infante Ferreira C.A., Zamfirescu C., Zaytsev D. 2006. Twin screw oil-free wet compressor for compression–absorption cycle. *International Journal of Refrigeration* 29:556–565.
- IPCC 2007. Climate change 2007: Synthesis report. Intergovernmental panel on climate change. IPCC Plenary XXVII, Valencia, Spain.
- Jaffe L.D. 1983. Dish concentrators for solar thermal energy. *Journal of Energy* 7:304-312.
- Jaffe L.D., Poon P.T. 1981. Secondary and compound concentrators for distributed point focusing solar thermal power systems. *Proceedings of the Intersociety Energy Conversion Engineering Conference*, Atlanta, Ga., pp. 1752-1758.
- Jonsson M., Yan J. 2001. Gas turbine with Kalina bottoming cycle versus evaporative gas turbine cycle. In: Proceedings of the 2001 International Joint Power generation Conference, New Orleans, June 4-7, pp. 77-85.
- Kalina A. 1984. Combined-cycle system with novel bottoming cycle. *Journal of engineering for gas turbines and power* 106:737-742.
- Kalina A.I. 1983. Combined Cycle and Waste Heat Recovery Power Systems Based on a Novel Thermodynamic Energy Cycle Utilizing Low-Temperature Heat for Power Generation. ASME Paper 83-JPGC-GT-3.
- Kanlikar S.G., Grande W.J. 2003. Evolution of microchannel flow passages – Thermohydraulic performance and fabrication technology. *Heat Transfer Engineering* 24:3-17.
- Keenan J.H., Neumann E.P., Lustwerk F. 1950, An investigation of ejector design by analysis and experiment. *ASME Journal of Applied Mechanics* 72:299-309.

- Khaliq A., Choudhary K., Dincer I. 2009b. Exergy analysis of a gas turbine trigeneration system using the Brayton refrigeration cycle for inlet air cooling. In: Proceedings of IMechE Part A: *Journal of power and energy* 224:449-461.
- Khaliq A., Kumar R., Dincer I. 2009a. Performance analysis of an industrial waste heat-based trigeneration system. *International Journal of Energy Research* 33:737-744.
- Khatri K.K., Sharma D., Soni S.L., Tanwar, D. 2010. Experimental investigation of CI engine operated micro-trigeneration system. *Applied Thermal Engineering* 30:1505-1509.
- Khattab N.M., Barakat M.H. 2002. Modeling the design and performance characteristics of solar steam-jet cooling for comfort air conditioning. *Solar Energy* 73:257-267.
- Kim H. J., Lee E.S., Joo N.S., Rha P.C. 2001. Design of scroll expander. In: Proceedings of the 3rd International Compressor Technique Conference, Wuxi City 261-267.
- Kim H. J., Lee E.S., Joo N.S., Rha P.C. 2001. Design of scroll expander. In: Proceedings of the 3rd International Compressor Technique Conference, Wuxi City 261-267.
- Kim M.-H., Bullard C.W. 2001. Development of a microchannel evaporator model for a CO₂ air-conditioning system. *Energy* 26:931-948.
- Klein S.A. 2013. Engineering Equation Solver (EES). F-Chart Software.
- Kohlenbach P., Bongs C., White S., Ward J. 2006. Performance modelling of a desiccant-evaporative sorption air conditioning system driven by micro-turbine waste heat in tropical climates. *EcoLibrium*, December, 25-31.
- Koji T., Suguru F., Kiyoshi S., Tooru S., Hirotohi S., Mitsunobu M. 2004. Heat Recovery Power Generation by Rankine Cycle with Ammonia Working Fluid. *Hitachi Zosen Technical Review* 65:6-9.
- Kong X.Q., Wang R.Z., Huang X.H. 2004. Energy efficiency and economic feasibility of CHCP driven by Stirling engine. *Energy Conversion and Management* 45:1433-1442.
- Lariola J. 1995. Electricity from industrial waste heat using high speed organic Rankine cycle (ORC). *International Journal of Production Economics* 41:227-235.
- Lee, Y.-R., Wu, W.-F. 1995. On the profile design of a scroll compressor. *International journal of refrigeration* 18:308-317.
- Lemort V., Quoilin S., Cuevas C., Lebrun J. 2009. Testing and modeling a scroll expander integrated into an Organic Rankine Cycle. *Applied Thermal Engineering* 29:3094-3102.
- Lin L., Wang Y., Al-Shemmeri T., Ruxton T., Turner S., Zeng S., Huang J., He Y., Huang X. 2007. An experimental investigation of a household size trigeneration. *Applied Thermal Engineering* 27:576-585.
- Litch A.D., Hrnjak P.S. 1999. Condensation of Ammonia in Microchannel Heat Exchangers. Air Conditioning and Refrigeration Center. College of Engineering. University of Illinois at Urbana-Champaign.

- Mago P.J., Chamra L.M., Srinivasan K., Somayaji C. 2008. An examination of regenerative organic Rankine cycles using dry fluids. *Applied Thermal Engineering* 28:998-1007.
- Marques R.P., Hacon D., Tessarollo A., Parise J.A.R. 2010. Thermodynamic analysis of trigeneration systems taking into account refrigeration, heating and electricity load demands. *Energy and Buildings* 42:2323-2330.
- Marston C.H. 1992. Development of the adjustable proportion fluid mixture cycle. *Mechanical engineering* 114:1992 76-81.
- Maurer T., Zinn T. 1999. Experimentelle Untersuchung von Entspannungsmaschinen mit mechanischer Leistungsauskopplung für die transkritische CO₂-Kältemaschine. *DKV-Tagungsbericht* 26.
- Meunier F. 2002 Co- and trigeneration contribution to climate change control. *Applied Thermal Engineering* 22:703–718.
- Meyer A.J., Harms T.M., Dobson R.T. 2009. Steam jet ejector cooling powered by waste or solar heat. *Renewable Energy* 34:297-306.
- Míguez J.L., Murillo S., Porteiro J., López L.M. 2004. Feasibility of a new domestic CHP trigeneration with heat pump. *Applied Thermal Engineering* 24:1409–1419.
- Minciuc E., Le Corre O., Athanasovici V., Tazerout M., Bitir I. 2003. Thermodynamic analysis of trigeneration with absorption chilling machine. *Applied Thermal Engineering* 23:1391-1405.
- Mlcak H. 2002. Kalina cycle concepts for low temperature geothermal. *Geothermal Resources Council Transactions* 26:707-713.
- Munday J.T., Bagster D.F. 1977. A new ejector theory applied to steam jet refrigeration. *Industrial Engineering Chemistry Process Design and Devices* 16:442-449.
- Mustafah M., Yamada N. 2010. Efficiency of Compact Organic Rankine Cycle System with Rotary-Vane-Type Expander for Low-Temperature Waste Heat Recovery. *Journal of Thermal Science and Technology* 5:61-74.
- Nagatomo S., Ootaka T., Morishima A. 1999. Effects of operating conditions on expander performance characteristics. *Transaction of Japanese Society of Refrigeration and Air Conditioning Engineers* 16:59-66
- Nagatomo S., Ootaka T., Morishima A. 1999. Effects of operating conditions on expander performance characteristics. *Transaction of Japanese Society of Refrigeration and Air Conditioning Engineers* 16:59-66.
- Oralli E., Dincer I., Zamfirescu C. 2014. Modeling and analysis of scroll compressor conversion into an expander for Rankine cycles. *International Journal of Green Energy* 11:1-22.

- Oralli E., Tarique Md.A., Zamfirescu C., Dincer I. 2010. Modeling and Analysis of Scroll Compressor conversion into Expander for Rankine Cycle. Second International Conference on Nuclear and Renewable energy resources. Ankara July 4-7.
- Oralli E., Tarique Md.A., Zamfirescu C., Dincer I. 2011. A study of scroll compressor conversion into expander for Rankine cycles. *International Journal of Low Carbon Technologies* 6:200-206.
- Papadopoulos A.I., Stijepovic M., Linke P. 2010. On the systematic design and selection of optimal working fluids for Organic Rankine Cycles. *Applied Thermal Engineering* 30:60–769.
- Park C.Y., Hrnjak P. 2008. Experimental and numerical study on microchannel and round-tube condensers in a R410A residential air-conditioning system. *International Journal of Refrigeration* 31:822-831.
- Park Y.M., Sontag R.E. 1990. A preliminary study of the Kalina power cycle in connection with a combined cycle system. *International Journal of Energy Research* 14:153-162.
- Pouraghaie M., Atashkari K., Besarati S.M., Nariman-zadeh N. 2010. Thermodynamic performance optimization of a combined power/cooling cycle. *Energy Conversion and Management* 51:204–211.
- Puff R., Krueger M. 1992. Influence of the main constructive parameters of a scroll compressor on its efficiency. In: Proceedings of the International Compressor Engineering at Purdue 107-118.
- Quoilin S., Lemort V., Lebrun J. 2010. Experimental study and modeling of an Organic Rankine Cycle using scroll expander. *Applied Energy* 87:1260–1268.
- Ratlamwala T.A.H, Gadalla M.A., Dincer I. 2010. Evaluation and analysis of an integrated pem fuel cell with absorption cooling. In: Proceedings of the 10th International Conference Enhanced Buildings Operations, Kuwait, October 26-28, paper # ESL-IC-10-10-80.
- Romero M., Buck R., Pacheco J.E. 2002. An Update on Solar Central Receiver Systems, Projects, and Technologies. *Journal of Solar Energy Engineering* 124:98-108.
- Roy P., Desilets M., Galanis N., Nesreddine H., Cayer E. 2009. Thermodynamic analysis of a power cycle using a low temperature source and a binary NH₃–H₂O mixture as working fluid. *International Journal of Thermal Sciences* 49:48–58.
- Ruehl C. 2012, BP Energy Outlook 2030. British Petroleum: Washington DC.
- Saleh B., Koglbauer G., Wendland M., Fischer J. 2007. Working fluids for low temperature organic Rankine cycles. *Energy, The International Journal* 32:1210-1221.
- Schuster A., Karellas S., Aumann R. 2010. Efficiency optimization potential in supercritical Organic Rankine Cycles. *Energy* 35:1033-1039.
- Shao L.-L., Yank L., Zhang C.-L., Gu B. 2009. Numerical modeling of serpentine microchannel condensers. *International Journal of Refrigeration* 32:1162-1172.

- Smith I.K., Stosic N., Aldis I.K. 1996. Development of the trilateral flash cycle system Part 3: The design of high efficiency two-phase screw expanders. In: Proceedings of Institute of Mechanical Engineering, Part A, 210(A2):75-93.
- Sokolov M., Hershgal D. 1990. Enhanced ejector refrigeration cycles powered by low grade heat. Part 1. Systems characterization. *International Journal of Refrigeration* 13:351–356.
- Srikhirin P., Aphornratana S., Chungpaibulpatana S. 2001. A review of absorption refrigeration technologies. *Renewable and Sustainable Energy Reviews* 5:343-372.
- Stoecker W.F. 1958. Steam-jet refrigeration. Boston, MA: McGraw-Hill.
- Statistics Canada 2008. Report on energy supply and demand in Canada. Catalogue 57-003-X.
- Sun D.W. 1997. Solar powered combined ejector-vapour compression cycle for air conditioning and refrigeration. *Energy Conversion and Management* 38:479–791.
- Tarique Md.A. 2011. Experimental investigation of scroll based organic Rankine cycle systems. MSc Thesis, University of Ontario Institute of Technology: Oshawa.
- Tarique Md.A., Dincer I., Zamfirescu C. 2014. Experimental investigation of a scroll expander for an organic Rankine cycle. *International Journal of Energy Research* DOI: 10.1002/er.3189.
- Tarique Md.A., Dincer I., Zamfirescu C. 2014. Experimental investigation of scroll based organic Rankine cycles. In: Proceedings of the International Green Energy Conference, Eskisehir: Turkey.
- Tarique Md.A., Dincer I., Zamfirescu C. 2014b. Energy and Exergy Analyses of solar-driven ORC integrated with fuel cells and electrolyser for hydrogen and power production. In: Progress in Exergy, Energy and the Environment. DOI 10.1007/978-3-319-04681-5_7: Springer International: Switzerland.
- Taylor B.N., Kuyatt C.E. 1994. Guidelines for Evaluating and Expressing the Uncertainty of NIST Measurement Results, National Institute of Standards and Technology Technical Note 1297.
- Tchanche B.F, Papadacos G. Lambrinos, G. Frangoudakis, A. 2008. Criteria for working fluids selection in low-temperature solar organic Rankine cycles. Proceedings of Eurosun Conference, Lisbon, Portugal, 7–10 October.
- Tillner-Roth R., Firend D.G. 1998. A Helmholtz free energy formulation of the thermodynamic properties of the mixture {water + ammonia}. *Journal of Physical Chemistry Reference Data* 27:63.
- Tojo K., Igekawa M., Maeda N., Machiela S., Shiibayashi M., Uchikiawa N. 1986. Computer modeling of scroll compressor with self-adjusting back-pressure mechanism. In: Proceedings of the International Compressor Engineering at Purdue 872-886.
- Tuo H., Bileskus A., Hrnjak P. 2012. Experimentally validated model of refrigerant distribution in a parallel microchannel evaporator. *SAE International Journal of Materials and Manufacturing* 5:365-374.

- Uehara H., Ikegami Y. 1993. Parametric performance analysis of OTEC using Kalina cycle. In: Proceedings of the Joint Solar Engineering Conference. ASME pp. 203-207.
- United Nations 2013. World Population Prospects: The 2012 Revision, Key Findings and Advance Tables. Department of Economic and Social Affairs, Population Division. Working Paper No. SA/P/WP.227.
- US EIA 2009. Forms EIA-457 A and C of the 2009 Residential Energy Consumption Survey. U.S. Energy Information Administration, Office of Energy Consumption and Efficiency Statistics
- Wagar W.R., Zamfirescu C., Dincer I. 2010. Thermodynamic Performance Assessment of an Ammonia-Water Rankine Cycle for Power and Heat Production. *Energy conversion and management* 51:2501-2509.
- Wang B., Li X., Shi W. 2005. A general geometrical model of scroll compressors based on discretional initial angles of involute. *International Journal of Refrigeration* 28:958-966.
- Wang B., Li X., Shi W. 2005. A general geometrical model of scroll compressors based on discretional initial angles of involute. *International Journal of Refrigeration* 28:958-966.
- Wang X., Zhao L., Wang J., Zhang W., Zhao X., Wu W. 2010. Performance evaluation of a low-temperature solar Rankine cycle system utilizing R245fa. *Solar Energy* 84:353-364.
- Yamamoto T. 2001. Design and testing of the organic Rankine cycle. *Energy* 26:239-251.
- Yanagisawa T., Shimizu T., Fukuta M., Handa T. 1988. Study on fundamental performance of scroll expander. *Japanese Society of Mechanical Engineers* 54:2798-2803.
- Yanagisawa T., Shimizu T., Fukuta M., Handa T. 1988. Study on fundamental performance of scroll expander. *Japanese Society of Mechanical Engineers* 54:2798-2803.
- Zamfirescu C., Dincer I. 2008. Thermodynamic analysis of a novel ammonia-water trilateral Rankine cycle. *Thermochimica Acta* 477:7-15
- Zamfirescu C., Dincer I. 2008. Thermodynamic analysis of a novel ammonia-water trilateral Rankine cycle. *Thermochimica Acta* 477:7-15.
- Zamfirescu C., Dincer I., Stern M., Wagar W.R. 2012. Exergetic, environmental and economic analyses of small-capacity concentrated solar-driven heat engines for power and heat cogeneration. *International Journal of Energy Research* 36:397-408.
- Zanelli R., Favrat D. 1994. Experimental investigation of a hermetic scroll expander-generator. In: Proceedings of International Compressor Engineering Conference, Purdue, 459-464.
- Ziher D., Poredos A. 2006. Economics of a trigeneration system in a hospital. *Applied Thermal Engineering* 26:680-687.